VOLUME 119 NUMBER 3

# THE ASTROPHYSICAL JOURNAL

AN INTERNATIONAL REVIEW OF SPECTROSCOPY AND ASTRONOMICAL PHYSICS

MAY 1954

THE SECONDARY COMPONENT IN THE SPECTRUM OF CAPELLA *K. O. Wright* 471
EMISSION-LINE STARS ASSOCIATED WITH THE NEBULOUS CLUSTER NGC 2264 *George H. Herbig* 483
SPECTROGRAPHIC OBSERVATIONS OF EMISSION-LINE STARS *E. Margaret Burbidge and G. R. Burbidge* 496
A GROUP OF PECULIAR SHELL STARS *E. Margaret Burbidge and G. R. Burbidge* 501
EMISSION-LINE PROFILES FROM EXPANDING ENVELOPES *M. K. Vainu Bappu and D. H. Menzel* 508
RADIO DETERMINATION OF THE VELOCITY AND RADIANT OF THE DELTA AQUARID METEORS . . . *D. W. R. McKinley* 519
MODEL SOLAR CHROMOSPHERES . . . *J. H. Piddington* 531
SOLAR FLARES AND ASSOCIATED 2800 MC/SEC (10.7 CM) RADIATION *Helen W. Dodson, E. Ruth Hedeman, and A. E. Covington* 541
INTENSITY MEASURES OF CALCIUM *PLAGES* FOR COMPARISON WITH 10.3-CENTIMETER SOLAR RADIATION, OCTOBER 16, 1951 . . . *Helen W. Dodson* 564
BRIGHTNESS OF THE SOLAR DISK AT A WAVE LENGTH OF 10.3 CM *A. E. Covington and N. W. Broten* 569
A REVISED ANALYSIS OF THE SOLAR SPECTRUM FROM 2990 TO 2635 A *N. L. Wilson, R. Tousey, J. D. Purcell, F. S. Johnson, and C. E. Moore* 590
THE APPLICATION OF AN OSCILLOSCOPIC MICROPHOTOMETER TO THE SPECTRAL CLASSIFICATION OF LATE-TYPE STARS . . . *William R. Hossack* 613
PHOTOMETRIC AND SPECTROSCOPIC OBSERVATIONS OF STARS IN IC 348 *D. L. Harris, W. W. Morgan, and N. G. Roman* 622
THE SPACE MOTIONS OF AE AURIGAE AND $\mu$ COLUMBAE WITH RESPECT TO THE ORION NEBULA . . . *A. Blaauw and W. W. Morgan* 625
THREE-COLOR PHOTOELECTRIC PHOTOMETRY OF HD 199140 . *Merle F. Walker* 631
THE TRANSFER OF RADIATION BY AN EMITTING ATMOSPHERE. III *Henry G. Horak* 640
MAGNETOHYDRODYNAMIC WAVES UNDER THE ACTION OF THE CORIOLIS FORCE . . . *B. Lehnert* 647
ANALYSIS OF COUNTS OF THE EXTRAGALACTIC NEBULAE IN TERMS OF A FLUCTUATING DENSITY FIELD. II . . . *D. Nelson Limber* 655
A STOCHASTIC MODEL OF A FLUCTUATING DENSITY FIELD. II *Alladi Ramakrishnan* 682

NOTES
THE COMPOSITE SPECTRUM OF HD 50820 . . . *E. Margaret Burbidge and G. R. Burbidge* 686
THE POLARITY OF THE SUN'S MAGNETIC FIELD AND THE RICHARDSON-SCHWARZSCHILD OSCILLATION . . . *Horace W. Babcock* 687
REVIEWS . . . 689
ABSTRACTS OF ASTROPHYSICAL JOURNAL: SUPPLEMENT SERIES
PHOTOMETRIC INVESTIGATION OF THE ECLIPSING BINARY UX URSAE MAJORIS *H. L. Johnson, Barbara Perkins, and W. A. Hiltner* 690
INDEX . . . 693

THE UNIVERSITY OF CHICAGO PRESS
CHICAGO, ILLINOIS, U.S.A.

May 1954 Vol. 119, No. 3

# THE ASTROPHYSICAL JOURNAL

## AN INTERNATIONAL REVIEW OF SPECTROSCOPY AND ASTRONOMICAL PHYSICS

Founded in 1895 by George E. Hale and James E. Keeler

Published in Collaboration with the American Astronomical Society

S. CHANDRASEKHAR
*Managing Editor*

GERARD P. KUIPER
*Associate Editor*

Yerkes Observatory of the University of Chicago

EDITORIAL BOARD

MARTIN SCHWARZSCHILD, JR. (1954-58)
Princeton University Observatory

O. HERZBERG (1952-56)
National Research Council, Ottawa

H. W. BABCOCK (1953-57)
Mount Wilson Observatory of the Carnegie Institution of Washington

FRED L. WHIPPLE (1952-54)
Harvard College Observatory

C. D. SHANE (1952-55)
Lick Observatory, University of California

---

**The Astrophysical Journal** is published bimonthly by the University of Chicago at the University of Chicago Press, 5750 Ellis Avenue, Chicago 37, Illinois, during January, March, May, July, September, and November. ¶Two volumes are published per year, one beginning with the January issue and the other beginning with the July issue. The subscription price is $6.00 per volume or $12.00 per year; the price of single copies is $3.00. (Orders for service of less than a volume will be charged at the single copy rate.) ¶Postage is prepaid by the publishers on all orders from the United States and its possessions. No extra charge is made for postage to countries in the Pan American Postal Union. ¶Postage is charged extra as follows: for Canada, 20 cents per volume, 40 cents per year (total $6.20 per volume, $12.40 per year); on single copies 5 cents (total $3.05); for all other countries in the Postal Union, 40 cents per volume, 75 cents per year (total $6.40 per volume, $12.75 per year), on single copies 10 cents (total $3.10). ¶Subscriptions are payable in advance. Please make all remittances payable to The University of Chicago Press, in United States currency or its equivalent by postal or express money orders or bank drafts.

The following is an authorized agent:

For the British Empire, except North America and Australasia: The Cambridge University Press, Bentley House, 200 Euston Road, London, N.W. 1, England. Prices of yearly subscriptions and of single copies may be had on application.

Claims for missing numbers should be made within the month following the regular month of publication. The publishers expect to supply missing numbers free only when losses have been sustained in transit, and when the reserve stock will permit.

Business correspondence should be addressed to The University of Chicago Press, Chicago 37, Illinois.

Communications for the editors and manuscripts should be addressed to: S. Chandrasekhar, Editor of THE ASTROPHYSICAL JOURNAL, Yerkes Observatory, Williams Bay, Wisconsin.

Line drawings and photographs should be made by the author, and all marginal notes such as co-ordinates, wave lengths, etc., should be included in the cuts. It will not be possible to set up such material in type.

One copy of the corrected galley proof should be returned as soon as possible to the editor, Yerkes Observatory, Williams Bay, Wisconsin. Authors should take notice that the manuscript will not be sent to them with the proof.

The cable address is "Observatory, Williamsbay, Wisconsin."

The articles in this journal are indexed in the *International Index to Periodicals*, New York, N.Y.

Applications for permission to quote from this journal should be addressed to The University of Chicago Press, and will be freely granted.

Microfilms of complete journal volumes are available to regular subscribers only and may be obtained at the end of the year. Orders and inquiries should be addressed to University Microfilms, 313 North First Street, Ann Arbor, Michigan.

Notice to subscribers: If you change your address, please notify us and your local postmaster immediately.

Entered as second-class matter, July 31, 1940, at the Post-Office at Chicago, Ill., under the Act of March 3, 1879.
Acceptance for mailing at special rate of postage provided for in United States Postal Act of October 3, 1917, Section 1103, amended February 28, 1925.
Copyright 1954 by the University of Chicago.

[PRINTED IN U.S.A.]

# THE ASTROPHYSICAL JOURNAL

AN INTERNATIONAL REVIEW OF SPECTROSCOPY AND ASTRONOMICAL PHYSICS

VOLUME 119 MAY 1954 NUMBER 3


## THE SECONDARY COMPONENT IN THE SPECTRUM OF CAPELLA*


K. O. WRIGHT

Dominion Astrophysical Observatory



*Received December 1, 1953*



ABSTRACT

A spectrophotometric study of the spectrum of Capella has been made in the region λλ 3700–6700. Intensity tracings of high-dispersion spectra of Capella obtained near the elongations and near the conjunctions of the two stars have been combined with tracings of the spectra of β Draconis, G2 II, and η Draconis, G8 III, to obtain the intensity profile of selected regions in the secondary spectrum. Examination of these data indicates that the system consists of two normal, giant stars and that the spectral type of the primary component is G5 III and that of the secondary is G0 III. Measures made from the tracings of the radial-velocity displacements of the two components combined with Struve and Kilby's orbital elements for the system, give $K_2 = 27.6 \pm 0.5$ km/sec and a mass ratio, $m_1/m_2 = 1.05 \pm 0.02$, from which it is found that $m_1 = 3.09 \odot$ and $m_2 = 2.95 \odot$. If the ratio of the luminosities of the two components is assumed to be 1.25 at λ 5500, the absolute magnitudes are found to be $M_1 = 0.12$ and $M_2 = 0.37$ and these results are consistent with the mass-luminosity relation derived by Petrie.


The spectrum of Capella[1] has been under investigation for more than half a century. It was found to be a spectroscopic binary, independently, by Campbell[2] and by Newall.[3] Several orbits have been determined from radial-velocity measurements;[4, 5] but in each case the authors have noted that the lines of the spectrum of the secondary component, though undoubtedly present, have been difficult to measure. Reese made a few tentative measures of the secondary lines but did not include them in his orbit; Goos measured twelve lines of the secondary spectrum and found a mass ratio of 1.35. In 1900 and 1901 observers at the Greenwich Observatory, using the 28-inch refractor, observed Capella as a double star having a maximum separation of 0".1; and Christie[6] found the inclination of the orbit to be 30°. Later, Anderson[7] and Merrill[8] observed Capella with the inter-


* *Contributions from the Dominion Astrophysical Observatory*, No. 36, published by permission of the Deputy Minister, Department of Mines and Technical Surveys, Ottawa, Canada.


[1] α Aurigae, HD 34029, α (1950) = 5h13m0; δ (1950) = 45°57'; $m_v = 0.21$; spectral type = G0 (Harvard), G1 (Mount Wilson), G5 + F6 (Morgan).

[2] *Ap. J.*, **10**, 177, 1899.

[3] *M.N.*, **60**, 2 and 418, 1899.

[4] H. M. Reese, *Lick Obs. Bull.*, **1**, 32, 1901; F. Goos, dissertation, Bonn, 1908; W. Struve, *Zs. f. Ap.*, **17**, 61, 1939.

[5] O. Struve and Ruth F. Kilby, *Ap. J.*, **117**, 272, 1953.

[6] *M.N.*, **61**, 70, 1901.

[7] *Ap. J.*, **51**, 263, 1920.

[8] *Ap. J.*, **56**, 40, 1922.

ferometer attached to the Mount Wilson 100-inch telescope, and Merrill obtained the value 41° for the orbital inclination and stellar masses of 4.2⊙ and 3.3⊙. The visual observers agreed that the visual magnitudes of the components were not equal but could not be greatly different.

Recently Struve[9, 10] and his co-workers[11, 12] have made a study of the spectrum of Capella, using high-dispersion plates, and concluded that the observed spectrum does not seem to correspond to a simple superposition of two normal stellar spectra of types G and F. Struve's conclusions concerning the peculiar nature of the spectrum of Capella influenced the writer to make a spectrophotometric study of its spectrum in the belief that a quantitative investigation of the intensities of the lines in the two components would lead to an understanding of the apparent anomalies noted in a visual inspection of the spectrograms. The method and the results are described briefly below and will appear in more detail as a *Publication of the Dominion Astrophysical Observatory*.

## THE OBSERVATIONS

High-dispersion spectrograms of Capella were obtained with Bausch and Lomb grating No. 84 in the Littrow mounting of the spectrograph attached at the Cassegrain focus of the 72-inch telescope. In the second order over the region λλ 4700–6700 the dispersion is 7.0 A/mm, and in the third order from λ 3700 to λ 4600 it is 4.5 A/mm. A slit-width of 0.025 mm was used, and the photographic plates were Cramer Hi-Speed and Kodak II-D and II-F. Observations were begun in the summer of 1951 and continued until the fall of 1953, in order to obtain spectra at phases near the $V_0$-axis and near maximum separation of the components. For this investigation Struve and Kilby's period of 104.023 days was used and also their zero epoch, JD2,433,459.856, corresponding approximately to inferior conjunction of the primary component. Struve has requested that two errata be corrected here: In *Ap. J.*, **117,** 276, 1953, the zero epoch given above should appear rather than J.D. 2,433,549.856. In *Ap. J.*, **117,** 6, 1953, $\mathfrak{M}_F$ should replace $\mathfrak{M}_G$ in lines 5, 7, and 8 and therefore, according to Struve and Kung's data, $\mathfrak{M}_F = 2.5\odot$; $\mathfrak{M}_G = 2.3\odot$. As Struve points out, "the difference is entirely within the uncertainty of these values" and does not change the argument.

The complete spectrum has not been analyzed, but short regions have been examined in detail, and it is believed that the principal features in the spectra of the two components have been noted. Two or more spectrograms were obtained at each phase studied. Microphotometer tracings were reduced to intensities relative to the continuum. Most of the grain effect of the plates was eliminated by superposing several tracings and drawing a mean intensity profile for each phase. Such a profile was obtained at each elongation and at each crossing of the $V_0$-axis at phases 0 and 52 days. For the latter, no observations were used if the phases were more than 2 days from the crossing points, but even then small displacements between the components were detectable. No systematic differences between observations taken at the two crossing points could be detected, except for the expected velocity displacements, and the adopted intensity profile for the $V_0$-phase was obtained by combining all plates taken at those phases. This mean profile was assumed, as a first approximation, to represent the spectrum of the primary component of the system; it was expected to be sufficiently accurate for wave lengths longer than λ 5000, since, in that region, a preliminary inspection of the plates taken at maximum separation indicated that the lines of the spectrum of the secondary component were noticeably weaker than those of the primary and that the line shapes in the spectra were quite similar. Preliminary results indicated that the intensity of the con-

[9] *Sky and Telescope*, **10,** 135, 1951.

[10] *Proc. Nat. Acad., Washington*, **37,** 327, 1951.

[11] O. Struve and S. M. Kung, *Ap. J.*, **117,** 1, 1953.

[12] K. L. Franklin, dissertation, University of California, 1953.

tinuum of the primary spectrum was about twice that of the secondary. However, further investigation showed that the spectrum of $\beta$ Draconis, G2 II, represented the primary better than did the blended spectrum at conjunction, and, as the lines of $\beta$ Draconis were considerably deeper, revised estimates made the luminosities of the two components more nearly equal.

### SEPARATION OF THE SPECTRA OF THE TWO COMPONENTS

The principle of separating the two components in a composite spectrum such as Capella is simple. A spectrum, in this case that of $\beta$ Draconis, is chosen which may be taken to represent the spectrum of the primary component as a first approximation. The intensity profile of the spectrum of $\beta$ Draconis is obtained and compared with that of the composite spectrum observed near maximum velocity displacement. In the regions of longer wave length, the spectrum lines are usually not seriously blended, and lines of primary and secondary can be separated. A direct comparison of the central intensities of numerous lines in the primary component of the composite spectrum with those for the same lines in the spectrum of $\beta$ Draconis gives a measure of the luminosity of the primary relative to that of the sum of the two components. The whole intensity profile of this region of the spectrum of $\beta$ Draconis is reduced by this value and superposed on the composite profile to coincide with the principal lines of the primary spectrum. Differences between the two tracings then represent the intensity profile of the secondary component, and the displacement of the lines thus indicated in the secondary, relative to the same lines in the primary, is a measure of the difference in velocity of the two components.

The intensitometer of this observatory, designed and described by Beals,[13] is very suitable for separating the two components in a composite spectrum as described above. Basically, it consists of two movable transport mechanisms to move the original microphotometer tracing and the final intensity tracing, set at right angles to each other. Between them is a ground-glass plate, mounted to move perpendicularly to the motion of the intensity tracing, and to which the pen recording the intensities is attached. The calibration-curve is drawn on the glass plate; under it are a thin strand of wire perpendicular to the direction of motion of the microphotometer tracing, which acts as a standard line, and a pointer that intersects the standard line and that may be set at the level of the continuous background on any tracing. The whole glass plate is illuminated from below, and, by means of two mirrors and a condensing lens, the calibration and standard marks are projected upon the microphotometer tracing. In this investigation the intensitometer has been used in two new, though obvious, ways. In order to change the intensity scale, a tracing may be inserted in the machine in place of the microphotometer tracing, and, by drawing a straight line on the illuminated plate at the desired angle instead of the usual calibration-curve, the reduced tracing will appear when the run through the machine is completed.

Secondly, the ordinate of one intensity tracing can be subtracted from another and a tracing obtained showing the variation with wave length of these intensity differences. In the present case the intensity profile of the secondary spectrum is derived. The box containing the original (or microphotometer) tracing can be moved parallel to the standard line. Therefore, as the tracing, on which both composite and primary spectra have been superposed, is moved in wave length, one operator moves the box to keep the intensity profile of the primary spectrum superposed on the mark indicated by the pointer which registers the level of the continuum. At the same time, a second person performs the usual operation of keeping superposed the intensity profile of the composite spectrum, the line drawn on the glass plate (at 45° in this case when a 1:1 ratio is required), and the standard line. With a little practice the simultaneous motions can be maintained, and tracings can be duplicated well within the errors of the originals.

[13] *J.R.A.S. Canada*, **38**, 65, 1944.

In this study of the spectrum of Capella the above method has been followed, and all tracings of the secondary spectrum have been produced in this way. Intensity tracings of the primary spectrum (either the $V_0$-spectrum or that of $\beta$ Draconis), reduced in the correct proportion, were subtracted from tracings of the composite spectrum, taken at phases near maximum separation of the components.

## THE SECONDARY SPECTRUM

Intensity tracings and spectra of representative regions in the spectrum of Capella are reproduced in Figures 1–7. The spectra are photographs of single plates, but the tracings are averages of two or more plates in each case, and most of the effect of grains in the photographic emulsion has been eliminated. The relative luminosities of the components adopted for these diagrams must not be considered definitive, though they appear to fit the present data within about 5 per cent of the adopted continuum (which itself is somewhat uncertain, particularly in the shorter-wave-length regions). The criteria used in deriving the relative luminosities are (1) that the intensities of lines in the primary spectrum should agree with those in the composite spectrum if the latter are not blended with other lines in the secondary and (2) that the secondary spectrum determined from different phases and therefore different velocity displacements should agree. If the derived secondary spectrum can be related to observed stellar spectra, then it can be assumed that the primary spectrum, as adopted, is approximately correct and that the system consists of only two normal stars. No bright star has yet been found that has precisely the same spectrum as the secondary component of Capella; however, the general features are not inconsistent with the spectrum of a normal giant of late F or early G spectral type. The principal features that have been examined in the spectrum are described briefly as follows:

The absorption line *Hα* is strong in the spectrum of Capella, and, in spectra obtained at the elongations, the line in the secondary spectrum appears on the Victoria plates as a weak wing displaced in approximately the expected position. The *Hα* line in the spectrum of $\eta$ Draconis, G8 III, is quite similar to the mean *Hα* observed in the spectrum of Capella at the conjunctions; the *Hα* in the spectrum of $\beta$ Draconis is considerably broader. Therefore, $\eta$ Draconis was assumed to be similar to the primary component of Capella for this line, and the relative luminosities of primary and secondary components thus derived are 0.60 and 0.40. The *Hα* line in the secondary spectrum is appreciably wider than that of the primary, and the wings extend at least 12 A, corresponding to the spectrum of a star appreciably earlier in spectral type than that of the primary component.

Both components of the sodium D lines, λ 5890 and λ 5896, can be seen clearly in spectra taken at the elongations, though the lines of the secondary spectrum are definitely weaker than those of the primary. The spectrum of $\eta$ Draconis is again a better fit for the primary spectrum than that of $\beta$ Draconis, and with it relative luminosities of primary and secondary of 0.55 and 0.45 are obtained. As shown in Figures 1, *a*, and 2 the spectrum of the secondary component appears to have lines considerably broader than those in the spectrum of $\theta$ Ursae Majoris, F6 III, though the central intensities in both spectra are comparable; the lines are more similar in shape to the D lines in the spectrum of $\epsilon$ Leonis, G0 II, though the latter may be deeper.

The region λλ 5400–5560 has been studied in some detail because in this region numerous lines of *Fe* I and other atoms appear in the spectrum, and many of these lines are almost free from blends. Spectra and tracings from λ 5495 to λ 5540 are shown in Figures 1, *b*, and 3; the two components of the *Fe* I line, λ 5497, can be seen clearly on the tracings of the plates taken near elongation, but the line in the secondary spectrum is considerably weaker than that in the primary. In this region $\beta$ Draconis is considered to be a fair representation of the primary spectrum, and, if a ratio of 55:45 for the luminosities of the components of Capella is assumed, the lines in the secondary

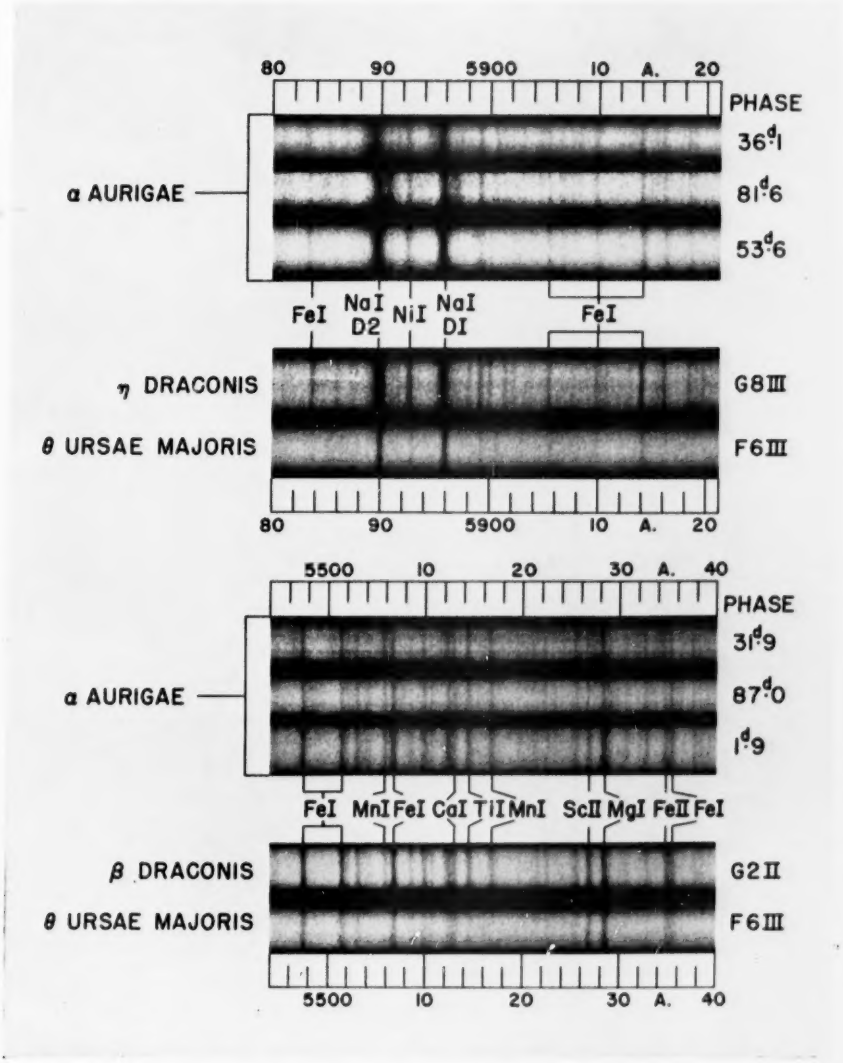


FIG. 1.—Spectra of Capella at elongations and at conjunction and of $\eta$ Draconis G8 III, $\beta$ Draconis G2 II, and $\theta$ Ursae Majoris F6 III. The spectra of Capella have been displaced to place the lines of the primary spectrum directly above one another. (*a*) *above*, in the region λλ 5880–5921; (*b*) *below*, in the region λλ 5494–5540.

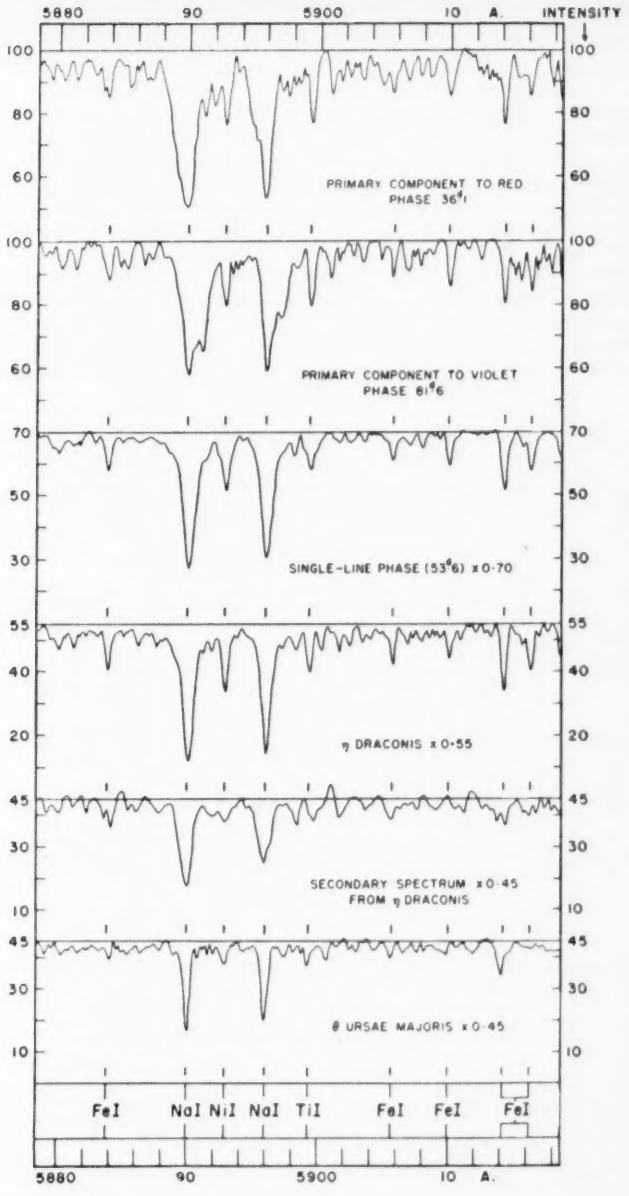


FIG. 2.—Intensity tracings of the spectrum of Capella, $\eta$ Draconis, and $\theta$ Ursae Majoris in the region $\lambda\lambda$ 5878–5918. These tracings should be compared with the spectra shown in Fig. 1, *a*. Note the sodium D lines in the secondary spectrum both on the tracings and on the spectra taken at elongations. The relative displacement of the lines in the two components is about 1.0 A.

spectrum are approximately the same strength as those in the spectrum of $\theta$ Ursae Majoris. However, the *Mn* I lines at $\lambda$ 5506 and $\lambda$ 5516 are definitely present in the spectrum of the secondary star, and therefore it seems probable that the luminosity ratio should be increased slightly to make the line strengths appear more like those in $\epsilon$ Leonis. The *Sc* II line, $\lambda$ 5526, is stronger in $\beta$ Draconis than in the primary spectrum, as is shown by a rise above the continuum in each of the separate determinations of the secondary spectrum; therefore, the primary star is probably less luminous than $\beta$ Draconis. The ratio of the intensities of the two lines at $\lambda$ 5534, *Fe* II and *Fe* I, also appears to be a criterion of absolute magnitude, as the *Fe* II line is much the stronger in $\gamma$ Cygni, F8 I*b*. This ratio in the secondary spectrum depends on whether the $V_0$-spectrum or that of $\beta$ Draconis is taken to represent the primary; but, with the latter, the absolute magnitude of the secondary star would appear to be lower than that of $\theta$ Ursae Majoris.

In the region $\lambda\lambda$ 4200–4425 the luminosities of the two components seem to be nearly equal when the primary spectrum is assumed to be similar to that of $\beta$ Draconis; but, when the $V_0$-spectrum is used as the primary, the ratio of primary to secondary is about

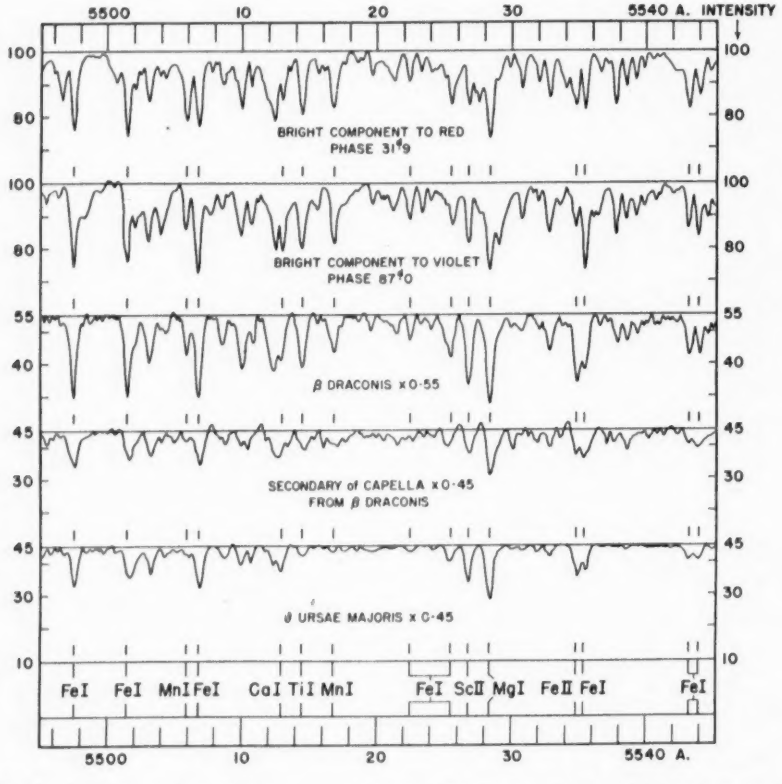


FIG. 3.—Intensity tracings of the spectrum of Capella, $\beta$ Draconis, and $\theta$ Ursae Majoris in the region $\lambda\lambda$ 5495–5545. The relative displacement of the lines in the two components is 0.9 A. These tracings should be compared with the spectra shown in Fig. 1, *b*.

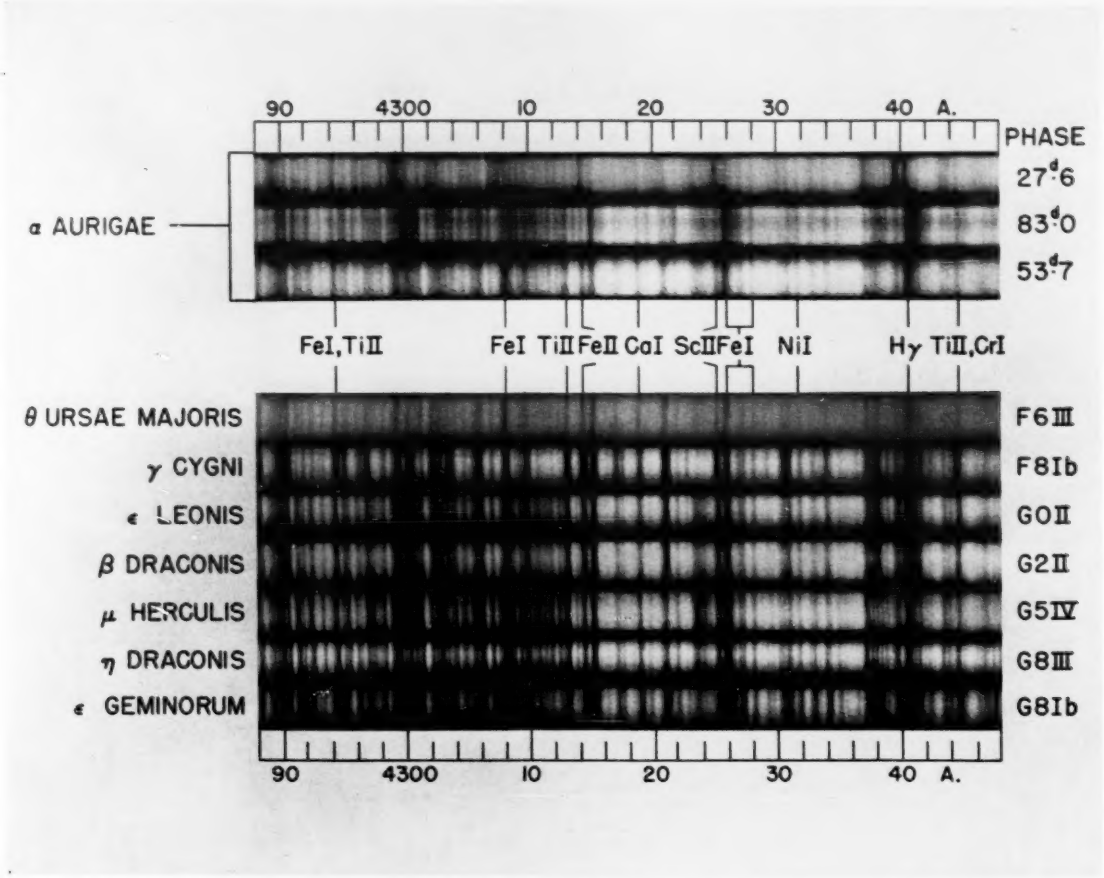


FIG. 4.—Spectra of Capella at elongations and at conjunction and of stars of similar spectral type in the region λλ 4288–4348. The spectra of Capella have been displaced to place the lines of the primary spectrum directly above one another, and the identification marks refer to the primary spectrum.

60:40. The spectrum from λ 4288 to λ 4350 is shown in Figures 4 and 5. The intensity of the lines at λ 4325 is comparable to, though less than, that of $H\gamma$ at λ 4340, which places the spectral type of the secondary component at G0 or somewhat earlier. The strength of the G band, λλ 4298–4312, also places the type close to G0.

Spectra of Capella at the two elongations and at the $V_0$-axis and of other stars of possibly similar spectral type in the region λλ 4027–4080 are shown in Figure 6, and tracings from which the secondary spectrum was obtained are given in Figure 7. A preliminary estimate of the height of the continuum in the composite spectrum was too low and gave a deceptively simple appearance to the secondary spectrum, but several

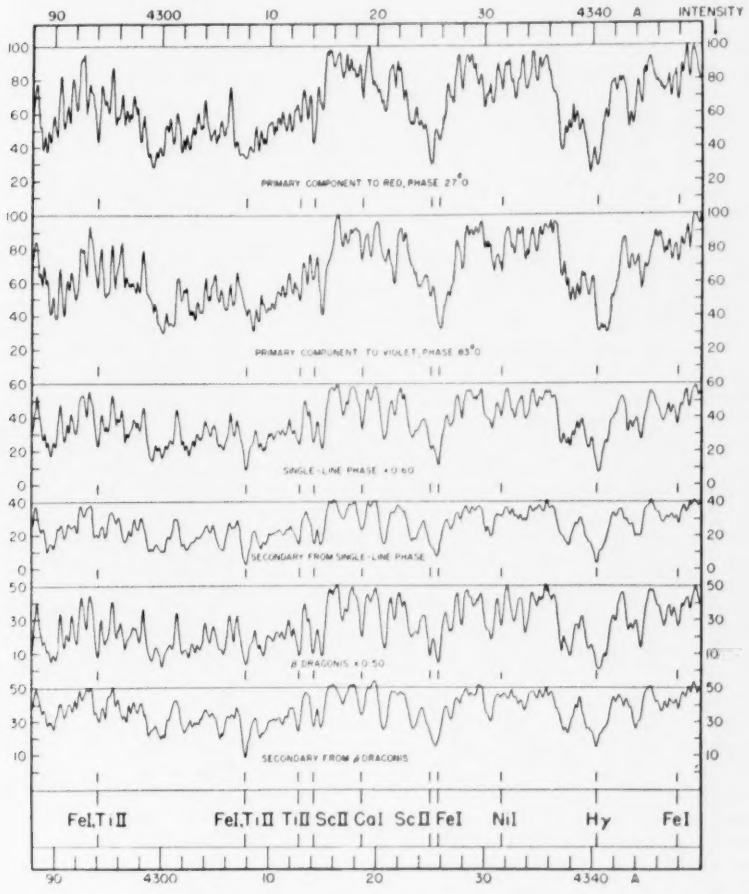


FIG. 5.—Intensity tracings of the spectrum of Capella and of β Draconis in the region λλ 4288–4350. The relative displacement of the lines in the two components is 0.7 A. These tracings should be compared with the spectra shown in Fig. 4. The contributions of the two components to the composite spectra are almost equal in this region. The G band in the secondary spectrum shows that the spectral type is about G0.

points rose far above the continuum. The continua of tracings at elongation were then raised 7 per cent, with the results shown here, assuming that the luminosities of the two components are equal when $\beta$ Draconis is taken to represent the primary star and that the ratio is 55:45 when the $V_0$-spectrum represents the primary. In this region the spectral type is not readily defined, though the ratio $\lambda$ 4072:$\lambda$ 4078 is often used as a luminosity criterion.

The principal features to be noted in this region are the apparent strengths of the strong *Fe* I lines at $\lambda\lambda$ 4046, 4064, and 4072 at the elongations. As noted by Struve and Kung,[11] the spectrum at the normal position of the line in the primary spectrum (indicated by a vertical dash in the diagrams) seems to be weaker than the displaced line in the secondary spectrum. The tracings show that this effect, while a real phenomenon on the plates is not a spectroscopic anomaly. When the normal lines in the primary spectrum, represented either by $\beta$ Draconis or by the $V_0$-spectrum, are subtracted from the composite spectra taken at either elongation, normal lines in the secondary spectrum are the result, without the appearance of any unusual or unexpected lines or intensities. The apparent enhancement of the lines in the displaced secondary spectrum at the elongations is the result of the superposition of the secondary line upon the broad wing of the same line in the primary spectrum.

In spectra of Capella at wave lengths shorter than $\lambda$ 4000, the H and K lines of *Ca* II are normal for late-type stars and have very broad wings and central intensities of a few per cent. The emission at the center of the lines noted by Struve[10, 11] is also observed on the Victoria plates. The hydrogen line $H\zeta$ at $\lambda$ 3889 is considerably weaker in the spectrum of the secondary component of Capella than the same line in the spectrum of $\theta$ Ursae Majoris, which indicates a spectral type later than F6. Further, there is a well-defined *CN* band with head at $\lambda$ 3883. As this band does not appear to any extent in late F-type stars, it seems almost certain, therefore, that the secondary component in the spectrum of Capella must be as late as G0. In the region $\lambda\lambda$ 3720–3780 the secondary spectrum is noticeably stronger than the primary, and, in spectra taken at elongation, some of the principal features belong to the secondary component, in marked contrast to the remainder of the spectrum. The hydrogen lines and the *Ti* II lines at $\lambda$ 3759 and $\lambda$ 3761 are stronger in the secondary spectrum than in the primary and thus confirm the statement that the spectral type of the secondary component is earlier, but not much earlier, than that of the primary.

As the general appearance of the $V_0$-spectrum is quite similar to that of a G2 star, it seems probable that the true primary spectrum is somewhat later in spectral type, perhaps G5. The visual magnitude of Capella is 0.21, and its adopted parallax is 0".070. This value for the parallax is the mean of two: 0".073 given in the *Yale General Catalogue of Trigonometric Stellar Parallaxes*[14] and 0".068 found by combining the data from the interferometric orbit[8] with those from the spectroscopic orbit[8] and the value of $K_2$ as determined in the following section. Assuming that the primary star is 1.25 times as luminous as the secondary star at $\lambda$ 5500, the absolute magnitudes of the components are 0.12 and 0.37, which correspond to Morgan's class III, normal giants. Therefore, it is proposed that the spectra of the components of Capella be considered as G5 III and G0 III. This classification is partially confirmed by the ratio of the luminosities found at the various wave lengths studied. According to Keenan and Morgan,[15] the effective temperature of a G5 III star is 4650° K and that of a G0 III star is 5300° K. Assuming a luminosity ratio of 1.25 at $\lambda$ 5500 and a Planckian distribution of energy, the calculated relative intensities of primary to secondary for the spectral regions studied agree very well with the empirical values adopted from the intensity profiles, ranging from 45:55 at $\lambda$ 3900 to 60:40 at $\lambda$ 6500.

[14] New Haven: Yale University Press, 1952.

[15] *Astrophysics*, ed. J. A. Hynek (New York: McGraw-Hill Book Co., 1951), p. 12.

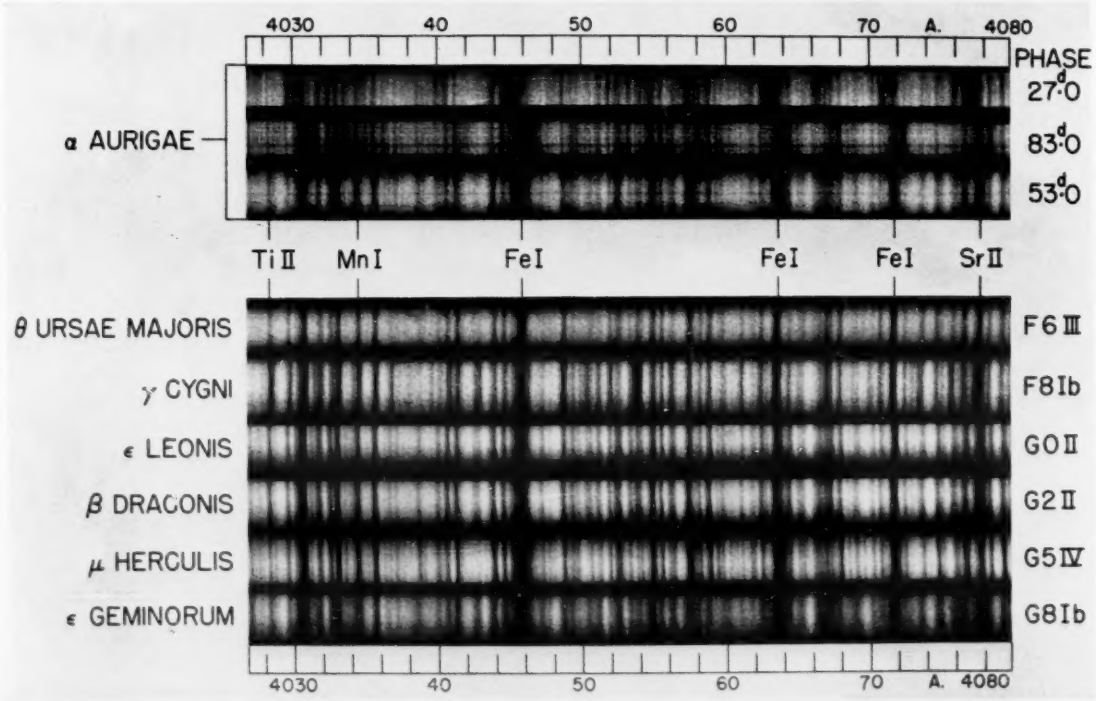


FIG. 6.—Spectrum of Capella at elongations and at conjunction and of stars of similar spectral type in the region λλ 4027–4089. The spectra of Capella have been displaced to make the positions of the lines in the primary spectrum agree with the identifications marked.

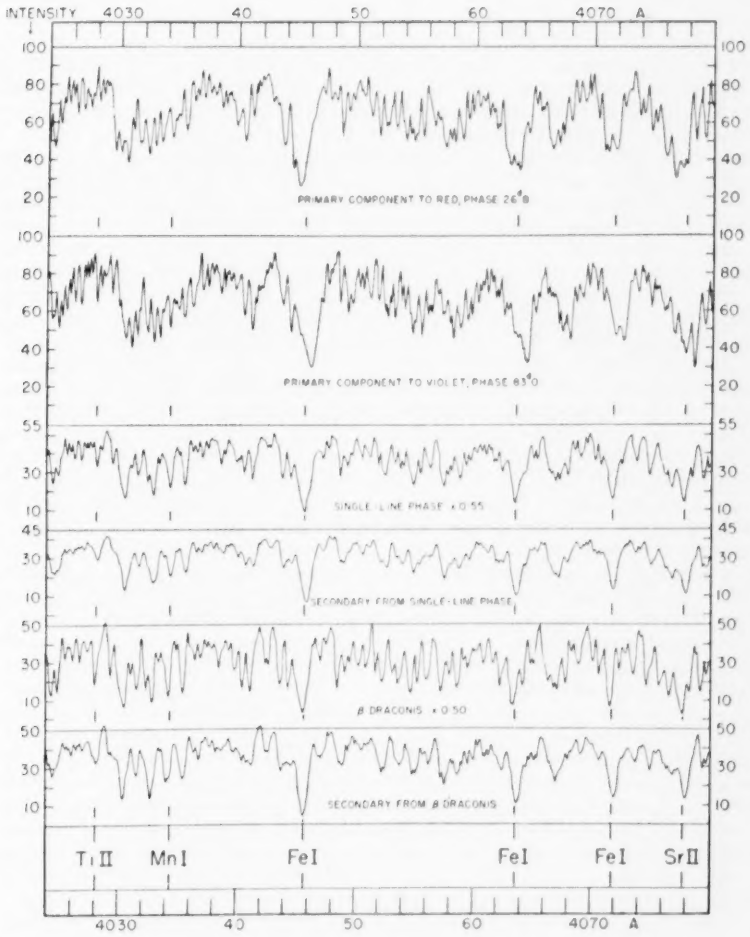


FIG. 7.—Intensity tracings of the spectrum of Capella and of $\beta$ Draconis in the region $\lambda\lambda$ 4024–4080. These tracings should be compared with the spectra shown in Fig. 6. The tracings of the double-lined phases have been shifted to make the identification marks refer to the primary spectrum; the lines in the secondary spectrum are displaced 0.7 A in each case. The center of the *Fe* I line at $\lambda$ 4046 is not at the position expected for either component but is the result of the superposition of the two spectra.

RADIAL-VELOCITY MEASURES OF THE SECONDARY COMPONENT

The tracings that were made to determine the intensity profile of the secondary component were also used to measure velocity displacements of the secondary relative to the primary component. Although it is possible to measure the positions of a few lines directly on the spectrograms, as Struve and Kung[11] have done for the sodium D lines and for a few other lines, the weakness of the lines in the secondary spectrum to the red of λ 5000 and the serious effects of accidental blending with lines of the primary to the violet of λ 5000 make such measures uncertain.

On the other hand, there was no difficulty in matching the lines of the primary spectrum on plates taken near elongation with the same lines in the adopted primary spectrum (either β Draconis or the $V_0$-spectrum), and tracings of these spectra had already been superposed, in order to obtain the secondary spectrum. As the lines of the secondary component are well defined, it was necessary only to superpose this intensity profile on the two already drawn and then to measure the displacements for unblended lines or for lines that appeared to have the same components in the two stars. For any given tracings, the matching of the primary and secondary spectra was most easily done by noting the points where the intensity profile of the secondary spectrum crossed the continuum; for at those points the intensity tracings of the composite spectrum and of the primary spectrum also crossed. These points were well defined and could be superposed; thus the displacement between the two components could be measured quite accurately. The magnification, in the direction of the dispersion, of all tracings used in this study was 200 times that of the original spectrograms, and the measured displacements were about 30 mm. The displacements of several lines were measured on each tracing and were reduced to velocities by applying the appropriate factors. For all measures except those of the D lines, the lines of the spectrum of β Draconis were used for the primary component; for the D lines the observed profiles obtained from the $V_0$-spectra were used. It is believed that no serious systematic errors were introduced by this method, since the lines in the spectrum of β Draconis had been drawn in the original superposition to agree in position with unblended lines in the composite spectrum.

The important quantity to be determined is the value of $K_2$, the amplitude of the secondary component, in order to obtain the mass ratio of the two stars. Struve and Kilby's orbital elements[5] for the primary spectrum were assumed, and the velocity of the primary component, $V_1$, was calculated for each phase. This value, combined with the velocity displacement, $V_2 - V_1$, gave the velocity of the secondary component, $V_2$, which, in turn, by assuming the value of $e$ and $\omega$ given by Struve and Kilby, yielded a value of $K_2$. The results are shown in Table 1 and give a weighted mean value of $K_2 = 27.6 \pm 0.5$ km/sec. This method is independent of any difference in $V_0$ between Mount Wilson and Victoria plates, and, although the range in $K_2$ is from 22 to 32 km/sec, the probable error does not seem unduly large in view of the difficulty in seeing the lines on the original plates.

The mass ratio of the two components is found directly from the amplitudes:

$$\frac{m_1}{m_2} = \frac{K_2}{K_1} = \frac{27.6}{26.4} = 1.05 \pm 0.02 .$$

The mass function, $f(m) = m_2^3 \sin^3 i/(m_1 + m_2)^2$, given by Struve and Kilby is $0.198\odot$; and, adopting Merrill's value[8] of $i = 41°$, it is found that $m_1 = 3.09\odot$ and $m_2 = 2.95\odot$. The absolute magnitudes derived in the previous section are $M_1 = 0.12$ and $M_2 = 0.37$. These values for mass and luminosity place both primary and secondary stars very close to the mass-luminosity-curve given by Petrie[16] and well within the scatter shown by his other double stars. Struve[11] suggests a mass ratio of 0.9, but the uncertainty in his measures is believed to be greater than those of the present study.

[16] *Pub. Dom. Ap. Obs. Victoria*, **8**, 341, 1950.

## CONCLUSIONS AND SUMMARY

The present spectrophotometric study of the two components in the spectrum of Capella suggests that the composite spectrum consists of two normal stars. According to the well-determined parallax, they are normal giants and the intensities of the lines in their spectra confirm this conclusion. The primary star, which appears brighter in the visual region of the spectrum, may be classed somewhat later than G2; and G5 III seems to be a reasonable estimate of its spectral type and luminosity. The secondary star, which is shown by the spectrophotometric work to be the brighter in the ultraviolet region of the spectrum, though the general visual appearance of the spectrum does not

TABLE 1

RADIAL VELOCITIES OF THE SECONDARY COMPONENT IN THE SPECTRUM OF CAPELLA

| PHASE (DAYS) | $V_2-V_1$ (KM/SEC) | $V_2$ (KM/SEC) | $K_2$ (KM/SEC) | WT. | PHASE (DAYS) | $V_2-V_1$ (KM/SEC) | $V_2$ (KM/SEC) | $K_2$ (KM/SEC) | WT. |
|---|---|---|---|---|---|---|---|---|---|
| | λλ 4000–4100 | | | | | λλ 5100–5600 | | | |
| 26.785 | −49.3 | + 6.5 | 22.3 | 3 | 13.639 | −42.8 | + 5.7 | 32.0 | 5 |
| 38.062 | −41.4 | + 7.6 | 28.8 | 2 | 31.858 | −51.1 | + 3.0 | 27.5 | 5 |
| 72.544 | +51.8 | +56.4 | 29.4 | 3 | 86.986 | +46.5 | +53.0 | 27.8 | 5 |
| 83.010 | +51.7 | +55.8 | 28.2 | 3 | | | | | |
| | λλ 4210–4290 | | | | | λλ 5890–5896 | | | |
| 26.990 | −49.1 | + 6.1 | 22.7 | 3 | 31.838 | −50.5 | + 3.7 | 26.8 | 2 |
| 74.051 | +47.8 | +51.8 | 23.7 | 3 | 88.518 | +43.6 | +51.4 | 27.5 | 2 |
| 83.008 | +52.7 | +56.8 | 29.2 | 3 | 36.056 | −45.0 | + 6.0 | 28.0 | 1 |
| | | | | | 81.633 | +56.4 | +60.0 | 31.9 | 2 |

Mean $K_2 = 27.6 \pm 0.5$

emphasize this fact, is a late F- or early G-type star. The presence of molecular absorption bands at λ 3883 and λ 4312 indicates a spectral classification of early G, but the weakness of the lines in the visual region suggests a late F. Therefore, it is judged to be G0 III, rare though these stars are, with some uncertainty in the exact classification. Preliminary estimates of the relative luminosities of the components from the line strengths suggested that the primary component was about twice as bright as the secondary at λ 5500; but, assuming that the spectrum of β Draconis, G2 II, represents the primary spectrum reasonably well and that the lines in the secondary spectrum are somewhat weaker than in a normal G0 III star, the ratio of 1.25 at λ 5500 seems reasonable and, as stated by Merrill,[17] is within the limits set by the observers at the interferometer. The lines in the secondary spectrum may be somewhat broadened by turbulence, as they appear wider than those in some sharp-lined stars, but they are little, if any, broader than the lines in the spectrum of α Persei. The relative luminosities determined for each region of the spectrum agree well with a Planckian distribution for the temperatures of the adopted spectral types.

These conclusions do not agree with some of the findings of Struve,[10, 11] who suggests

[17] Private communication.

that the observed spectrum of Capella is peculiar and, in particular, that some veiling or emission must be present to weaken strong lines of neutral iron in the primary spectrum as observed at the elongations. The Victoria spectrograms, examined visually, do not contradict Struve's observations, since the spectra do appear extremely complex; however, the spectra of other double-lined binary stars of late type have a somewhat similar complex and "washed-out" appearance. The writer believes that additional quantitative information concerning stellar spectra can be obtained from a study of the intensities of their spectral lines. The present investigation indicates that the observed spectra of Capella can be explained, with the possible exception of the varying emission at the center of the *Ca* II H and K lines, in terms of two normal giant stars of types G5 III and G0 III moving as a binary system with a period of 104 days. Throughout the regions of the spectrum that have been studied from λ 3700 to λ 6700, the secondary spectrum always appears approximately normal for a G0 star when the spectrum of $\beta$ Draconis is subtracted from the composite spectrum. Although it seems probable that an even better determination of the secondary spectrum could be obtained if the spectrum of a star of precisely the correct spectral type were adopted for the primary component, the present conclusions concerning the secondary spectrum seem justified, and no serious discrepancies have been noted.

Throughout most of the spectrum the principal features of the composite spectra at elongations belong to the primary G5 component. It is well known and indicated by the spectra reproduced in Figures 1–6 that the lines of the neutral metals predominate in G- and K-type spectra and that many of these lines increase in strength with advancing spectral type. However, the wings of the strong lines tend to obscure many of the strongest features in composite spectra. Therefore, it is not surprising that the numerous lines of moderate intensity that have increased in strength from types G0 to G5 should stand out on the spectrograms, to be identified, in this case, as belonging to the primary spectrum of Capella. At the longer wave lengths the continuum of the primary spectrum predominates, and the lines of the secondary spectrum appear even weaker than might be expected, because they are somewhat broadened, presumably by turbulence. In the ultraviolet region of the spectrum, where the secondary spectrum is stronger than that of the primary, the lines of the secondary do dominate portions of the spectrum; but the spectrum itself is so complex that many of the observed features are produced by the superposition of blends in the two component spectra; however, the hydrogen and some ionized lines are stronger in the secondary spectrum, while the molecular absorption bands are stronger in the primary.

The masses and luminosities of the components of Capella derived in the present investigation are of interest, since Eddington[18] used the data for the primary component (spectral type = G0; $m = 4.18\odot$; $M_{bol} = -0.36$) as the base-point for his original mass-luminosity relation. While the spectral type of the primary component has been found to be later than that of the sun, the mass ratio has been reduced, and therefore the data for Capella place it very near the normal values for Petrie's mass-luminosity relation.[16] Thus it is found once again that Eddington's original results, though often based on incomplete material, are not changed markedly by modern data.

[18] *The Internal Constitution of the Stars* (Cambridge: At the University Press, 1926).

# EMISSION-LINE STARS ASSOCIATED WITH THE NEBULOUS CLUSTER NGC 2264*

GEORGE H. HERBIG
Lick Observatory, University of California
*Received December 2, 1953*

ABSTRACT

Eighty-four faint stars having the *Hα* line in emission have been found in and around the nebulous cluster NGC 2264. The photographic magnitudes of these stars range from about 14.0 to 19.5, corresponding to $M_{pg} = +4.5$ to $+10$; many, if not all, are variable. With the exception of one Ae-type star, those objects for which slit spectrograms have been obtained are late-type stars of the T Tauri group. Over the entire obscured area surveyed, the mean surface density of emission-*Hα* stars is 0.38 star/psc$^2$ down to $M_{pg} = +8.5$, but within the most populous region the surface density rises to 1.6 stars/psc$^2$. Volume densities may be obtained if a model of the dark cloud is assumed: the highly idealized model adopted yields emission-*Hα* star densities of 0.25 and 1.1 stars/psc$^3$ for the entire obscured area and for the central region, respectively, down to $M_{pg} = +8.5$. These correspond to about 20 and 85 times, respectively, the star density in the solar neighborhood for the same interval of absolute magnitude. The survey is increasingly incomplete for fainter magnitudes, so that these densities are all minimum values. It was found that 75 per cent of the known variable stars in the region exhibited *Hα* emission during the rather short period of observation.

## I. INTRODUCTION

The nebulous cluster NGC 2264 is associated with an extensive dark nebula (see Figs. 1 and 2) that has been the subject of investigations by Max Wolf[1] and by L. B. Andrews.[2] The region has been studied by B. J. Bok, M. Olmsted, and B. Boutelle,[3] and spectra and magnitudes in the cluster have been obtained by R. J. Trumpler[4] and by J. A. Pearce.[5] The distances derived for the cluster and/or the dark cloud by various investigators show considerable dispersion, with a range of from 400 to 1000 parsecs. A distance of 700 parsecs was adopted for the purpose of the present work. The fact that the brightest stars of the cluster have little or no color excess shows that the cluster must lie near the front of the dark cloud.

The nebulosity mentioned in the NGC is that aligned with HD 47732 ($m_{pg} = 7.7$, B8), HD 47755 ($8^m1$, B9), and HD 261810 ($9^m0$, B8), some or all of which furnish its illumination. As may be expected from the spectral types of these stars, the nebulosity is of the reflection type, shown by slit spectrograms obtained with the nebular spectrograph of the Crossley reflector and by the relative weakness of the nebulosity on direct photographs in the red. Photographs in the blue with ordinary glass objectives, which transmit little λ 3727 light, show the nebulosity near HD 47887 ($6^m8$, B3) only faintly,[6]

* *Contributions from the Lick Observatory*, Ser. II, No. 52. A preliminary account of some of the work reported in this paper was published in *J.R.A.S. Canada*, **46**, 222, 1952. Some general conclusions derived from the study of NGC 2264 were given at that time; the present paper contains the detailed observational results from which those conclusions were drawn. However, the present paper is based upon somewhat more extensive material than was available in 1952.

[1] *Festschrift für Hugo v. Seeliger* (Berlin: J. Springer, 1924), p. 312.

[2] *Pub. A.A.S.*, **7**, 211, 1933.

[3] *Ap. J.*, **110**, 21, 1949.

[4] *Lick Obs. Bull.*, **14**, 154, 1930 (No. 420); *Pub. A.S.P.*, **47**, 249, 1935; see also A. Van Maanen, *Mt. W. Contr.*, No. 405, 1930.

[5] Unpublished.

[6] See Fig. 2, this paper; *Pub. Lick Obs.*, **11**, Pl. 28, 1913; and the Ross-Calvert *Atlas of the Milky Way* (Chicago: University of Chicago Press, 1936), Pl. 35.

but it is bright in the red[7] and in the ultraviolet.[8] This behavior is due to strong line emission at *Hα* and at λ 3727 [*O* II]. It is puzzling that this strong emission nebulosity apparently is excited by a B3 star. The presence of λ 3727 on almost all the slit spectrograms of stars in NGC 2264 and the appearance, in addition, of several bright hydrogen lines on the plates of longest exposure demonstrate the presence of fainter emission nebulosity over the entire field. This larger nebulosity is strikingly shown in the red-

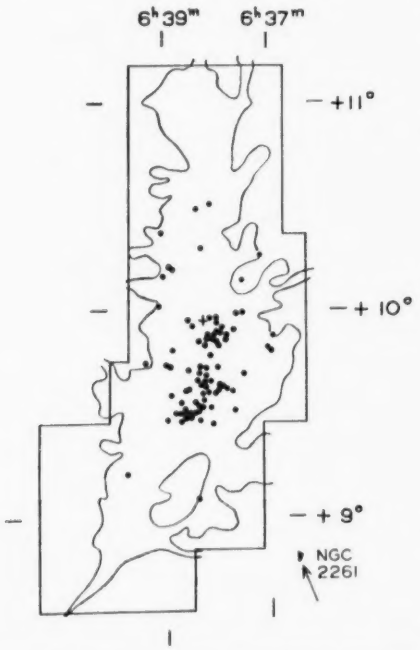


FIG. 1.—The region of NGC 2264. The area searched for emission-line stars is inclosed by the straight boundaries, and the approximate positions of 84 emission-*Hα* stars are indicated by the filled circles. In crowded regions the positions of the circles are only schematic. The boundary of the region of heavy obscuration, as estimated on a plate taken with the 20-inch Astrograph, which has a limiting magnitude near $m_{pg} = 19$, is indicated by the irregular lines. In some parts of the figure the position of the boundary of the nebula depends upon the limiting magnitude of the plate used. For this reason the boundaries shown are not everywhere those that would be chosen, for example, on the plates reproduced in Figs. 2 and 3. The cross indicates the position of S Monocerotis. The triangle in the lower-right-hand corner marks the position of NGC 2261, Hubble's Variable Nebula. North is at the top and east to the left. The α's and δ's indicated are for the equinox of 1950. The scale is 1° ≈ 31 mm.

light photograph of the region reproduced as Plate 15 of the *Atlas* of Shajn and Gaze. The spectrum of the extensive emission nebulosity has been observed by J. L. Greenstein and L. G. Henyey[9] and by O. Struve and C. T. Elvey;[10] the nebulosity probably

[7] The region of HD 47887 is shown on a photograph, taken with the 200-inch telescope, that is reproduced in W. K. Krogdahl's *The Astronomical Universe* (New York: Macmillan Co., 1952), p. 466. See also Plate 15 in *Atlas Diffuznykh Gazovykh Tumannostei* by G. A. Shajn and V. F. Gaze (Moscow: Academy of Sciences of U.S.S.R., 1952), which covers the entire area.

[8] On plates taken with aluminized mirrors, like Fig. 4 of this paper (Fig. 3 was taken in 1915 with a silvered mirror).

[9] *Ap. J.*, **87**, 79, 1938.

[10] *Ap. J.*, **89**, 517, 1939; *McDonald Contr.*, No. 9.

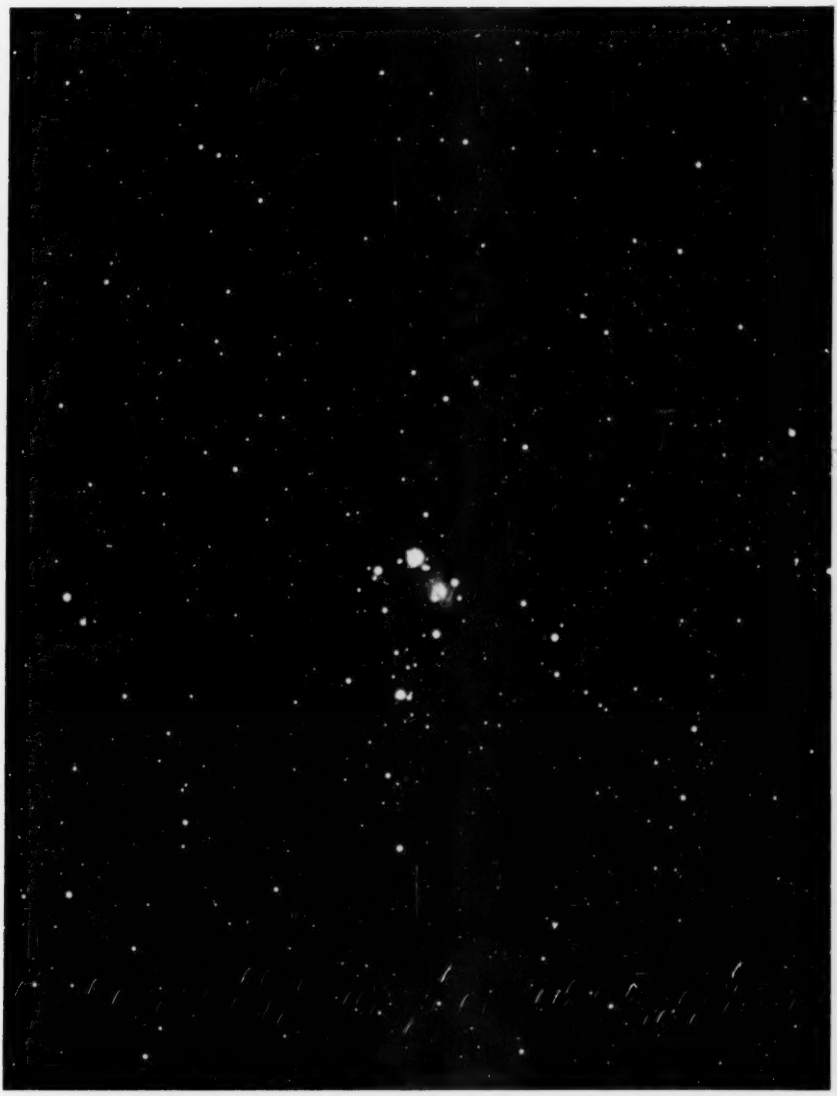

FIG. 2.—The region of NGC 2264. The original negative, taken on November 7, 1953, by C. A. Wirtanen, was exposed for 2 hours on an Eastman 103*a*-O plate with the 20-inch Astrograph. The brightest star, near the center, is S Monocerotis. The area shown is $2^{\circ}6 \times 3^{\circ}4$; the scale is $1^{\circ} = 48$ mm. North is at the top and east to the left.

owes its excitation to S Monocerotis ($4^m7$, O7), the brightest star in NGC 2264.

In 1924, Wolf[11] discovered 20 faint variable stars, apparently associated with the bright and dark nebulosity in the region of NGC 2264. Additional variables in this area have been found by E. P. Hubble,[12] W. Baade,[13] C. Hoffmeister,[14] and the writer. The spectra of 11 of these variable stars were observed in 1950 with the Crossley nebular spectrograph. At that time, 5 stars were discovered to have bright lines in the photographic region, 2 were suspected of possessing emission, while the remaining 4 showed no bright lines.[15] Work on the bright-line stars in NGC 2264 was taken up again in 1951 with a new spectrograph.

## II. THE SLITLESS SPECTROGRAPH

The instrument used for the survey work to be described is the grating slitless spectrograph of the Crossley reflector. This device is mounted in the center of the tube of the telescope, with its first optical element 15 inches in front of the focal plane of the primary mirror. The first (or lowermost) element is the negative component of the zero-power coma-correcting lens designed for the Crossley by F. E. Ross and made by J. W. Fecker in 1935. This negative element is of crown glass, with a diameter of 7 inches and a focal length of about $-15$ inches. It is now placed so as to collimate, for the wave length of *Hα*, the converging beam from the main mirror. The light then enters a replica transmission grating, cast of a plastic and bonded to the surface of a rectangular piece of glass $\frac{1}{2}$ inch thick. The master grating from which this replica was cast has 1444 lines/inch and was ruled by R. W. Wood.[16] The ruled area of the replica is $4 \times 6$ inches, and a large percentage of the incident light is thrown in the direction of the first-order red on one side. This replica was manufactured by the Perkin-Elmer Corporation and was presented to the Observatory by Dr. J. G. Baker, to whom the writer is also indebted for a valuable discussion of some of the optical principles involved in the design of this spectrograph. In passing through the grating, the first-order *Hα* light is diffracted through an angle of 2°.1, so a large thin prism has been placed immediately behind the grating to refract the *Hα* light into parallelism with its direction before entering the grating. This crown-glass prism, of 4° angle, was made by the Herron Optical Company, of Los Angeles. Although the deviations of grating and prism for first-order *Hα* light cancel, the dispersions are additive, so that the angular dispersion of the combination is slightly higher than that of the grating alone. After the light leaves the prism, it passes through the positive component of the Ross corrector, of aperture 7 inches and focal length $+15$ inches, which reconverges the light. Immediately in front of the plate is a red filter (Schott RG-2), which absorbs essentially all light of $\lambda < 6300$. The dispersion is about 450 A/mm. The plates generally used are Eastman 103*a*-E or 103*a*-E(2), which have a sensitivity peak slightly shortward of *Hα* and whose sensitivity extends to about $\lambda$ 6700. The clear field is about $44' \times 54'$, and the quality of the first-order spectra is uniform over this area; the removal of coma is entirely satisfactory. Other orders pass through the grating-prism combination with nonzero deviations. Consequently, their path through the lenses is not symmetric, and serious aberrations appear. The zero orders, for example, which appear for stars brighter than about 2.5 mag. above the plate limit, show comatic tails as well as a variation in structure over the field.

Tests on Selected Area 51 indicated that the plate limit, for unwidened continuous spectra, is near $m_{red} = 16$ for exposures of 1 hour. Since these tests were made, both surfaces of the two components of the Ross corrector, of the 4° prism, and of the red filter have been coated with magnesium fluoride films of the proper thickness to minimize

[11] *A.N.*, **221**, 379, 1924.

[12] *Pub. A.S.P.*, **32**, 161, 1920.

[13] Unpublished; private communication.

[14] *Ergebn. A.N.*, **12**, A10, 1949; *Mitt. A. Gesellsch.*, p. 20, 1951.

[15] *Pub. A.S.P.*, **62**, 142, 1950.

[16] See F. Zwicky, *Pub. A.S.P.*, **53**, 242, 1941.

surface losses in red light. The computed improvement in the limiting magnitude is about 0.3 mag.

### III. RESULTS FROM THE SLITLESS OBSERVATIONS

During the winter of 1951–1952, the region of NGC 2264 was surveyed for stars having the *Hα* line in emission. Four spectrograms, each of 1-hour exposure, were supplemented in 1952–1953 by an additional 1-hour exposure and one of 3 hours in length. The 1952–1953 plates were obtained with the coated optics. A total of 84 stars having bright *Hα*, found on the spectrograms, are listed in Table 1. It is intended that the numbering system in the table will be continued in future lists of such objects. The positions were obtained by measurement of a glass-contact print of an exposure of the region made with the 20-inch Astrograph by C. A. Wirtanen; they are based upon four reference stars in the $+8°$, $+9°$, and $+10°$ zones of the *A.G. Catalogue*, as reobserved at Yale. The emission-line stars are identified on Crossley photographs of the region that are reproduced as Figures 3, 4, and 5.

The photographic magnitudes in Table 1 were obtained by inspection of the Astrograph negative, of exposure 2 hours. The magnitudes of 88 stars in the region between magnitudes 4.7 and 15.1, as determined by Trumpler, have been tabulated by Van Maanen,[17] who also estimated magnitudes of other stars. These magnitudes may be extrapolated to the limit of the Astrograph plate by use of the images produced by a coarse grating over the objective; the computed $\Delta m$ between zero- and first-order images is 4 mag. The magnitudes of the bright-line stars on the plate were estimated twice, independently, by comparison with either zero- or first-order images of known brightness. The mean value, rounded off to the nearest full- or half-magnitude, appears in Table 1. Since most, if not all, of these emission-line stars may be variable, even these rounded-off magnitudes, based as they are on only one plate, should be considered only as approximations to the true mean brightnesses. For several stars listed in Table 1, only the nearest full magnitude is given. These stars could not be estimated on the Astrograph plate because of interference by other images or defects, or for some other reason; the magnitudes of these stars were obtained from a Crossley negative.

In the region of NGC 2264, the heavy obscuring cloud is greatly extended north-south, with a width varying from 15′ to 1° in the east-west direction. The NGC cluster of bright stars, together with its group of fainter emission-*Hα* stars, is located nearly centrally in the widest part of the dark nebula. Most of the bright-line stars are concentrated in a rectangular area of dimensions 25′ (in the east-west direction) by 35′ (north-south), whose center lies approximately midway between S Monocerotis and HD 47887. All but 16 of the 84 emission objects fall in this area. Only 2 objects have been found in the surveyed region to the south of this rectangle, despite the presence of extensive obscuration there. Ten bright-line stars have been found within 30′ of the northern boundary of the rectangle; but in the next 30′-wide strip to northward no more such stars have been observed. Figure 1 is a plot of the location of each of the 84 bright-*Hα* objects, together with the limits of the surveyed area and the boundary of the dark nebula. The latter was estimated from inspection of the Astrograph plate; different boundaries would be drawn on a plate of different limiting magnitude. Only three of the bright-line stars fall outside the boundary of the dark cloud, and each of these stars occurs near an edge where precise location of the boundary of the nebula is quite difficult. This fact again demonstrates the intimate association between emission-*Hα* stars of this type and nebular material.

Within the $25′ \times 35′$ rectangle, the bright-line stars cluster in two groups with a definite frequency minimum between. The more populous cluster, which has 45 members, is centered about 4′ north and slightly west of HD 47887. The sparser group, of

[17] *Mt. W. Contr.*, No. 405, 1930.

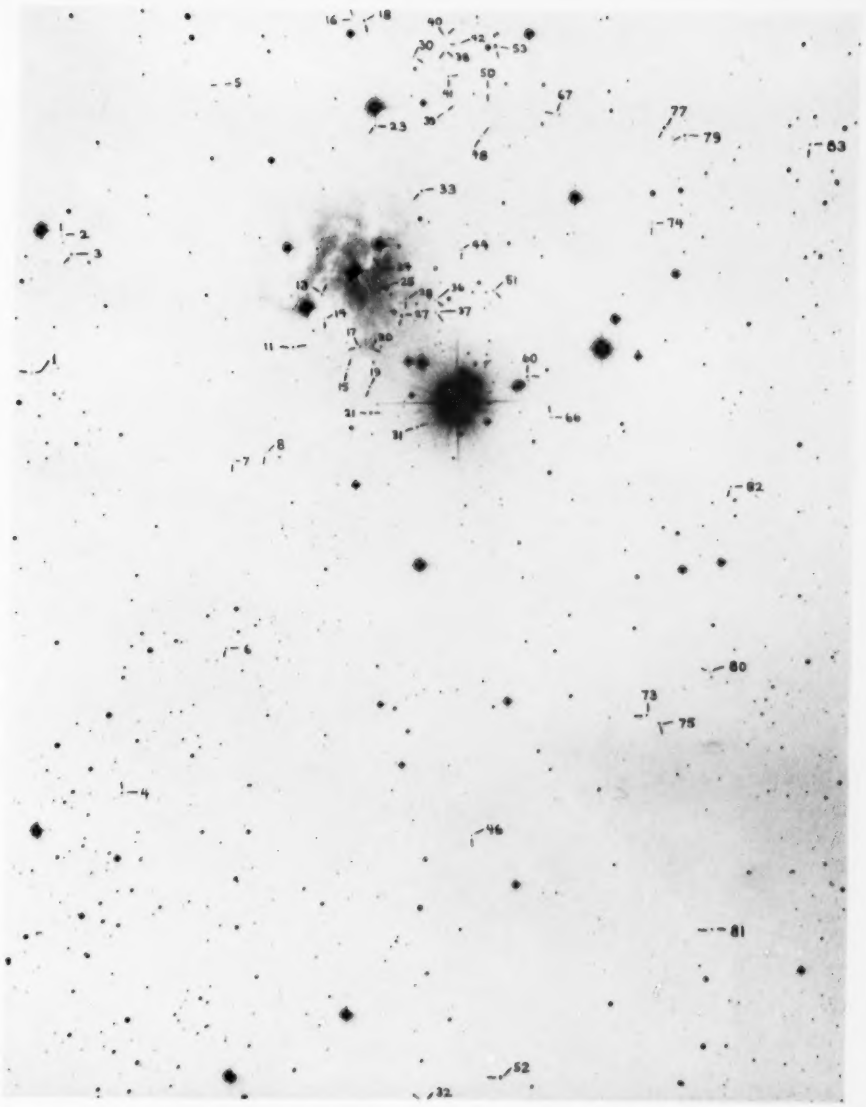


FIG. 3.—The northern part of NGC 2264. Emission line stars are marked with their LHα numbers. The bright star above the center is S Monocerotis. North is at the bottom and east to the right. The area shown has the dimensions $42' \times 53'$; the scale is 1 mm = 19″. The top edge overlaps with Fig. 4. The original Crossley negative, taken by H. D. Curtis on November 11, 1915, is a 2-hour exposure on a Seed Gratlex plate

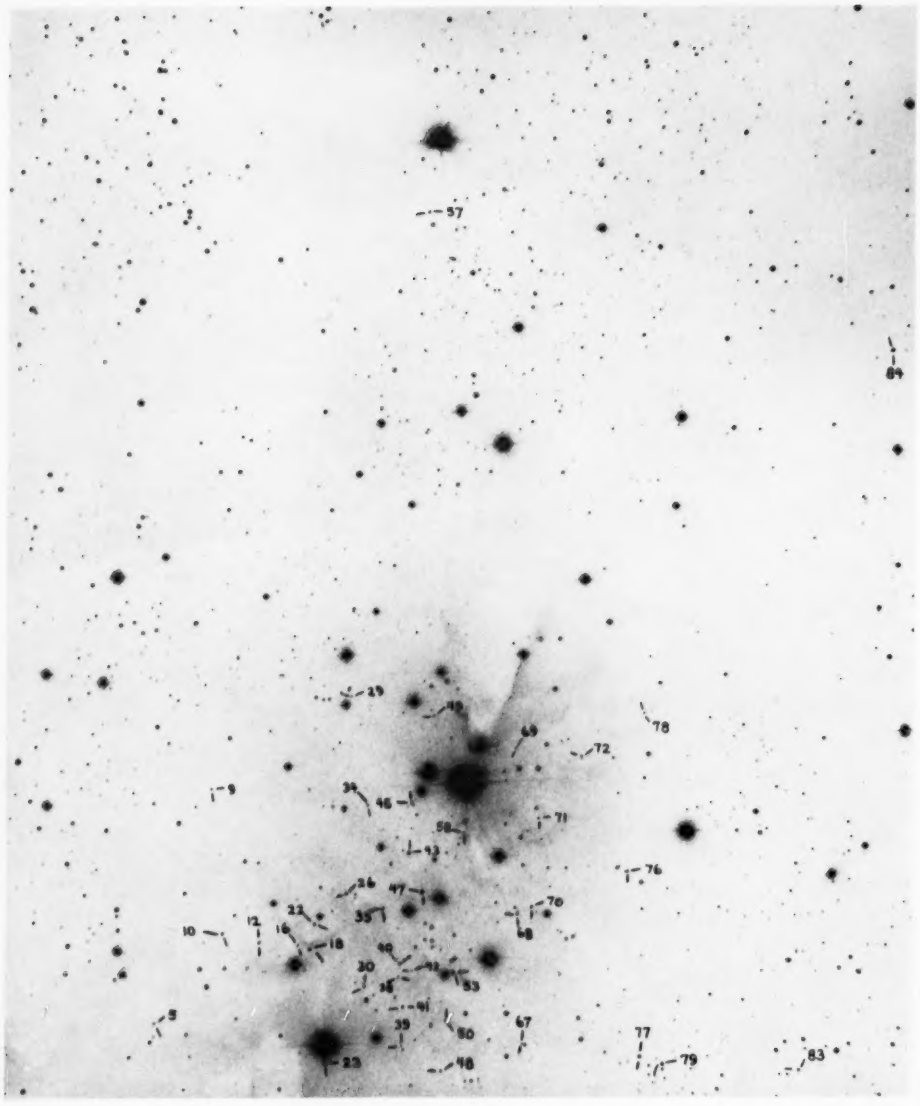


FIG. 4.—The southern part of NGC 2264. Emission-line stars are marked with their LHα numbers. The brightest star, midway between the center and the bottom edge of the figure, is HD 47887. The region immediately around this star is shown with a larger scale in Fig. 5. The area shown has the dimensions 41′ × 49′; the scale is 1 mm = 18″. The bottom edge overlaps with Fig. 3. The original Crossley negative, taken on November 28, 1951, is a 30-minute exposure on an Eastman IIa-O plate.

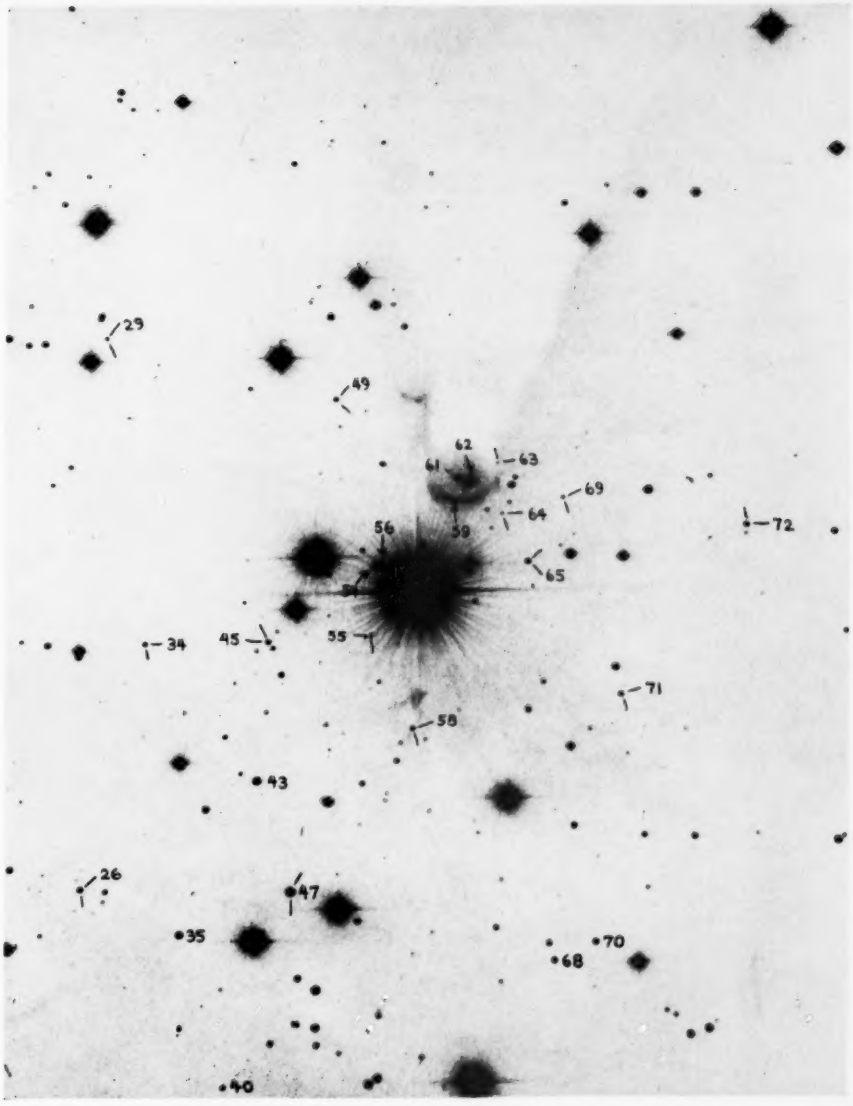


FIG. 5.—The region of HD 47887. Emission-line stars are marked with their LHα numbers. The enlargement is from the same negative as was used for Fig. 4. The area shown has the dimensions 14′ × 18′; the scale is 1 mm = 6″. North is at the bottom and east to the right.

TABLE 1

LIST OF BRIGHT-$H\alpha$ STARS NEAR NGC 2264

| LH$\alpha$ | $\alpha$ (1950) | $\delta$ (1950)* | $m_{p\alpha}$ | | $H\alpha$ Intensity |
|---|---|---|---|---|---|
| | | | G. H. | Tr.; V.M.† | |
| 1 | 6$^h$36$^m$48$^s$ | 9°54'.8 | 17 | | w |
| 2 | 6 36 54 | 9 48 .0 | 16 .5 | | w |
| 3‡ | 6 36 56 | 9 49 .1 | 15 .0 | | s |
| 4 | 6 37 06 | 10 15 .4 | 15 .0 | | w |
| 5 | 6 37 26 | 9 40 .9 | 17 .0 | | m |
| 6 | 6 37 27 | 10 08 .5 | 17 .0 | | w |
| 7 | 6 37 28 | 9 59 .3 | 17 .5 | | s |
| 8 | 6 37 35 | 9 58 .9 | 17 .0 | | w |
| 9 | 6 37 38 | 9 30 .5 | 17 .5 | | w |
| 10 | 6 37 39 | 9 37 .0 | 16 .0§ | | m |
| 11‡ | 6 37 41 | 9 53 .8 | 18 .0§ | | m |
| 12 | 6 37 46 | 9 37 .5 | 15 .5 | | w |
| 13 | 6 37 47 | 9 51 .2 | 16 .5 | | s |
| 14‡ | 6 37 47 | 9 52 .4 | 17 | | s |
| 15 | 6 37 52 | 9 54 .9 | 16 .5 | | s |
| 16 | 6 37 53 | 9 37 .8 | 17 .5 | | w |
| 17‡ | 6 37 54 | 9 53 .8 | 16 .0 | | s |
| 18‡ | 6 37 55 | 9 37 .9 | 15 .0 | | w |
| 19 | 6 37 56 | 9 55 .8 | 16 .0 | | s, var |
| 20‡ | 6 37 56 | 9 53 .9 | 16 .0 | | s, var |
| 21‡ | 6 37 56 | 9 57 .1 | 14 .5 | 14 .38 | w |
| 22 | 6 37 56 | 9 36 .8 | 16 .0 | | s |
| 23 | 6 37 57 | 9 43 .0 | 16 | | s |
| 24‡ | 6 37 58 | 9 49 .9 | 17 | | w |
| 25‡ | 6 38 00 | 9 50 .9 | 14 .0 | 12 .84 | s |
| 26 | 6 38 02 | 9 35 .6 | 16 .0 | | m |
| 27‡ | 6 38 02 | 9 52 .4 | 14 .5 | 14 .9 | m |
| 28 | 6 38 03 | 9 51 .5 | 18 .5 | | s |
| 29 | 6 38 05 | 9 26 .7 | 16 .0 | | m |
| 30 | 6 38 05 | 9 39 .7 | 15 .5 | | s |
| 31 | 6 38 05 | 9 57 .8 | 15 .5 | | m |
| 32 | 6 38 06 | 10 31 .0 | 16 .5 | | s |
| 33 | 6 38 07 | 9 46 .3 | 15 .0 | 14 .9 | w |
| 34 | 6 38 07 | 9 31 .6 | 16 .0 | | m, var |
| 35‡ | 6 38 09 | 9 36 .3 | 14 .5 | | m |
| 36 | 6 38 09 | 9 51 .6 | 18 .5 | | s |
| 37‡ | 6 38 09 | 9 52 .2 | 17 .5 | | s |
| 38 | 6 38 11 | 9 39 .4 | 16 .5 | | w |
| 39 | 6 38 11 | 9 42 .3 | 18 .5 | | m |
| 40 | 6 38 12 | 9 38 .8 | 18 .0§ | | m |
| 41‡ | 6 38 12 | 9 40 .7 | 15 .5 | | s |
| 42 | 6 38 14 | 9 39 .1 | 18 | | w |
| 43‡ | 6 38 14 | 9 33 .8 | 15 .0 | | w |
| 44 | 6 38 14 | 9 49 .2 | 17 .0 | | w |
| 45 | 6 38 15 | 9 31 .6 | 16 .5 | | m |
| 46‡ | 6 38 16 | 10 17 .8 | 18 .0 | | s |
| 47‡ | 6 38 16 | 9 35 .6 | 14 .5 | | m |
| 48 | 6 38 18 | 9 43 .6 | 17 .0 | | m |
| 49‡ | 6 38 20 | 9 27 .8 | 16 .0 | | m |
| 50 | 6 38 20 | 9 41 .4 | 18 .5 | | m |
| 51 | 6 38 21 | 9 51 .2 | 15 .0 | | m |

* The sign of all declinations is positive.

† Photographic magnitude determined by Trumpler (if expressed to 0m01) or by Van Maanen (if given only to 0m1).

‡ See notes, below.

§ The light is variable.

TABLE 1—*Continued*

| LHα | α (1950) | δ (1950)* | $m_{pg}$ | | Hα Intensity |
|---|---|---|---|---|---|
| | | | G. H. | Tr.; V.M.† | |
| 52‡ | 6h38m21s | 10°29′.6 | 14.0 | ..... | m |
| 53‡ | 6 38 21 | 9 39.3 | 14.0 | ..... | w |
| 54‡ | 6 38 22 | 9 30.4 | 14.5 | ..... | s |
| 55 | 6 38 22 | 9 31.6 | 18.5§ | ..... | m? |
| 56 | 6 38 22 | 9 30.4 | 17.0 | ..... | m |
| 57 | 6 38 23 | 9 05.2 | 16.5 | ..... | w |
| 58 | 6 38 24 | 9 33.0 | 17.5 | ..... | m |
| 59‡ | 6 38 27 | 9 29.4 | 15.5 | ..... | w |
| 60‡ | 6 38 28 | 9 55.4 | 14.5 | ..... | s |
| 61‡ | 6 38 28 | 9 29.2 | 15.0 | ..... | s |
| 62‡ | 6 38 29 | 9 29.1 | 15.5 | ..... | s |
| 63 | 6 38 30 | 9 28.8 | 19.5§ | ..... | s, var |
| 64 | 6 38 30 | 9 29.6 | 18.0 | ..... | m |
| 65 | 6 38 32 | 9 30.4 | 15.5 | ..... | s |
| 66 | 6 38 32 | 9 57.4 | 15.5 | ..... | m |
| 67 | 6 38 33 | 9 42.6 | 17.5 | ..... | m |
| 68‡ | 6 38 34 | 9 36.8 | 15.0 | ..... | s |
| 69 | 6 38 34 | 9 29.4 | 18.0 | ..... | s |
| 70 | 6 38 36 | 9 36.5 | 15.0 | ..... | s |
| 71 | 6 38 38 | 9 32.6 | 16.0 | ..... | w |
| 72‡ | 6 38 46 | 9 29.9 | 14.5 | ..... | s |
| 73‡ | 6 38 51 | 10 12.1 | 15.0 | ..... | s |
| 74 | 6 38 52 | 9 48.0 | 16.0 | ..... | w, var |
| 75‡ | 6 38 54 | 10 12.5 | 15.0 | ..... | s |
| 76 | 6 38 54 | 9 35.2 | 15.5 | ..... | s |
| 77‡ | 6 38 55 | 9 43.4 | 14.0 | ..... | s |
| 78 | 6 38 58 | 9 28.1 | 17.0 | ..... | m |
| 79 | 6 38 59 | 9 43.8 | 15.0 | 14.9 | w |
| 80 | 6 39 04 | 10 10.0 | 18.0 | ..... | m |
| 81 | 6 39 04 | 10 22.5 | 17.0 | ..... | s |
| 82 | 6 39 08 | 10 01.0 | 15.0 | 14.9 | m |
| 83‡ | 6 39 24 | 9 44.4 | 15.0 | ..... | s |
| 84‡ | 6 39 46 | 9 12.4 | 15.0 | ..... | m |

## NOTES TO TABLE 1

*LHα 3.*—A weak continuum without any conspicuous emission lines is shown by an underexposed plate taken on February 19, 1953.

*LHα 11.*—Emission was probably present at *Hβ*, *Hγ*, and *Hδ* on February 19, 1950, but nebular emission lines cross the spectrum at these wave lengths and make the intensities of the star lines uncertain. The continuous spectrum had an energy distribution about like that of a dG star.

*LHα 14.*—Relatively strong hydrogen (*Hβ* through *H8*) and *Ca* II emission lines on a weak continuous spectrum were present on February 19, 1950; possibly *He* I λ 4026 was present as well. The decrement of the Balmer emission lines was slow. $H\delta = K$; $K \cong H + H\epsilon$.

*LHα 17.*—No certain line emission was present on February 19, 1950, but moderately strong bright hydrogen lines would have been masked by the nebular emission lines.

*LHα 18.*—Weak *H* and *Ca* II emission may be present on an underexposed slit spectrogram taken on January 27, 1952. The strongest *TiO* band heads are present.

*LHα 20.*—*Hβ* is strong in emission on a plate taken on February 13, 1950, but the Balmer decrement is steep, and *Hε* is the last hydrogen line visible. K is very weak. $H + H\epsilon > K$, and $K = H\delta$.

*LHα 21.*—No certain emission lines appeared on February 19, 1953. The G band was visible in absorption, and the spectral type was G or early K. The energy distribution was approximately that of a dK0 star.

*LHα 24.*—*Hβ* may be bright on a slit spectrogram exposed on February 18, 1950, but interference by the nebular emission lines is very serious. The energy distribution is estimated to be about that of a dK star.

*LHα 25.*—Three exposures were made of the spectrum of this star, on October 31, 1951, and February 19, 1953. The hydrogen lines are strong in absorption, the Balmer jump is large, and a weak K line is

NOTES TO TABLE 1—*Continued*

present. No bright lines are visible in the photographic region, but the $H\beta$ line is weak and may be affected by emission. The spectral type is A2 or A3.

*LHα 27.*—A slit spectrogram taken on February 19, 1953, may show weak emission at $H\beta$ and $H\gamma$. The energy distribution is approximately that of a dK star.

*LHα 35.*—Weak emission was present at $H\beta$ on April 3, 1953. The energy distribution was like that of a late dG- or a dK-type star.

*LHα 37.*—A slit spectrogram taken on February 22, 1950, shows $H\beta$, $H\gamma$, and $H\delta$ in emission, as well as the *Ca* II lines, which are very strong. K > H + $H\epsilon$, and K ≫ $H\delta$.

*LHα 41.*—The Balmer series from $H\beta$ through $H10$ appeared strongly in emission on January 19, 1952. The K line of *Ca* II was bright, but H + $H\epsilon$ ≫ K.

*LHα 43.*—No emission in the photographic region can be seen on a slit spectrogram exposed on October 31, 1951. The G band appears in absorption with a strength consistent with a spectral type of G5 or K0. The energy distribution is about that of a dK0 star.

*LHα 46.*—This star lies just to the north of an arc of bright nebulosity convex toward S Monocerotis and NGC 2264.

*LHα 47.*—Two slit spectrograms taken on October 31, 1951, show rather weak emission at $H\beta$, $H\gamma$, and $H\delta$, while H and K are strong in emission. K = H + $H\epsilon$; K ≫ $H\delta$. The energy distribution corresponds to that of a star of type somewhat later than dK0.

*LHα 49.*—On February 23, 1950, the hydrogen lines were bright from $H\beta$ through $H9$, with a slow decrement. The K line was not visible.

*LHα 52.*—A slit spectrogram exposed on January 27, 1952, shows a K-type spectrum, with no emission apparent in the photographic region. The energy distribution resembles that of a dK0 star.

*LHα 53.*—An absorption spectrum of about type G5 was present on October 31, 1951, but no emission was visible in the photographic region. It is estimated that the energy distribution was that of a late dG- or early dK-type star.

*LHα 54.*—The hydrogen lines from $H\beta$ through $H12$ were strong in emission on October 31, 1951. The K line was bright, but H + $H\epsilon$ ≧ K and K < $H\delta$. A few absorption features indicated a spectral type of late G or K. The energy distribution was approximately that of a dK0 star, except that the ultraviolet seemed to be stronger than expected for a normal star of that type. LHα 56 is about 6″ distant.

*LHα 59.*—Two slit spectrograms are available, having been taken on February 22, 1950, and January 19, 1952. The hydrogen lines from $H\beta$ through $H\delta$ are certainly bright, although interference by nebular emission is serious. H and K are weakly present in emission, with H = K.

*LHα 60.*—On October 31, 1951, $H\beta$, $H\gamma$, and $H\delta$ were in emission, although not strongly. The *Ca* II lines were bright, with H + $H\epsilon$ > K and K > $H\delta$. The energy distribution was that of a dG star.

*LHα 61.*—A plate exposed on January 19, 1952, shows strong *H* and *Ca* II emission lines, with the former visible at least to $H11$. H + $H\epsilon$ = K and K ≧ $H\delta$. The continuous spectrum runs well into the ultraviolet.

*LHα 62.*—The spectrum of this star appears on the same plate as that of LHα 61, which is only 7″ distant and was, at that date, considerably the brighter. Because of the proximity of LHα 61, only bright $H\beta$ through $H\delta$ can be seen with certainty.

*LHα 68.*—On April 3, 1953, rather weak hydrogen emission was present from $H\beta$ through $H8$. The K line may have been bright, but, if so, K ≪ $H\delta$.

*LHα 72.*—Only a weak $H\beta$ emission line appears on a slit spectrogram taken on February 19, 1953. The energy distribution resembles that of an early dK star.

*LHα 73.*—Only weak $H\beta$ and $H\gamma$ emission were present on April 3, 1953. The energy distribution was approximately that of an early dK star.

*LHα 75.*—Northeastern and fainter component of a close pair of stars.

*LHα 77.*—A spectrogram taken on October 31, 1951, shows strong hydrogen emission lines from $H\beta$ through $H9$, as well as *He* I λ 4026 in emission. The *Ca* II lines are bright, with H + $H\epsilon$ > K and K = $H\delta$. A few metallic emission lines are visible in the ultraviolet. The energy distribution resembles that of a late dG- or a dK-type star.

*LHα 83.*—An underexposed slit spectrogram taken on April 3, 1953, shows no emission except possibly at $H\beta$.

*LHα 84.*—No emission can be seen with certainty on a plate taken on January 19, 1952, but $H\gamma$ may be bright. The energy distribution resembles that or a dG5 or dK0 star.

23 members, has its center about 5′ southwest of S Monocerotis. The diameters of the two groups are about 20′ and 15′, respectively.

The frequency distribution of bright-line stars with respect to magnitude is shown in Table 2, where $M_{pg}$'s are given as well, computed with a modulus of +9.2 mag. The third column of Table 2 lists the number of emission-line stars, in the area searched, between $m_{pg}$ + 0.25 and $m_{pg}$ − 0.25. Toward fainter magnitudes, emission-line stars begin to appear at $M_{pg}$ = +4.5 or 5.0. As already mentioned, continued observations would

undoubtedly yield, for the brightest stars at maximum light, brighter $M_{pg}$'s than are indicated by the magnitudes in Table 1. For this reason, the value of $M_{pg} = +4.5$ to 5.0 is not immediately comparable with the figure of $M_{pg} = +3$ for the later-type emission-line variables in the Orion Nebula at their maxima. In the Orion Nebula there are, in addition to the later-type variables, two Ae-type variables (T Orionis and BD $-6°1253$), which at maximum light are 2 mag. brighter than the stars of later type. One Ae star (LH$\alpha$ 25) is known in NGC 2264 and is discussed in Section VI.

The data contained in the third and fourth columns of Table 2 seem to indicate that the number of emission-*Hα* stars in NGC 2264 per magnitude interval does not increase indefinitely as the stars become fainter; instead, a maximum apparently exists in the frequency function at $m_{pg} = 15.0$ or 16.0. However, the data are affected by a selection effect that would be expected to introduce a spurious trend of this type. The greatest difficulty arises from the fact that the photographic magnitudes in Table 1 were de-

TABLE 2

DISTRIBUTION WITH RESPECT TO MAGNITUDE OF EMISSION-*Hα* STARS NEAR NGC 2264

| $m_{pg}$ | $M_{pg}$ | No. Bright-Line Stars in Each Half-Magnitude Interval | | No. Bright-Line Stars per Cubic Parsec in Each Half-Magnitude Interval | | No. Stars per Cubic Parsec in Each Half-Magnitude Interval in Region of Sun* |
|---|---|---|---|---|---|---|
| | | In Entire Obscured Area Surveyed | In Central 25′×35′ Area | In Entire Obscured Area Surveyed | In Central 25′×35′ Area | |
| 13.5 | +4.3 | 0 | 0 | 0.000 | 0.00 | 0.0008 |
| 14.0 | +4.8 | 4 | 3 | .014 | .06 | .0011 |
| 14.5 | +5.3 | 7 | 7 | .025 | .13 | .0013 |
| 15.0 | +5.8 | 15 | 8 | .054 | .15 | .0015 |
| 15.5 | +6.3 | 9 | 9 | .032 | .17 | .0016 |
| 16.0 | +6.8 | 11 | 11 | .039 | .20 | .0017 |
| 16.5 | +7.3 | 8 | 5 | .029 | .09 | .0016 |
| 17.0 | +7.8 | 8 | 6 | .029 | .11 | .0015 |
| 17.5 | +8.3 | 8 | 8 | .029 | .15 | .0014 |
| 18.0 | +8.8 | 6 | 4 | .021 | .07 | .0015 |
| 18.5 | +9.3 | 6 | 6 | .021 | .11 | .0017 |
| 19.0 | +9.8 | 0 | 0 | .000 | .00 | .0020 |
| 19.5 | +10.3 | 1 | 1 | 0.004 | 0.02 | 0.0025 |

* According to P. Van Rhijn, *Groningen Pub.*, No. 47, p. 17, 1936.

termined from an Astrograph plate exposed in January, 1951, while almost all the bright-line stars were discovered on spectrograms taken 9–12 months later. Since most of the emission-*Hα* stars probably are variable, the magnitudes and emission-line intensities given in Table 1 are not entirely consistent. For example, assume that the search for *Hα* emission is complete to some limiting magnitude (which depends upon the strength of the bright line), say $m = 17$. Only those stars that happened to be at least this bright when the spectrograms were taken would be detected, while those that were fainter would be missed. When the photograph in the blue was taken, however, the stars that were between $m = 16$ and $m = 17$ on the dates that the spectrograms were exposed might scatter between magnitudes 15 and 18. Therefore, a frequency diagram constructed from such data would show a few emission-*Hα* stars of magnitude 18, because their emission would actually have been detected when they were near maximum light. The true distribution of numbers of emission-line stars as a function of mean

magnitude, or of magnitude at minimum light, could be extricated from the observed frequency function only if proper allowance could be made for this effect, as well as others like it that also enter. For example, the probability of discovery of an emission-line star depends not only upon the strength of the continuous spectrum, which is expressed by the magnitude, but also upon the intensity of the bright-*Hα* line, which is not constant, with respect to the continuum. The degree of incompleteness involves the unknown relationship between these two factors.

There is, nevertheless, some additional evidence that very faint emission-line stars do not exist in large numbers in NGC 2264: a plate of 3 hours' exposure time revealed no bright-*Hα* stars that were invisible on plates on the 1-hour series. It is true that a few emission-line objects were discovered on the long-exposure plate, but they were all stars in which emission had been suspected on one 1-hour spectrogram and which consequently lacked confirmation until the long-exposure plate was examined. It may be concluded that there certainly is an upper limit, near $M_{pg} = +4.5$, to the luminosity of the T Tauri-like stars in NGC 2264. Furthermore, although there is no indication of the existence of a lower limit, at least there is not now any evidence of large numbers of very faint emission-*Hα* stars.

### IV. VOLUME AND SURFACE DENSITIES OF EMISSION-*Hα* STARS

A very approximate estimate of the volume of the dark nebula in which the bright-line stars are found may be made in the following way. An inspection of direct photographs reveals that, at the edge of the nebula, a typical value of the distance in which the background star density falls to its minimum value is 1′–2′. At the adopted distance of 700 parsecs, these angles correspond to 0.2–0.4 parsec. Since this limiting optical depth is reached by looking through the edge of a dark cloud whose density probably increases toward the interior, these depths of penetration observed at the "limb" are not representative of the depth of penetration for normal incidence. An estimate of the latter depth may be made by assuming a very idealized situation; let the nebula be represented as cylindrical in shape (the axis lying in the plane of the sky), with the density increasing toward the axis of the cylinder according to some reasonable law. Then it is possible to compute the radial distance from the surface, for normal incidence, at which an optical depth will be attained equal to the limiting value observed at the edge. Two radial-density laws were tried, one giving a linear, and the other a hyperbolic, increase toward the center; both indicated that a "normal incidence" penetration of 1–2 parsecs would be attained. It will therefore be assumed that an average penetration of 1.5 parsecs is the proper value to be used over the area of the dark nebula where most of the bright-line stars are found. The area of the dark cloud searched for emission-line objects is 1.25 square degrees, or 186 square parsecs; accordingly, the whole volume searched is 280 cubic parsecs.

The fifth and sixth columns of Table 2 give the number of emission-line stars found in NGC 2264, reduced to the unit of 1 cubic parsec, for the entire obscured area surveyed and for the central 25′ × 35′ rectangle, respectively. The increasingly serious incompleteness of these data for the fainter magnitudes is to be kept in mind in evaluating the following results. The volume corresponding to the central region was computed on the assumption that the depth of penetration was 1.5 parsecs, as for the whole nebula, although a somewhat smaller value would be more correct in this case. This central area is seen to contain, between $M_{pg} = +4.0$ and $+8.5$, about 1.1 stars/psc$^3$, while the average for the entire obscured area that was surveyed is 0.25 star/psc$^3$. The seventh column of Table 2 gives, in each half-magnitude interval,[18] the number of stars per cubic parsec near the sun. The average star densities for the central area of NGC 2264 and

[18] The luminosity function of P. Van Rhijn (*Groningen Pub.*, No. 47, p. 17, 1936) was used. The reduction to a half-magnitude interval from a full magnitude unit was made by dividing Van Rhijn's frequencies by 2.

for the whole obscured area are about 85 and 20 times, respectively, the star density in the region of the sun for this same interval of absolute magnitude. Because of search incompleteness, these numbers are to be regarded as minimum values. Furthermore, the nature of the correlation between the magnitudes of constant stars upon which the Van Rhijn luminosity function is based and the magnitudes determined for the irregular variables in NGC 2264 from a single observation is not obvious, so that the precise meaning of the figures quoted is not clear. It must be remembered, moreover, that, in order to determine the frequencies per unit volume, a highly simplified model of the dark nebula has been assumed. The actual cloud must have a very complex and intricate structure, and there is some question as to how much confidence should be placed in the results of calculations based on the idealization used here.

The projected surface density of emission-*Hα* stars is much less susceptible to uncertainties involving the spatial structure of the nebula. The data already presented show that to $m_{pg} = 17.75$, or to about $M_{pg} = +8.5$, there are 70 emission-line stars in the entire obscured area surveyed, or 0.38 star/psc$^2$ projected on the plane of the sky. The surface density in the central $25' \times 35'$ rectangle is 1.6 stars/psc$^2$. Inclusion of the very incomplete sample of stars still fainter would raise these values to 0.45 and 1.9 stars/psc$^2$, respectively.

## V. EMISSION *Hα* IN THE VARIABLE STARS

Most, but not all, of the known variables in NGC 2264 show *Hα* emission on the present series of slitless plates. Since variability in the strength of the emission-*Hα* line has been observed in a number of these stars, it is probable that continued observation would remove some variables from the nonemission group. It would be better to have either the average percentage of bright-*Hα* stars among the variables, as observed *at any one time*, or the percentage resulting from a long series of observations, which would presumably approach some limit as the material accumulates. The present results, based as they are on a very limited number of observations in only two seasons, undoubtedly lie nearer the first case. On the other hand, G. Haro's extensive work on the stars in the Orion Nebula[19] gave results that fall in the second category.

The presence or absence of emission in the known variable stars in NGC 2264 is noted in Tables 3 and 4. For only those 24 stars in which the presence or absence of emission is certain did 18 variables, or 75 per cent, exhibit bright *Hα* consistently enough during the period of observation for its presence to be established. This value is substantially higher than that previously found for the Orion Nebula (47 per cent) from similar spectroscopic material.[20] These percentages, however, are influenced by important selection effects. The search for variables in the Orion Nebula is much more complete than in NGC 2264; furthermore, NGC 2264 is much the more favorable nebula to examine for emission-line stars, because the brightness of the nebulosity in the central part of the Orion Nebula limits the search in that area to the brighter objects. Until the effects of such selection factors can be studied, no special emphasis should be placed upon the apparently greater percentage of bright-*Hα* variables in NGC 2264 than in the Orion Nebula.

## VI. RESULTS FROM SLIT SPECTROGRAMS

Slit spectrograms were taken with the low-dispersion nebular spectrograph of the Crossley reflector of as many of the bright-*Hα* and variable stars in NGC 2264 as was practicable. This instrument gives a dispersion of 430 A/mm at *Hγ*, and exposures of about 2 hours enable unwidened spectra of stars of magnitude 17 to be obtained that are adequate for purposes of very rough classification. Since the slit of this spectrograph may be rotated to any position angle, it was often possible to obtain spectra of two or

[19] *Ap. J.*, **117**, 73, 1953.

[20] *J.R.A.S. Canada*, **46**, 222, 1952; *Dom. Ap. Obs. Contr.*, No. 27 (Part 3).

TABLE 3

PRESENCE OF *Hα* EMISSION IN THE KNOWN VARIABLE STARS NEAR NGC 2264

| Variable-Star Designation | K No.* | Other Designations | Remarks | References for Variability† |
|---|---|---|---|---|
| 4. 1924 Mon‡ | 805 | Wolf 1‡ | See notes | 1 |
| 5. 1924 | 809 | 2 | = LHα 3 | 1 |
| 6. 1924 | 812 | 3 | = LHα 11 | 1 |
| 7. 1924 | 813 | 4 | = LHα 14 | 1 |
| 8. 1924 | 814 | 5 | No emission | 1 |
| 9. 1924 | 815 | 6 | = LHα 20 | 1 |
| GP Mon | | 7 | No emission; see Table 4 | 1, 2 |
| 11. 1924 | 818 | 8 | = LHα 24 | 1 |
| 12. 1924 | 819 | 9 | No emission; see Table 4 | 1 |
| 13. 1924 | 820 | 10 | = LHα 28 | 1 |
| 14. 1924 | 821 | 11 | = LHα 37 | 1 |
| GQ Mon | | 12 | = LHα 38 | 1, 2 |
| 16. 1924 | 823 | 13 | No emission | 1 |
| 17. 1924 | | 14 | No emission | 1 |
| 18. 1924 | 825 | 15 | = LHα 49 | 1 |
| 19. 1924‡ | 827 | 16‡ | See below | 1 |
| 20. 1924 | 828 | 17 | = LHα 58 | 1 |
| 21. 1924 | 829 | 18 | = LHα 59 | 1 |
| 22. 1924 | 830 | 19 | No emission | 1 |
| 23. 1924 | 833 | Wolf 20 | = LHα 78 | 1 |
| | 822 | S 4001 | = LHα 43 | 2 |
| | 824 | S 4002 | = LHα 47 | 2 |
| GR Mon | | S 4003 | Probably = LHα 60 | 2 |
| | 832 | S 4004 | = LHα 66 | 2 |
| SS Mon | | | = LHα 52 | 3 |
| | | Anon. 1 | Probably no emission; see Table 4 | 4 |
| | | Anon. 2 | = LHα 40 | 4 |

* Numbers assigned by B. V. Kukarkin *et al.* in *Katalog Zvezd Zapodozrennykh v Peremennosti* (Moscow: Academy of Sciences of U.S.S.R., 1951).

† The references are:

1. Max Wolf, *A.N.*, **221,** 379, 1924.
2. C. Hoffmeister, *Ergebn. A.N.*, **12,** A10, 1949.
3. E. P. Hubble, *Pub. A.S.P.*, **32,** 161, 1920; P. Parenago, *N.N.V.S.*, **4,** 225, 1933.
4. This paper.

‡ Wolf 1 and 16: emission *Hα* probably is present on one plate, but not on any others.

TABLE 4

VARIABLE STARS IN NGC 2264 SHOWING NO EMISSION LINES ON SLIT SPECTROGRAMS

| Designation | Dates | Note | Designation | Dates | Note |
|---|---|---|---|---|---|
| 8. 1924 Mon = Wolf 5 | 1950 Feb. 13 | ..... | 12. 1924 Mon = Wolf 9 | 1950 Feb. 22 | 2 |
| GP Mon = Wolf 7 | 1950 Feb. 18; 1950 Apr. 16 | 1 | Anon. 1 | 1950 Feb. 19; 1950 Apr. 16 | 3 |

NOTES TO TABLE 4

1. The energy distribution is that of a late-type star.

2. Any weak hydrogen emission in either the variable or its companion would be masked on the slit spectrogram by the moderately strong nebular emission lines, but there is no suspicion of bright *Hα* on the slitless plates.

3. The variability of the star was discovered on Crossley plates. It lies $2^{s}.5$ west and $13''$ south of LHα 17. Emission at *Hβ* may be present on both slit spectrograms, but the presence of nebular *Hβ* makes the reality of the stellar line uncertain. Again, weak *Hα* emission was suspected on some of the slitless plates but could not consistently be confirmed.

three stars with one exposure. The general field emission nebulosity, which is moderately strong over most of the area of interest in NGC 2264, produced bright lines of *H* and of [*O* II] on all but the shortest exposures (see Fig. 6). This circumstance frequently made it difficult to decide whether bright hydrogen lines are actually present in a star's spectrum or were due only to the nebular emission lines, intensified where they crossed the continuous spectrum of the star. Slit spectrograms of representative bright-line stars are shown in Figure 6.

The results for the individual stars are contained in the notes to Table 1, and the observations of four variable stars without emission lines are described in Table 4. Except for a few of the brighter objects, these spectrograms were always unwidened, so that it was difficult to learn much more from them than whether the stronger bright lines were present or not and whether an absorption spectrum could be seen. If dark lines appeared, some estimate could be made of the spectral type. Rough estimates of color, from the energy distribution with wave length, could also be made from these plates. Despite the limitations of the material, the following conclusions can be drawn.

1. The great majority of the emission-*Hα* stars associated with NGC 2264 are T Tauri stars;[21] the known exceptions are one Ae-type star (see below) and a few that may be foreground dwarfs. There seems to be no gross spectroscopic difference between the T Tauri stars in NGC 2264 and those found in the Taurus-Auriga dark clouds, the Orion Nebula, and elsewhere. Less obvious differences, such as have been described by Joy for Taurus-Auriga-Orion stars,[22] may appear when higher-dispersion spectrograms are obtained and better spectral types become available.

2. Joy's[22] results indicate that there is a progression in the character of the emission spectra of the T Tauri stars with the spectral type of the accompanying absorption spectrum. As the type of the absorption spectrum changes from G through K to M, in general the bright *Ca* II lines tend to become weaker with respect to *H*, and the rich emission spectrum of lines of the neutral and ionized metals fades. This progression is a tendency rather than a rigid rule, and departures from it can easily be found in individual objects. The unwidened 430 A/mm spectra are adequate to show only the strongest *Fe* II and *Ti* II lines when present in emission, to judge from a test on RW Aurigae. Consequently, only the most advanced spectra of Joy's type *a*, which usually accompany G-type stars, would be detectable as such on these plates. The fact that none have been noted indicates that extreme examples of type *a* spectra are probably not present, but stars such as LH*α* 54, 61, and 77 should be observed with higher dispersion before this conclusion is adopted. Some indication of the type of the emission spectrum can be gained from the relative strengths of the *H* and *Ca* II lines. For this reason, estimates of the relative strength of the K line of *Ca* II to H (*Ca* II) + *Hε*, and of K to *Hδ*, are given for many stars in the notes to Table 1.

3. It is interesting that one A-type star with bright *Hα* (LH*α* 25) has been found in NGC 2264. Such objects are common enough among other groups of emission-line stars that a separate category (group B of the classification scheme described in *J.R.A.S. Canada*, **46**, 222, 1952) has been proposed to contain them. No variation in the light of LH*α* 25 has been observed on the four Crossley direct photographs that are available, but its image is sufficiently overexposed to be insensitive to small changes in brightness. The photographic magnitude given for this star by Trumpler, however, is 1 mag. brighter than the value estimated on the Astrograph plate and given in Table 1. This discrepancy might be enough to indicate variability, if it were not for the bright nebulous background upon which LH*α* 25 appears and which makes the brightness estimate on the Astrograph plate somewhat uncertain. If the magnitude in Table 1 is correct, this star is

[21] This term is used here to describe only those objects falling within group A of the bright-line stars associated with nebulae, as described in n. 20. This usage is more restrictive than has sometimes been the case.

[22] *Ap. J.*, **110**, 424, 1949.

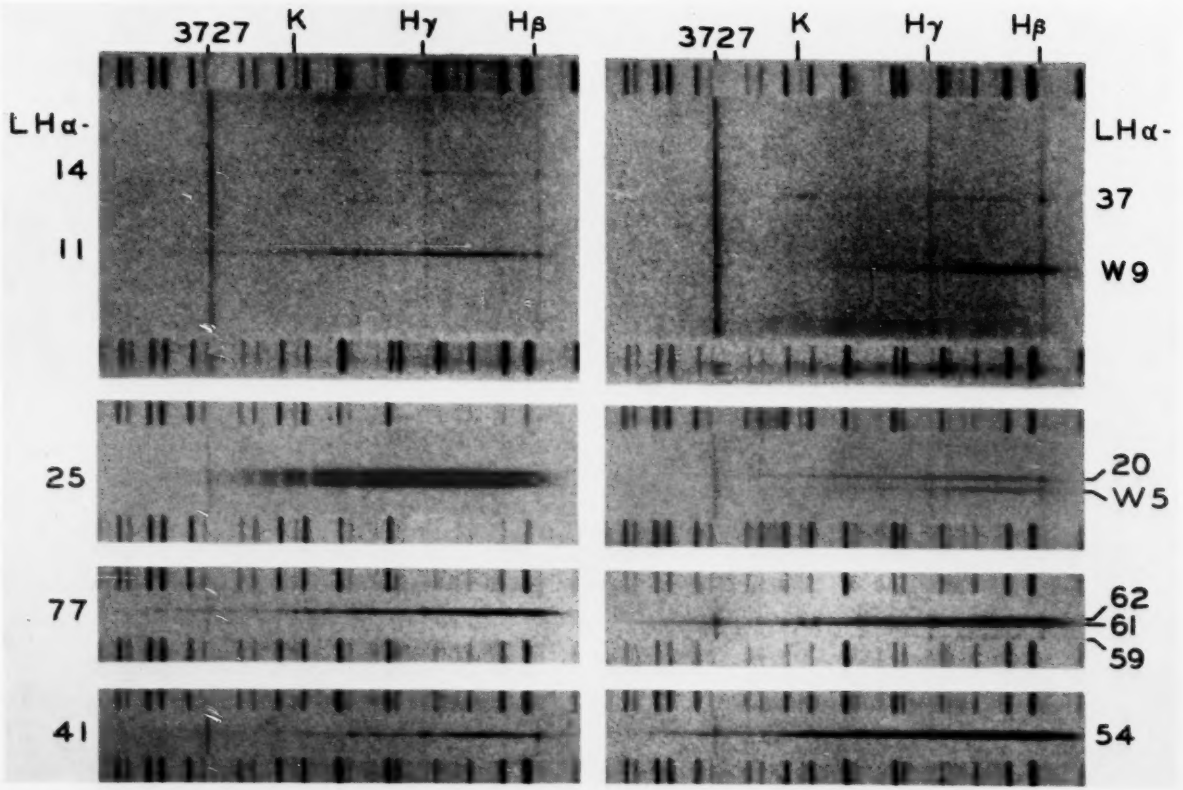


FIG. 6.—Slit spectrograms of some emission-$H\alpha$ stars in NGC 2264. The spectrograms were obtained with the nebular spectrograph of the Crossley reflector (dispersion 430 A/mm at $H\gamma$) and are described more fully in the notes to Table 1 and in Section VI of the paper. The numbers on the right- and left-hand margins are the LH$\alpha$ numbers of the stars so indicated, except that W5 and W9 denote Wolf's variables Nos. 5 and 9. The continuous spectrum in the two uppermost spectrograms is that of the reflection nebulosity near HD 47755.

about 3 mag. fainter than expected for a normal A2 or A3 dwarf at the adopted distance of NGC 2264. A color measurement should show whether the star is reddened a proportional amount and thus whether the discrepancy is due to obscuration.

The relationship of the cluster NGC 2264 with the dark cloud upon which it is seen projected is an important problem but will not be discussed in detail at this time. The nearly central location of the cluster, together with its group of emission-*Hα* stars, in the widest part of the dark cloud (see Fig. 1), suggests that the association of cluster with cloud is not an accidental one. If extensive and accurate proper-motion data were to become available for stars in NGC 2264, some significant light might be shed upon this question. The proper motions published by Van Maanen[23] should be extended, with higher accuracy, to more and fainter stars. No attempt was made to measure the radial velocities from the stellar emission lines on the slit spectrograms available for this study, first, because of the low dispersion and, second, because the velocities of T Tauri-like stars as determined from the emission lines are known to differ systematically from the absorption-line velocities. For this second reason, the meaning of any velocities obtainable from the present material would be uncertain.

[23] *Op. cit.* Six of the bright-line stars in Table 1 of the present paper are contained in Van Maanen's list of proper motions: LHα 21, 25, 27, 33, 79, and 82 are Van Maanen Nos. 32, 43, 46, 38, 104, and 122, respectively. Four of these stars seem to share the group motion of the cluster reasonably well, but LHα 33 and 79 deviate markedly. Both stars are near the edge of the area measured by Van Maanen, however, and their measured motions may be affected by some systematic error.

# SPECTROGRAPHIC OBSERVATIONS OF EMISSION-LINE STARS*

E. MARGARET BURBIDGE AND G. R. BURBIDGE
Cambridge, England
*Received December 2, 1953*

ABSTRACT

Observations of the spectra of the emission-line stars HD 12302, 27 CMa, HD 58978, HD 195407, HD 15238, HD 15239, HD 192954, $\epsilon$ Cap, HD 68468, HD 177291, HD 193182, HD 13867, HD 37967, and HD 408 are described.

## I. INTRODUCTION

In this paper we shall describe spectrographic observations of emission-line stars which were made at the McDonald Observatory and Yerkes Observatory between December, 1951, and November, 1952. Stars photographed at the McDonald Observatory were, with one exception, taken with the Cassegrain quartz spectrograph (dispersion 40 A/mm at $\lambda$ 3933). The majority of the Yerkes spectra were taken with the small spectrograph and 12-inch camera (dispersion 60 A/mm at $H\gamma$) attached to the 40-inch refractor. Plates taken at McDonald will be designated "M," and those at Yerkes "Y."

The stars were chosen from the list of Merrill and Burwell,[1] some of them being those for which there have previously been very few observations. It will be convenient to divide the stars into groups. First we shall describe some shell stars which are subdivided into (*a*) stars with helium shells and (*b*) stars with later-type shells. The second group consists of two "pole-on" stars, and finally we shall briefly describe MWC 1, an O-type star.

## II. SHELL STARS

### *a*) HELIUM SHELLS

*HD 12302 = MWC 23.*—A plate taken on January 11, 1952 (M), shows the hydrogen lines as sharp absorptions with emission borders ($R \gg V$), superposed on broad underlying absorptions. The mean velocity separation between the emission components of $H\beta$, $H\gamma$, $H\delta$, and $H\epsilon$ is 240 km/sec. The *He* I lines are very broad absorptions except for the lines arising from metastable levels, i.e., $\lambda$ 3965 (visible as a weak, narrow absorption line) and $\lambda$ 3889 (visible as an apparent strengthening of the $H\zeta$ core). No metallic shell lines are visible, and the *Mg* II and *Si* II lines are rather broad.

Swings and Struve[2] observed this star in 1942, and its spectrum at that time was very similar to its appearance on the plate described here as far as the shell absorption lines are concerned. The emission lines are possibly slightly stronger on our plate, since Swings and Struve found that only $H\beta$ showed emission. However, between these two dates, in July, 1945, Merrill and Burwell[3] reported that the absorption cores of hydrogen were weak or absent. On a plate taken on August 19, 1952 (Y), the emission appeared to be slightly stronger than it had been the previous January, but this plate was taken with the 6-inch camera (dispersion 125 A/mm at $H\gamma$), and this makes it difficult to estimate the difference accurately.

* *Contributions from the McDonald Observatory, University of Texas*, No. 232.

[1] *Mt. W. Contr.*, No. 471; *Ap. J.*, **78**, 87, 1933; *Mt. W. Contr.*, No. 682; *Ap. J.*, **98**, 153, 1943; *Mt. W. and P. Reprints*, No. 8; *Ap. J.*, **110**, 387, 1949.

[2] *Ap. J.*, **97**, 194, 1943.

[3] *Ap. J.*, **110**, 387, 1949.

*27 CMa = MWC 170.*—The variations in radial velocity of this star, which first led to the suggestion that it was a binary with anomalously high mass, have been extensively studied, mainly by Struve.[4] He finally concluded that the measured variations were caused, instead, by a variable absorption shell, giving rise sometimes to sharp absorption lines with variable velocity. Four plates taken on January 13, 1952 (M), show a well-developed helium and hydrogen shell spectrum, similar to that described by Struve and Kao, except that the *He* I triplet lines $2^3P-n^3D$ have sharp absorption cores originating in the shell, in addition to the *He* I lines λλ 3889, 5016, 3965, and 3614 arising from metastable levels. The absorption cores can be clearly seen right along the series, from λ 4471 as far as λ 3554. However, the lines λλ 4388, 4144, 4009, 4713, and 4121 appear as broad absorptions, similar to the broad lines which underlie the sharp cores in λ 4471, etc. The sharp absorption cores in the hydrogen lines, also superposed on broad absorptions, can be resolved as far as *H*24. No emission lines can be seen. However, on Decem-

FIG. 1.—Microphotometer tracing showing the structure of $H\gamma$ in 27 CMa (the ordinate does not measure direct intensity).

ber 16, 1951, a plate was obtained with the coudé spectrograph at McDonald (8½ A/mm), and this shows a weak emission line bordering the shell absorption at $H\gamma$ on the long-wave-length side. A microphotometer tracing of $H\gamma$ on this plate, reproduced in Figure 1, shows this structure. The plate is underexposed at $H\beta$; but the same structure can be seen in the rest of the hydrogen lines and in the *He* I lines λ 4471, etc., where, however, the emission lines are much weaker and do not rise above the level of the continuous background.

Since the fine details of this line structure are not resolved on plates of lower dispersion, it is easy to see that the presence of the emission lines, which are probably variable, will contribute to the measured line shifts, although the main effect must be due to a variable shell, as deduced by Struve. McLaughlin[5] first suggested that the apparent velocity variations of this star might be due to variable hydrogen emission lines, but this did not explain the shifts of the *He* I lines which showed no emission.

[4] See, for example, O. Struve, *Ap. J.*, **104**, 459, 1946; O. Struve and S.-K. Kao, *Ap. J.*, **108**, 537, 1948.

[5] *Ap. J.*, **75**, 60, 1932.

It is interesting that Finsen[6] has recently announced that this star is a visual double, with a separation of 0".102 and a difference in visual magnitude of less than 0$^m$.5. The separation between the two stars is of the order of 20 a.u., and this is too large to cause the sort of tidal effects which occur in close spectroscopic binaries. It is probable that the stars are of similar spectral type, since the recorded spectrum will always be the combined spectrum, and the stars are of nearly the same brightness. The spectrum underlying the shell on our lower-dispersion plates is earlier than the type B5 which is usually quoted; B2 V describes it better.

*HD 58978 = MWC 179.*—Plates taken on January 13, 1952 (M), show double emission lines at $H\beta$ and $H\gamma$, with $R > V$. Their separation is about 300 km/sec. The central absorption lines are not very strong; emission at $H\delta$ is very weak, and there is a moderately strong central absorption core, but $H\epsilon$ and the Balmer lines from $H9$ onward appear as broad absorptions only. The *He* I lines not arising from metastable levels are very broad, diffuse absorptions, indicating a high velocity of rotation. *He* I 3965 is a narrow, fairly weak absorption line, and *He* I 3889 appears as a strong, narrow absorption line, superposed on the broad absorption of $H\zeta$. Thus this star has a fairly strong *He* I shell, with a considerable dilution factor, and a rather weak hydrogen shell, with fairly weak emission lines present. The type of the underlying star is about B1 V.

The spectrum of this star has changed since 1949. Slettebak[3] noted that in 1949 the hydrogen emission lines in the photographic region had disappeared. Gerasimovic[7] had previously described the spectrum as a normal Be type, with *H* and *Fe* II emission lines.

*HD 195407 = MWC 346.*—This star has a strong hydrogen and helium shell. Changes in the spectrum have been described by Swings and Struve[2] and by Merrill.[8] A plate taken on September 17, 1952 (Y), shows strong emission at $H\beta$; $H\gamma$, $H\delta$, and $H\epsilon$ have sharp, narrow absorptions with emission borders ($R > V$) in $H\gamma$ and $H\delta$, superposed on broad absorptions. Shell absorption lines of *He* I 4471, 4026, and 3965 are strong (the plate does not extend as far as λ 3889). *He* I 4922, 4388, 4144, 4009, and 4121 are broad and diffuse. Thus the star resembles 27 CMa. There does not seem to have been much change since Merrill's last observation in 1951. The underlying star has a spectral type of B1 V. The mean velocity from the hydrogen and helium lines, derived by Merrill, was −72 km/sec, and this probably means that there is a predominant outward streaming of the gases giving rise to the sharp lines.

### *b*) LATER-TYPE SHELLS

*HD 15238 = MWC 47; HD 15239.*—The first of these two stars has long been known as a Be star with a typical shell spectrum.[9, 10] W. W. Morgan suspected that the near-by star HD 15239 showed a similar although less marked shell spectrum on plates taken at Yerkes. He suggested that we should observe both stars with somewhat higher dispersion at McDonald. The two stars were observed on January 12 and 13, 1952 (M). HD 15238 shows a definite hydrogen shell spectrum, and the absorption at $H\beta$ has emission borders ($V > R$). In the spectrum of HD 15239, $H\beta$, $H\gamma$, and $H\delta$ have definite absorption cores superposed on the broad absorption lines, although these are not nearly so marked as in HD 15238. Also, they are not visible in the higher Balmer members, and no emission lines are present. We believe that HD 15239 does have a weak hydrogen shell, not nearly so extended as that in HD 15238. The *He* I lines are very broad in both stars. The HD magnitudes of HD 15238 and HD 15239 are 8.4 and 8.2, respectively; the spectral type of the former is B5 V, and that of the latter is about the

[6] *Observatory*, **72**, 125, 1952.

[7] *Harvard Bull.*, **851**, 14, 1927.

[8] *Ap. J.*, **115**, 47, 1952.

[9] P. W. Merrill *et al.*, *Mt. W. Contr.*, No. 456; *Ap. J.*, **76**, 156, 1932.

[10] P. Swings and O. Struve, *Ap. J.*, **98**, 91, 1943.

same. The two stars are spatially close, since their angular separation is only 1.4 minutes of arc, and they are situated in a small clustering of stars near the cluster IC 1805.

On September 16, 1952 (Y), a spectrogram of the visual region of HD 15239 was obtained, and there was found to be no emission at $H\alpha$.

*HD 192954 = MWC 335.*—This star was observed on August 23, 1952 (Y). The spectrum is probably the same as it was when Broyles[11] observed it in 1942 and found it to have a well-developed shell of hydrogen and both neutral and ionized metals. On our plate the hydrogen lines have sharp, narrow absorption cores on broad underlying absorptions, and the metallic-line shell spectrum is as described by Broyles.

$\epsilon$ *Cap = MWC 373.*—Plates taken on August 23 and September 20, 1952 (Y), show that the spectrum of this shell star has changed since it was described in 1944.[12] At that time, the shell absorption lines and the emission lines of hydrogen had disappeared, although in the past they had remained constant even while considerable changes had occurred in the metallic-line shell spectrum.[13] At the time of our observations no emission lines were visible in the photographic region on our low-dispersion plates, but a definite hydrogen shell was present. $H\beta$, $H\gamma$, and $H\delta$ have sharp, narrow absorption cores superposed on broad underlying absorptions. Lines of *He* I, *Mg* II, and *Si* II are broad and diffuse, and no metallic-line shell is present. The type of the underlying star is B3 V.

*HD 68468 = MWC 577.*—Two plates of this star, taken on January 12 and 13, 1952 (M), show a well-developed shell spectrum, with narrow absorption lines of *H*, *Fe* II, *Ti* II, *Ca* II, *Sc* II, *Si* II, *V* II, *Fe* I, *Ca* I, *Sr* II, *Ni* II, and *Cr* II, in approximate order of importance. Thus the shell is rather a late-type one. Broad lines of *He* I and *Si* III are present, while *Mg* II 4481 is intermediate in width between the *He* I lines and those of the ionized metals, showing that it probably arises in the lower strata of the shell. On the other hand, the *Si* II lines are as narrow as the majority of the ionized metal lines. $H\beta$ and $H\gamma$ have two fairly weak emission components bordering the sharp absorption cores, with $V > R$. The underlying hydrogen absorption lines are very broad; the sharp absorption cores are visible at least to *H*26. The mean separation of the two emission components of $H\beta$ is 300 km/sec, and that of $H\gamma$ is 290 km/sec. The radial velocity derived from the shell lines agrees with that derived from the broad lines of *He* I and *Si* III; the mean value for all lines is +12.5 km/sec.

The HD class of this star is B2, and that assigned by Neubauer[14] is B4sek. The shell is evidently variable; at the time of our observations it was of considerable extent and fairly low excitation, and the gases forming it were not in large-scale motion with respect to the star.

*HD 177291 = MWC 973.*—Merrill and Burwell[3] remarked that a plate taken in 1947 showed that the spectrum of this star was probably of the shell type. A plate was obtained on September 17, 1952 (Y); unfortunately it was rather underexposed, but the star is clearly seen to possess a shell spectrum. $H\beta$ has an emission component on the *R* side of a narrow absorption; $H\gamma$ has a sharp absorption core superposed on a broad absorption. *He* I 4471 and *Mg* II 4481 are of moderate width. Absorption lines due to *Fe* II, *Fe* I, *Ti* II, *Si* II, and *Ca* I were identified between $H\beta$ and $H\delta$.

*HD 193182 = MWC 632.*—Merrill[15] has recently described a series of spectra of this star covering the period 1921–1950. He finds that it is one of the relatively few examples of stars which have stable shells, since no changes have been detected over the whole period of observations. The shell is an exceptionally rich one, with very sharp lines of

[11] *Ap. J.*, **97**, 234, 1943.

[12] O. Struve and A. Deutsch, *Ap. J.*, **100**, 390, 1944.

[13] See statement by D. B. McLaughlin quoted by P. W. Merrill and C. G. Burwell, *Ap. J.*, **98**, 153, 1943; see particularly p. 164, under "MWC 373."

[14] *Ap. J.*, **97**, 300, 1943.

[15] *Ap. J.*, **115**, 42, 1952.

hydrogen and neutral and ionized metals. It is generally classified as A0, but Struve[16] wondered whether very broad, shallow lines of *He* I might be present, arising in a fast-rotating B star underlying the shell. It was hoped that a greatly widened spectrogram might show these. A plate taken on August 23, 1952 (Y), was carefully searched in the region near λ 4471 and λ 4026, but the *He* I lines, if present, could not be picked out among the strong shell lines near each wave length.

### III. "POLE-ON" STARS

*HD 13867 = MWC 442.*—This is a beautiful example of a "pole-on" Be star. On a plate taken on September 17, 1952 (Y), $H\beta$, $H\gamma$, and $H\delta$ show narrow, single emission components centrally superposed on broad absorptions, while the *He* I lines are all quite narrow absorption lines. The type is B5 V, and there is no sign of an absorption shell. Thus our observation confirms that of Swings and Struve[10] that the star is not a supergiant or a shell star, as had previously been tentatively suggested.

*HD 37967 = MWC 122.*—This is a "pole-on" star in which Morgan and Hansen[17] detected weak *Fe* II emission lines in the photographic region. The spectral type is B3 V. A plate taken on January 10, 1952 (M), shows strong emission at $H\beta$, and emission is visible as far as $H\epsilon$, superposed on very broad absorption lines. The emission can be resolved into two components at $H\gamma$, $H\delta$, and $H\epsilon$, and the mean velocity separation is 145 km/sec. The absorption lines of *He* I are narrow. The interstellar *Ca* II lines are clearly visible. A plate of the visual region, taken on November 11, 1952 (Y), shows $H\alpha$ as a single, very strong emission line. Narrow, weak emission lines of *Fe* II 4924, 5169 and 5317 are present; *He* I $D_3$ appears as a narrow absorption line, and the interstellar absorption at λ 6284 is fairly strong.

### IV. HD 408 = MWC 1

The emission lines of this high-luminosity Of star have long been known to be variable. A decrease in emission-line strength in 1940, followed by an increase until 1942, was recorded by Swings and Struve.[18] Beals [19] recorded the fading of the same lines in 1944–1945, and Merrill and Burwell[3] noted that the hydrogen lines were in absorption in 1945 and 1947. Observations on January 12, 1952 (M), and October 4, 1952 (Y), show no emission in the hydrogen lines; the only emission lines in the photographic region are *He* II 4686 and *N* III 4634 and 4640. These three emission lines have always been more constant in appearance than the hydrogen, *He* I, and *C* III lines.

All the observational work was carried out while the authors were working at the Yerkes and McDonald Observatories. We are indebted to Professor R. O. Redman for the use of a measuring machine at the Observatories, University of Cambridge.

[16] *Ap. J.*, **99**, 205, 1944.
[17] *Ap. J.*, **103**, 379, 1946.
[18] *Ap. J.*, **96**, 254, 1942.
[19] *Pub. Dom. Ap. Obs. Victoria*, **9**, 1, 1951.

# A GROUP OF PECULIAR SHELL STARS*

E. MARGARET BURBIDGE AND G. R. BURBIDGE
Cambridge, England
*Received December 2, 1953*

ABSTRACT

Spectrographic observations of the stars AX Mon, HD 50138, HD 31648, HD 218393, and HD 236031, made in 1952 and 1953, are described. The various features which these stars have in common are discussed. These are principally the occasional appearance and rapid variations of displaced absorption components in the hydrogen lines. It is suggested that the infall of material from the shell may occur, in addition to outward surges, like prominence activity, previously suggested by Struve.

There is a group of shell stars whose spectra exhibit remarkable changes in the structure of the lines of hydrogen and ionized calcium. Emission components may be present and may vary, but the most striking feature is the presence of sharp absorption cores and the occasional appearance of additional absorption components. The sharp cores may vary in position, but they are usually displaced to the violet, and the additional components are usually displaced much farther to the violet.

Some examples are AX Mon, 17 Lep, HD 31293, HD 31648, HD 190073, HD 163296, HD 218393, and HD 236031. Merrill *et al.*[1] have pointed out the similarity between HD 31293, HD 31648, HD 163296, and HD 236031. Swings and Struve[2] have pointed out the similarity between HD 31648, 17 Lep, and HD 190073. Both Struve[3] and Merrill[4] have pointed out the similarity between HD 218393 and AX Mon. Two other stars, studied by Merrill and by Swings and Struve, may also bear some resemblance to this group. They are HD 45677 and HD 50138. These stars resemble each other, not only in the variable structure of their hydrogen lines but also because each shows forbidden emission lines.

We have made observations on AX Mon, HD 50138, HD 31648, HD 218393, and HD 236031, and the spectrograms are described below. The observations were made mainly at the McDonald Observatory, but some were made at the Yerkes Observatory. The McDonald plates were taken with the Cassegrain quartz spectrograph (dispersion 40 A/mm at λ 3933) and will be designated "M"; the Yerkes plates were taken with the small spectrograph and 12-inch camera (dispersion 60 A/mm at $H\gamma$) and will be denoted by "Y."

## AX MONOCEROTIS = HD 45910

The remarkable variations which this peculiar Be star undergoes have been discussed in several papers, the most recent being by Struve,[5] Merrill,[6] and Beals.[7] The appearance of violet-displaced *H* and *Ca* II absorption lines, in addition to the usual absorption cores, occurs at irregular intervals; the "α Cygni" spectrum, consisting of narrow absorption lines of ionized metals, varies irregularly; the emission lines of *H* vary in strength; and lines of *Fe* II sometimes appear in emission. These variations have been recorded at different times by the three authors mentioned above and previously by

* *Contributions from the McDonald Observatory, University of Texas*, No. 234.

[1] *Pub. A.S.P.*, **60**, 68, 1948.
[2] *Ap. J.*, **99**, 75, 1944.
[3] *Ap. J.*, **98**, 91, 1943.
[4] *Ap. J.*, **110**, 420, 1949.
[5] *Ap. J.*, **98**, 212, 1943.
[6] *Ap. J.*, **108**, 481, 1948.
[7] *Pub. Dom. Ap. Obs. Victoria*, **9**, 1, 1951.

Plaskett,[8] and no permanent periodicity has been found. We describe below a set of variations recorded on ten plates (M) and one plate a year later (Y).

JANUARY 8, 1952

*H*.—P Cygni structure—single absorptions with emission on the red side. Emission is fairly strong at $H\beta$, weaker at $H\gamma$, and very weak at $H\delta$. Underlying broad absorptions are weak or absent, but the Balmer discontinuity is well marked and retains the same appearance on all plates. The last resolvable line is *H*26.

*Ca II*.—The K line is a strong, narrow, single absorption. There is a faint broad emission on the violet side of the absorption line and possibly on the red side also.

*He I*.—Fairly strong, fairly broad, single absorption lines.

*Fe II*.—λ 4233 shows weak, narrow emissions on both sides of a weak, narrow absorption line, with $V > R$. λ 4352 has a weak, narrow, violet-displaced emission line on the violet side of a very weak, sharp absorption. λ 4179 and λ 4173 both appear as single, narrow, weak, violet-displaced emission lines.

*Si II*.—Absorption lines of λ 4128 and λ 4131 are fairly narrow; λλ 3863, 3856, and 3854 are narrower.

*Mg II*.—λ 4481 is fairly strong, but weaker and somewhat narrower than *He* I 4471.

There are several sharp absorption lines in the ultraviolet. *Ni* II 3514 is the strongest (*Ni* II 4067 is present as a weak, sharp absorption). *Ti* II 3761 and 3759 are narrow absorptions, fairly strong. *N* II 3995 is strong and rather broad; the strength of this line and of *Mg* II 4481 give the spectrum almost the appearance of a B5 supergiant.

JANUARY 10, 1952 (TWO PLATES)

*H*.—The emission lines are the same. Violet-displaced weak absorption lines are just visible at $H\beta$, $H\gamma$, and $H\zeta$ (presumably due to *He* I 3889).

*Fe II*.—At λ 4233 the emission is weaker, the absorption stronger and sharp. At λ 4352 both emission and absorption are very weak.

JANUARY 12, 1952 (THREE PLATES)

*H*.—The violet-displaced components are stronger but are still weaker than the red components (as they remain on all plates). The relative strength of the two components varies along the series—the *V* component is strongest relative to the *R* at $H\beta$. The *V* component of $H\epsilon$ is suppressed, but there is a trace visible, having about the same strength relative to the *R* component as in *H*11 (the *V* components are not visible beyond *H*11). The *V* component due to *He* I 3889 is strong. The separation between the two components is about 230 km/sec.

*Ca II*.—K is still a strong single absorption and remains single on all plates.

*Fe II*, *Si II*, *Mg II*.—All weaker.

*Ni II*.—Lines in the ultraviolet remain strong.

JANUARY 13, 1952 (FOUR PLATES)

*H*.—The *V* components are still present, having about the same relative strengths as on January 12. $H\epsilon$ has the same appearance as on January 12.

JANUARY 12, 1953

*H*.—The emission lines are much stronger than they were the year before. $H\beta$ has P Cygni structure, with very strong emission; emission is strong at $H\gamma$ and visible at $H\delta$ and $H\epsilon$ (the plate is underexposed at $H\zeta$). The secondary, violet-displaced absorptions are not present, and underlying broad absorptions are not seen.

*Fe II*.—There are numerous emission lines in the region between $H\beta$ and $H\delta$. The α Cygni lines are not seen.

[8] *Pub. Dom. Ap. Obs. Victoria*, **4**, 1, 1927.

*He I, Mg II, Si II 4128–4131, N II 3995.*—These absorption lines appear with about the same intensity they had the year before.

*Ca II.*—Both H and K have a narrow emission on the violet side of the absorption, and the absorption line at K may be double.

A plate of the visual region, obtained on February 18, 1953 (Y), shows $H\alpha$ as a strong, overexposed emission line. The *Na* I ($D_1 + D_2$) line is fairly strong, about twice the strength of *He* I $D_3$. Interstellar λ 6284 is weak. The faint M2 absorption spectrum of neutral metals, observed by Merrill[8] in the visual region, does not appear on our low-dispersion plate.

It will be noted that several plates were taken, at intervals of a few hours, on three of the nights, in order to see if there were any very rapid changes occurring. However, no changes occupying only a few hours were observed.

The secondary, violet-displaced absorption components have been attributed by Struve to a phenomenon resembling prominence activity, i.e., localized outward surges of gas. The suppression of the violet-displaced absorption of $H\epsilon$, observed by us, was first observed and discussed by Struve,[5] and he has discussed the problem again in connection with other stars as well as AX Mon.[9] In the earlier paper he suggested two possible explanations; the second of these, in terms of a hydrogen layer expanding outward so that the atoms have a velocity of recession relative to *Ca* II atoms emitting the H line, seems to us to be a probable solution.

HD 50138

This shell star has been observed by Merrill and by Swings and Struve. The former author in his first paper[10] described a series of spectrograms covering the period 1920–1930. During this time the hydrogen lines showed large $V/R$ variations; absorption lines of *He* I, *Mg* II, and *Fe* II were present. Velocities derived from these latter agreed with each other and were fairly constant, while velocities from the *H* cores were variable and usually algebraically less than those from the *He* I group. In 1940 Swings and Struve[11] recorded the appearance of *Fe* II in emission. Later[2] they described a plate taken in 1943 and remarked that an unusual feature of this star was that the *He* I absorption lines, although diffuse and presumably broadened by rotation, indicated a smaller rotational speed than that given by the over-all widths of the *H* emission lines. They suggested that the *He* I lines originated in the deeper strata of the shell.

Recently, Merrill[12] has described a series of thirteen coudé spectra covering the period 1943–1951. It is interesting to note that on four plates he recorded the appearance of additional violet-displaced, weaker absorption components, and on one plate there were red-displaced, weaker components. These observations suggest to us that this star may resemble AX Mon and the other stars described here.

Three plates of this star were obtained on January 12 and 13, 1952 (M). The appearance of the spectrum is similar to the description by Swings and Struve.[2] The last resolved shell line of *H* is *H*25. The mean separation of the emission components is 280 km/sec. The mean velocity given by the *He* I, *Mg* II, and *Si* II lines is +37 km/sec, and that given by the shell lines of *H*, *Ca* II, *Fe* II, and *Ti* II is +17 km/sec. Thus, whether the lines of the *He* I group arise in the star itself or in the deeper strata of the shell, the hydrogen and ionized-metal lines arise in a region with an outward velocity, relative to the *He* I region. No additional absorption components in the *H* lines were seen.

On our plates the *R* emission component at $H\beta$ is considerably stronger than the *V*, and the *R* edge of the *R* component is shaded slightly and is not as sharp as the *V* edge. The fact that the *R* component is usually the stronger has been discussed by Merrill in terms of absorption of the *V* component by outward-moving gas. He noted that, although

[9] *Pub. A.S.P.*, **64**, 288, 1952.

[10] *Ap. J.*, **73**, 348, 1931.

[11] *Pub. A.S.P.*, **52**, 294, 1940.

[12] *Ap. J.*, **116**, 501, 1952.

the relative strength of the $R$ and $V$ components in $H\gamma$ was correlated with that in $H\beta$, it differed in the sense that the ratio $V/R$ was always larger in $H\gamma$. When $V/R = 0.5$ at $H\beta$, $V/R = 1$ at $H\gamma$; when $V/R = 0.07$ at $H\beta$, $V/R = 0.5$ at $H\gamma$; and so on. He remarked that this was a curious anomaly. We can understand qualitatively the reason for this phenomenon. The problem of the transfer of line radiation through a gas which is dense enough not to be considered transparent to the Balmer series leads to a Balmer decrement in which the strengths of $H\alpha$ and $H\beta$ are reduced much more than those of the higher Balmer members. When we are considering the absorption by moving gas, the problem is much more complicated, but the usual explanation of $V/R$ variations, namely, the absorption of the emission lines by gas moving outward or inward, would be expected to lead to a progression in $V/R$ along the Balmer series.

On our plates this progression is not so marked as it apparently has been in the past. However, a plate was obtained on January 12, 1953 (Y), and on this the $V$ and $R$ components at $H\beta$ are approximately equal, while $V \gg R$ in $H\gamma$, $H\delta$, $H\epsilon$, *Fe* II 4233, and *Ca* II H and K. We have the same phenomenon here, i.e., a slower Balmer decrement in the $V$ than in the $R$ component, but if we assume that this is due to self-absorption, then we need to assume that the "unabsorbed" $V$ component is much stronger than the $R$, and this is hard to explain if we have a symmetrical ring or equatorial disk of gas. We suggest that the additional displaced absorption lines sometimes observed by Merrill[12] probably play a part and that they are caused by some kind of prominence activity, on a smaller scale than that occurring in AX Mon and consisting of motion both inward to and outward from the star.

A study of the problem of the transfer of line radiation in a moving atmosphere should in theory be able to determine the different regions responsible for the emission and absorption and their relative velocities, but would be very complicated.

Finally, since Merrill[10] observed [*O* I] lines in the spectrum, the total extent of the outer atmosphere of the star must be very large.

### HD 31648

The hydrogen lines in the spectrum of this star have a variable and complicated structure. Merrill *et al.*[13] remarked that the wave lengths of the absorption cores of the hydrogen lines changed by 2 or 3 A and that the *Ca* II K line was sometimes double. Swings and Struve,[2] in a note describing a plate taken in 1943, said that the H lines had violet-displaced cores of considerable intensity, suggesting an expanding shell. The *Ca* II K line was double.

A plate was obtained on January 12, 1952 (M). On this the hydrogen lines $H\beta$–$H10$ are double, with a diffuse absorption on the red side and a sharp, stronger absorption on the violet side; the sharp absorptions have quite strong P Cygni emission lines bordering them on the red side. *Ca* II K has a similar structure. A metallic-line shell, or set of "$\alpha$ Cygni" lines, is present, with narrow absorption lines of the following elements: *Fe* II, *Fe* I, *Ti* II, *V* II, *Ca* I, and *Sr* II. Absorption lines of *Mg* II, *Si* II, and *Si* III are present and are more diffuse than the lines of the other elements. Besides the *Ca* II K line, only two other lines of the metallic-line shell show P Cygni structure, i.e., *Ti* II 3761 and 3759.

At first sight it would seem that the diffuse $H$ absorptions arise in the reversing layer of the star itself, and the sharp absorptions in an expanding shell. However, the values given in Table 1 show that the diffuse components have very large recession velocities. The progression in velocity, from $H\beta$ to $H10$, suggests that we are dealing with a broad absorption line in which the emission and sharp absorption components are superposed on and blot out the violet wing. The $H$ lines beyond $H10$ can be used to test this hypothesis. There is a steady weakening of the sharp absorptions relative to the diffuse absorptions along the series as $n$ increases, and from $H11$ onward the lines appear as

[13] *Ap. J.*, **96**, 15, 1942.

single broad absorptions. Their mean velocity is +55 km/sec. This is a large value to be the radial velocity of the star itself. Correcting for the local solar motion, we get +46 km/sec. The distance of the star may be about 500 parsecs, and the galactic longitude is 141°; at this place the velocity due to galactic rotation is very small and negative. Thus the star would have a very large peculiar motion relative to its surroundings if the value given above represented its own radial velocity.

The mean velocity from the single absorption lines of *Fe* II, *Fe* I, *Ti* II (excluding λ 3761 and λ 3759), *V* II, *Ca* I, and *Sr* II is −5 km/sec. The mean velocity from the lines of *Mg* II, *Si* II, and *Si* III is +16 km/sec. This suggests stratification in which the outer level of the shell is expanding faster than the inner level, and the P Cygni lines arise at a higher level than the α Cygni lines (as suggested by Struve in the case of HD 218393). Possibly the star is a binary of the β Lyrae kind, with a common shell

TABLE 1

VELOCITIES GIVEN BY LINES OF *H*, *Ca* II, AND *Ti* II (KM/SEC)

| | Diffuse Absorption Lines | Emission Lines | Sharp Absorption Lines |
|---|---|---|---|
| *Hβ* | +319 | +73 | −64 |
| *Hγ* | +216 | +64 | −67 |
| *Hδ* | +159 | +49 | −65 |
| *Hζ* | +167 | +48 | −49 |
| *H*9 | +139 | ..... | −50 |
| *H*10 | +196 | +60 | −45 |
| *Ca* II K | +195 | +46 | −54 |
| *Ti* II 3761 | ..... | +46 | −35 |
| *Ti* II 3759 | ..... | +42 | −43 |

giving rise to the α Cygni lines. If this is the case, however, it is difficult to locate the gases giving rise to the P Cygni structure of *H*, *Ca* II, and the two *Ti* II lines and to explain why two lines alone of *Ti* II should show P Cygni structure.

Another possibility is that we are observing the sort of prominence activity postulated in HD 50138, HD 218393, and HD 236031 to account for the occasional appearance of diffuse, red-shifted absorption components. But in this star the diffuse lines are almost as strong as the sharp absorptions. Perhaps we have a combination of effects: the sharp absorption and emission lines overlie the violet wing of a broad stellar absorption line, and a weak, red-shifted absorption line, caused by material falling back toward the star, reinforces part of the red wing of the broad stellar line, causing it to be measured too far to the red. Alternatively, it is possible that the star really does have a very large peculiar velocity.

A plate taken on January 12, 1953 (Y), which could not be measured for radial velocities, shows that the emission lines are definitely weaker—emission is only visible at *Hβ*. The sharp cores appear to be superposed on broad absorptions, and the lines are not double. The α Cygni lines are the same, and *Mg* II 4481 is still the strongest except for *Ca* II K.

HD 218393

Two plates of this star, taken on September 30 and October 4, 1952 (Y), do not show the secondary, violet-displaced absorption components in the hydrogen lines, found by Struve[3] to appear irregularly at 11–18-day intervals. On our two plates *Hβ*, *Hγ*, and *Hδ* have emission components on the *R* side of sharp, narrow absorptions, superposed on

broad underlying absorptions. Absorption lines of *Mg* II and *Si* II are fairly strong and intermediate in width between the *H* cores and the very diffuse lines of *He* I. *Ca* II K is a strong absorption line. There is a weak metallic-line shell present (Struve observed this to vary between invisibility and moderate strength and thus to resemble the $\alpha$ Cygni lines in AX Mon). *Fe* II 4233 has an emission border on the *R* side of the narrow absorption, and in this respect it resembles the two *Ti* II lines on our plate of HD 31648.

A plate taken in the visual region on September 16, 1952 (Y), shows that *Ha* is a broad, very strong emission, not resolved on our dispersion into any structure. Absorption lines in this region are due mainly to *Fe* II, while the *Na* I D lines are very strong, *He* I $D_3$ is moderately strong, and the interstellar line at $\lambda$ 6284 is visible but weak.

Struve[3] described in detail a remarkable sequence of rapid changes in the spectrum of this star and pointed out their similarity to those occurring in AX Mon. In this star also he suggested that outward surges of matter were the cause of the secondary, violet-displaced absorption lines.

Merrill[4] discussed a series of coudé spectrograms taken between 1943 and 1948. He described the "Balmer progression" (also noted by Struve), in which the velocities of the *H* lines had progressively larger positive values on going to higher Balmer members, and he concluded that this was due to the presence on most plates of a diffuse wing bordering the sharp absorption cores on the red side. This wing became stronger relative to the cores on going to higher Balmer lines. On a few of his plates this wing had the appearance of a separate, diffuse line, shifted to the red. It seems that here again we may have the falling downward into the star of material, giving rise to weak absorption components with large positive relative velocities, in addition to the strong, outward-moving prominence activity in which the velocities reach 200 km/sec or more.

### HD 236031

Two spectrograms of this star were obtained on September 16, 1952 (visual region) and September 20, 1952 (photographic region) (both Y). The first shows very strong emission at *Ha*; the *Na* I D absorption lines and the interstellar line at $\lambda$ 6284 are moderately strong. The second plate shows a strong emission line at *H*$\beta$, on the *R* side of an absorption core; both are superposed on a broad underlying absorption line. *H*$\gamma$ has a very sharp absorption core over a broad underlying absorption, and no emission line is visible. Thus the Balmer decrement is steep. Numerous narrow absorption lines are present, evidently arising in the shell: lines of *Fe* II, *Ti* II, *Mg* II, *Si* II, *Sc* II, and *Ca* II were identified, and *Cr* II and *Fe* I may also be present. *Mg* II 4481 is strong and very sharp and definitely arises in the shell; thus the effect of dilution is not very marked. Lines of *He* I are broad and diffuse.

The shell is variable: Merrill *et al.*[1] remarked that the HD spectral type was B3 and that shell lines of *H*, *Ca* II, *Fe* II, and *Mg* II were present at the time of their observations. The shell spectrum is apparently stronger on our plate than it was then.

Merrill *et al.* found that the *H* lines had variable negative displacements, and in addition there were weaker diffuse components which shifted from one side of the core to the other. Displaced components were not visible on our plate, but it may require higher dispersion to distinguish them from the broad underlying absorptions, which did appear to be stronger on the *R* side. Prominence activity probably occurs in this star also, in addition to the more stable shell.

## CONCLUDING REMARKS

Further observations of these stars with high dispersion may elucidate the problem of the red-displaced absorption components which have been observed in some of them. However, the basic problem of the instability of stars of this sort is a difficult one. In the first place, one does not know how deep the instability arises. The stars probably all rotate rapidly, but there are many other fast-rotating shell stars which do not show

this sort of violent prominence activity. The stars described here are probably all of main-sequence luminosity, or at least we are not dealing with highly luminous stars like P Cygni (as indicated by their apparent magnitudes and the appearance of the interstellar features).

In AX Mon[6] and in 17 Lep[14] (which was mentioned in the Introduction) traces of a weak M-type spectrum have been found, which might arise in a separate late-type companion. They are reminiscent of the still more peculiar stars with "combination" spectra such as, for example, Z And and AG Peg. AX Mon has been found in the past to have small light-fluctuations, and it would be interesting if these could be investigated further and compared with the spectral variations.

All the observational work was carried out while the authors were working at the Yerkes and McDonald Observatories. We are indebted to Professor R. O. Redman for the use of a measuring machine at the Observatories, University of Cambridge.

[14] A. Slettebak, *Ap. J.*, **112**, 559, 1950.

# EMISSION-LINE PROFILES FROM EXPANDING ENVELOPES

M. K. Vainu Bappu and D. H. Menzel
Harvard College Observatory, Cambridge, Massachusetts
*Received August 11, 1952; revised November 30, 1953*

ABSTRACT

We have developed a method for calculating the emission-line profiles from an expanding envelope. The method applies to an envelope where the emission intensity varies with latitude. Some typically illustrative cases are considered.

## I. INTRODUCTION

There is little doubt that the breadth of the emission lines in Wolf-Rayet stars and the novae arises from the relative motion of the atoms in a shell of gas surrounding the core. The presence of catastrophic explosions, as in the case of novae, justifies the postulate of expanding shells of luminous gas which account for the observed profiles during and immediately after the outburst. Menzel[1] and Beals[2] considered the simplest case of a shell expanding with constant velocity. The profile from such an envelope is essentially flat-topped. Gerasimović[3] studied the line profiles from an expanding gaseous shell surrounding a nova whose velocity of expansion is a function of the radius and whose emission at a point depends on the density. Chandrasekhar[4] extended this earlier work in an important study of expanding envelopes in general and was the first to stress the necessity of considering the "occultation effect" caused by the body of the star. Wilson[5] modified Chandrasekhar's method of analysis to facilitate the actual fitting of the observed profiles of novae to theoretical ones. We develop here a general method for the determination of an emission-line profile, based on certain specific assumptions. The analysis facilitates the easy derivation of profiles in cases characterized by lack of symmetry.

## II. THE CONTOURS OF THE EMISSION BANDS

The problem has three distinct parts. The first is purely geometrical and refers to the choice of co-ordinates and assumptions regarding the atmospheric structure. The second is physical, defining the origin of luminosity and its dependence on density, velocity, etc. The third is kinematical and fixes the variation of velocity in the shell.

We adopt a conventional system of polar co-ordinates, $r$, $\theta$, $\phi$, with the axis of symmetry directed toward the observer. Let $i(r, \theta, \phi)$ be the emission per unit volume. Then the emission from the volume element will be

$$i(r, \theta, \phi)\, r^2 \sin\theta\, dr\, d\theta\, d\phi\,. \tag{1}$$

If this element expands radially with a uniform velocity $v$, the projected velocity $u$, in the line of sight of the observer, will be

$$u = -v\cos\theta\,. \tag{2}$$

Line-of-sight velocities toward the observer are conventionally negative. Now, since the volume element extends over $d\theta$, the velocity component will range over $du$, according to the law

$$du = v\sin\theta\, d\theta\,. \tag{3}$$

[1] *Pub. A.S.P.*, **41**, 344, 1929.
[2] *M.N.*, **91**, 966, 1931.
[3] *Zs. f. Ap.*, **7**, 335, 1933.
[4] *M.N.*, **94**, 522, 1934.
[5] *Ap. J.*, **80**, 259, 1934.

We can therefore change variables and say that the emission from the volume element is

$$i\left(r, \frac{u}{v}, \phi\right) r^2 dr\, d\phi \frac{du}{v}, \tag{4}$$

since, by virtue of equation (2), we can say that $\theta$ is a function of $(u/v)$. Chandrasekhar eliminates $r$ rather than $\theta$, a choice that complicates slightly the selection of the integration limits. It also makes more difficult the extension of the model to nonuniform emission over the disk, a case that we shall discuss later.

If $\lambda_0$ is the position of the undisplaced line, the volume element will contribute to the emission at a new wave length, $\lambda$, such that

$$\lambda = \lambda_0 \left(1 + \frac{u}{c}\right). \tag{5}$$

Atoms in the volume element, over the range $du$, will contribute radiation to the wavelength interval

$$d\lambda = \lambda_0 \frac{du}{c}. \tag{6}$$

Therefore, we can say that the volume element contributes radiation at $\lambda$ over the range $d\lambda$, of amount

$$i\left(r, \frac{\lambda - \lambda_0}{\lambda_0} \frac{c}{v}, \phi\right) \frac{c}{v} r^2 dr\, d\phi \frac{d\lambda}{\lambda_0}. \tag{7}$$

To get the total emission in the range $d\lambda$, we have to define $i$ as a function of $r$ and $\phi$, allowing for possible dependence on $\theta$ by means of equations (2) and (3). We next integrate over the co-ordinates $r$ and $\phi$. Or

$$E_\lambda p\lambda = \int\int i\left(r, \frac{\lambda - \lambda_0}{\lambda_0} \frac{c}{v}, \phi\right) \frac{c}{v} r^2 dr\, d\phi \frac{d\lambda}{\lambda_0}. \tag{8}$$

Let

$$l = \frac{\lambda - \lambda_0}{\lambda_0}, \qquad dl = \frac{d\lambda}{\lambda_0}, \tag{9}$$

and measure the position within the line, so that $l = 0$ refers to the undisplaced center. Then

$$E_l dl = \int\int i\left(r, l\frac{c}{v}, \phi\right) \frac{c}{v} r^2 dr\, d\phi dl. \tag{10}$$

Our next concern is with the physics of the problem. We should expect that the emission in so highly ionized an atmosphere would depend on the square of the density. To achieve slightly greater generality, we shall adopt

$$i = C\rho^2 \left(\frac{v}{v_0}\right)^\beta, \tag{11}$$

where $v_0$ is a constant that we shall shortly define. If radial currents are responsible for the maintenance of the density distribution, so that $v$ is radial and dependent solely upon $r$, we have recourse to the equation of continuity,

$$\nabla \cdot (\rho \boldsymbol{v}) = -\frac{\partial \rho}{\partial t}. \tag{12}$$

For a steady state, $\rho$ is independent of $t$, and we get

$$\frac{d}{dr}(\rho r^2 v) = 0; \tag{13}$$

and hence

$$r^2 \rho v = \text{Constant} = r_0^2 \rho_0 v_0, \tag{14}$$

where $\rho_0$ and $v_0$ represent the values of these parameters at some specially chosen value of the radius $r = r_0$. We shall eventually identify $r_0$ with the effective inner boundary of a shell surrounding the star. With this equation,

$$i = C\rho_0^2 \left(\frac{r_0}{r}\right)^4 \left(\frac{v}{v_0}\right)^{\beta-2}. \tag{15}$$

As far as our equations are concerned, $\rho_0$ may still be a function of $\theta$ and $\phi$ and therefore of $u$ and $\phi$. Hence we write

$$E_l dl = \frac{C r_0^3 c}{v_0} \int\int \rho_0^2 \left(\frac{r_0}{r}\right)^2 \left(\frac{v}{v_0}\right)^{\beta-3} d\left(\frac{r}{r_0}\right) d\phi dl. \tag{16}$$

For the simplest case of all, wherein $\rho_0$ is independent of $\theta$ and $\phi$ and where $v = \text{Constant} = v_0$, we get

$$E_l dl = \frac{2\pi C r_0^3 c \rho_0^2}{v_0} \left[\frac{r_0}{r}\right]_{r_{\min}}^{r_{\max}} dl. \tag{17}$$

The coefficient of $dl$ is a constant, i.e., it is independent of $l$ as long as

$$|l| \leqslant \frac{v_0}{c}. \tag{18}$$

If, for example, we take $r_{\min} = r_0$ and $r_{\max} \gg r_0$, for the inner and outer radii of the shell, we have

$$E_l dl = \frac{2\pi C r_0^3 \rho_0^2 c}{v_0} dl. \tag{19}$$

This analysis pertains to the previously mentioned case, first discussed by Beals, where the profile is flat-topped.

To make further progress, one must know the kinematical picture, or the dependence of $v$ upon $r$. We assume the following law, which lends itself to a variety of physical interpretations:

$$v = v_0 \frac{(b - a[r_0/r])^\gamma}{(b-a)^\gamma}. \tag{20}$$

The constants $a$, $b$, and $\gamma$ represent arbitrary dimensionless parameters. We have included extra constants to facilitate substitution later on. Differentiating equation (20), we get

$$\left(\frac{r_0}{r}\right)^2 d\left(\frac{r}{r_0}\right) = \frac{b-a}{\gamma a} \left(\frac{v}{v_0}\right)^{(1-\gamma)/\gamma} d\left(\frac{v}{v_0}\right). \tag{21}$$

In terms of the variable $v$, equation (16) becomes

$$E_l dl = \frac{C r_0^3 c}{v_0} \frac{(b-a)}{\gamma a} \int\int \rho_0^2 \left(\frac{v}{v_0}\right)^{(1-\gamma)/\gamma+\beta-3} d\left(\frac{v}{v_0}\right) d\phi dl. \tag{22}$$

At first sight this integrand appears to be independent of the basic variable $l$. However, the afore-mentioned stepwise character of the function is all-important. With $\rho_0$ constant, each velocity interval $dv$ corresponds to a given interval $dr$, wherein we can consider the velocity constant. A given element of velocity $v$ contributes to the integral only over the half-range,

$$|l| = \frac{\lambda - \lambda_0}{\lambda_0} = \frac{v}{c}. \tag{23}$$

Thus, if our shell has minimum and maximum velocities, $v_1$ and $v_2$, the integral is the limit of a sum, as indicated schematically in Figure 1. The line is flat-topped from $l = 0$ to $l_1 = v_1/c$. Thereafter the intensity declines to zero at $l_2 = v_2/c$. The only values of

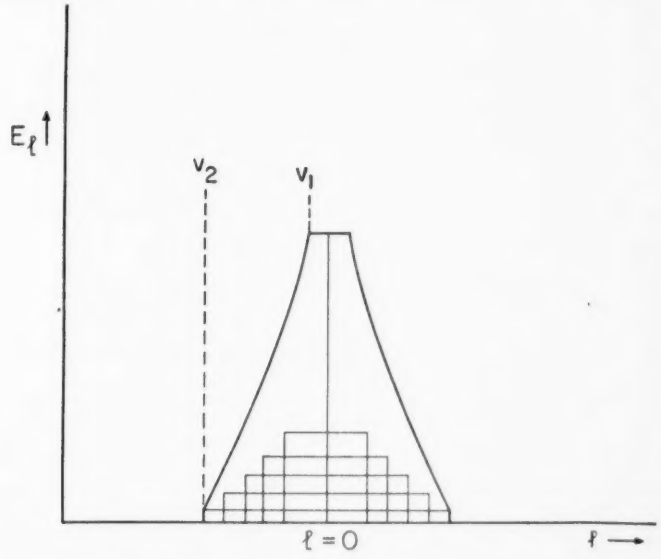


FIG. 1.—Theoretical line profiles for the values of the parameters indicated

$v$ that contribute to the intensity at a given $l$ are those for which $v \geq cl$, when $l > v_1/c$. The integral, therefore, has two sets of limits. Over the range $-l \leq v_1/c \leq l$, we integrate from $v_1$ to $v_2$, and the result is independent of $l$. Over the range $v_2/c \geq |l| \geq v_1/c$, we integrate from $v = cl$ to $v_2$. Thus

$$E_l dl = 2\pi C r_0^3 \rho_0^2 \frac{(b-a)}{\gamma a} \left(\frac{c}{v_0}\right)^{\alpha+1} \frac{l_2^\alpha - l_1^\alpha}{\alpha} dl \qquad (|l| \leqslant l_1); \tag{24}$$

$$E_l dl = 2\pi C r_0^3 \rho_0^2 \frac{(b-a)}{\gamma a} \left(\frac{c}{v_0}\right)^{\alpha+1} \frac{l_2^\alpha - l^\alpha}{\alpha} dl \qquad (l_2 \geqslant |l| \geqslant l_1),$$

where

$$\alpha = \frac{1-\gamma}{\gamma} + \beta - 2. \tag{25}$$

### III. NONUNIFORM DISTRIBUTION OF EMISSION

Before discussing the physical consequences of these formulae, let us consider one further general case. Suppose that the emission is not uniform over the surface of the sphere. Assume, for example, that

$$\rho_0^2 = \rho_1^2 \cos^2\theta' , \tag{26}$$

where $\theta'$ is the angle measured from the pole. In other words, we assume that the emission is greatest near the poles, from which point it declines to zero at the equator. The emission thus occupies a dumbbell-shaped volume surrounding each pole. We further

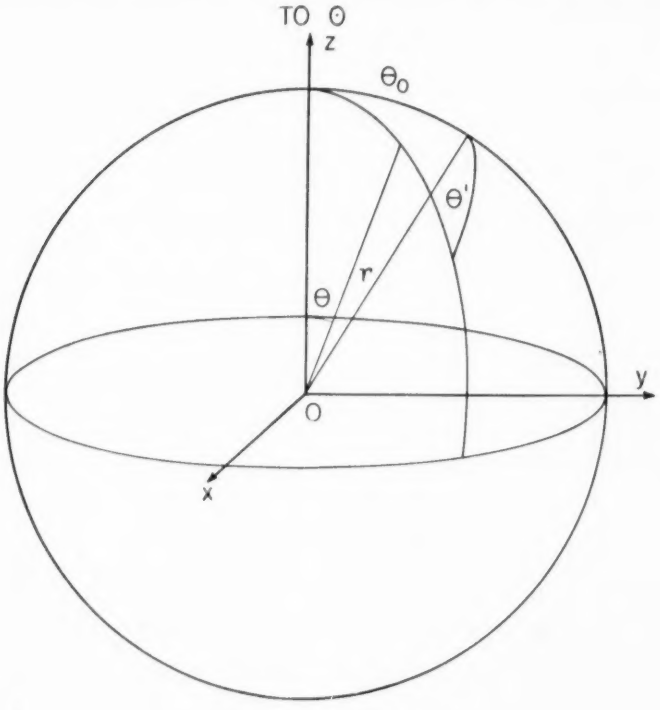


FIG. 2.—The co-ordinate system

take the axis inclined at an angle $\theta_0$ to the observer's line of sight, as shown in Figure 2. By spherical trigonometry,

$$\cos\theta' = \cos\theta \cos\theta_0 + \sin\theta \sin\theta_0 \cos\phi , \tag{27}$$

which equation enables us to express cos $\theta'$ in the co-ordinate system of the observer. We substitute from equations (26) and (27) in equation (22) and integrate first with respect to $\varphi$. As

$$\int_0^{2\pi} \cos^2\theta' d\phi = \pi [ (3 \cos^2\theta_0 - 1) \cos^2\theta + \sin^2\theta_0] ,$$

equation (24) becomes

$$E_l' dl = \frac{\pi C r_0^3 c}{v_0} \frac{(b-a)}{\gamma a} \rho_1^2 \int \left[ (3\cos^2\theta_0 - 1) l^2 \frac{c^2}{v_0^2} \left(\frac{v_0}{v}\right)^2 + \sin^2\theta_0 \right] \left(\frac{v}{v_0}\right)^{a-1} d\left(\frac{v}{v_0}\right) dl \,. \quad (28)$$

The limits of integration stand as in the earlier problem. Hence

$$E_l' dl = \pi C r_0^3 \rho_1^2 \left(\frac{c}{v_0}\right)^{a+1} \frac{(b-a)}{\gamma a} \left[ \frac{l_2^{a-2} - l_1^{a-2}}{a-2} l^2 (3\cos^2\theta_0 - 1) + \frac{l_2^a - l_1^a}{a} \sin^2\theta_0 \right] \quad (|l| \leqslant l_1) \,; \quad (29)$$

$$E_l' dl = \pi C r_0^3 \rho_1^2 \left(\frac{c}{v_0}\right)^{a+1} \frac{(b-a)}{\gamma a} \left[ \frac{l_2^{a-2} - l^{a-2}}{a-2} l^2 (3\cos^2\theta_0 - 1) + \frac{l_2^a - l^a}{a} \sin^2\theta_0 \right] \quad (|l| \geqslant l_1) \,.$$

The symbol $E_l'$ refers to the emission in the dumbbell-shaped region around the two poles. As an alternative, if the emission is greatest at the equator and zero at the poles, we can write, instead of equation (26),

$$\rho_0^2 = \rho_1^2 \sin^2\theta \,. \quad (30)$$

Denoting this emission by $E_l''$, we get

$$E_l'' dl = (E_l - E_l') dl \,, \quad (31)$$

with $\rho_1$ substituted for $\rho_0$ in equation (24). This emission occupies a doughnut-shaped volume around the star's equator.

## IV. CHANDRASEKHAR'S MECHANISMS *A* AND *B*

Among the numerous possibilities governing the over-all dynamical situation, Chandrasekhar considers two main types of ejection which he calls mechanisms *A* and *B*. In the first mechanism the atoms at the boundary of the star are repelled by some kind of force that is proportional to the gravitational attraction. In mechanism *B* the atom at the boundary of a star might receive a large initial velocity and, in escaping from the star, be continually decelerated in the gravitational field of the star. The atom either may escape from the star with a finite outward velocity or may fall back after ascending a certain distance.

The postulate of mechanism *A* depended much on Milne's theories of radiation pressure. As is now well known, radiation pressure cannot exert such large forces as would be necessary to produce such large-scale ejection, and hence mechanism *A* acquires an artificial aspect if radiation pressure is to play a dominant role. However, it would be of theoretical interest to consider the effects of a velocity law as postulated in mechanism *A*.

We are now prepared to discuss certain of the cases in which the physical conditions fix the parameters. The *vis viva* integral for matter moving in an inverse-square field gives

$$v = v_0 \left( \frac{b - a[r_0/r]}{b-a} \right)^{1/2} . \quad (32)$$

This equation postulates the existence of a repulsive force so that the velocity increases outward. If we take $a = b$, so that $v_0 = 0$ at $r = r_0$, the solution degenerates to the second equation of equations (24). Since $\gamma = \frac{1}{2}$, we have $\alpha = -1$ when $\beta = 0$. Then

$$E_l dl \alpha \rho_0^2 (b-a)(l^{-1} - l_2^{-1}) dl \quad (33)$$

with

$$l_2 = \frac{v_\infty}{c},$$

where $v_\infty$ is the terminal velocity. Here, as Chandrasekhar has noted, we encounter several problems. The first is that $(b - a)$ vanishes by hypothesis. The second is that $\rho_0$ becomes infinite at $r_0$, because $v_0 = 0$. Third, we note that $l^{-1} \to \infty$ as $l \to 0$, so that the line attains infinite central intensity. The first two of these problems we can overcome by making $\rho_0^2(b - a) = \infty \cdot 0$ approach a finite limit. The third difficulty, however, is serious. After all, according to our analysis, we should expect infinite intensity from a thin stationary layer of infinite density. The difficulty is formal, of course, and lies in the character of the mathematical approximation.

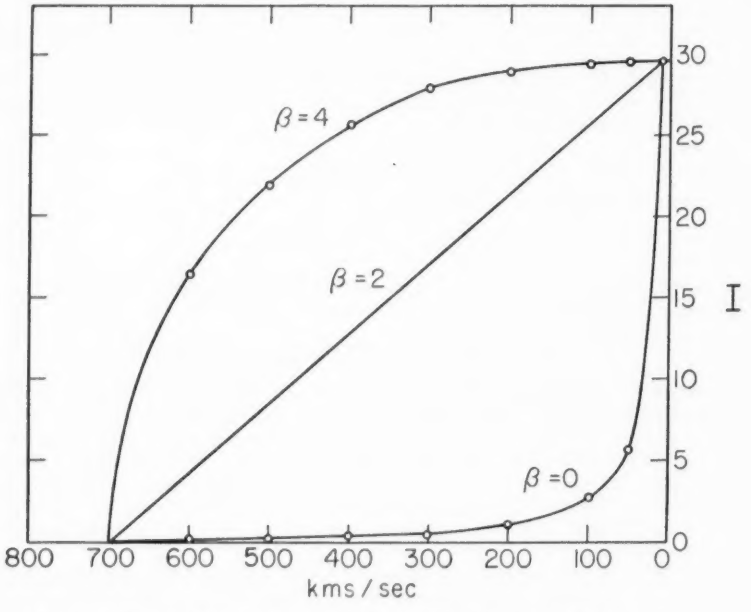


FIG. 3.—Theoretical line profiles for the values of the parameters indicated

To obtain a solution, we may adopt a nonzero value of $\beta$, as does Chandrasekhar, or we can start the solution at some finite $v_0$ and get a finite, flat-topped profile in place of the infinite, peaked one. Also, since $\alpha$ determines the form of the profile, we have the choice of altering $\gamma$ or selecting a nonzero $\beta$. If we adopt the former procedure, we obtain an arbitrary velocity law corresponding to an arbitrary and noninverse-square field.

The case of mechanism $B$ requires that the atoms move outward with a large starting velocity. Thereafter, they are subject to deceleration. For an inverse-square field we take

$$v = v_0\left(\frac{b + a\,(r_0/r)}{b + a}\right)^{1/2},$$

where $a$ is positive. Then the character of the solution depends on the sign of $b$. If $b$ is positive, the envelope extends to infinity with a finite terminal velocity. If $b$ is nega-

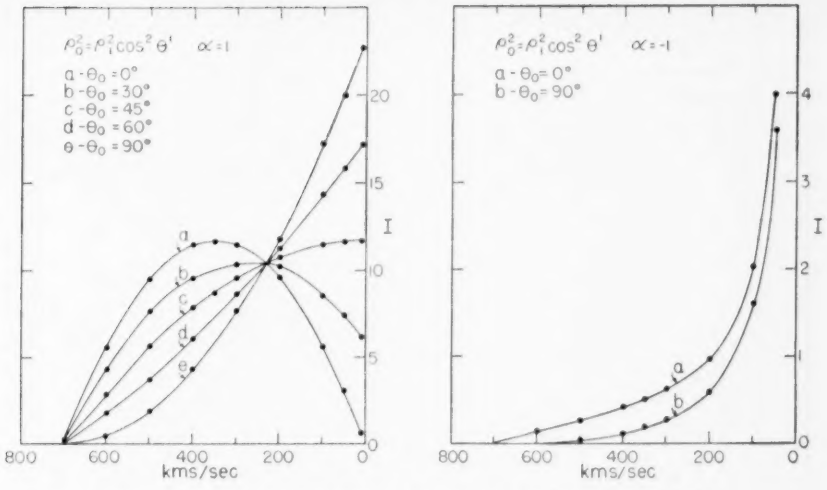


FIG. 4.—Theoretical line profiles for the values of the parameters indicated

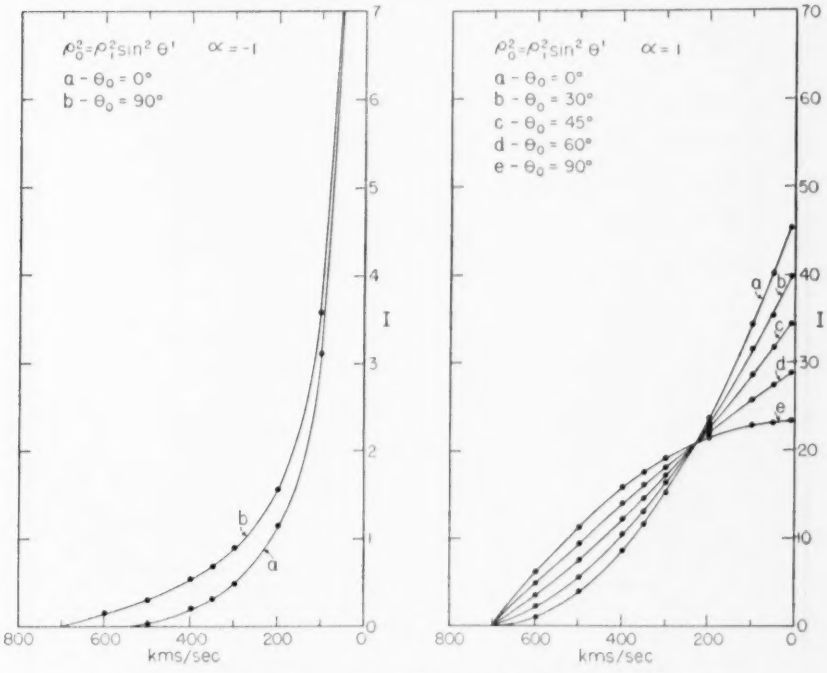


FIG. 5.—Theoretical line profiles for the values of the parameters indicated

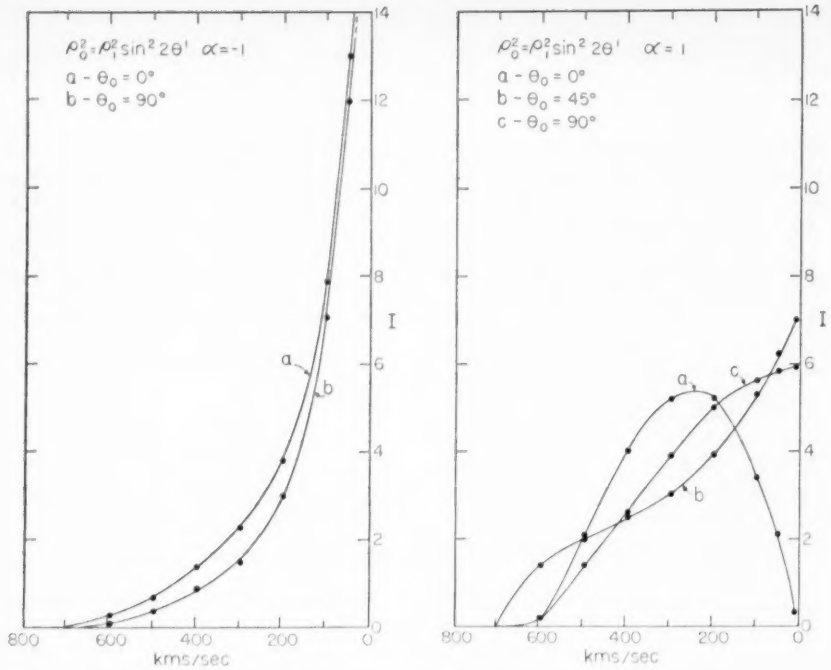


FIG. 6.—Theoretical line profiles for the values of the parameters indicated

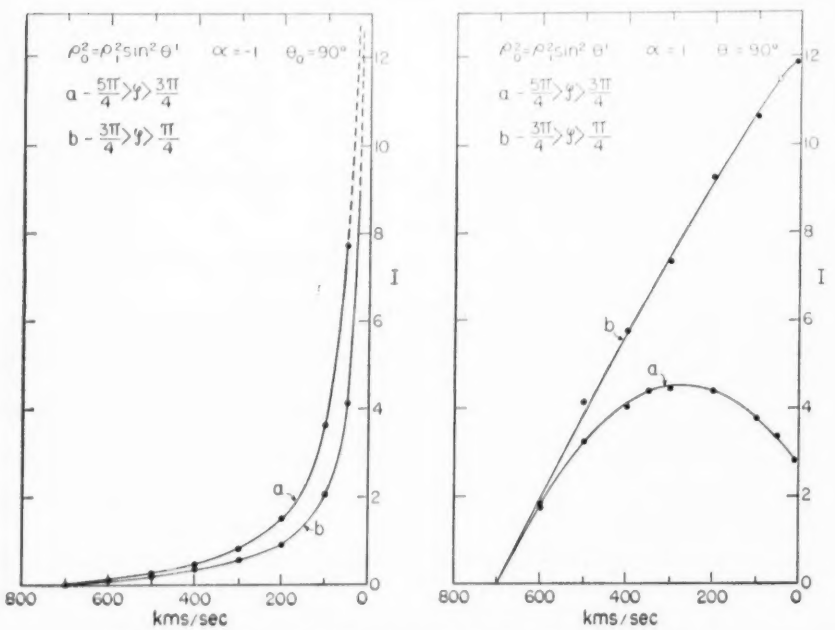


**FIG. 7.—Theoretical line profiles for the values of the parameters indicated**

tive, the velocity falls to zero at the finite distance $r = -ar_0/b$. Whenever $v \to 0$, indeterminacy arises as before, because $\rho_0$ must then be infinite.

Figure 3 demonstrates the change in form of the line contour for different values of $\beta$. The profiles result from the assumption that the emission envelope is spherically symmetrical and that the limiting velocities $v_2$ and $v_1$ are 700 and 10 km/sec, respectively. With these same limiting values of velocity, the profiles calculated for cases of nonuniform distribution of emission appear in Figures 4, 5, 6, and 7.

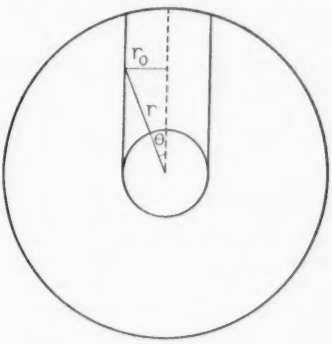


FIG. 8.—The occultation effect

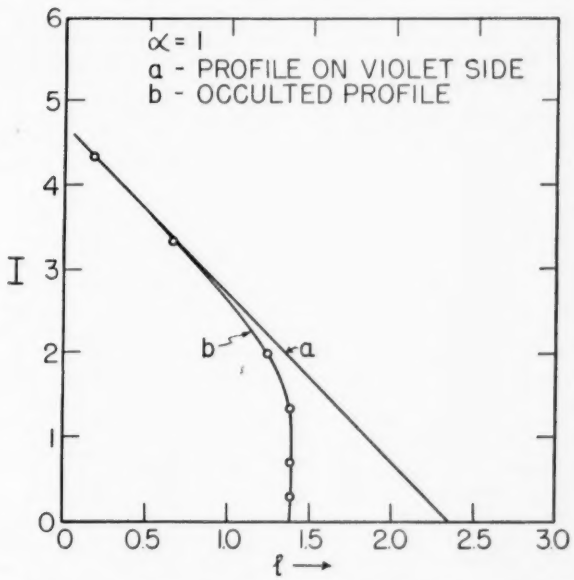


FIG. 9.—The influence of the occultation effect on the line profiles

## V. THE OCCULTATION EFFECT

The co-ordinate system and the order of integration here used lend themselves naturally to the consideration of the occultation effect. The geometry of the situation is shown in Figure 8. The star occults the portion of the shell that lies behind it, this region being defined by a tangent cylinder along the line of sight to the surface of the star. We can take care of this effect by using proper limits for the evaluation of the intensity at any value $l$. We get

$$1 - \frac{u^2}{v^2} = \sin^2\theta = \left(\frac{r_0}{r}\right)^2,$$

where $r_0$ is the radius of the star and $r$ is the radical distance of a point along the limiting visible boundary. Then the limiting value becomes

$$l_i = \frac{v}{c}\left[1 - \left(\frac{r_0}{r}\right)^2\right]^{1/2}. \tag{34}$$

The part played by occultation is then merely to shift the intensities for any value $l$ to its correspondingly modified value, $l_i$. Figure 9 demonstrates the effect when the motion in the envelope follows mechanism $B$ with the previously considered limiting velocities and the assumption that the radius of the envelope is ten times that of the parent-star.

## VI. MISCELLANEOUS COMMENTS

We point out that laws (26) and (30), here used to describe the latitude variation, are specific examples of a more general procedure, viz., expansion of the excitation function in terms of spherical harmonics.

Menzel and Payne[6] noted certain peculiar characteristics observed in the spectrum of Nova Aquilae 1918. They pointed out that the "dipped" and "peaked" profiles observed at different times in the spectral lines of this nova could be explained on the basis of ejection or excitation that was a function of latitude.

[6] *Proc. Nat. Acad. Sci.*, **19**, 641, 1933.

# RADIO DETERMINATION OF THE VELOCITY AND RADIANT OF THE DELTA AQUARID METEORS

D. W. R. McKinley
National Research Council, Ottawa, Canada
*Received November 12, 1953*

ABSTRACT

Several selection principles are applied to separate δ Aquarid shower meteors from background meteors and from other showers with near-by radiants, using radio-echo data obtained on July 26–29, 1949. The observed mean valocity of the δ Aquarid meteors was 40.20 ± 0.1 km/sec, and the radiant co-ordinates R.A. 339° ± 2°, dec. −17° ± 2°. Two near-by radiants were found; the stronger of these was located at R.A. 340° ± 5°, dec. 0° ± 5°, with a mean meteor velocity of 41.0 ± 0.5 km/sec. δ Aquarid meteors were also observed on July 18–20, 1949, with a mean velocity of 40.3 ± 1 km/sec, radiant at R.A. 342° ± 5°, dec. −15° ± 5°, and with rates about one-fifth the July 26–29 rates. It is suggested that speculations about the history of the shower, based on data available up to the present, would be of dubious value.

An earlier paper[1] described the radio techniques used for measuring meteor velocities at Ottawa and the observed velocities of more than 10,000 meteors, obtained over a period of 15 months, were presented in condensed tabular form. Among the data were velocity measurements for the period July 26–29, 1949, grouped hourly by 5-km/sec class intervals. This period embraces the δ Aquarid shower; and Lindblad[2] graciously gave us credit for providing a velocity value for the shower meteors. In actual fact, the tables contained the coarse velocity-distribution data only, and Lindblad's velocity of 40.4 km/sec was deduced by his own careful analysis of our published results. For each meteor in our records there is available the time of occurrence, the radar range to the nearest kilometer, the echo duration to 0.1 second, and the velocity computed to the nearest kilometer per second; but, owing to space limitations, all this material was omitted in the original report. In this paper we shall utilize all our available information to obtain a statistical value of the velocity of the δ Aquarid meteors. Because the detailed presentation of the numerical data requires cumbersome tables, most of the results of this work will be displayed in graphic form.

## SELECTION OF OBSERVED VELOCITIES

Velocity records were obtained continuously from 1700 hours E.S.T., July 26, to 1400 hours E.S.T., July 29, 1949, except for time lost through breakdown or film changes. The over-all velocity distribution for this period was given in Figure 5 and in Table A10 by the author[1] and showed a pronounced maximum in the 40–44-km/sec class, which was attributable to the δ Aquarid meteors. A secondary maximum in the neighborhood of 55–64 km/sec was due partly to the presence of some Perseid meteors and partly to the normal distribution of nonshower or background meteors, which also has a peak in this region.

Obviously, an appreciable number of meteors other than Aquarids was included in these data, and a number of selection principles should be applied to purify the distribution. First, the δ Aquarid radiant was above the horizon from approximately 2200 to 0700 E.S.T., so naturally only this interval need be considered. Second, if a normal nonshower velocity distribution can be deduced by using data from periods before and after the shower, this distribution may be subtracted from that of the shower period, to remove to a large extent the effect of the background meteors. Third, the minimum

[1] D. W. R. McKinley, *Ap. J.*, **113**, 225, 1941.
[2] B. A. Lindblad, *Trans. Chalmers Univ. Technol., Gothenburg*, No. 129, 1952.

range of the δ Aquarid meteors will be given by $R_{min} = H/\cos h$, where $H$ is the height at which the meteors occur and $h$ the angle of elevation of the radiant.[3] The distribution of meteors with range will therefore show a peak that increases in range as the radiant rises; and, by accepting only those echoes falling in a small range bracket about this peak, many of the nonshower meteors can be eliminated. Fourth, meteors of the well-established showers appear to have a size distribution that differs from the normal background,[4] as indicated by an increase in the percentage of long-enduring echoes during the shower activity. Therefore, if one sets an arbitrary dividing line, e.g., a duration of 0.5 second, the longer-duration group is likely to contain a higher proportion of shower meteors than is the shorter-duration group. Finally, of course, the meteor velocity itself is a most important criterion of whether or not it may be a shower meteor. While any one of these selection methods can be applied to the original data with good effect, some care should be exercised if more than one, or all of them, were to be applied in sequence. For example, the range and the duration selections operate on the individual meteors,

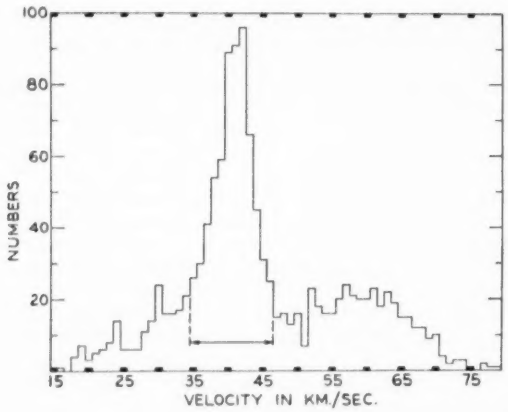


FIG. 1.—Observed velocity distribution of numbers of meteors per 1 km/sec class interval, observed between the hours of 2200–0700 E.S.T. on July 26/27, 27/28, and 28/29, 1949. Total number 1,260 meteors, in a net observing time of 22.5 hours. Arrow indicates velocity spread used in computing the mean velocity.

but the subtraction of the normal background distribution is a statistical procedure that ignores the individual identity.

The original velocity distribution, replotted in 1-km/sec steps, is shown as the histogram in Figure 1. This represents 1260 meteor velocities obtained in a total observing time of 22.5 hours, between 2200 and 0700 E.S.T. on July 26/27, 27/28, and 28/29, 1949. There is a strong maximum in the range 40–43 km/sec, which is assumed to be due to the δ Aquarid meteors, as it is absent in similar distributions obtained during other summer periods. In computing mean velocities, we shall arbitrarily select the spread of velocities between the points where the numbers are 25 per cent of the peak numbers. In this case the velocity limits are 35 and 46 km/sec, and it is found that the mean velocity of the 653 meteors in this interval is 40.60 km/sec. The data may be broken down by separate days, or they may also be divided into two periods, one when the radiant is rising and the other when it is setting. The histograms for these five cases are not

[3] D. W. R. McKinley and Peter M. Millman, *Proc. I.R.E.*, **37**, 364, 1949.

[4] D. W. R. McKinley, *Canadian J. Phys.*, **29**, 403, 1951.

shown, but the mean velocities are given in Table 1, in each case computed for the spread of velocities 35–46 km/sec.

It will be noted in Table 1 that the mean velocity decreases slightly from the July 26/27 period to the July 28/29 period; but this is not likely to be significant; as will be seen later, this trend is no longer apparent when the distribution is purified. The mean velocity for the period of radiant rising is slightly higher than that for the radiant setting, the difference being attributable to the earth's rotation. (The radiant transits about 0230 E.S.T., hence the hour 0200–0300 E.S.T. was included in both periods.) The velocity distribution of the background meteors shifts toward higher velocities as morning approaches. Therefore, if these meteors were removed, the observed diurnal aberration in the shower velocities should be somewhat greater than indicated in Table 1. Since the diurnal-aberration correction is self-canceling to a large extent, when the observing period brackets the radiant transit time symmetrically, we shall henceforth use the entire interval 2200–0700 E.S.T., and, in most cases, we shall consider the 3 days together.

### SELECTION BY REMOVAL OF BACKGROUND METEORS

The velocity distribution of Figure 1 can be purified by subtracting a "standard" distribution of normal background meteors. For this purpose data for the interval 2200–

TABLE 1

MEAN VELOCITY OF METEORS IN THE RANGE 35–46 KM/SEC

| Period | No. of Meteors | Velocity (Km/Sec) | Period | No. of Meteors | Velocity (Km/Sec) |
|---|---|---|---|---|---|
| July 26–29, 2200–0700 E.S.T. | 653 | 40.60 | July 28/29, 2200–0700 E.S.T. | 238 | 40.40 |
| July 26/27, 2200–0700 E.S.T. | 141 | 40.84 | July 26–29, 2200–0300 E.S.T. | 356 | 40.68 |
| July 27/28, 2200–0700 E.S.T. | 274 | 40.66 | July 26–29, 0200–0700 E.S.T. | 371 | 40.54 |

0700 E.S.T. were taken from observations made on July 11–13, 1949, and August 11–14, 1949. (The period July 18–20, 1949, for which observations were also available, was not suitable because it appeared to contain some $\delta$ Aquarid meteors, as will be seen later.) Only velocities between 20 and 50 km/sec were used, as the Perseid meteors were very prominent in the range 55–65 km/sec during the August period. The smooth curve *A*, of Figure 2, shows the adopted standard distribution in terms of hourly rates per 1-km/sec class interval. The histogram of Figure 1 has been converted to hourly rates also, and the portion between 20 and 50 km/sec is shown as graph *B*, drawn through the circled points of Figure 2.

It is now assumed that the standard distribution should correspond with the observed distribution for the period July 26–29 for velocities up to about 33 km/sec. The agreement is good and can be made better by multiplying the standard values by 1.2. This procedure is valid because the equipment might easily have been slightly less sensitive on one or more of the standard days, which would reduce the hourly rates without otherwise affecting the velocity distribution. The amended standard values are subtracted from the ordinates of graph *B*, to yield the corrected distribution shown by the histogram *C*, Figure 2. We are now justified in narrowing the velocity limits to the range 37–45 km/sec when averaging the velocities. The mean velocity thus obtained is 41.05 km/sec. The purity of the corrected distribution should be high as far as the elimination of normal background meteors is concerned, but there remains the possibility that the meteors in the solid-line histogram of Figure 2 may come from more than one prominent radiant, though, if so, one would expect the shower velocities to be nearly equal, since the spread is small.

SELECTION BY ECHO DURATION

The original data may be arbitrarily divided into two categories, one in which the echo durations are less than a selected arbitrary value and the other containing longer-duration echoes. The longer-duration category will have a higher proportion of shower meteors to background meteors, and the proportion will increase if larger values are selected for the dividing line. At the same time, of course, the numbers in the long-duration category will fall off sharply, so some compromise must be reached. Lindblad[2] found the value 0.5 second to be a reasonably satisfactory value; and, as his equipment was roughly comparable in sensitivity and wave length to ours, we shall follow the same

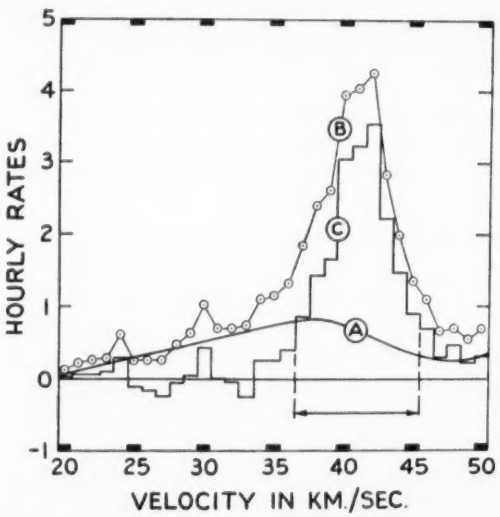


FIG. 2.—*Curve A:* hourly rate–velocity distribution of the "standard" or background meteors, taken from 2200 to 0700 E.S.T., July 11–13, and August 11–14, 1949. *Graph B:* observed velocity distribution, 2200–0700 E.S.T., July 26–29, 1949, from Fig. 1, reduced to hourly rates. *Histogram C:* purified velocity distribution obtained by multiplying the ordinates of curve *A* by 1.2 and subtracting them from graph *B*.

procedure. Figure 3, solid-line histogram, shows the velocity distribution of echoes with durations of 0.5 second and over, for the hours 2200–0700 E.S.T. on all three nights, July 26–29, 1949; and the dashed histogram is the distribution for echoes less than 0.5 second in duration. It is apparent that there may still be an appreciable number of shower meteors in the short-duration distribution; but, judging from the greater sharpness of the maximum for the longer-duration echoes, it is probable that the longer-duration category contains a higher proportion of shower meteors. We again apply our arbitrary criterion for determining the spread of velocities to be used in finding the mean, namely, the 25 per cent points. For echoes less than 0.5 second, this is 36–46 km/sec, and, for echoes 0.5 second and over, it is 37–44 km/sec. The short- and long-duration echo velocities are given in Table 2, which also lists the values for each day separately: no graphs are shown for the individual days.

There does not appear to be any significant change in velocity from day to day for either the short- or the long-duration echoes. In this respect the values in Table 2 differ slightly from those in Table 1, both because of the selection by duration and because

the velocity spreads used in computing the velocities in Table 2 are slightly different. On the other hand, the velocity of all the short echoes in Table 2 may be significantly greater than that of the long echoes, and the true differential is probably even larger than the table indicates. This follows if one subtracts the standard distribution-curve of background meteors (curve *A*, Fig. 1) from the short-echo distribution, which is justified here because most of the background meteors are less than 0.5 second in duration. Since this standard curve falls in amplitude as the velocity increases from 38 to 45 km/sec, the resultant distribution will have a still higher velocity. We would be less justified in doing this for the long-duration distribution, which should contain few back-

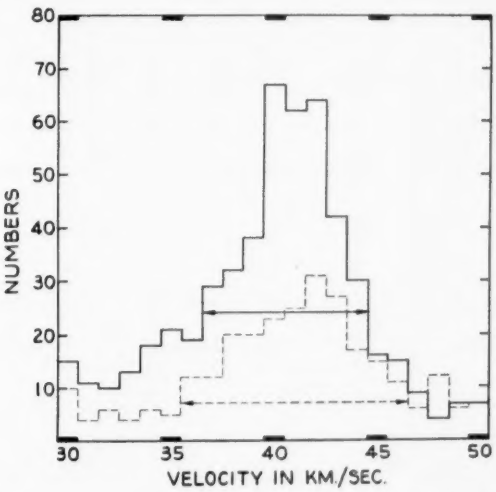


FIG. 3.—*Solid-line histogram:* velocity distribution of echoes with durations 0.5 sec and over, 2200–0700 E.S.T., July 26–29, 1949. *Dashed-line histogram:* velocity distribution of echoes with durations less than 0.5 sec, 2200–0700 E.S.T., July 26–29, 1949.

TABLE 2

MEAN VELOCITY OF METEORS WITH SHORT- AND LONG-DURATION ECHOES

| Period | Echo Category | No. of Echoes | Mean Velocity (Km/Sec) | Period | Echo Category | No. of Echoes | Mean Velocity (Km/Sec) |
|---|---|---|---|---|---|---|---|
| July 26–29, 1949 2200–0700 E.S.T. | $<0.5$ | 213 | 41.07 | July 27/28, 1949 2200–0700 E.S.T. | $<0.5$ | 108 | 40.77 |
| | $\geqq .5$ | 364 | 40.62 | | $\geqq .5$ | 129 | 40.79 |
| July 26/27, 1949 2200–0700 E.S.T. | $< .5$ | 35 | 41.66 | July 28/29, 1949 2200–0700 E.S.T. | $< .5$ | 70 | 41.25 |
| | $\geqq 0.5$ | 85 | 40.66 | | $\geqq 0.5$ | 150 | 40.47 |

ground meteors; hence the conclusion is that there may be a real difference in the velocities of small and large meteors of the $\delta$ Aquarid shower. On the other hand, it might happen that an appreciable number of the short-duration echoes are due to a second radiant, which may be transiting at about the same time but at a higher elevation. Be-

cause of their greater average ranges, the observed durations of such meteors would be less than if they had occurred nearer the zenith.[5]

SELECTION BY ECHO RANGE

If the numbers of meteors in equal range intervals are plotted against range, a smooth curve will usually be obtained, during nonshower conditions, which rises steeply to a maximum at 110–130 km and then falls off slowly with increasing range. The presence

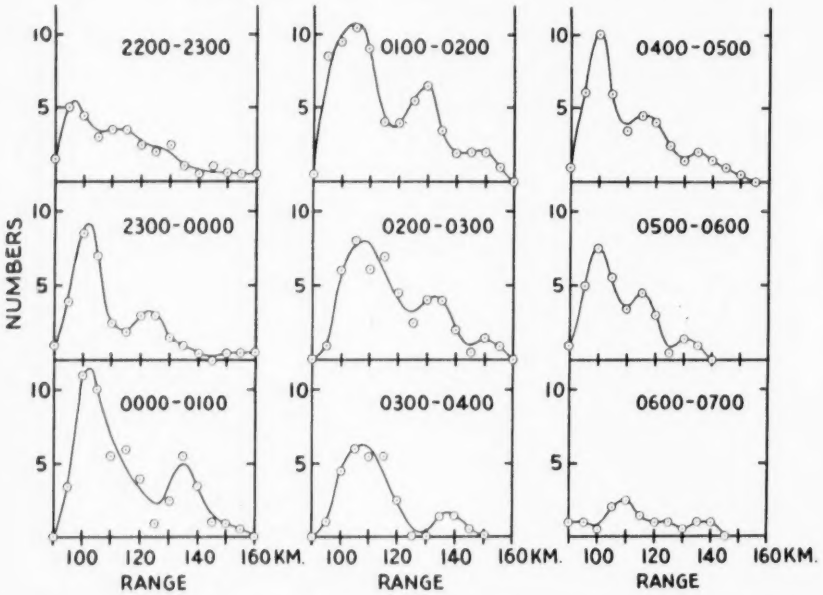


FIG. 4.—Hourly range distributions of echoes with durations 0.5 sec and over and with velocities in the intervals 37–44 km/sec, 2200–0700 E.S.T., July 26–29, 1949. The ordinates are the 3-day total numbers per 5 km class interval of range.

of a strong shower will produce a hump on this curve, which moves out in range as the shower radiant rises. The technique of determining shower radiants from a set of range-curves has been described elsewhere[3] and will be applied here, both to obtain the coordinates of the δ Aquarid radiant and to isolate that radiant from other shower radiants that might be active at the same time.

Only those echoes with durations 0.5 second and greater and in the velocity spread 37–44 km/sec are used, as these are likely to contain the highest percentage of shower meteors. Figure 4 shows the hourly-range-distribution-curves obtained with a class interval of 5 km. A sliding scale of 2 intervals was used to smooth out some of the minor fluctuations. There is a strong maximum at 97 km for 2200–2300 hours, which moves out in range until about 0200–0300 hours and then recedes slightly. The amplitude of this maximum is considerably in excess of the peak of the standard distribution and is due to the δ Aquarid meteors. The modal ranges of this maximum will be used later to compute the elevation of the δ Aquarid radiant. The importance of Figure 4 at this

[5] D. W. R. McKinley, *Canadian J. Phys.*, **31**, 758, 1953.

point is that there is a pronounced secondary maximum at longer ranges on each of the curves, together with a smaller tertiary maximum in some cases. As we have already restricted our attention to meteors with long durations in the velocity range 37–45 km/sec, we now conclude that an appreciable fraction of these meteors must belong to a second radiant, with the possibility of a few being attributable to a third radiant.

We can therefore purify further the selection made in the preceding sections by excluding all meteors with ranges in excess of 120 km, say. This will inevitably result in the loss of some δ Aquarids, too, but the percentage of δ Aquarids in the residue should be greater than before. Figure 5, solid-line histogram, shows the distribution of velocities of these selected meteors, over the interval 35–47 km/sec. Applying our 25 per cent criterion, we have a velocity spread of 36–44 km/sec for averaging purposes, and the mean velocity of the 268 meteors in this interval is 40.20 km/sec. The standard deviation is 2.1 km/sec, and the probable error of the mean is about 0.1 km/sec. This is the best mean value of the observed velocity that we can assign to the δ Aquarid shower meteors.

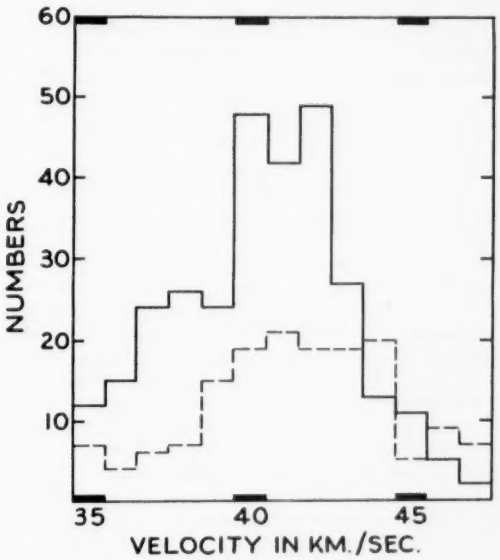


FIG. 5.—*Solid line histogram:* velocity distribution of echoes with durations 0.5 sec and over and with ranges less than 120 km. *Dashed line histogram:* velocity distribution of echoes with durations 0.5 sec and over and with ranges 120 km and greater.

Figure 5, dashed histogram, shows the distribution of velocities of meteors with ranges over 120 km and durations 0.5 sec and over. The majority of these is probably due to the radiant causing the secondary hump in the range-curves of Figure 4. Using the velocities between 37 and 44 km/sec, we obtain 41.0 km/sec ± 0.5 km/sec as a minimum value of the mean velocity of the meteors from the second radiant. The subtraction of any arbitrary proportion of the standard background meteor distribution would increase this value slightly. This will not be attempted, because the factor of proportionality is now uncertain, owing to the earlier selection processes. As mentioned in the previous section, some of the echoes of duration less than 0.5 second may be due to this

second radiant: the velocity obtained for all short-duration echoes, 41.21 km/sec, is comparable to the above velocity and both are significantly higher than the value, 40.20 km/sec, which we have obtained for the purified δ Aquarid distribution.

### RADIO DETERMINATION OF THE δ AQUARID RADIANT

From the curves of Figure 4 we may read the ranges corresponding to the modal values of the first or most prominent maximum in the range distribution each hour. If we were to follow closely the procedure outlined in a previous paper,[3] we would first attempt to subtract typical standard or background range distributions from the curves of Figure 4. However, as we have already taken steps to reduce the percentages of background meteors by duration selection, the subtraction of the range distribution of any estimated remainder of the background meteors will have an insignificant effect. The modal ranges are inserted in the formula $R_{\min} = H/\cos h$, where $H$ is the height of the meteoric layer and $h$ the radiant elevation; $H$ is not known, a priori, but previous experience suggests that the most likely height for the maximum meteoric shower activity will occur between 90 and 100 km. Accordingly, in Figure 6 we have plotted four curves corresponding to selected values of $H = 93$, 95, 97, and 100 km.

From the hourly velocity distributions (these are not shown, though Fig. 7 effectively summarizes the data) it can be deduced that the strong activity, which we are tentatively associating with the δ Aquarid radiant, commenced shortly after 2200 E.S.T. and ended about 0700 E.S.T. On examining Figure 6 it is immediately apparent that $H = 100$ km cannot be correct, as it puts the radiant below the horizon at 2300 E.S.T. and on the horizon at 0500 E.S.T. Similarly, the curve for $H = 97$ km is not satisfactory, because it requires the radiant to be on the horizon at 2230 E.S.T., and we know there was moderate shower activity prior to this. The curve for $H = 93$ km, on the other hand, is also unacceptable, because, if extrapolated, it predicts measurable activities well before 2200 E.S.T. and after 0700 E.S.T. We conclude that $H = 95$ km is the most probable height of the meteoric ionization due to the δ Aquarid meteors. Having established this, it follows from Figure 6 that $h = 28°$ is the most likely elevation of the radiant at upper transit, with a probable error of about 2°. This corresponds to a declination of the apparent radiant of $-17° \pm 2°$. It may be noted that if the co-ordinates of a strong shower radiant were known accurately from other techniques, e.g., photographic or visual, the above method applied in reverse should yield a very accurate height for the maximum meteoric activity associated with that radiant.

The time of the upper transit of the radiant may be read directly from Figure 6. The best value is 0230 E.S.T., with a probable error of 30 minutes, because the maximum is rather flat. A better estimate of the time of transit may be obtained by plotting hourly rates against time, as in Figure 7, using meteors less than 120 km in range and with durations 0.5 second and over. The circled points are the observed hourly rates, corrected only for time lost, and a smooth curve has been drawn through them. The time of upper transit is read from this curve as 0213 E.S.T., with an error of 10 minutes. The weighted mean of the time of transit, from both Figure 6 and Figure 7, is 0217 E.S.T. ± 8 minutes, corresponding to R.A. 339° ± 2°.

It is possible to obtain a value for the declination of the radiant from Figure 7 by fitting computed curves to the observed points, based on assumed radiant positions. These theoretical curves are not simple cosine functions, because the probability function[1] for the radio equipment must be included in the calculations. The method is not very accurate for a radiant that is low in the sky, and the technique illustrated in Figure 6 is to be preferred.

It is apparent from Figure 4 that a second radiant of lesser activity must be present to cause the secondary maxima in the curves. Despite the considerable fluctuation of the modal values of this secondary maximum, it is possible to determine the approximate radiant co-ordinates. The greatest modal range is about 135 km, which corresponds to

a maximum elevation of the radiant of 45°, if we assume the meteoric layer to be at a height of 95 km. The time of transit was determined to be between 0200 and 0300 E.S.T., from an examination of the hourly rate-curve for meteors with ranges over 120 km (not shown). Thus the co-ordinates of the second radiant are estimated to be R.A. 340° ± 5°, dec. 0° ± 5°. Very little can be said about a possible third radiant of weak activity which may be causing the small tertiary maximum in the curves of Figure 4, other than that its right ascension is probably in the neighborhood of 340° and its declination may be about +10°.

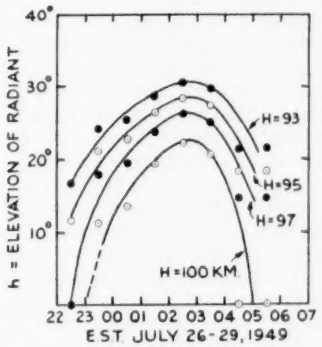


FIG. 6

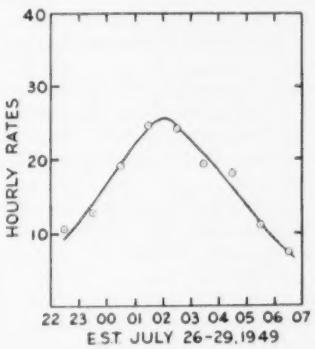


FIG. 7

FIG. 6.—Computed elevation of the δ Aquarid radiant, using data from Fig. 4 and assuming the height of maximum meteor activity to be, respectively, $H$ = 93, 95, 97, and 100 km.

FIG. 7.—Hourly rates of echoes with durations 0.5 sec and over, with velocities in the interval 36–44 km/sec, and with ranges less than 120 km.

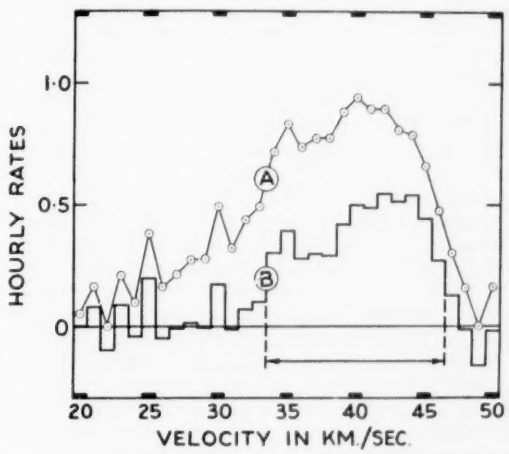


FIG. 8.—*Graph A:* observed velocity distribution of all echoes, 2200–0700 E.S.T., July 18–20, 1949, reduced to hourly rates. *Histogram B:* purified velocity distribution obtained by multiplying the ordinates of curve *A*, Fig. 2, by 0.6 and subtracting them from graph *A*.

### DELTA AQUARID ACTIVITY, JULY 18–20, 1949

In preparing the standard distribution of background meteors used in an earlier section for purifying the shower distribution, it was found that in the period July 18–20, 1949, there was an unexpectedly large number of meteors with velocities between 35 and 45 km/sec. As it appeared likely that these meteors were early δ Aquarids, this period was deleted from the standard distribution data.

The observed velocity distribution, from 20 to 50 km/sec, of all meteors between 2200 and 0700 E.S.T. on July 18–20, 1949, is shown in Figure 8 as graph *A*, through the circled points. Comparing the standard distribution (curve *A*, Fig. 2) with this distribution between 20 and 33 km/sec, we conclude that the best fit may be obtained if the ordinates of the standard distribution were multiplied by 0.6 before subtracting. The resultant distribution is shown by the histogram *B*, of Figure 8. The hourly rates per 1-km/sec class interval in the vicinity of 40 km/sec are about one-fifth the rates for the July 26–29 period, and the spread of velocities is greater; but it is nevertheless apparent that a moderately strong shower was present during the July 18–20 period. The average velocity of the meteors in the interval 34–46 km/sec is 40.3 km, with a probable error of 1 km/sec.

The relatively small number of meteors in the July 18–20 period suggests that little would be gained by attempting to purify them by a selection based on echo duration. We have, however, made hourly plots of the range distributions of all meteors with velocities between 35 and 46 km/sec (not shown), to determine the declination of the shower radiant by the method previously outlined. These curves showed no evidence of more than one maximum; hence it was considered unnecessary to segregate the echoes in range. The corrected hourly rate-curves (not shown) were also examined to determine the time of radiant transit. The co-ordinates of the single radiant that was detected on July 18–20 were R.A. $342° \pm 7°$, dec. $-15° \pm 5°$.

It is therefore highly probable that this is the δ Aquarid radiant, with an activity of about one-fifth to one-sixth its maximum activity. On comparing the radiant co-ordinates for the July 18–20 and the July 26–29 periods, it would seem that the changes in both right ascension and declination are in the opposite directions to the changes usually observed for other strong showers, e.g., Perseids and Geminids. Little weight can be attached to this tentative evidence, in view of the large probable errors associated with the radiant position for the earlier period. While the observed shower velocities for the two periods are in remarkably good agreement, it should be remembered that the computed heliocentric velocities could be appreciably different. However, owing to the uncertainty of the July 18–20 radiant position, no useful conclusions about the history of the δ Aquarid shower can be drawn by computing orbits for the two periods.

### DISCUSSION

In considering the various methods of purifying the basic observations in order to obtain a group of meteors that would contain the highest percentage of δ Aquarid meteors, it was concluded that the best selection was reached by using observations between 2200 and 0700 E.S.T., July 26–29, 1949, with durations of 0.5 second and longer, and with ranges less than 120 km. Because of the presence of a second active radiant, purification by removal of the background meteors was not considered satisfactory in this case, although where only a single strong radiant is present, both methods yield about the same mean velocity values. Of the 268 meteors selected by the range, duration, and velocity criteria, it is estimated that probably more than 95 per cent were δ Aquarids. The spread of the velocities associated with any strong shower, of which the standard deviation is a measure, is due both to observational errors and to deceleration of the meteors. Shower meteors at the higher heights will have appreciably higher velocities than meteors of the same shower detected at lower heights. If the parameter had been

readily available, say from three-station triangulation measurements, it would have been interesting to attempt a further selection by means of the height.

One may use the radio radiant position and the radio velocity to compute a mean orbit for the δ Aquarids, after applying corrections for deceleration, zenith attraction, etc. Most of these corrections are mechanical in nature and follow accepted rules. The exception is the deceleration correction, which depends to a large extent on the interpretation to be applied to current physical theories of meteors. Two methods of working out the decelerations may yield corrected velocities that differ by a significant fraction of 1 km/sec, and, unless the steps are given in detail, it is difficult to assess the result. We shall not attempt to compute an orbit here, because it is felt that our radiant determination, while fully comparable to measurements made by other radio methods, is not so accurate as a position based on good photographic observations. Unfortunately, to date there does not appear to be a reliable and unambiguous radiant position for the δ Aquarids. The strong point of the radio techniques in computing meteor orbits is the determination of the velocity, not of the radiant. In the case of daylight meteors there is at present no alternative to obtaining the radiant position by radio methods, of course. The narrow-beam antenna technique employed by the Manchester group effectively provides a still different selection of shower meteors. However, narrow-beam antenna systems are usually operated on shorter wave lengths, to keep the physical dimensions within reason, and the echo rates fall off rapidly with decreasing wave length. The advantages of the narrow-beam method thus tend to be offset to some extent by the greatly reduced number of observations that can be obtained.

Miss Almond[6] derived a velocity of 40.5 ± 2.7 km/sec from 32 meteor echoes observed on July 28–29, 1952, with a narrow-beam antenna. She did not give a radio determination of the δ Aquarid radiant in her paper (although radio determinations of the radiant were made there in previous years) but used a mean visual radiant of R.A. 340°, dec. −15°, together with the above velocity, to compute a set of orbital elements. On the other hand, Lindblad[2] employed his own radar observations to determine a radiant position, R.A. 339°, dec. −12°, but appears to have used a radiant position R.A. 340°.5, dec. −17°, combined with a velocity, 40.4 km/sec, deduced from our radio observations, to compute an orbit. Incidentally, Lindblad's velocity is remarkably close to our final value of 40.2 km/sec, and it might have been even closer if he had been able to eliminate the effect of the second radiant.

Lindblad's radar observations extended from July 25 to August 3, 1950, and he considered that there was a peak in the hourly rates of short-duration echoes on July 26, whereas the main peak of the long-duration echoes occurred about July 29. He interprets this as evidence that the fainter meteors encountered earlier were on the fringe of the main δ Aquarid stream and that the Poynting-Robertson effect has dispersed the meteors selectively over a period of a few thousand years. We did not find similar evidence in our July 26–29, 1949, observations to lend appreciable support to Lindblad's hypothesis, although the bimodal effect in some of the distributions, e.g., Figure 5, might be regarded as favorable evidence. We have data from the period July 18–20, 1949, which shows the presence of the δ Aquarids at that early date; and, though the computed radiant position is not reliable, the mean observed velocity, 40.3 km/sec, is close enough to the July 26–29 value of 40.20 km/sec to suggest that little, if any, change occurred in the mean apparent velocity of the stream between the two periods.

The slightly skew symmetry of the various velocity distribution-curves shown in this paper may be remarked, i.e., the more gradual tapering-off for lower velocities compared to higher velocities. This is not an uncommon feature of the velocity distributions of strong showers (for example, see Fig. 7 of n. 1). The low-velocity "tail" to the distribution might be interpreted as due to a lower-velocity component of the shower, but we think it may be explained largely by deceleration in the atmosphere. That is, meteors

[6] *Jodrell Bank Ann.* (Manchester), Ser. 1, No. 1, p. 22, 1952.

detected at the top of the meteoric region will have suffered relatively little deceleration, and, apart from experimental error, no shower meteor velocities should be observed higher than this upper limit. On the other hand, and especially for radiants low in the sky, there will be an appreciable number of shower meteors that will have traveled a considerable distance through the meteoric region before reaching the $t_0$ point at which their velocities were actually observed, and these velocities may be 3 or 4 km/sec lower than the mean, with the lower limit being indefinite.

Öpik[7] lists a visual radiant at R.A. 340°, dec. +15°, among several strong radiants for this period, which might be compared with our second radiant, or possibly with our third radiant. Both Öpik and Ceplecha[8] show several possible positions for the δ Aquarid radiant, or radiants, as well as for other minor radiants in the general vicinity which were observed at the same time. The Manchester group have shown that this activity continues into the daylight hours. It thus appears to be a difficult problem to isolate the main δ Aquarid stream, if, indeed, it exists in the sense of having a unique velocity and radiant position, and the precision of the photographic methods of radiant determination may be needed to resolve the situation. Our radio determinations of velocity and radiant position for the δ Aquarid meteors are mean values, and while their accuracies compare quite favorably with previous determinations, there is no definite assurance that we have not averaged the effects of a number of closely grouped radiants, each with slightly different characteristic velocities. With the data available at the present time we feel that it would be inadvisable to speculate on the history of the δ Aquarid meteor stream.

[7] *Harvard Obs. Circ.*, No. 388, 1934.

[8] *Bull. Cent. Ap. Inst. Czechoslovakia*, **111**, 95, 1952.

# MODEL SOLAR CHROMOSPHERES

J. H. Piddington
Division of Radiophysics, Commonwealth Scientific and Industrial Research Organization, Australia
*Received November 12, 1953*

## ABSTRACT

Nine different model solar chromospheres have been proposed during the last six years. The data on which these are based are indicated and the models discussed. Reasons are given for rejecting most of the models as either theoretically unsound or inconsistent with too many observational data. The most promising model seems to be one based entirely on a combination of optical and radio measurements. A corresponding model for sunspot minimum conditions is obtained from extrapolated radio data.

## I. INTRODUCTION

In the last seven years, at least nine attempts have been made to determine the distributions of temperature and density throughout the gases of the solar chromosphere.[1–9] Some are based on a selection from the available experimental data, others on certain theoretical assumptions or a combination of the two. These data and assumptions are mutually inconsistent. This is reflected in the models, which differ widely, as shown by the various temperature, $T$, distribution-curves of Figure 1.

The objectives of the present paper are: (*a*) to list and briefly discuss the experimental data used in deriving, or otherwise relevant to, the models; (*b*) to criticize the models and suggest a possible small modification to one; and (*c*) to derive a model appropriate to sunspot minimum conditions.

## II. EXPERIMENTAL RESULTS

The observational data, optical and radio, used in the models are briefly listed below.

### *a*) INTENSITIES OF SPECTRAL LINES AND CONTINUA

Chromospheric spectra have been recorded during a number of eclipses. The results have been reduced by Wildt[1] and others to provide values of the function $N^2T^{-3/2}$, $N$ and $T$ being the electron density and temperature. The results may be summarized[5] by the equation

$$N^2T^{-3/2} = 8.7 \times 10^{16} \exp\left[-1.2 \times 10^{-8} z\right], \qquad (1)$$

where $z$ is the level above the base of the chromosphere and c.g.s. units are used. Observations extend from a few hundred kilometers to above 8000 km, with a single measurement at 12,000 km.

[1] R. Wildt, *Ap. J.*, **105**, 36, 1947.
[2] R. G. Giovanelli, *Australian J. Sci. Res.*, *A*, **1**, 360, 1948.
[3] R. N. Thomas, *Ap. J.*, **109**, 480, 1949.
[4] E. Schatzman, *Ann. d'ap.*, **12**, 203, 1949.
[5] J. H. Piddington, *Proc. Roy. Soc. London*, *A*, **203**, 417, 1950.
[6] R. v. d. R. Woolley and C. W. Allen, *M.N.*, **110**, 358, 1950.
[7] J. F. Denisse, *Ann. d'ap.*, **13**, 181, 1950.
[8] A. Koeckelenbergh, *Bull. Acad. Roy. Belgique*, **37**, 252, 1951.
[9] J. P. Hagen, *Ap. J.*, **113**, 547, 1951.

*b*) CHROMOSPHERIC TEMPERATURES

Several observers[5] have measured the relative *intensities* of different spectral lines and of parts of the Balmer continuum and so estimated the electron temperature at levels of 1000–2000 km. The value found was about 5000° K. Observations of spectral line *widths* were interpreted by Redman[10] as indicating a kinetic temperature of atoms of about 30,000° K at the 1500-km level.

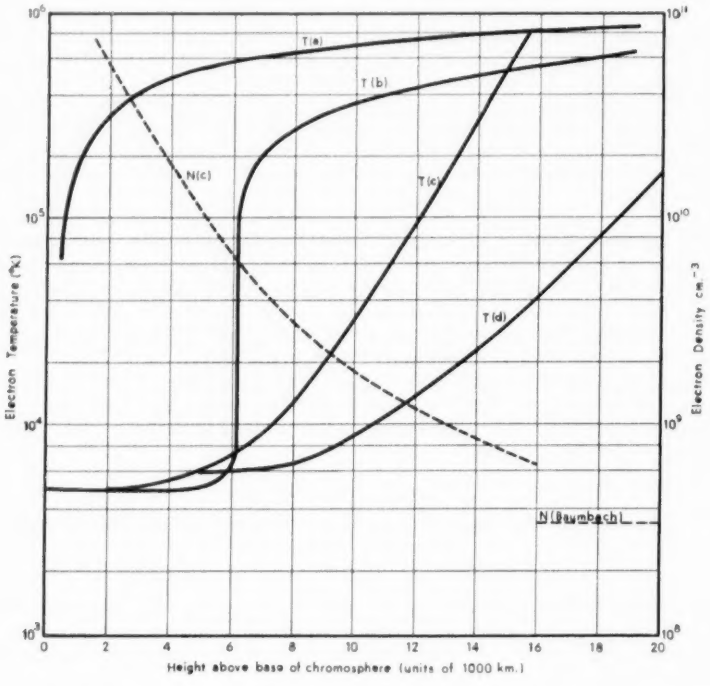


FIG. 1.—Chromospheric distributions of electron temperature, $T$, and density, $N$. *a*, Koeckelenbergh (n. 8); *b*, Woolley and Allen (n. 6); *c*, Piddington (n. 5); and *d*, Hagen (n. 9).

*c*) RADIO EMISSION

At frequencies above about 500 Mc/sec, solar radio radiation is mainly from the chromosphere. It apparently consists of a stable basic component (called $B$ here) on which is superimposed a slowly varying sunspot component. The two have been separated[11] by plotting daily values of the total radiation against sunspot area. A straight line drawn through the resulting scatter of points and extrapolated to zero-spot area then indicates the value of $B$. It is this component which has been used as a basis for some of the models.

Values of $B$, expressed as apparent solar-disk temperatures, are given in the third

[10] *M.N.*, **102**, 140, 1942.

[11] J. L. Pawsey and D. E. Yabsley, *Australian J. Sci. Res.*, *A*, **2**, 198, 1949.

column of Table 1.[12] To use these data in obtaining a model, they must first be reduced to values of brightness at the center of the disk, that is, allowance must be made for limb brightening and for radiation from outside the visible disk. This allowance, expressed as a percentage reduction of $B$, is given in the second column.[13] The central-brightness temperature is deduced from the second and third columns and given in the fourth column. The spectrum intensities of the third column are plotted in Figure 2, and a smooth curve, *a*, is drawn through them. The curve *b* corresponds to the spectrum of the fourth column (the central-brightness temperature).

Although the foregoing data differ somewhat from those used in the two models concerned,[5, 9] the changes they would cause in the models themselves are small and unimportant. It should also be noted that the radio data were not generally available when some of the earlier models were evolved. Their use even as a check of the models was thus lost to these workers.

TABLE 1

TEMPERATURE OF RADIO EMISSION FROM SUN AT DIFFERENT FREQUENCIES

| Frequency (Mc/sec) | Estimated Excess Radiation near and beyond Limb (Per Cent) | Average Spot-free Sun (*ca.* 1948) | | Sun after Prolonged Absence of Spots | |
|---|---|---|---|---|---|
| | | Apparent Disk Temperature ($10^6$° K) | Central-Brightness Temperature ($10^6$° K) | Apparent Disk Temperature ($10^6$° K) | Central-Brightness Temperature ($10^6$° K) |
| 600 | 40 | 50 | 30 | 19 | 11 |
| 1200 | 36 | 28 | 18 | 6.9 | 4.4 |
| 2800 | 32 | 6.0 | 4.1 | 3.3 | 2.2 |
| 9400 | 26 | 1.7 | 1.3 | 1.6 | 1.2 |
| 24,000 | 16 | 1.0 | 0.84 | 1.0 | 0.84 |
| 35,000 | ..... | 0.67 | < 0.67 | ..... | ~ 0.6 |

The result mentioned above of an atomic temperature of 30,000° K below 2000 km cannot reasonably be reconciled either with other temperature measurements or with the radio data.[5] The latter are not consistent with a *uniform* chromospheric temperature of 5000° K (or any other value) but do indicate a temperature of about this value at low levels.

## III. THEORETICAL RESULTS

Some of the model chromospheres have been based partly or wholly on theoretical rather than experimental results. Thus in two models the assumption is made that the chromosphere is in hydrostatic equilibrium; this provides a relationship between the gas parameters and the gravitational force. Another theoretical treatment is based on the assumption that all chromospheric heat is conducted radially inward from the corona and dissipated by radiation.

Since the models were derived, theoretical work has been carried out in interpreting the foregoing experimental radio data. This is very relevant to the models and so is briefly discussed here. One investigation[14] showed that the sunspot component men-

[12] They are based on measurements made during 1946–1949, and most are given in n. 5. However, the 35,000 Mc/sec result became available more recently (see n. 9). The values for 1200 and 2800 Mc/sec have been revised from $2.0 \times 10^6$° and $5.4 \times 10^4$° K to those given here, so as to conform with more recent aerial-gain measurements and other refinements.

[13] These results were found experimentally (see n. 5), except the 1200 Mc/sec value, which is interpolated here.

[14] J. H. Piddington and H. C. Minnett, *Australian J. Sci. Res.*, *A*, **4**, 131, 1951.

tioned above had a thermal origin in regions of excessively high temperature ($10^{7}$° K or more) and pressure. These regions were usually above sunspots or the sites of dead sunspots, and they constituted irregularities in the upper chromosphere as well as in the corona.

Another investigation[15] showed that the above-mentioned statistical method of separating basic and sunspot components was unsatisfactory. The method is based on the assumption that the sunspot component is roughly proportional to the sunspot area. The investigation showed that the contribution of dying spots decreased much more slowly than did their area. At the lower frequencies concerned, even dead spots were generally effective. During a period of generally high sunspot activity, occasional low values of

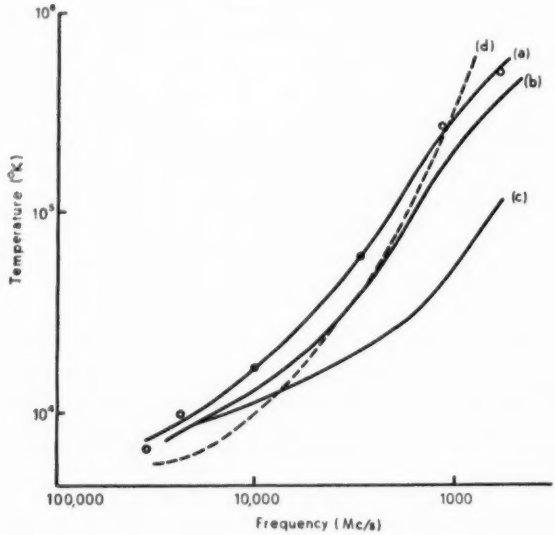


FIG. 2.—Solar spectra. *a*, experimentally determined apparent disk temperature of the spot-free sun, *ca.* 1948; *b*, corresponding derived central-brightness temperatures; *c*, estimated central-brightness temperatures after prolonged absence of spots; *d*, the spectrum (giving the closest fit to *b*) derived by Woolley and Allen.

spot area usually included contributions from the small remnants of large spots. Such small spots provided disproportionately high radio emission. This resulted in the proportion of sunspot component estimated by the daily plot method being much too low.

The position was largely rectified by plotting monthly (or, better still, solar-rotational) mean values of radiation and spot area, thus averaging the two over large parts of their lifetimes. When this was done, the values of $B$ at 1200 and 600 Mc/sec were found to be less than half the earlier estimates and to remain constant over the period 1947–

[15] J. H. Piddington and R. D. Davies, *Nature*, **171**, 692, 1953; also J. H. Piddington, *M.N.*, **113**, 188, 1953.

1951.[16] When an allowance is made for dead (as well as dying) spots, the spectrum of Table 1, fifth column, is found. Corresponding values of central disk temperature given in the sixth column are derived by making the same percentage allowance as before for excess limb radiation. The corresponding spectrum-curve is plotted as curve *c* of Figure 2. These results are the basis of a new model chromosphere presented in Section IX and believed to represent conditions after the prolonged absence of spots.

## IV. UNIFORM-TEMPERATURE MODELS

Wildt[1] has derived a model chromosphere from his values of $N^2T^{-3/2}$ and an assumed uniform temperature of about 5000° K. Giovanelli[2] and Thomas[3] have used similar methods, with an assumed temperature of 30,000° K.

The assumption of a uniform temperature of either 5000° or 30,000° K is quite inconsistent with the radio data.[5] Table 1 shows that, for frequencies between 2800 and 35,000 Mc/sec, the apparent temperature of the center of the solar disk (*ca.* 1948) falls from about $6 \times 10^4$° to $7 \times 10^3$° K. Little of the radiation comes from the corona, which is nearly transparent at these frequencies. The radiation at higher frequencies comes from successively lower levels in the chromosphere, and the steady decrease in apparent temperature indicates a fairly steady temperature gradient at least down to the level where $T < 7000$° K. This is quite contrary to the assumption made in the models. The position cannot be retrieved by postulating an irregular chromosphere with alternating columns of hotter and cooler gas (at, say, 5000° and 30,000° K). The observed temperature variation with frequency would not be explained, and, furthermore, the proportion of hot gas would have to be small (less than 7 per cent) to accord with the 35,000 Mc/sec measurement. It would seem that the evidence against the isothermal models is great.

## V. MODELS ASSUMING HYDROSTATIC EQUILIBRIUM

A chromospheric model has been proposed by Schatzman[4] based entirely on theoretical considerations. He combined the assumption of hydrostatic equilibrium with a theory that the chromosphere is heated by hydrodynamic shock waves moving up from photospheric levels. Koeckelenbergh,[8] on the other hand, combined the assumption of hydrostatic equilibrium with a relationship between $N$ and $T$ found from the radio data[5] (also given as eq. [5] below). Piddington had concluded that this relationship was inconsistent with hydrostatic equilibrium, but Koeckelenbergh has derived a model which apparently satisfies both requirements. His model, which is rather similar to that of Schatzman, is represented by the temperature distribution $T(a)$ of Figure 1.

Both these models are grossly inconsistent with the optical data mentioned in Section II*a* above. For example, these data indicate values of the function $N^2T^{-3/2}$ at 2000 and 6000 km of about $8 \times 10^{15}$ and $6 \times 10^{13}$, respectively. The corresponding values in Koeckelenbergh's model are $2.1 \times 10^9$ and $1.1 \times 10^8$, smaller by factors of $4 \times 10^6$ and $6 \times 10^5$, respectively. Even allowing for possible large errors in the eclipse data, the discrepancies appear excessive. Again, the models are not in agreement with the determinations of gas temperature near 1000–2000 km, where Koeckelenbergh's model gives values in the range $1.5 \times 10^5$° to $2.8 \times 10^5$° K.

As the assumption of hydrostatic equilibrium is itself open to doubt and the results conflict so strongly with experimental data, it is concluded that these ingeniously derived models must be rejected.

## VI. WOOLLEY AND ALLEN'S MODEL

Woolley and Allen[6] assumed a model identical with that of Wildt up to a level of 5000 km. Above this level they assumed a transition region in which the temperature

[16] Additional experimental data for 1950–1951 were then available. It may be noted that the old method of finding the *nonsunspot* component showed a large drop in this component during 1950, when *sunspot* activity was falling.

was governed only by radial thermal conduction and by radiation. Finally, they assumed a uniform spherical shell corona at a temperature of $10^6$° K in which lay the whole source of chromospheric and coronal energy. They derived a series of alternative models, which they checked against certain radio data. The model providing the best agreement is shown as curve $T(b)$ of Figure 1.

Four of the assumptions basic to this model are open to doubt; at least one is almost certainly unjustified. The results mentioned in Section III indicate that most energy is released, not in a uniform shell, but in localized areas. The spread of energy would then be largely tangential rather than radial and would probably be due to mass movements of gas as well as to conductivity. Again the assumed values of thermal conductivity would be completely altered by the presence of stray transverse magnetic fields; field strengths of $10^{-2}$ gauss or less would be effective. The widespread presence of much stronger fields has recently been reported by Babcock and Babcock.[17] Finally, the assumption that no energy is released in the region of temperature transition and that convection plays no part is open to some doubt.

A crucial test of the model lies in its comparison with the best radio data. The data used by Woolley and Allen for their comparison included many early and inaccurate results. The scatter was so great that they were justified in concluding that the model showed fair agreement. However, when their predicted central disk spectrum[18] (curve *d* of Fig. 2) is compared with the experimental spectrum (curve *b*), the discrepancy is found to be well beyond reasonable experimental error. As will be seen later, the difference suggests that the large jump in temperature in the model (curve *b* of Figure 1) is fallacious.

## VII. MODELS BASED WHOLLY ON EXPERIMENTAL DATA

Model chromospheres based on a combination of radio and optical data have been derived by Piddington,[5] Denisse,[7] and Hagen.[9] The radio data comprise values of total emission over a range of frequencies; each value depends on the effects of both emission and absorption over a wide range of chromospheric levels. The data may be summarized in an integral equation involving radio frequency $f$ and the electron temperature $T$ and density $N$ at height $z$ above the base of the chromosphere. The optical data are summarized in equation (1) above, also in $N$, $T$, and $z$. To determine a model chromosphere requires the simultaneous solution of these two equations, and, although this presents difficulties, methods avoiding these difficulties are not valid.

In deriving his model, Piddington[5] first found an empirical expression for the radio brightness temperature near the center of the sun's disk:

$$T_0 = a + b f^{-1} + c f^{-2} , \tag{2}$$

where $a$, $b$, and $c$ are constants found from the experimental data.[19] The relation is confined to frequencies above about 600 Mc/sec. The well-known theoretical expression for $T_0$ is

$$T_0 = \int_0^\infty T e^{-\tau} d\tau , \tag{3}$$

where $\tau$ is the optical depth measured from outside the solar atmosphere. This equation is also valid in the range above 600 Mc/sec, where the refractive index (in the regions

[17] *Pub. A.S.P.*, **64**, 282, 1952.

[18] This curve is one of three published. It is chosen to give the closest agreement with the experimental curve.

[19] In the paper under discussion the coronal contribution to $T_0$ was estimated from the Allen and van de Hulst electron distribution and was subtracted from the total. The remainder was found to be $a + bf^{-1}$, so that the term in $c$ was due to the corona. The more general treatment described here better displays the power of the method because not only is allowance for the corona made incidentally, but it is shown that the actual form of the corona (high temperature, low optical depth) is indicated by the radio spectrum.

concerned) does not depart appreciably from unity. It is convenient to replace $\tau$ by $a = \tau f^2$, which is the optical depth at unit frequency. Equations (2) and (3) then give

$$af^2 + bf + c = \int_0^\infty T e^{-a/f^2} da . \tag{4}$$

Now, since $T$ is a function of $a$, the right-hand side is the Laplace transform of $T$ with $f^{-2}$ as the transform variable. The equation is solved by finding an expression whose Laplace transform is equal to the left-hand side. The expression is $a + b(\pi a)^{-1/2} + c\delta(a)$, where $\delta(a)$ is a discontinuous function, large near the origin and zero elsewhere. In other words, the term $cf^{-2}$ in equation (2) represents a *finite* contribution to the total emission from a region *outside* the chromosphere and having *negligible* optical depth. The region must, therefore, have a much higher temperature than the chromosphere itself. Thus the radio data indicate the presence of a "corona." If a temperature of $10^6$° K and density distribution as found by Allen and van de Hulst are assumed, the calculated value of $c$ is in good agreement with that found from the radio spectrum.

The chromospheric temperature distribution in terms of $a$ is now given by

$$T = a + b(\pi a)^{-1/2}, \qquad \text{where} \qquad a = 0.07 \int_z^\infty N^2 T^{-3/2} dz . \tag{5}$$

This does not itself constitute a model chromosphere, but it may be used to test any model against the radio data. For example, it is clearly inconsistent with the assumption of uniform temperature.

The strength of this method lies in its generality. If the radio spectrum of a slab of gas may be expressed as a function $\psi(f)$ of the frequency[20] and if a second function is found such that its Laplace transform (with $f^{-2}$ as the variable) is $f^2\psi(f)$, then a relationship between $N$ and $T$ is given which, if satisfied, will provide the observed emission spectrum. This relationship may be combined with other data to give a model chromosphere; combined with equation (1), it gives the model[5] illustrated by curves $N(c)$ and $T(c)$ of Figure 1.

Hagen seems to have avoided the above difficulties by making unjustified assumptions regarding the optical data. These, as given by Wildt and others, provide values of $N^2T^{-3/2}$ over a range of levels. Neither $N$ nor $T$ is given individually. In order to estimate values of $N$, Wildt assumed a constant value of $T$ of about 5000° K and so derived a model. His assumption was hypothetical and, as seen above, not correct, although it was justified by the absence of suitable data at the time. Nevertheless, Hagen appears to have used the electron density distribution so found, together with the radio data, to find a temperature distribution. He thus evaluates a temperature distribution, although one had *already been assumed*. The results, shown as curve $T(d)$ of Figure 1, are seen to differ widely from curve $T(c)$, which uses largely similar data. The difference is due mainly to the erroneous values of $N$ on which $T(d)$ is based.

The treatment of Denisse[7] appears to be similarly defective. He also assumes an electron density distribution, but the source of these data is obscure; the reference given does not appear to provide the data listed. In any case, values of $N$ would have been obtained by assuming values of $T$, and the evaluation of a new plot of $T$ from the radio data is not justified. The actual plots of both $N$ and $T$ given by Denisse are very similar to $N(c)$ and $T(c)$ of Figure 1 and are not reproduced here.

### VIII. DISCUSSION OF MODEL *c*

Serious objections have been raised to all models except $c$, which tends to evade criticism by utilizing (and therefore presumably agreeing with) nearly all the experi-

[20] And is not appreciably affected by refraction.

mental data and by avoiding theoretical assumptions. However, some weaknesses may be listed and possible modifications indicated.

*a*) THE RANGE OF DATA USED

The optical data cover levels from zero to about 8000 km, with a single value at 12,000 km. The radio data lie in the brightness-temperature range about 6000° to $3 \times 10^6$° K, which, from the model, correspond to levels between about 5000 and 14,000 km. A certain amount of extrapolation of both sets of data is required. However, the position is strengthened by other optical results which have not been used in the model. These comprise Baumbach's values of coronal electron density (shown over a short height interval in Fig. 1) and temperature measurements of about 5000° below 2000 km and $10^6$° K in the corona (above, say, 20,000 km). All these results are reasonably consistent with the model.

*b*) DEPARTURES FROM SPHERICAL SYMMETRY

The results of Section II show that the radio spectrum on which the model was based contained a considerable proportion of the sunspot component of radiation. This component probably had an irregular source of origin and indicated the presence of irregularities in the chromosphere. Thus the radio and optical data and the model itself represent averaged values over a substantial portion of the solar disk. Fortunately, this limitation does not apply to the lower part of the model. Table 1 shows that the proportion of sunspot component was not large for frequencies of 9400 Mc/sec and over, indicating that irregularities are probably unimportant below about 8000 km.

*c*) A "STEP" IN THE TEMPERATURE-CURVE

There is considerable, although far from conclusive, evidence of a "step" or discontinuity in the chromospheric temperature at about the 8000-km level. A small step would not be inconsistent with the radio data and might have certain advantages as indicated below.

Wildt's[1] optical data (prior to smoothing and modifying to the form of eq. [1]) show a marked drop in intensity at about 8000 km. This is partly due to uncorrected intensities of lines of low quantum number and may also reflect experimental uncertainties. Nevertheless, it does suggest the likelihood of a sudden drop in $N^2T^{-3/2}$ on reaching that level. Theoretical considerations also favor a step at the same level. According to model *c*, the transition from a low to a high proportion of ionized hydrogen occurs near 8000 km. In this range a small change in temperature causes a large change in the partial pressures of $H1$ and $H11$, so that a discontinuity might be anticipated. However, since the hydrogen is almost fully ionized at temperatures below 20,000° K, the step should be a small one. Again, a temperature step in the hydrogen transition region would reduce the amount of ultraviolet emission to a value which might accord better with ionospheric requirements.[21] Finally, a step could explain the emission, apparently from the same chromospheric level, of spectrum lines of helium and singly ionized metal atoms.

A tentative step in model *c* is introduced at the 8000-km level by assuming that the total pressures on either side are equal and that the proportion of ionization changes from a rather low value (say 0.4) to a high value (say 0.9). The calculations were made by the method of Woolley and Allen[22] and the new temperature-curve is shown as $T(S)$ of Figure 3. At high and low levels it merges into the original curve $T(c)$, also reproduced there. The electron density-curve is not appreciably altered.

[21] The calculated emission from model *d* is much higher than the ionospheric requirements suggested by Woolley and Allen (*op. cit.*) and probably higher than more recent, and larger, estimates (see J. H. Piddington, *J. Geophys. Res.*, **56**, 409, 1951; and D. R. Bates, *Proc. Phys. Soc.*, **64**, 805, 1951). When the ultraviolet energy incident on the earth's atmosphere is known reasonably accurately, the size of the step (if any) may be estimated.

[22] *M.N.*, **108**, 292, 1948.

It is of interest to note that if the step does exist, then the region above contains irregularities, as indicated by the sunspot component of radio emission, while that below is more or less uniform. This might possibly be construed as further evidence of a step.

### *d*) OUTWARD INCREASES OF PRESSURE

In parts of model *c* the pressure actually increases outward. While this seems anomalous, there is considerable evidence of chromospheric forces, other than gravity and gas pressure, which may be responsible.

## IX. THE CHROMOSPHERE AT SUNSPOT MINIMUM

The fifth and sixth columns of Table 1 give estimated solar radio spectra after prolonged absence of spots. They apply irrespective of whether the basic component varies during the cycle or only the proportion of sunspot radiation, as suggested above. It is proposed to use the sixth column as a basis of a sunspot minimum model chromosphere.

The data may be represented by equation (2), where now $a = 5800$, $b = 4.1 \times 10^{13}$, and $c = 1.1 \times 10^{22}$. As before, the third term is provided by the corona, but it is only

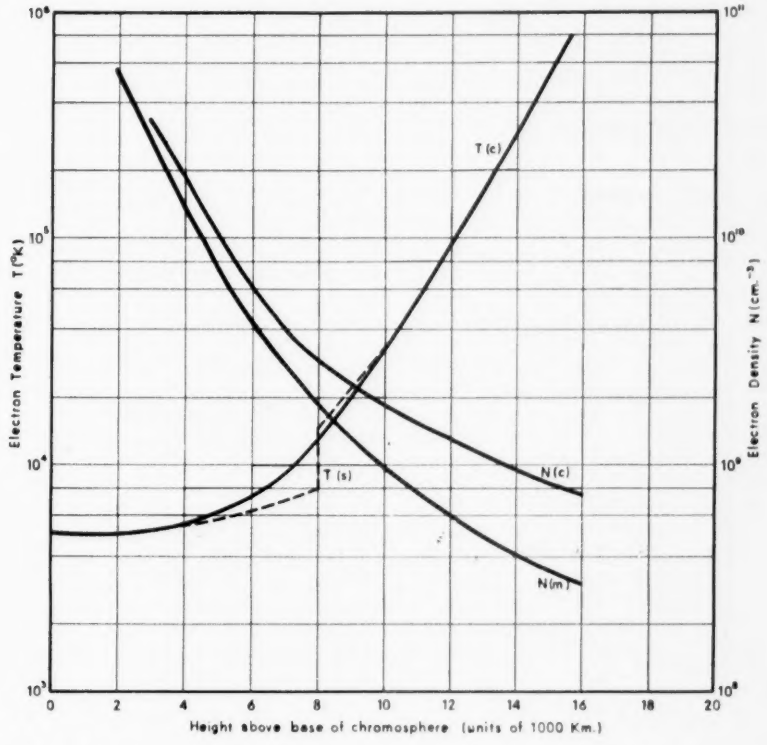


FIG. 3.—Model chromospheres. $N(c)$, $T(c)$, reproduced from Fig. 1; $N(c)$, $T(S)$, the same model with a temperature "step" introduced; $N(m)$, $T(c)$, a model for sunspot minimum.

about 10 per cent of its previous value. The chromospheric $N$-$T$ relationship then becomes

$$T = 5800 + 8.7 \times 10^{13} \left\{ \int_z^\infty N^2 T^{-3/2} dz \right\}^{-1/2}. \quad (6)$$

This equation is a criterion for testing sunspot minimum models. Actually to derive a model, optical data are required corresponding to equation (1) but applying to sunspot minimum conditions. Such data are not available, but reasonable estimates may be inferred from the observed trends in the radio spectra. The analysis of these spectra[15] (largely summarized in Table 1) indicates that the region of origin of the highest frequencies, that is, below about 8000 km, does not change much during the spot cycle. The upper regions of the chromosphere show a steadily increasing change in optical depth up to a factor of about 10 in the corona.[23] This suggests that for spot-minimum conditions the value of $N^2T^{-3/2}$ in equation (1) might reasonably be changed by a factor varying from unity to 10 between levels of zero and, say, 20,000 km. This is done by changing the exponential factor from $-1.2 \times 10^{-8}$ to $-1.32 \times 10^{-8}$.

The new model is shown in Figure 3. The temperature-curve differs so little from $T(c)$ that it is not reproduced. The electron density-curve $N(m)$ may be compared with $N(c)$, also shown in Figure 3. It will be seen that the ratio of values rises from unity at low levels to about 2.5 at the top of the chromosphere.

One earlier attempt has been made to interpret changes in radio spectra during the spot cycle in terms of corresponding changes in electron density. Hatanaka and Moriyama[24] were able to explain the radio data, but, unfortunately, the latter were very limited and unsatisfactory because of the presence of an unknown proportion of the sunspot component.

The author is grateful to Dr. J. A. Roberts for considerable help with the manuscript and to Dr. C. W. Allen and Dr. R. G. Giovanelli for helpful discussion.

[23] The effect is not caused by a large change in electron temperature, because the brightness temperatures at frequencies for which the corona is optically thick (200 Mc/sec and less) have not fallen appreciably in the last few years.

[24] *Astr. Soc. Japan. Pub.*, **4**, 145, 1952.

# SOLAR FLARES AND ASSOCIATED 2800 MC/SEC (10.7 CM) RADIATION*

HELEN W. DODSON, E. RUTH HEDEMAN
McMath-Hulbert Observatory of the University of Michigan
AND
A. E. COVINGTON
National Research Council, Canada
*Received December 16, 1953*

ABSTRACT

Study of 2800 Mc/sec solar radiation at the time of 213 flares and 173 subflares has shown distinctive radio events associated with 57 per cent of the flares and 19 per cent of the subflares. The flare-associated distinctive events at 2800 Mc/sec can be described by essentially the same types and categories already used to report outstanding disturbances at this radio frequency: single bursts; single-simple bursts with and without a postburst increase; single-complex bursts with and without a postburst increase; gradual rises and falls of flux. In addition, there is the designation "null," or no distinctive event. There is strong evidence that there is an outstanding event or disturbance in 2800 Mc/sec solar radiation only when a flare or subflare is in progress.

Time relationships between $H\alpha$ flares and 2800 Mc/sec events suggest that two quite different types of phenomena may be represented in the flare-associated 2800 Mc/sec radiation. One is a sudden burst-type feature which occurs during the rise to maximum of the $H\alpha$ flare. The other is the more gradual rise and fall of flux and "postburst increase," which lasts as long as, or longer than, the flare itself. Both types of phenomena appear to start with the $H\alpha$ flare. Flares associated with large "postburst increases" or "gradual rises and falls" show a high concentration toward the central part of the solar disk. This is not the case for the strictly "burst-type" disturbances.

The importance of the flare, the position of the flare on the solar disk, and accompanying ionospheric disturbances are considered with respect to the form and energy excess of the associated events at 2800 Mc/sec.

## I. INTRODUCTION

The long series of records of solar radiation at 2800 Mc/sec secured at the Radio and Electrical Engineering Division of the National Research Council of Canada, located in Ottawa, constitute valuable data for the study of radio radiation at the time of solar flares. Early in 1953 a co-operative program was undertaken by the authors to carry out such a project. The investigation covered all available 2800 Mc/sec records for the times of all flares and subflares known to the authors for 1951 and the first six months of 1952 and for those flares in 1948–1950 that had been studied previously at 200 Mc/sec.[1] A total of 213 flares and 173 subflares was included in the study.

The $H\alpha$-flare data included photographic records and photometric light-curves secured at the McMath-Hulbert Observatory, supplemented by reports of flares from the *Quarterly Bulletin of Solar Activity* of the International Astronomical Union and the monthly reports from the Central Radio Propagation Laboratory of the National Bureau of Standards. The optics and techniques of the McMath-Hulbert Observatory are fully described in the literature.[2]

The 2800 Mc/sec data were all recorded in Ottawa with a 4-foot radio telescope, for which the characteristics have already been described.[3] Even though the original 2800 Mc/sec records were re-examined for the purpose of this study, it was found possible to describe the flare-associated distinctive events with essentially the same vocabulary and

* This paper is supported in part by contract with the Office of Naval Research.

[1] Dodson, Hedeman, and Owren, *Ap. J.*, **118**, 169, 1953.

[2] R. R. McMath, *Pub. Obs. U. Michigan*, **7**, 1, 1939.

[3] A. E. Covington, *J.R.A.S. Canada*, **45**, 15, 1951.

by the same classifications as those already used in the reports of principal "outstanding disturbances" of 2800 Mc/sec solar radiation published by the National Research Council of Canada.

## II. PRESENTATION OF DATA

### A. TABULAR PRESENTATION

Much of the basic observational data used in this investigation is summarized in Tables 1 and 2. The same conventions have been followed that were used in the tabulation of flare and 200 Mc/sec data in an earlier publication.[1] In the flare data, if the starting or stopping times are underscored, the times refer to the beginning or ending of the flare itself. If the times are not underscored, they refer to the period during which the flare was observed to be in progress. For 40 flares and subflares in this study, photometric light-curves are available and are indicated by an asterisk in the first column of Tables 1 and 2.

### B. TYPES OF FLARE-ASSOCIATED EVENTS ON 2800 MC/SEC RECORDS

Six types of flare-associated events were found on the 2800 Mc/sec records. The "association" here considered is a time association. In only 9 cases did the reported starting times of the flare and radio event differ by more than 10 minutes. In comparison to lower frequencies, the 2800 Mc/sec records show so few "events" or bursts that there was but little ambiguity in identifying 2800 Mc/sec events associated in time with flares. The six types of flare-associated distinctive events are described below and are illustrated in Figure 1.

1. Single burst (*Single*): any one burst without reference to structure, but usually applied to bursts of short duration and with intensity only a few times receiver noise. For the smallest single bursts there is a 50-50 chance that the event is set-noise rather than a distinctive event associated with the flare.

2. Single-simple burst ($Single_s$): A single burst with only one maximum.

3. Single-simple burst with postburst increase ($Single_s$, *Post*): A single-simple burst for which the postburst level is greater than the preburst level. The gradual return to normal flux may require as long as several hours.

4. Single-complex burst ($Single_c$): A single burst which shows two or more comparable maxima before the activity has declined to zero.

5. Single-complex burst, with postburst increase ($Single_c$, *Post*): A single-complex burst for which the postburst level is greater than the preburst level. The gradual return to normal flux may require as long as several hours.

6. Gradual rise and fall in flux (*GR* and *F*): A distinct, but less sudden, increase in flux than the usual burst. It may last from tens of minutes to several hours. These events range from large distinct features on the records to tiny bursts, only a few times receiver noise. For the smallest examples of this type there is a 50-50 chance that the event is set-noise rather than a distinctive event associated with the flare.

In addition to the foregoing types of distinctive events, there are the null cases, cases in which there was no distinct change in the 2800 Mc/sec radiation, even though a flare was in progress. These cases are recorded in Table 2.

The foregoing classification indicates that the most general form of flare-associated distinctive event at 2800 Mc/sec is a *single* burst, which may be either simple or complex and which may or may not be followed by a "postburst increase." In the published lists of outstanding disturbances at 2800 Mc/sec, radio events were classified as *single bursts*, in contradistinction to *groups of bursts*. This latter type does not appear in the list of flare-associated events. There were 11 such "groups" within the scope of this study. For 5 of these cases it was found that the separate single bursts making up the "group" corresponded to separate flares or to the brightening of new regions in the development of a

flare (for examples see the first half of Fig. 2). In 3 other cases one member of a group of two corresponded to an observed flare, and lack of complete optical records made further identification impossible. For the remaining 3 "groups of two bursts," the disturbances were so similar to complex bursts that a change in classification seemed justified. In view of the foregoing situations, it did not seem wise to include "groups of bursts" as a separate type of flare-associated event at 2800 Mc/sec.

Likewise, the rare type of 2800 Mc/sec event called "period of irregular activity" in the published lists of disturbances does not appear as a separate class of flare-associated event. Only 9 such events were recorded for the time interval under investigation in this study. Five of these periods cover times of known flares, and 4 occurred when no observa-

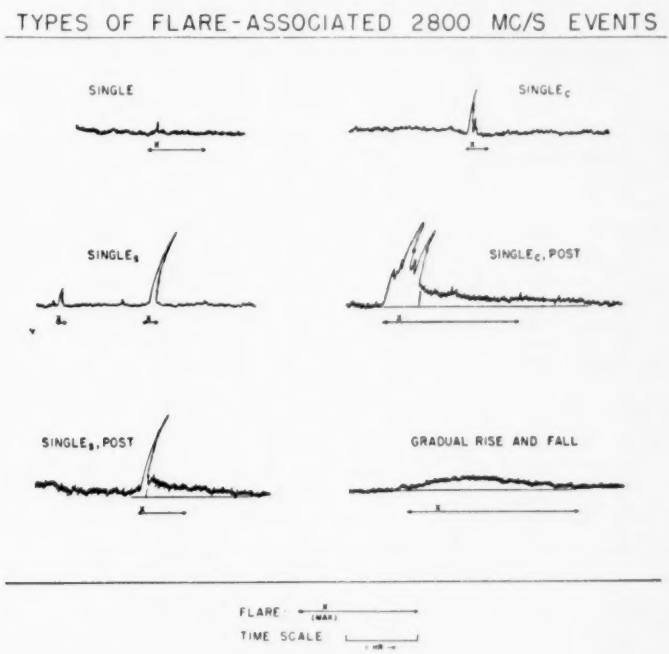


FIG. 1

tions were in progress. For the times when *Hα* data are available, 2–4 flares were observed within each of the reported "periods of irregular activity." The 2 flares associated with the irregular activity of October 4, 1949, are omitted from the present study, because incomplete records made it inadvisable to attempt detailed associations.

Prior to this investigation, the type "gradual rise and fall" had appeared only once (May 21, 1952) in the list of outstanding 2800 Mc/sec events published by the National Research Council of Canada. Examination of the records for the times of flares, however, revealed a number of instances of small but definite changes in flux that fell within this category. Furthermore, a small number of events previously classified as "single-simple bursts" seemed to resemble more closely the event of May 21, 1952, the prototype of the "gradual rise and fall." These events have accordingly been changed to the latter

TABLE 1

SUMMARY OF FLARES WITH DISTINCTIVE EVENTS ON 2800 MC/SEC RECORDS

| NO. | DATE | SOURCES | Hα FLARE OBSERVED FROM TO (UT) | Hα FLARE MAXIMUM (UT) | Hα FLARE IMPORTANCE | Hα FLARE POSITION LAT. | Hα FLARE POSITION CM DIST. | SID FROM TO (UT) |
|---|---|---|---|---|---|---|---|---|
| | 1948 | | h m h m | h m | | ° | ° | h m h m |
| 1 | Nov. 13 | b | 1648 - 1652 | - | 2 | 08S | 63E | 1649 - 1715 |
| 2 | Dec. 10 | b | 1758 - 1808 | - | 2 | 09S | 49E | No |
| 3 | Dec. 24 | b | 1704 - 1719 | - | ? | 15S | 10W | 1634 - 1805 |
| | 1949 | | | | | | | |
| 4 | Feb. 9 | b | 1706 - 1719 | - | 2 | 09S | 56W | 1651 - 1810 |
| 5 | Feb. 17 | b | 1707 - 1717 | - | 1 | 11S | 13W | 1704 - 1730 |
| 6 | Apr. 27 | b | 2147 - 2208 | 2152 | 2 | 12S | 36W | 2143 - 2200 |
| 7 | May 10* | a,b | 2000 - 2220 | 2010 | 3+ | 20S | 12E | 2002 - 2200 |
| 8 | May 31* | a,b | 1553 - 1635 | 1603 | 1 | 02N | 03W | No |
| 9 | May 31* | a,b | 1854 - 1930 | 1857 | 2 | 02N | 03W | 1858 - 1920 |
| 10 | June 1 | a | 1755 | - | 1 | 05N | 10W | No |
| 11 | June 2 | a,b | 1539 - 1625 | 1550 | 1+ | 05N | 25W | No |
| 12 | June 4* | a,b | 1605 - 1730 | 1621,1635 | 2 | 04N | 51W | 1613 - 1920 |
| 13 | June 22* | a,b | 1703 - 1900 | 1714 | 2 | 09N | 55E | 1705 - 1925 |
| 14 | July 15 | b | 1729 - 1815 | 1733 | 1 | 19N | 04W | No |
| 15 | July 17 | b | 1725 - 1736 | 1729 | 1 | 19N | 34W | No |
| 16 | July 31 | a,b | 1411 - 1610 | 1430,1513 | 2 | 21S | 06E | 1420 - 1600 |
| 17 | Aug. 16* | a,b | 1739 - 1820 | 1748 | 2 | 13N | 22E | 1745 - 1820 |
| 18 | Aug. 19* | a,b | 2104 ->2205 | 2111, 2118 | 3 | 13N | 10W | 2110 - 2210 |
| 19 | Sept.12 | b | 1520 - 1548 | - | 2 | 16S | 45W | 1522 - 1600 |
| 20 | Sept.12 | b | 2009 - 2037 | 2011 | 2 | 16S | 50W | 2010 - 2050 |
| 21 | Sept.16* | a,b | 1423 - 1500 | 1430 | 1+ | 15S | 04E | 1429 - 1510 |
| 22 | Sept.17 | a,b | 1716 - 2051 | 1719 | 3 | 15S | 10W | 1717 - 2040 |
| 23 | Sept.24 | b | 1946 - 2024 | 2008 | 2 | 16S | 18W | 1944 - - - |
| 24 | Sept.24 | b | 2005 - 2019 | 2011 | 1 | 08S | 20E | 2000 - 2045 |
| 25 | Oct. 1 | b | 1705 - 1723 | 1710 | 1 | 08N | 76E | 1710 - 1750 |
| 26 | Oct. 11 | b | 1514 - 1654 | 1523 | 2 | 19N | 22E | 1517 - 1740 |
| 27 | Oct. 15 | b | 1456 - 1630 | - | 1 | 20N | 30W | 1512 - 1625 |
| 28 | Oct. 15 | b | 1630 - 1700 | 1638 | 2 | 20N | 31W | 1635 - 1800 |
| 29 | Nov. 1* | a,b | 1954 - 2050 | 1957 | 2 | 25N | 37E | No |
| 30 | Nov. 5 | b | 1827 - 1907 | 1829 | 1 | 26N | 01E | 1830 - 1905 |
| 31 | Nov. 11 | b | 1512 - 1532 | 1527 | 3 | 10N | 35E | 1520 - 1600 |
| | 1950 | | | | | | | |
| 32 | Feb. 18 | a,b | 1506 - 1536 | 1511 | 1 | 12N | 10E | 1513 - 1540 |
| 33 | Feb. 20 | b | <1618 - 1630 | - | ? | 11N | 16W | 1522 - 1620 |
| 34 | Apr. 11 | b | 2005 - 2100 | 2014 | 2 | 14N | 24E | 1959 - 2130 |
| 35 | Apr. 12 | b | 1840 - 2212 | 1911 | 2 | 14N | 10E | 1839 - 2120 |
| 36 | Apr. 13 | c | 1724 - 1804 | - | (1-) | 13N | 05E | 1722 - 1800 |
| 37 | Apr. 13 | b | 2200 - 2212 | 2204 | 1 | 14N | 06W | 2155 - 2210 |
| 38 | Apr. 14 | c | 1649 - 1720 | 1652 | (1) | 12N | 11W | 1649 - 1720 |
| 39 | Apr. 18 | b | 1905 - 1917 | 1909 | 1 | 14N | 09E | 1903 - 1920 |
| 40 | Apr. 26 | b | 1632 - 1640 | 1635 | 1 | 11S | 14E | No |
| 41 | Apr. 26 | b | 1747 - 1758 | 1752 | 1 | 13S | 12E | 1751 - 1805 |
| 42 | May 5 | c | 1720 - 1815 | 1746 | (1) | 18N | 27W | 1722 - 1845 |
| 43 | May 5 | b | 1935 - 2016 | 1951 | 1 | 14N | 35W | 1937 - 2045 |
| 44 | May 16 | c | 1950 - 2020 | 2002 | (1-) | 03S | 65W | No |
| 45 | May 22 | b | 2041 - 2102 | 2044 | 1 | 09N | 49E | 2040 - 2110 |
| 46 | June 1* | a,b | <1811 - 1859 | 1816? | 2 | 05N | 03E | 1803 - 1830 |
| 47 | June 9 | b | 2003 - 2046 | 2016 | 1 | 18S | 62E | 2003 - 2030 |
| 48 | June 9 | c | 2150 - 2250 | 2155 | 2 | 13S | 63E | 2201 - 2225 |
| 49 | June 13 | b | 1904 - 1945 | 1906 | 1 | 19S | 10E | 1913 - 1930 |
| 50 | June 20 | a,c | 2024 - 2145 | 2028 | 1 | 10N | 20E | No |
| 51 | July 19 | a,b | 1500 - 1547 | 1504 | 1 | 20N | 48W | No |
| 52 | July 21* | a,b | 1311 - 1344 | 1318 | 2+ | 10N | 10E | 1315 - 1340 |
| 53 | Aug. 1 | b | 1635 - 1710 | 1646 | 1+ | 10S | 40E | No |
| 54 | Aug. 1 | c | 2054 - 2115 | 2100 | 1 | 10S | 40E | No |
| 55 | Aug. 15 | b | 1748 - 1851 | 1804 | 1 | 15N | 04E | 1752 - 1818 |

TABLE 1

SUMMARY OF FLARES WITH DISTINCTIVE EVENTS ON 2800 MC/SEC RECORDS

| NO. | TYPE | PRECURSOR (START) | 2800 MC/S RADIO EVENT BURST FROM | TO | POST BURST INCREASE (END) | MAX. (UT) | ENERGY (BURST) | EXCESS** (POST-BURST) | REMARKS |
|---|---|---|---|---|---|---|---|---|---|
| | | h m | h m | h m | h m | h m | | | |
| 1 | $Single_C$ | - | 1643.6 | - 1703.6 | - | 1645.6 | 226 | - | Group(2);combined |
| 2 | $Single_S$ | - | 1757 | - 1805 | - | 1758 | 80 | - | |
| 3 | $Single_S$;Post | - | 1635.7 | - 1643.7 | ...1944 | 1637.1 | 273 | 1452 | |
| 4 | $Single_S$;Post | - | 1648.6 | - 1653.4 | ...1833 | 1650.8 | 387 | 703 | |
| 5 | $Single_S$;Post | - | 1704.8 | - 1711 | ...1851 | 1705.4 | 467 | 335 | |
| 6 | $Single_C$;Post | - | 2146.2 | - 2201.2 | ...2221 | 2148 | 481 | 103 | |
| 7 | †Burst; Post | - | <2002 | - 2020 | ...2220 | ? | >3425 | 1986 | |
| 8 | Gr.Rise,Fall | - | 1555 | - 1655 | - | 1616 | 155 | - | |
| 9 | $Single_C$ | - | 1854.1 | - 1904 | - | 1856.8 | 112 | - | |
| 10 | Gr.Rise,Fall | - | 1716 | - 1816 | - | 1720 | 116 | - | |
| 11 | Gr.Rise,Fall | - | 1535 | - 1615 | - | 1600 | 64 | - | |
| 12 | $Single_C$;(Neg) | 1606... | 1616 | - 1655 | - | 1616.9 | 3192 | Neg? | Multiple Hα maxima |
| 13 | $Single_C$;Post | - | 1703.5 | - 1730 | ...2000 | 1713 | 936 | 793 | Multiple Hα maxima |
| 14 | $Single_S$;Post | - | 1731.5 | - 1735.5 | ...1821 | 1732.3 | 75 | 119 | |
| 15 | Single | - | 1727 | - 1729 | - | 1728 | 4 | - | |
| 16 | $Single_C$;Post | 1401... | 1421 | - 1646 | ...1806 | 1421,1512 | >50,000 | 598 | Multiple maxima, Hα and 2800 Mc/sec |
| 17 | Single | - | 1740 | - 1750 | - | 1744 | 19 | - | |
| 18 | $Single_C$;Post | - | 2103.0 | - 2115 | ...2220 | 2112 | 387 | 365 | Broad Hα maximum |
| 19 | $Single_S$;Post | - | 1519.5 | - 1525 | ...1535 | 1521.0 | 361 | 99 | |
| 20 | $Single_C$;Post | - | 2008.2 | - 2016 | ...2024 | 2010.3 | 516 | 36 | |
| 21 | Single | - | 1428 | - 1430 | - | 1428 | 5 | - | |
| 22 | $Single_S$;Post | - | 1718 | - 1724 | ...2209 | 1719.3 | 464 | 3471 | |
| 23 | $Single_S$ | - | 1939.6 | - 1954.6 | - | 1946.1 | 72 | - | Group(2) |
| 24 | $Single_S$ | - | 2004 | - 2011 | - | 2007.3 | 54 | - | |
| 25 | $Single_C$ | - | 1707.6 | - 1715.6 | - | 1708.9 | 72 | - | |
| 26 | †Burst; Post | - | <1528 | - 1600 | ...1705 | ? | >3896 | 730 | |
| 27 | $Single_S$;Post | - | 1449.3 | - 1453.3 | ...1513 | 1451.7 | 19 | 58 | |
| 28 | $Single_C$;Post | - | 1631.3 | - 1646 | ...1711 | 1635.3 | 526 | 206 | |
| 29 | $Single_C$;Post | - | 1954.5 | - 2001.5 | ...2101 | 1956.4 | 39 | 445 | |
| 30 | $Single_S$;Post | - | 1827.5 | - 1830.7 | ...2000 | 1829.1 | 122 | 258 | |
| 31 | $Single_C$;Post | - | 1517.2 | - 1547.4 | ...1652 | 1531.7 | 636 | 270 | Group(2);combined |
| 32 | $Single_C$ | - | 1508 | - 1525 | - | 1509.9 | 173 | - | |
| 33 | $Single_C$;Post | - | 1518.3 | - 1528.3 | ..(1655) | 1520.2 | 785 | ? | |
| 34 | $Single_S$;Post | - | 2003.8 | - 2009.8 | ...2310 | 2006 | 206 | 1335 | |
| 35 | $Single_S$;Post | - | 1847 | - 1915 | ...2247 | 1903.5 | 1075 | 2357 | |
| 36 | $Single_S$;Post | - | 1724 | - 1729 | ...1744 | 1725.8 | 142 | 64 | |
| 37 | $Single_S$;Post | - | 2159 | - 2206.5 | ...2256.5 | 2200.0 | 413 | 264 | |
| 38 | Gr.Rise,Fall | - | 1645 | - 1730 | - | 1650 | 77 | - | |
| 39 | $Single_S$ | - | 1904.5 | - 1906.5 | - | 1905.2 | 9 | - | |
| 40 | $Single_S$ | - | 1631.5 | - 1634.5 | - | 1632.3 | 13 | - | |
| 41 | $Single_S$ | - | 1749.6 | - 1758 | - | 1750.2 | 188 | - | |
| 42 | Single | - | 1733 | - 1738 | - | 1735.8 | 22 | - | |
| 43 | $Single_S$;Post | 1945... | 1949 | - 1953 | ...2018 | 1950.7 | 109 | 77 | |
| 44 | $Single_S$ | - | 2006 | - 2009 | - | 2007.9 | 12 | - | |
| 45 | Single | - | 2040.7 | - 2043.7 | - | 2041.7 | 14 | - | |
| 46 | Single | - | 1807 | - 1808 | - | (1807.5) | 3 | - | Second member Group (2) |
| 47 | Single | - | 2008 | - 2026 | - | 2010 | 28 | - | |
| 48 | $Single_C$ | - | 2158.8 | - 2216.8 | - | 2205.1 | 71 | - | |
| 49 | Single | - | 1901.6 | - 1903.1 | - | 1902 | 8 | - | |
| 50 | $Single_S$ | - | 2020.4 | - 2024.4 | - | 2021.2 | 26 | - | |
| 51 | $Single_S$;Post | - | 1500.7 | - 1503.2 | ...1733 | 1501.5 | 45 | 645 | |
| 52 | †Recov.fr.burst | - | <1320 | - 1420 | - | ? | (>13) | - | |
| 53 | Single | - | 1639.4 | - 1640.4 | - | 1639.7 | 4 | - | |
| 54 | Single | - | 2058 | - 2100 | - | 2059 | 6 | - | |
| 55 | $Single_S$;Post | - | 1751.6 | - 1756.6 | ...1810 | 1753.3 | 58 | 58 | |

TABLE 1 (Continued)

SUMMARY OF FLARES WITH DISTINCTIVE EVENTS ON 2800 MC/SEC RECORDS

| NO. | DATE | SOURCES | Hα FLARE OBSERVED FROM - TO (UT) | Hα FLARE MAXIMUM (UT) | Hα FLARE IMPORTANCE | Hα FLARE POSITION LAT. | Hα FLARE POSITION CM DIST. | SID FROM - TO (UT) |
|---|---|---|---|---|---|---|---|---|
| | 1950 (Cont.) | | h m - h m | h m | | ° | ° | h m - h m |
| 56 | Sept.19* | a,b | 1705 - 1740 | 1712 | 2+ | 13S | 22W | 1710 - 1750 |
| 57 | Dec. 6 | c | 2005 - 2016 | 2010 | (1-) | 14S | 48E | No |
| 58 | Dec. 13 | b | 1434 - 1450 | - | 1 | 15N | 00E | No |
| | 1951 | | | | | | | |
| 59 | Jan. 22 | b | 1625 - 1700 | - | 1 | 12N | 90E | 1620 - 1800 |
| 60 | Feb. 19 | b | 1401 - 1527 | 1410 | 2+ | 10N | 80E | 1400 - 1620 |
| 61 | Feb. 28 | c | 2015 - 2045 | 2020 | (1-) | 10N | 61W | No |
| 62 | Feb. 28 | c | 2150 - 2230 | 2155 | (1-) | 12N | 49W | No |
| 63 | Apr. 2 | c | 1706 - 1900 | 1718 | 2 | 08N | 69W | 1710 - 1820 |
| 64 | Apr. 12 | c | 2010 - 2300 | 2022 | (1) | 14N | 76E | 2014 - 2110 |
| 65 | Apr. 13 | b | 1559 - 1625 | 1605 | 1+ | 07S | 50E | 1558 - 1625 |
| 66 | Apr. 13 | c | 2220 - 2325 | 2241 | (1-) | 06S | 44E | No |
| 67 | Apr. 14 | c | 1600 - 1850 | 1818 | (1-) | 12N | 52E | No |
| 68 | Apr. 17 | c | 2015 - 2050 | 2029 | (1-) | 11N | 09E | 2015 - 2040 |
| 69 | Apr. 17 | c | 2120 - 2240 | 2140 | (1) | 12N | 10E | No |
| 70 | Apr. 18 | c | 2045 - 2340 | 2117 | (2+) | 10N | 05W | 2045 - 2145 |
| 71 | Apr. 19 | b | 1521 - 1653 | 1534 | 2 | 11N | 12W | 1507 - 1740 |
| 72 | Apr. 20* | a,b | 1554 - 1625 | 1606 | 1- | 12N | 20W | No |
| 73 | Apr. 20* | a | 1955 - 2100 | 2001 | 1 | 12N | 20W | No |
| 74 | Apr. 27 | a,b | 1945 - 2000 | 1950 | 1 | 17N | 16W | No |
| 75 | May 8* | a,b | 1506 - 1530 | 1508 | 2 | 10N | 90E | 1506 - 1530 |
| 76 | May 11 | c | 1620 - 1716 | 1633 | (1) | 10N | 61E | No |
| 77 | May 11 | c | 1716 - 1845 | 1735 | (1) | 10N | 61E | No |
| 78 | May 16 | a,b | 1402 - 1525 | 1418 | 1 | 10N | 05E | No |
| 79 | May 16 | a,c | 1500 - 1556 | 1508 | 1- | 10N | 30E | No |
| 80 | May 16 | a,b | 1556 - 1647 | 1609 | 1 | 10N | 05E | No |
| 81 | May 16 | a,b | 1659 - 1810 | 1702 | 2 | 15N | 05W | 1705 - 1740 |
| 82 | May 16 | a,c | 1820 - 1915 | 1840 | (1) | 15S | 75E | No |
| 83 | May 16 | c | 2110 - 2231 | 2129 | (1) | 11N | 23E | No |
| 84 | May 17 | b | 1442 - 1525 | 1451 | 1 | 15N | 16W | 1450 - 1520 |
| 85 | May 17 | b | 1637 - 1643 | - | 1 | 15N | 21W | 1637 - 1700 |
| 86 | May 17 | c | 1710 - 1819 | 1719 | (1-) | 23N | 24W | No |
| 87 | May 17 | b | 1754 - 1912 | 1758 | 2 | 11N | 10W | No |
| 88 | May 18 | a,b | 1020 - 1415 | - | 3 | 15N | 30W | 1040 - 1200 |
| 89 | May 18* | a,b | 1953 - 2110 | 2002 | 2+ | 17N | 35W | 1955 - 2040 |
| 90 | May 19* | a,b | 1345 - 1440 | 1348 | 2 | 12N | 43W | 1343 - 1410 |
| 91 | May 19* | a,b | 1443 - 1515 | 1446 | 1+ | 18N | 44E | 1445 - 1500 |
| 92 | May 19 | a | 1710 - 1711 | - | 1- | 14N | 40W | No |
| 93 | May 19 | a | 1801 - 1825 | 1803 | 1- | 15N | 40W | No |
| 94 | May 19* | a,b | 1950 - 2050 | 1957 | 3- | 12N | 43W | 1950 - 2110 |
| 95 | May 20 | a,c | 1437 - 1515 | 1442 | 1 | 11N | 60W | No |
| 96 | May 20 | b | 1735 - 1810 | 1738 | 1 | 15S | 25E | 1738 - 1805 |
| 97 | May 20 | a,b | 1820 - 1850 | 1825 | 1 | 15S | 25E | No |
| 98 | May 20 | a,b | 1953 - 2100 | 1957 | 1+ | 13N | 60W | No |
| 99 | May 21 | b | <1255 - 1303 | - | 1 | 08N | 75W | 1212 - 1222 |
| 100 | May 22 | b | 1201 - 1208 | - | 1+ | 14S | 06E | 1155 - 1205 |
| 101 | May 22 | b | 1332 - 1522 | - | 1+ | 16N | 06E | 1325 - 1440 |
| 102 | May 22 | c | 1820 - 1910 | 1827 | (1) | 14S | 00W | No |
| 103 | May 22 | c | 1910 - 1956 | 1915 | (1-) | 14S | 00W | No |
| 104 | May 22 | c | 2155 - 2225 | - | (1) | 06N | 90W | No |
| 105 | May 23 | c | <1426 - 1454 | - | (1-) | 17S | 11W | No |
| 106 | May 23 | a | 1808 - 1840 | 1812 | 1- | 17N | 13W | No |
| 107 | May 24 | c | 2030 - 2130 | 2040 | (1) | 21N | 29W | No |
| 108 | May 25 | a | 2005 - 2040 | 2012 | 1- | 16N | 40W | No |
| 109 | June 5 | a,b | 1955 - 2115 | 2004 | 1+ | 10N | 65E | 1947 - 2025 |
| 110 | June 7 | c | 1540 - | - | ? | 10N | 50E | No |

TABLE 1 (Continued)

SUMMARY OF FLARES WITH DISTINCTIVE EVENTS ON 2800 MC/SEC RECORDS

| NO. | TYPE | 2800 MC/S RADIO EVENT: PRECURSOR (START) | BURST FROM (UT) | BURST TO (UT) | POST BURST INCREASE (END) | MAX. (UT) | ENERGY EXCESS** (BURST) | ENERGY EXCESS** (POST-BURST) | REMARKS |
|---|---|---|---|---|---|---|---|---|---|
| | | h m | h m | h m | h m | h m | | | |
| 56 | $Single_s$ | - | 1704 | - 1712 | - | (1708) | >387 | - | |
| 57 | Single | - | 2003 | - 2010 | - | 2006 | 9 | - | |
| 58 | $Single_c$;Post | - | 1507 | - 1514 | ...1534 | 1511.5 | 61 | 36 | Ha record incomplete |
| 59 | $Single_c$;Post | 1623.8.. | 1625.3 | - 1650.3 | ...1720 | 1626.1 | 3415 | 103 | |
| 60† | Recov. from burst; Post | - | <1416 | - 1530 | ...1915 | ? | >9000 | 2320 | |
| 61 | Single | - | 2016 | - 2019 | - | 2018 | 8 | - | |
| 62 | $Single_s$ | - | 2144.5 | - 2152.5 | - | 2145.2 | 36 | - | |
| 63 | $Single_c$;Post | 1704.5.. | 1708.0 | - 1808 | ...1828 | 1716.8 | 3235 | 360 | |
| 64 | $Single_s$;Post | - | 2010.7 | - 2019.7 | ...2300 | 2015.8 | 474 | 1067 | |
| 65 | $Single_s$ | 1557.5.. | 1559.3 | - 1602.3 | - | 1559.7 | 45 | - | |
| 66 | $Single_c$ | 2229.5.. | 2232 | - 2245 | - | 2233 | 76 | - | |
| 67 | Gr.Rise,Fall | - | 1800 | - 1835 | - | 1808 | 77 | - | |
| 68 | Single | - | 2015 | - 2016 | - | 2015.5 | 3 | - | Period of irreg.act. |
| 69 | Single | - | 2126 | - 2130 | - | 2128 | 10 | - | Period of irreg.act. |
| 70 | Gr.Rise,Fall | - | 2043 | - 2313 | - | 2118 | 2095 | - | Formerly $Single_s$ |
| 71 | Gr.Rise,Fall | - | 1510 | - 1740 | - | 1600 | 1264 | - | Formerly $Single_c$ |
| 72 | Gr.Rise,Fall | - | 1552 | - 1652 | - | 1606 | 180 | - | |
| 73 | Gr.Rise,Fall | - | 1957 | - 2057 | - | 2008 | 193 | - | |
| 74 | $Single_s$ | - | 1949.3 | - 1953.3 | - | 1949.5 | 39 | - | |
| 75† | Recov. from burst | - | <1511.5 | - 1526 | - | ? | (>90) | - | |
| 76 | Single | - | 1629.4 | - 1634.4 | - | 1630.3 | 15 | - | |
| 77 | Gr.Rise,Fall | - | 1718 | - 1748 | - | 1729 | 48 | - | |
| 78 | $Single_s$;Post | - | 1406.7 | - 1421.7 | ...1542 | 1412.7 | 302 | 303 | Group(3) |
| 79 | Gr.Rise,Fall | - | 1502 | - 1532 | - | 1513 | 39 | - | |
| 80 | Gr.Rise,Fall | - | 1558 | - 1648 | - | 1606.5 | 116 | - | |
| 81 | Gr.Rise,Fall | - | 1700 | - 1800 | - | 1714 | 116 | - | |
| 82 | Single | - | 1828.5 | - 1832 | - | 1831 | 5 | - | |
| 83 | $Single_s$ | - | 2116 | - 2127 | - | 2121 | 43 | - | |
| 84 | $Single_s$;Post | - | 1441 | - 1446 | ...1606 | 1443.5 | 40 | 132 | Period of irregular activity |
| 85 | $Single_s$?;Post | - | 1633 | - 1635 | ...1643 | 1634.9 | 12 | 12 | |
| 86 | $Single_c$;Post | - | 1709.5 | - 1715.5 | ...1749 | 1713.5 | 84 | 108 | |
| 87 | Gr.Rise,Fall | - | 1755 | - 1915 | - | 1802 | 400 | - | |
| 88† | Burst | - | <1200 | - 1430 | - | ? | >3300 | - | |
| 89† | Burst; Post | - | <1959 | - 2002 | ...2122 | ? | >155 | 534 | |
| 90 | $Single_s$;Post | - | 1347 | - 1352 | ...1417 | 1348.7 | 101 | 107 | Group(2) |
| 91 | Gr.Rise,Fall | - | 1434 | - 1529 | - | 1447.7 | 184 | - | |
| 92 | Single | - | 1710 | - 1711 | - | (1710.5) | - | - | Period of irreg.act. |
| 93 | Single(3) | - | 1802.5 | - 1825 | - | 3 max. | 10 | - | |
| 94 | $Single_s$;(Neg) | 1948.7.. | 1952.2 | - 2008.7 | ..(2115) | 1956 | 586 | Neg. | |
| 95 | $Single_s$ | - | 1415.8 | - 1440 | - | 1420.1 | 213 | - | First member,Group(2) |
| 96 | Gr.Rise,Fall | - | 1747 | - 1802 | - | 1754 | 19 | - | End indeterminate due to onset of second flare |
| 97 | Gr.Rise,Fall | - | 1820 | - ... | - | - | - | - | |
| 98 | $Single_s$;Post | 1955... | 1956.0 | - 2006 | ...2106 | 1956.5 | 164 | 335 | |
| 99† | Burst | - | 1210 | ->1217 | - | 1212.5 | >54 | - | |
| 100† | Burst | - | 1155 | ->1210 | - | ? | >486 | - | |
| 101† | Burst; Post | - | <1330 | - 1350 | ...1500 | 1343.3 | >98 | 276 | |
| 102 | Single | - | 1823.5 | - 1827.5 | - | 1824.8 | 8 | - | 2nd member,Group(2) |
| 103 | Single | - | 1913.5 | - 1914.5 | - | 1914 | 1 | - | |
| 104 | $Single_c$;Post | - | 2125.9 | - 2130 | ...2356 | 2126 | 90 | 413 | |
| 105 | $Single_s$ | - | 1337 | - 1354 | - | 1340.9 | 116 | - | |
| 106 | $Single_s$;Post | - | 1808 | - 1813 | ...1823 | 1810 | 19 | 13 | |
| 107 | Gr.Rise,Fall | - | 2032 | - 2112 | - | 2040 | 52 | - | |
| 108 | Gr.Rise,Fall | - | 1952 | - 2027 | - | (2014) | 77 | - | |
| 109 | $Single_c$ | - | 1950.8 | - 2025.5 | - | 2010.2 | 278 | - | Group(3);combined |
| 110 | Single | - | 1525 | - 1527 | - | 1526 | 3 | - | |

TABLE 1 (Continued)

SUMMARY OF FLARES WITH DISTINCTIVE EVENTS ON 2800 MC/SEC RECORDS

| NO. | DATE | SOURCES | Hα FLARE OBSERVED FROM (UT) | Hα FLARE OBSERVED TO (UT) | Hα FLARE MAXIMUM (UT) | Hα FLARE IMPORTANCE | Hα FLARE POSITION LAT. | Hα FLARE POSITION CM DIST. | SID FROM (UT) | SID TO (UT) |
|---|---|---|---|---|---|---|---|---|---|---|
| | 1951 (Cont.) | | h m | h m | h m | | ° | ° | h m | h m |
| 111 | June 7 | a | 1625 | 1645 | 1629 | 1- | 10N | 50E | No | |
| 112 | June 7 | a,c | 1705 | 1725 | 1710 | 1- | 10N | 50E | No | |
| 113 | June 7 | a,b | 1826 | 1855 | 1828 | 1 | 08N | 49E | 1820 | 1850 |
| 114 | June 8 | b | 1503 | 1605 | 1512 | 2 | 10N | 45E | 1505 | 1540 |
| 115 | June 8 | b,c | 1539 | 1605 | 1542 | 1 | 05N | 32E | No | |
| 116 | June 9 | c | 1520 | 1540 | 1525 | (1-) | 11N | 24E | No | |
| 117 | June 9 | c | 2327 | 2350 | 2332 | (1) | 07N | 12E | No | |
| 118 | June 11 | c | (?)2022 | 2150 | 2026 | (1-) | 15N | 00W | 2010 | 2140 |
| 119 | June 12 | b | 1735 | 1742 | - | 1 | 09N | 13W | No | |
| 120 | June 15 | b | 1707 | .... | - | - | 16N | 44E | No | |
| 121 | June 15 | a,b | .... | 1939 | - | 1+ | 16N | 44E | No | |
| 122 | June 18* | a,b | 1634 | 1730 | 1640 | 1+ | 13S | 01W | 1635 | 1655 |
| 123 | June 19 | c | 2340 | .... | 2348 | (1) | 11S | 23W | 2342 | 2410 |
| 124 | June 20 | b | 1721 | 1736 | - | 1 | 09S | 31W | 1710 | 1740 |
| 125 | June 20 | a,b | 1855 | 1930 | 1904 | 1 | 15N | 27E | No | |
| 126 | June 22 | b,c | 1650 | 1730 | 1700 | 1 | 08S | 68W | 1700 | 1750 |
| 127 | June 28 | c | 2024 | 2355 | 2055 | (1+) | 15N | 17W | No | |
| 128 | July 10 | a | 1622 | 1638 | 1624 | 1- | 13S | 58E | No | |
| 129 | July 16 | c | 2120 | .... | 2127 | (1-) | 10S | 24W | No | |
| 130 | July 19 | b,c | 1430 | 1445 | 1434 | 1 | 11S | 61W | No | |
| 131 | Aug. 13 | a,b | 1936 | 2324 | 2112 | 1+ | 10N | 40W | No | |
| 132 | Aug. 16 | a,b | 2150 | | - | 1+ | 10N | 90W | No | |
| 133 | Sept. 1 | c | 1410 | 1500 | 1417 | 1+ | 10N | 70E | No | |
| 134 | Sept. 5* | a,b | 1714 | 1745 | 1720 | 1+ | 09N | 09E | 1715 | 1750 |
| 135 | Sept. 5 | c | 2255 | 2310 | 2300 | 1- | 05N | 02W | No | |
| 136 | Sept.14 | a,b | 1330 | 1510 | 1356 | 2 | 15S | 25E | 1352 | 1425 |
| 137 | Sept.15* | a,b | 1508 | 1550 | 1510 | 2 | 05N | 10W | 1510 | 1600 |
| 138 | Sept.15 | a,b | 1725 | 1810 | 1738 | 1 | 06N | 10W | No | |
| 139 | Sept.16 | c | 2035 | 2103 | 2045 | 1- | 09N | 32W | No | |
| 140 | Sept.17 | a,c | 1545 | 1605 | 1550 | 1- | 07N | 37W | No | |
| 141 | Sept.17 | a,b,c | 2050 | 2150 | 2103 | 2 | 08N | 35W | 2058 | 2125 |
| 142 | Sept.18* | a,b | 1812 | 1850 | 1815,1828 | 1 | 07N | 51W | No | |
| 143 | Sept.19 | c | 2155 | 2250 | 2205 | 1- | 08N | 58E | No | |
| 144 | Sept.23 | a,b | 2040 | 2222 | 2113 | 1+ | 12N | 45W | No | |
| 145 | Sept.25 | c | 1735 | 1759 | 1746 | 1- | 06N | 22W | No | |
| 146 | Oct. 13 | a,b | 1658 | 1730 | 1705 | 1 | 12S | 14E | No | |
| 147 | Oct. 29 | c | 1723 | 1748 | 1724 | 1 | 10S | 39E | No | |
| 148 | Dec. 26 | c | 1520 | 1559 | 1539 | 1- | 07N | 60W | No | |
| | 1952 | | | | | | | | | |
| 149 | Feb. 16 | c | 1555 | 1630 | 1605 | 1- | 20N | 41E | No | |
| 150 | Feb. 16 | c | 1835 | 1905 | 1850 | 1 | 10S | 22E | 1840 | 1950 |
| 151 | Apr. 8 | a | 1536 | 1600 | 1541 | 1- | 07N | 00E | No | |
| 152 | May 21* | a,b | 1256 | 1430 | - | 2+ | 08S | 07W | No | |
| 153 | June 23 | a | 1350 | 1414 | - | 1- | 17N | 42E | No | |
| 154 | June 24 | a | 1718 | | - | 1- | 10S | 68E | No | |
| 155 | June 24 | a,b | 1855 | 2114 | - | 1 | 16N | 29E | No | |

NOTES FOR TABLES 1 AND 2

Sources of flare data: (a) McMath-Hulbert Observatory; (b) Quarterly Bulletin of IAU; (c) Central Radio Propagation Laboratory, National Bureau of Standards, F Series; (d) Sonnen Zirculer, Freunhofer Institut.

All times are UT.

*Photometric light-curve for Hα flare is available.

( ) with flare importance, indicates value was assigned by authors on basis of reported intensity and area; with other quantities, indicates some uncertainty.

TABLE 1 (Continued)

SUMMARY OF FLARES WITH DISTINCTIVE EVENTS ON 2800 MC/SEC RECORDS

| NO. | TYPE | 2800 MC/S RADIO EVENT PRECURSOR (START) | BURST FROM (UT) | BURST TO (UT) | POST BURST INCREASE (END) | MAX. (UT) | ENERGY EXCESS** (BURST) | ENERGY EXCESS** (POST-BURST) | REMARKS |
|---|---|---|---|---|---|---|---|---|---|
| | | h m | h m | h m | h m | h m | | | |
| 111 | Single | - | 1617 | - 1618.5 | - | 1618 | 2 | - | |
| 112 | Single | - | 1702.8 | - 1703.3 | - | 1703 | - | - | Spike on radio record |
| 113 | $Single_s$;(Neg?) | - | 1825.5 | - 1828.5 | ..(1945) | 1827 | 49 | Neg? | |
| 114 | $Single_s$;Post | - | 1502.7 | - 1539 | ...1600 | 1504.7 | 658 | 166 | Group(2) |
| 115 | Single | - | 1539.0 | - 1545.7 | - | 1539.8 | 19 | - | |
| 116 | $Single_s$;Post | - | 1520.7 | - 1523.2 | ...1531 | 1521 | 26 | 10 | |
| 117 | $Single_s$;Post | - | 2327.8 | - 2330.3 | ...2340 | 2328.7 | 55 | 17 | |
| 118 | Gr.Rise,Fall | - | 2000 | - 2345 | - | 2024 | 2875 | - | Formerly Single |
| 119 | $Single_s$ | - | 1734.9 | - 1739.9 | - | 1735.7 | 19 | - | |
| 120 | $Single_c$ | - | 1707 | - 1716 | - | 1711 | 90 | - | |
| 121 | $Single_c$;Post | - | 1731 | - 1755 | ...1817 | 1735 | 438 | 64 | Group(2) |
| 122 | Single | - | 1634.1 | - 1634.6 | - | 1634.5 | 2 | - | |
| 123 | Single | - | 2345.3 | - 2347.3 | - | 2345.8 | 10 | - | |
| 124 | $Single_c$ | - | 1710 | - 1810 | - | 1717.3 | 165 | - | |
| 125 | Single | - | 1903 | - 1904 | - | 1903.5 | 1 | - | |
| 126 | Gr.Rise,Fall | - | 1653 | - 1808 | - | 1709 | 116 | - | Formerly Single |
| 127 | Gr.Rise,Fall | - | 2016 | - 2251 | - | 2115 | 645 | - | Formerly Single |
| 128 | $Single_c$ | - | 1622.3 | - 1632.3 | - | 1630 | 39 | - | |
| 129 | Gr.Rise,Fall | - | 2120 | - 2140 | - | 2127 | 19 | - | |
| 130 | Single | - | 1430 | - 1433 | - | 1431.5 | 4 | - | |
| 131 | Gr.Rise,Fall | - | 1935 | - 2320 | - | 2128 | 3000 | - | |
| 132 | $Single_s$ | - | 2150.5 | - 2153.0 | - | 2151.5 | 12 | - | |
| 133 | Single | - | 1413.3 | - 1415.3 | - | 1414.2 | 4 | - | |
| 134 | $Single_c$;Post | - | 1715 | - 1720 | ...1755 | 1718.3 | 52 | 52 | Broad Hα maximum |
| 135 | $Single_c$ | - | 2256 | - 2301 | - | 2257.6 | 71 | - | |
| 136 | $Single_c$;Post | - | 1336.2 | - 1358 | ...1543 | 1349.6 | 378 | 294 | |
| 137 | $Single_c$;Post | 1507.3.. | 1508.5 | - 1514.5 | ...1548 | 1509.5 | 210 | 239 | Multiple Hα maxima |
| 138 | Gr.Rise,Fall | - | 1722 | - 1917 | - | 1730 | 469 | - | |
| 139 | Single | - | 2041 | - 2045 | - | 2042 | 8 | - | |
| 140 | Gr.Rise,Fall | - | 1538 | - 1558 | - | 1545 | 26 | - | |
| 141 | $Single_c$;Post | - | 2055.8 | - 2059.8 | ...2135 | 2058 | 62 | 171 | |
| 142 | $Single_s$ | - | 1813 | - 1814.5 | - | 1813.5 | 6 | - | Two Hα maxima |
| 143 | Single | - | 2158.3 | - 2158.8 | - | 2158.7 | 1 | - | |
| 144 | Gr.Rise,Fall | - | 2045 | - 2205 | - | 2115 | 290 | - | |
| 145 | Single | - | 1740 | - 1743 | - | 1740.6 | 4 | - | |
| 146 | Single | - | 1700 | - 1704 | - | 1702 | 5 | - | |
| 147 | Single | - | 1729 | - 1734 | - | 1729.8 | 6 | - | |
| 148 | Single | - | 1524 | - 1528 | - | 1525.5 | 8 | - | |
| 149 | Gr.Rise,Fall | - | 1550 | - 1650 | - | (1625) | 77 | - | |
| 150 | $Single_s$;Post | 1843.5.. | 1844.5 | - 1856.5 | ...1931 | 1846.2 | 532 | 77 | |
| 151 | Gr.Rise,Fall | - | 1540 | - 1710 | - | 1600 | 181 | - | Light curve of decline only |
| 152 | Gr.Rise,Fall | - | 1240 | - 1555 | - | 1315 | 890 | - | |
| 153 | Single | - | 1351 | - 1403 | - | 1354 | 26 | - | |
| 154 | Single | - | 1716 | - 1721 | - | 1719 | 3 | - | |
| 155 | Gr.Rise,Fall | - | 1840 | - 2040 | - | 1945 | 196 | - | |

NOTES FOR TABLES 1 AND 2

† Radio record is incomplete and detailed classification is not possible.

** Units for energy excess are $10^{-20}$ $\frac{\text{joules}}{\text{meter}^2 \text{ cycle/sec}}$.

(Neg.) indicates temporary reduction in 2800 Mc/sec flux.

If classification of 2800 Mc/sec event was changed for this study, the earlier classification is shown under "Remarks."

TABLE 2

SUMMARY OF FLARES CLASSIFIED AS NULL AT 2800 MC/SEC

| DATE | SOURCE | OBSERVED FROM TO (UT) | IMP. | POSITION LAT. | CM DIST. | SID |
|---|---|---|---|---|---|---|
| 1948 | | h m h m | | | | |
| Aug. 30 | b | 1650-1705 | 1 | 25N | 54W | No |
| Oct. 21 | b | 1705-1711 | 1 | 11S | 32W | No |
| Oct. 27 | a | 1700-1750 | 2 | 05S | 50W | No |
| Nov. 10 | b | 1600-1620 | 1 | 11S | 06W | No |
| 1949 | | | | | | |
| June 27 | a,b | 1553-1627 | 1+ | 16N | 45W | No |
| June 28 | b | 1628-1636 | 1 | 06S | 05E | No |
| June 28 | b | 1734-1745 | 1 | 17N | 50W | No |
| Aug. 16* | a,b | 1701-1735 | 1 | 13W | 22E | No |
| Aug. 18* | a,b | 1952-2040 | 1 | 14N | 10E | No |
| Aug. 25* | a,b | 1538-1751 | 2 | 13S | 15E | Yes |
| Aug. 25* | a,b | 2000→2100 | 2 | 15N | 23W | Yes |
| Sept. 24 | b | 1721-1736 | 1 | 08S | 22E | No |
| Oct. 3 | b | 1609-1614 | 1 | 08N | 47E | No |
| Oct. 29* | a,b | 1525-1550 | 3 | 24N | 72E | Yes |
| Nov. 1* | a,b | 1637-1705 | 1+ | 25N | 32E | Yes |
| Nov. 1 | b | 1822-1852 | 1 | 08S | 90E | Yes |
| 1950 | | | | | | |
| Mar. 11 | b | 1522-1530 | 1 | 28N | 48W | No |
| Mar. 28 | c | 1525-1558 | (1) | 18S | 40W | No |
| Apr. 1 | c | <1548-1616 | (1) | 14N | 36E | Yes |
| Apr. 5 | c | 1700-1739 | (2) | 24N | 22W | Yes |
| Apr. 13 | c | 1850-1912 | (1-) | 13N | 05E | No |
| Apr. 13 | b | 2029-2037 | 1 | 14N | 05W | Yes |
| Apr. 14 | c | 1605-1620 | (1-) | 17N | 15W | No |
| Apr. 14 | c | 1756-1811 | (1-) | 10N | 12W | Yes |
| May 3 | b | 1644-1750 | 1 | 15N | 02E | Yes |
| May 31 | c | 1805-2345 | (1) | 04N | 13E | No |
| June 1* | a | 1615-1730 | 1+ | 05N | 03E | Yes |
| June 1 | a,b | 1720-1750 | 1 | 05N | 03E | Yes |
| June 2 | b | 1752-1832 | 1 | 05N | 15W | No |
| June 6 | a,b | 1713-1740 | 1- | 04N | 70W | No |
| June 20 | c | 1859-2103 | (2) | 22N | 15E | No |
| June 26 | b | 1920-2005 | 1 | 12N | 19W | No |
| June 29 | c | 1425-1500 | (1-) | 16S | 17W | No |
| June 29 | b | 1714-1736 | 1+ | 26S | 75W | No |
| June 29 | b | 1736-1838 | 1 | 09N | 63W | No |
| July 12* | a,b | 1517-1605 | 1+ | 08N | 55W | No |
| Aug. 1 | b | 1725-1900 | 1 | 10S | 40E | No |
| Aug. 1 | c | 1935-2015 | 1 | 10S | 40E | No |
| Aug. 22 | c | 1725-1915 | 1 | 12N | 14W | No |
| Aug. 22 | c | 2035-2120 | 1 | 12N | 14W | No |
| Aug. 24* | a | 1832-1855 | 1- | 13S | 33W | No |
| Aug. 24* | a | 1909-1940 | 1- | 13S | 33W | No |
| Aug. 29 | a,b | 1455-1520 | 1 | 13N | 64E | No |
| Aug. 29 | c | 1810-1845 | (1) | 14N | 69E | Yes |
| Aug. 30 | b | 1450-1515 | 1 | 14N | 58E | No |
| Aug. 30 | c | 1734-1750 | (1-) | 16N | 55E | No |
| Sept. 7 | a | 1800-1812 | 1- | 02S | 74E | No |
| Sept. 8 | b | 1952-2023 | 1 | 04S | 54E | No |
| Nov. 9 | b | 1601-1652 | 1 | 15S | 07E | No |
| Nov. 13 | c | 1905-1930 | (1) | 17N | 26E | No |
| Dec. 5 | c | 1925-1950 | (1-) | 19N | 37W | No |
| 1951 | | | | | | |
| Jan. 3 | c | 1855-1905 | (1-) | 06S | 33E | No |
| Jan. 3 | c | 1915-1928 | (1-) | 06S | 33E | No |
| Jan. 10 | c | 2045-2108 | (1) | 10S | 61W | No |
| Jan. 18 | c | 1803 | (1-) | 19N | 03W | No |
| Jan. 30 | c | 2055-2122 | (1-) | 22N | 27W | No |
| Mar. 1 | a | 1611-1618 | 1- | 13N | 70W | No |
| Mar. 5 | c | 1905-1945 | (1-) | 13S | 29W | No |
| Mar. 12 | b | 1600-1612 | 1 | 05S | 18E | No |
| Mar. 13 | c | 1733-2131 | (1) | 13N | 17W | No |

| DATE | SOURCE | OBSERVED FROM TO (UT) | IMP. | POSITION LAT. | CM DIST. | SID |
|---|---|---|---|---|---|---|
| 1951(Cont.) | | h m h m | | | | |
| Mar. 13 | c | 1808-1933 | (1) | 03S | 01E | No |
| Mar. 19 | c | 1550-2000 | (1-) | 10N | 55E | No |
| Mar. 20 | c | 2010-2140 | (1-) | 13N | 25E | No |
| Mar. 22 | c | 2220- | (1-) | 08N | 06E | No |
| Apr. 3 | c | 1725-1915 | (1) | 16S | 06E | No |
| Apr. 11 | b | 1525-1530 | 1 | 11S | 70E | No |
| Apr. 11 | c | 2000-2055 | (1-) | 10S | 78E | No |
| Apr. 13 | c | 1705-1755 | (1) | 05S | 48E | No |
| Apr. 13 | c | 1758-1840 | (1-) | 05S | 46E | No |
| Apr. 13 | c | 1845-1918 | (1-) | 05S | 48E | No |
| Apr. 14 | b,c | 1520-1542 | 1 | 05S | 35E | No |
| Apr. 14 | c | 1655-1720 | (1) | 05S | 39E | No |
| Apr. 14 | c | 1850-1910 | (1-) | 04S | 34E | No |
| Apr. 14 | c | 2000-2015 | (1-) | 12N | 51E | No |
| Apr. 15 | c | 2101-2205 | (1-) | 04S | 20E | No |
| Apr. 16 | c | 2000-2030 | (1-) | 14N | 16E | No |
| Apr. 16 | c | 2045-2250 | (1) | 10N | 35E | No |
| Apr. 16 | c | 2118-2124 | (1-) | 09N | 19E | No |
| Apr. 17 | b | 1540-1600 | 1 | 07S | 12W | No |
| Apr. 17 | b | 1540-1630 | 1 | 13N | 15E | No |
| Apr. 18 | c | 1630-1650 | (1-) | 10N | 04W | Yes |
| Apr. 18 | c | 1940-2040 | (1-) | 11N | 02E | No |
| Apr. 19 | a,b | 1910 | 1 | 12N | 05W | No |
| Apr. 20 | a,c | 2011 | 1- | 13S | 56E | No |
| Apr. 23 | b,c | 1700-1815 | 1 | 14N | 68W | Yes |
| Apr. 23* | a | 1837-1900 | 1- | 11N | 65W | No |
| Apr. 23* | a,c | 1954-2002 | 1- | 11N | 80W | No |
| Apr. 23 | c | 2055-2104 | (1-) | 13S | 08E | No |
| Apr. 23 | c | 2101-2120 | (1-) | 20N | 67W | No |
| Apr. 23 | c | 2140-2200 | (1-) | 13N | 69W | No |
| Apr. 24 | b | 1501-1512 | 1 | 10S | 02W | No |
| Apr. 24 | c | 2225-2231 | (1-) | 17N | 17E | No |
| Apr. 25 | c | 1440-1525 | (1-) | 15N | 11E | No |
| Apr. 25 | b | 1634-1719 | 1 | 15N | 88W | No |
| Apr. 25 | c | 1725-1810 | (1-) | 13S | 14W | No |
| Apr. 25 | c | 2050-2105 | (1-) | 14S | 21W | No |
| Apr. 27 | a,c | 1525-1547 | 1- | 15S | 59E | No |
| Apr. 27* | a,c | 1920-2010 | 1- | 12S | 55E | No |
| Apr. 27 | a | 1922→1935 | 1- | 16S | 38W | No |
| Apr. 27 | c | 2220-2229 | (1-) | 14S | 39W | No |
| May 2 | c | 2225-2255 | (1-) | 19S | 23W | No |
| May 4 | a,c | 1505-1610 | 1 | 16S | 43W | No |
| May 9 | c | 1515-1547 | (1-) | 16N | 81E | No |
| May 9 | c | 1635-1648 | (1-) | 15N | 74E | No |
| May 9 | c | 1945-2015 | (1-) | 15N | 74E | No |
| May 10 | c | 2325-2410 | (1-) | 09N | 71E | No |
| May 11 | c | 1605-1620 | (1-) | 10N | 54E | No |
| May 11 | c | 1625-1920 | (1-) | 01N | 67E | No |
| May 11 | c | 1925-... | (1) | 08N | 72E | No |
| May 15* | a | 2056-2102 | 1- | 12N | 10E | No |
| May 15* | a | 2131-2140 | 1- | 12N | 10E | No |
| May 16 | c | 2200-2231 | (1) | 17N | 08W | No |
| May 17 | b | 1525-1605 | 1 | 13N | 17W | Yes |
| May 18 | a | 1506-1535 | 1- | 10N | 30W | No |
| May 18 | a,b | 1546-1600 | 1- | 15N | 40W | No |
| May 18 | a,c | 1725-1815 | 1 | 17N | 55E | No |
| May 19 | a | 1645-1852 | 1- | 15N | 40W | No |
| May 19 | a | 1857-1905 | 1- | 15N | 40W | No |
| May 20 | c | 1645-1720 | (1) | 16S | 27E | No |
| May 20 | c | 1800-1815 | (1-) | 16S | 10E | No |
| May 20 | a,c | 1932-2045 | 1+ | 15S | 25E | Yes |
| May 20 | a | 1902-1913 | 1- | 11N | 60W | No |

TABLE 2 (Continued)

SUMMARY OF FLARES CLASSIFIED AS NULL AT 2800 MC/SEC

| DATE | SOURCE | OBSERVED FROM (UT) h m | TO h m | IMP. | POSITION LAT. | CM DIST. | SID |
|---|---|---|---|---|---|---|---|
| 1951(Cont.) | | | | | | | |
| May 20 | a,b | 2110 | 2210 | 1 | 15S | 25E | Yes |
| May 22 | b,c | 1510 | 1545 | 1 | 15N | 85W | No |
| May 22 | b | 1725 | 1740 | 1 | 15S | 01E | No |
| May 23 | a | 1525 | 1550 | 1- | 17N | 13W | No |
| May 25 | c | 1645 | 1705 | (1-) | 24S | 35E | No |
| May 25 | a | 1835 | 1837 | 1- | 18S | 42W | No |
| May 28 | c | 1605 | 1630 | (1-) | 24N | 81W | No |
| May 31 | a,c | 1804 | 1844 | (1) | 20S | 43W | No |
| May 31 | c | 1830 | 1945 | (1-) | 11N | 06W | No |
| June 1 | c | 1925 | 1942 | (1-) | 06S | 61E | No |
| June 5 | a,b | 1726 | | 1- | 10N | 65E | No |
| June 5 | a,b | 1800,1930 | | 1 | 09S | 30E | No |
| June 7 | a | 2023 | >2021 | 1- | 08N | 50E | No |
| June 9 | c | 1335 | 1353 | (1-) | 12N | 62E | No |
| June 9 | c | 1424 | 1435 | (1-) | 09S | 39W | No |
| June 11 | c | 1455 | 1504 | (1-) | 09N | 07W | No |
| June 11 | b | 1611 | 1613 | 1 | 08N | 01W | No |
| June 12 | b | 1657 | 1703 | 1 | 13S | 74E | No |
| June 13 | c | <1530 | 1630 | (1-) | 21N | 14W | No |
| June 13 | d | 1711 | 1721 | 1- | 13S | 62E | No |
| June 14 | a,b | 1604 | 1620 | 1- | 15S | 55E | No |
| June 15 | b | 2332 | 2504 | 1 | 12S | 33E | No |
| June 19 | b,c | 1620 | 1655 | 1 | 11S | 18W | Yes |
| June 21 | a | 1406 | 1420 | 1- | 14S | 40W | No |
| June 21 | a | 1435 | 1455 | 1- | 14S | 40W | No |
| June 25 | a,b | 1518 | 1525 | 1 | 14S | 90W | No |
| June 25 | a | 1614 | 1622 | 1- | 14S | 90W | No |
| June 25 | a | 1620 | 1640 | 1- | 14S | 90W | No |
| June 25 | c | 1945 | 1955 | (1-) | 19N | 39W | Yes |
| July 10 | a,c | 1730 | 1755 | 1- | 13S | 58E | No |
| July 11 | c | 1750 | 1755 | (1-) | 13S | 42E | No |
| July 16 | a,c | 1424 | 1437 | 1- | 13S | 20W | No |
| July 18 | c | 1415 | 1445 | (1-) | 08S | 72W | No |
| July 18 | c | 1505 | - | (1-) | 08S | 72W | No |
| Aug. 7 | c | 1600 | 1720 | (1-) | 15S | 88E | No |
| Aug. 21 | a,c | 1445 | 1540 | 1- | 18S | 29W | No |
| Sept. 6 | b | 1537 | 1549 | 1 | 08N | 12W | No |
| Sept.12 | a,c | 1830 | 1910 | 1- | 08N | 31E | No |
| Sept.14 | c | 1625 | 1634 | 1- | 03N | 14E | No |
| Sept.14 | b | 2220 | 2335 | 1 | 07N | 04E | No |
| Sept.15 | a,b | 1405 | 1420 | 1- | 06N | 10W | No |
| Sept.16 | c | 2135 | 2230 | (1-) | 05N | 22W | No |
| Sept.18 | a,c | 1635 | 1805 | 1- | 08N | 78E | No |
| Sept.18* | a,c | <2043 | 2114 | 1- | 07N | 51W | No |
| Sept.19 | c | 1625 | 1650 | 1- | 08N | 03E | No |
| Sept.21 | a | 1813 | 1840 | 1- | 12N | 14E | No |
| Sept.21 | a | 1840 | 1900 | 1- | 12N | 17W | No |
| Sept.22 | b,c | 1340 | 1425 | 1 | 12N | 03E | No |
| Sept.22 | b,c | 1425 | 1457 | 1 | 11N | 32W | No |
| Sept.22 | c | 1630 | 1710 | 1- | 05S | 56W | No |
| Sept.22 | c | 1955 | 2005 | 1- | 11N | 32W | No |
| Sept.23 | a | 1430 | | 1- | 12N | 13W | No |
| Sept.23 | b | 1502 | 1507 | 1 | 07N | 06E | No |
| Sept.23 | a,b | 1621 | 1656 | 1 | 08N | 02E | No |
| Sept.23 | a,b | 1852 | 1914 | 1 | 08N | 02E | No |

| DATE | SOURCE | OBSERVED FROM (UT) h m | TO h m | IMP. | POSITION LAT. | CM DIST. | SID |
|---|---|---|---|---|---|---|---|
| 1951(Cont.) | | | | | | | |
| Sept.23 | c | 1930 | 2140 | 1- | 08S | 74W | No |
| Sept.27 | a,c | 1805 | 1830 | 1- | 10N | 68W | No |
| Oct. 2 | a | 1720 | 1725 | 1- | 12N | 28W | No |
| Oct. 2 | a | 1912 | 1914 | 1- | 12N | 28W | No |
| Oct. 9 | c | 1800 | 1855 | 1- | 16S | 66E | No |
| Oct. 16 | a,d | 1358 | 1410 | 1- | 15S | 27W | No |
| Oct. 16 | a | 1538 | 1605 | 1- | 14S | 27W | No |
| Oct. 16 | d | 1620 | 1745 | 1- | 14S | 27W | No |
| Oct. 16 | a,c | 1938 | 2020 | 1- | 14S | 27W | No |
| Oct. 17 | a | 1458 | 1605 | 1- | 17S | 46W | No |
| Oct. 19 | c | 1625 | 1635 | 1- | 15S | 88W | No |
| Oct. 29 | c | 1525 | 1550 | 1- | 10N | 49W | No |
| Nov. 7 | c | 1830 | 1906 | 1- | 10S | 90W | Yes |
| Nov. 7 | c | 2000 | 2020 | 1- | 15S | 89W | No |
| Nov. 14 | c | 2040 | 2145 | 1- | 12N | 40W | No |
| Nov. 27 | b | 1431 | 1436 | 1 | 12N | 41E | No |
| Nov. 28 | a,b | 1505 | | 1 | 05N | 64W | No |
| Dec. 15 | c | 1600 | 1705 | 1 | 09N | 69E | No |
| Dec. 18 | c | 1800 | 1814 | 1- | 13N | 30E | No |
| Dec. 26 | c | 1716 | 1835 | 1- | 03N | 60E | No |
| Dec. 30 | c | 1515 | 1534 | 1 | 19N | 23E | No |
| 1952 | | | | | | | |
| Jan. 2 | b | 2026 | 2057 | 1 | 02N | 36W | No |
| Jan. 15 | c | 2025 | 2110 | 1- | 16N | 45E | No |
| Jan. 16 | a,c | 1440 | 1459 | 1- | 04N | 37E | No |
| Jan. 29 | d | 1306 | 1348 | 1- | 11N | 82E | No |
| Jan. 31 | a,c | 1955 | | 1+ | 12N | 56E | No |
| Feb. 4 | c | 1850 | 2005 | 1- | 25S | 39E | No |
| Feb. 5 | c | 1645 | 1720 | 1- | 19S | 19E | No |
| Feb. 11 | a,c | 1855 | 1920 | 1+ | 26S | 53W | No |
| Apr. 3 | c | 1511 | 1516 | 1- | 05S | 49W | No |
| Apr. 3 | c | 1832 | 1932 | (1-) | 05S | 49W | No |
| Apr. 7 | c | 2050 | 2115 | 1- | 02N | 09E | No |
| Apr. 12 | c | 1717 | 1737 | 1- | 06N | 47W | No |
| Apr. 14 | c | 2307 | - | 1 | 10N | 89W | No |
| Apr. 19 | c | 1516 | 1521 | (1-) | 08S | 12W | No |
| Apr. 19 | a,c | 1825 | 1838 | 1- | 10S | 11W | No |
| Apr. 19 | c | 2048 | 2113 | (1-) | 08S | 12W | No |
| Apr. 19 | c | 2131 | 2146 | 1- | 09S | 12W | No |
| May 5 | a,c | 1610 | | 1- | 11S | 33W | No |
| May 21 | a | 1822 | 1850 | 1- | 08S | 07W | No |
| May 27 | a,c | 1505 | 1525 | 1- | 19S | 37W | No |
| May 27 | a,c | 1618 | 1635 | 1- | 19S | 37W | No |
| May 27 | a,c | 1701 | 1715 | 1- | 19S | 37W | No |
| May 27 | a,b | 1825 | 1910 | 1 | 19S | 37W | No |
| May 27 | c | 2110 | | 1 | 19S | 37W | No |
| May 28 | a,b | 1451 | 1517 | 1- | 18S | 52W | No |
| May 31 | a | 1507 | 1522 | 1- | 02S | 41W | No |
| June 2 | a | 2003 | - | 1- | 00 | 69W | No |
| June 19 | a | 1420 | | 1- | 19S | 20W | No |
| June 23 | a,b | 1515 | 1535 | 1 | 17N | 42E | No |
| June 24 | a | 1745 | 1830 | 1- | 16N | 29E | No |
| June 25 | a | 1630 | | 1- | 11S | 54E | No |
| June 25 | a | 1915 | 1938 | 1- | 10S | 55E | No |
| June 27 | a,c | 1220 | 1310 | 1- | 05S | 18E | No |

NOTES TO TABLE 2 ARE SHOWN AT END OF TABLE 1

designation. Typical examples of this new class of "disturbance" on the 2800 Mc/sec records are shown in the second half of Figure 2.

Before an attempt is made to study the relationships between *Hα* flares and associated radio events, it should be emphasized that, in addition to the *Hα* brightenings customarily recognized as flares and so reported in the *Quarterly Bulletin* of the I.A.U., there are many brightenings on the sun which are less extensive and less bright than flares of importance 1. These features can be seen or photographed easily in *Hα* and *Ca+*

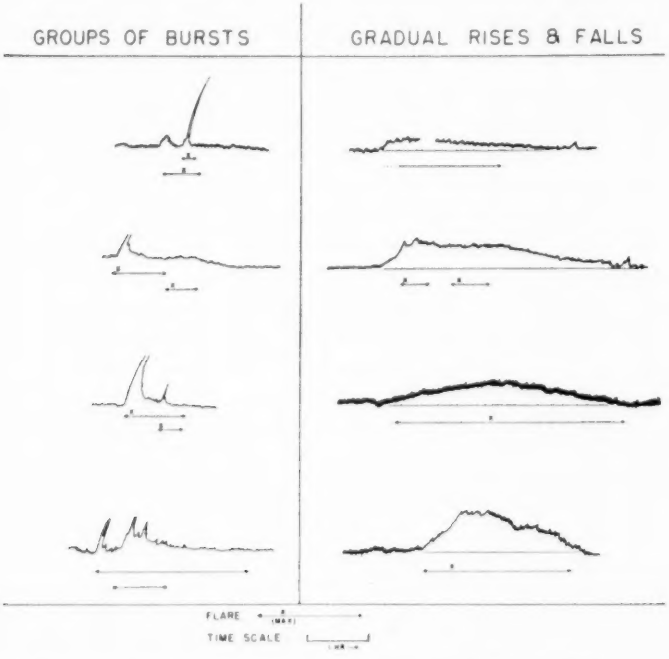


FIG. 2.—Examples of groups of bursts and gradual rises and falls on 2800 Mc/sec records

light and have been known for years. At times they have been called flares of importance "1−" and, as such, have been recognized as subflare phenomena. We have included 173 of these lesser *Hα* brightenings in this study. Seventy-two of these subflares have been taken from our own photographic records, and 30 of them were reported from at least two observatories. Although these subflares are well-established physical phenomena, they are generally smaller and fainter than the flares included in the *Quarterly Bulletin* of the I.A.U. Whenever possible in the following analyses, the "subflares" have been separated from the "flares."

### C. PERCENTAGE OF FLARES WITH ASSOCIATED 2800 MC/SEC EVENT

The 2800 Mc/sec records were examined for the times of 213 flares and 173 subflares, or a total of 386 sudden *Hα* brightenings. Distinctive events were identified for 57 per cent of the flares and for 19 per cent of the subflares. The distribution of the 386 bright-

enings by importance of flare and type of distinctive event on 2800 Mc/sec records is shown in Table 3.

### D. ENERGY EXCESS OF VARIOUS TYPES OF FLARE-ASSOCIATED EVENTS

The energy excess of each burst, postburst increase, and gradual rise and fall has been determined. The energy excess of these distinctive events on the 2800 Mc/sec records is the energy content of that part of the received radio-frequency radiation which exceeds the mean flux recorded at that frequency before the occurrence of the distinctive event. The energy excess is expressed in joules$(m)^{-2}(cycles/sec)^{-1}$. The values were determined by methods of graphical integration.

TABLE 3

DISTRIBUTION OF FLARES BY TYPE OF RADIO EVENT AND IMPORTANCE OF FLARE

| TYPE OF RADIO EVENT | SUB-FLARES | FLARES OF IMPORTANCE: | | | | | TOTAL FLARES | TOTAL |
|---|---|---|---|---|---|---|---|---|
| | | 1 | 1+ | 2 | 3 | ? | | |
| Single | 14 | 16 | 4 | 2 | ..... | 1 | 23 | 37 |
| Gradual rise and fall | 9 | 12 | 5 | 5 | ..... | ..... | 22 | 31 |
| $Single_s$; post | 3 | 14 | 1 | 6 | 1 | 1 | 23 | 26 |
| $Single_s$ | 3 | 11 | 3 | 3 | 1 | ..... | 18 | 21 |
| $Single_c$; post | 1 | 4 | 2 | 10 | 2 | ..... | 18 | 19 |
| $Single_c$ | 3 | 3 | ..... | 4 | ..... | 1 | 8 | 11 |
| Incomplete record and miscellaneous forms | ..... | 1 | 2 | 5 | 2 | ..... | 10 | 10 |
| Total distinctive events | 33 | 61 | 17 | 35 | 6 | 3 | 122 | 155 |
| Null cases | 140 | 77 | 8 | 5 | 1 | ..... | 91 | 231 |
| Total | 173 | 138 | 25 | 40 | 7 | 3 | 213 | 386 |
| Percentage with distinctive event | 19.1 | 44.2 | 68.0 | 87.5 | 85.7 | ..... | 57.3 | 40.2 |

Values of the energy excess have been determined for each of the flare-associated distinctive events and are shown, according to type of event, in Figure 3. The range in energy excess is very great, and the extreme values of the energy excess differ by a factor of 50,000. There is a steady progression on the energy scale from the small single burst, to single-simple, to single-complex bursts. The occurrence of a "postburst increase" greatly augments the energy of the event.

When the flare-associated events are broken down into their "bursts" and "postburst" components, as in Figure 4, we see that the energy excess of bursts followed by "posts" tends to be slightly higher than that of bursts of the same type but without the postburst increase. Nevertheless, there is a greater difference between the *simple* and *complex* bursts than between their respective members with and without a postburst increase. The average energy excess of the "gradual rises and falls" is very similar to that of the "postburst increases."

## III. DISCUSSION OF OBSERVATIONS

### A. TIME RELATIONSHIPS

Intercomparisons of the times of certain aspects of the flares with the times of certain aspects of the associated 2800 Mc/sec events reveal the following relationships.

1. On the average, the flare and the associated 2800 Mc/sec disturbance start together. This is indicated by all six types of 2800 Mc/sec events (see Fig. 5). The average difference in starting time for all flares and associated 2800 Mc/sec events in this study is only 0.6 minutes and is in the sense that the *Hα* flare precedes the radio event. This portion of the study is necessarily limited to those flares for which the time of start has supposedly been observed. Without photographic records at frequent intervals, it is very difficult to be certain of the starting time of a flare, and, even with photometric light-curves, the starting time is usually known only to the nearest minute. Small

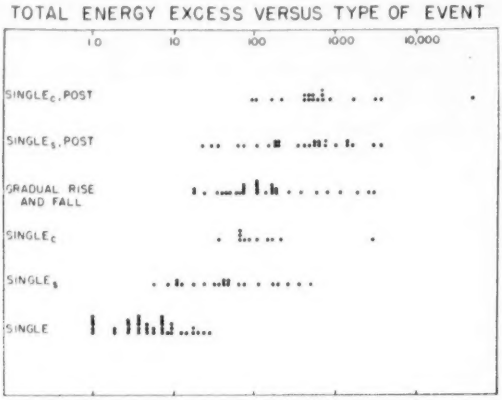


FIG. 3

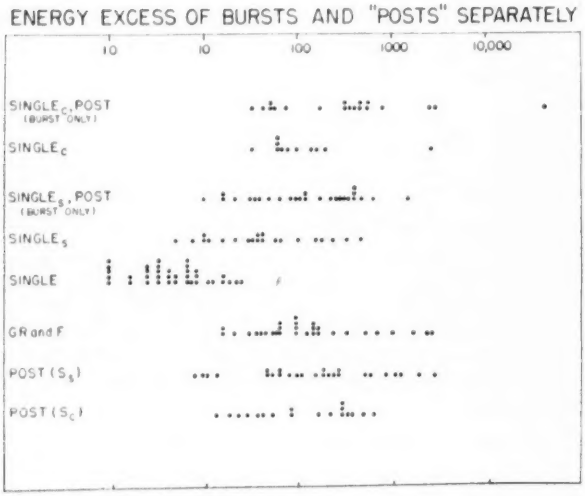


FIG. 4

brightenings often precede the principal increase in *Hα* intensity and thus introduce further uncertainty in the time that should be given as the starting time of the flare.

2. On the 2800 Mc/sec records there is sometimes a gradual increase in the solar noise preceding the very rapid increase which is characteristic of the 2800 Mc/sec burst. This gradual increase has been termed a "precursor."[4] For 11 of the flares in this study, the associated bursts are preceded by "precursors." They began, on the average, 1.3 minutes after the start of the *Hα* flare. From the data here considered, there is no indication that the phenomenon called a "precursor" at 2800 Mc/sec precedes in time the start of the *Hα* brightenings. For the study of time relationships, the start of the precursor has been used as the starting time of the 2800 Mc/sec burst.

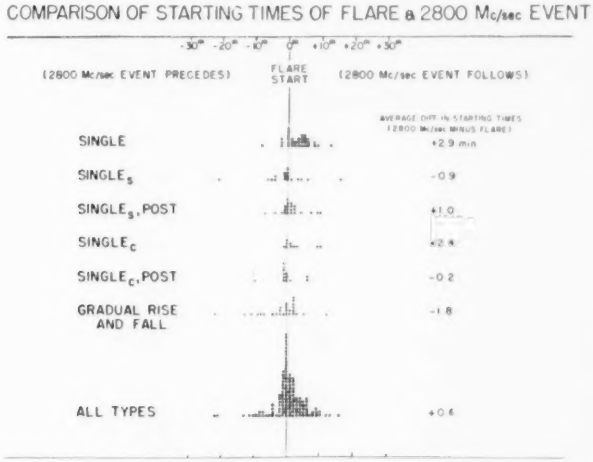


FIG. 5

3. Although the flare and the associated 2800 Mc/sec event apparently start together, the 2800 Mc/sec burst reaches its maximum before maximum intensity has been attained by the *Hα* flare. On the average, the maximum for the 2800 Mc/sec burst occurs 3.4 minutes before *Hα* maximum (see Fig. 6). For some flares, especially those with very rapid increase in intensity, the time of maximum of the flare and that of the associated 2800 Mc/sec burst are nearly coincident.

The type of 2800 Mc/sec event called "gradual rise and fall" does not share the above relationship. In general, these events have their maxima at the time of the *Hα* maximum or even considerably later.

4. The times of ending of the 2800 Mc/sec bursts (postburst increase excluded) cluster closely around the time of *Hα* maximum (see Fig. 7). This relationship, in conjunction with the coincident starting times of burst and flare, indicates that the 2800 Mc/sec bursts take place essentially during the period of increase in *Hα* intensity. Complex bursts tend to last beyond the reported time of the *Hα* maximum. For a number of these cases, the photometric light-curves show either a broad, flat *Hα* maximum or a flare with multiple maxima.

[4] *Ibid.*, p. 49; and *Tables of Daily Intensity and Outstanding Disturbances of 10.7 Cm Solar Radiation*, published on a current schedule.

5. It is apparent from the data in Figure 7 that the "gradual rises and falls" are different from the more sudden bursts. They continue long after flare maximum has been attained. Their duration is equal to, or greater than, the duration of the flare itself. In this respect they resemble the "postburst increases."

The time relationships here described are illustrated in Figure 8, where the photometric light-curve for the flare of June 4, 1949, is shown in juxtaposition to the simultaneous 2800 Mc/sec record. The two vertical straight lines permit comparison of the times of start and maximum of the 2800 Mc/sec event with features in the

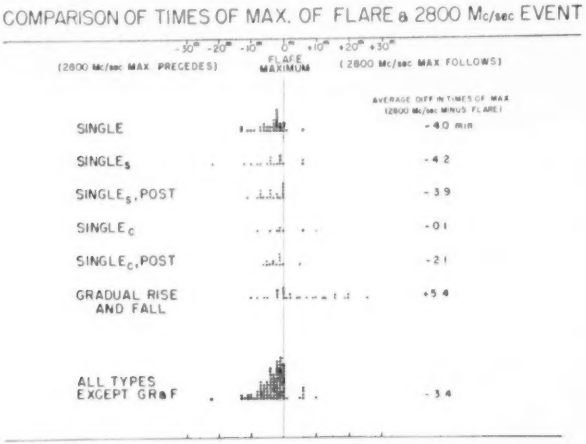


FIG. 6

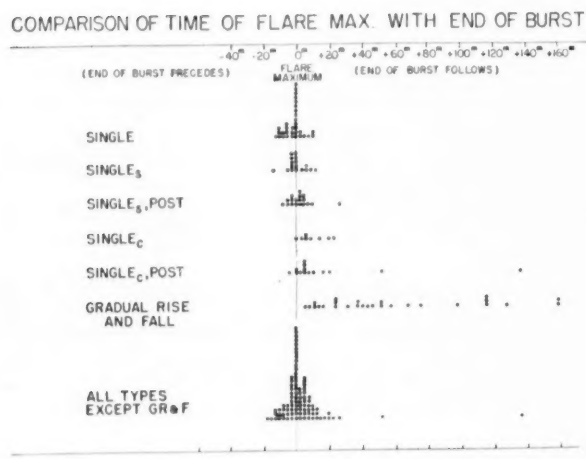


FIG. 7

photometric light-curve of the flare. On June 4, 1949, the 2800 Mc/sec burst was preceded by a "precursor," which began within 1 minute of the start of the *Hα* flare. Burst maximum preceded flare maximum by 4 minutes. Both the flare and the burst had complex variations in intensity.

### B. TWO TYPES OF PHENOMENA

The foregoing time relationships suggest that the flare-associated events at 2800 Mc/sec may include two quite different types of phenomena. One is a sudden burst-type feature which occurs during the rise to maximum of the *Hα* flare. The other is a more gradual rise and fall of flux which starts with the flare and lasts as long as, or longer than,

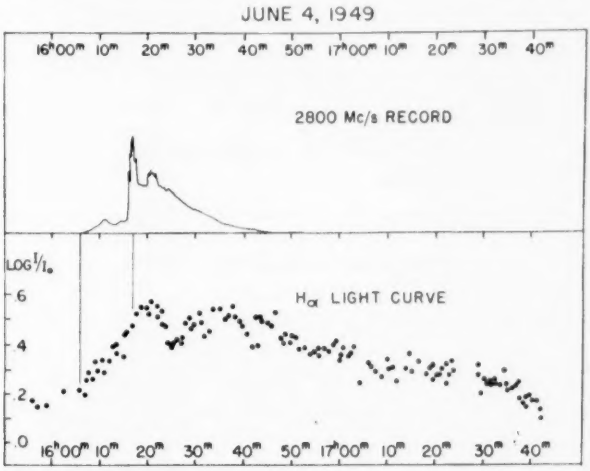


FIG. 8.—Comparison of 2800 Mc/sec disturbance with photometric light-curve of *Hα* flare

the flare itself. The two can occur in conjunction with each other, or either of the two can occur separately. This concept would identify the type of events called "gradual rise and fall" with the postburst increase that follows many of the single bursts. A similar impression can be gained from the mere appearance of the records. In 1951 Covington wrote as follows when he was describing certain characteristics of the bursts on records of 2800 Mc/sec solar radiation: "Sometimes a precursor and a post-burst increase both occur [with a burst] and give the impression that the burst is superimposed on another smaller burst of greater duration."[4]

### C. IMPORTANCE

The importance, or greatness, of the *Hα* flare appears to be related to both the magnitude and the type of distinctive event at 2800 Mc/sec solar radiation. First, the percentage of flares with some form of associated distinctive event at 2800 Mc/sec increases rapidly with increase in the importance of the flare. The proportion increases from 19 per cent for the subflares and 44 per cent for flares of importance 1 to 87 per cent for flares of importance 2 and 3 (see Table 3). Of the 213 flares in this study, 91 were null at 2800 Mc/sec. Eighty-five per cent of these null cases were flares of importance 1. Only 6 flares of importance 2 or 3 had no distinctive event at 2800 Mc/sec.

On the average, the energy excess of the associated 2800 Mc/sec event increases with

flare importance (see Fig. 9). For any one importance category, however, the scatter is very great. The situation remains essentially the same when the bursts alone are considered and when the "postburst increases" and the "gradual rises and falls" are studied as possible functions of flare importance. The average energy excess for both types of phenomena increases with the importance of the flare, but the scatter in each category is very wide.

A more detailed relation between type of radio event and importance of the flare is shown in Figure 10. It can be seen that flares of importance 2 or 3 were associated with all types of distinctive events at 2800 Mc/sec. These important flares, however, formed a much larger portion of the group associated with the single-complex type of burst than

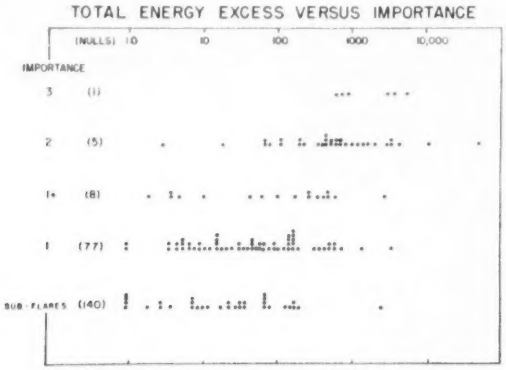


FIG. 9

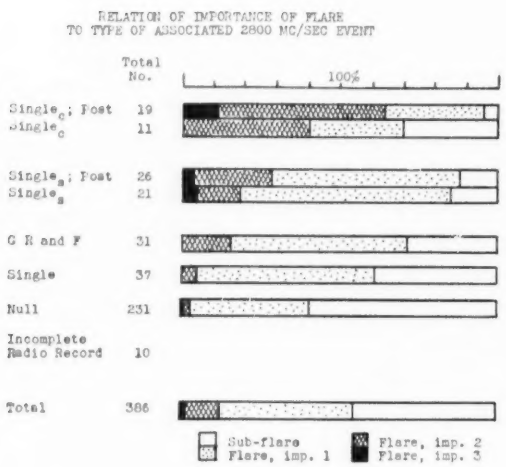


FIG. 10

with any other type. Furthermore, there appears to be a higher percentage of flares of importance 2 and 3 associated with both simple and complex bursts that are followed by a postburst increase than with simple and complex bursts alone.

### D. PERCENTAGE OF FLARES WITH SUDDEN IONOSPHERIC DISTURBANCES

Sudden ionospheric disturbances (SID's) were reported for 42 per cent of the flares in this study (see Table 4). Let the flares be divided into two groups on the basis of the occurrence or absence of a concomitant increase in 2800 Mc/sec radiation. It is then found that sudden ionospheric disturbances accompanied 61 per cent of the flares with associated 2800 Mc/sec events and only 18 per cent of the "null" cases. Furthermore, if the data are divided according to the importance of the flare, the higher percentage of SID's with flares having 2800 Mc/sec components is maintained in each importance category.

TABLE 4

PERCENTAGE OF FLARES WITH SUDDEN IONOSPHERIC DISTURBANCES

| Importance of Flare | Total Number of Flares and Subflares | | Flares with Sudden Ionospheric Disturbance | |
|---|---|---|---|---|
| | | | Number | Per Cent |
| 3 | With 2800 Mc/sec event | 6 | 6 | 100 |
| | Null | 1 | 1 | 100 |
| 2 | With 2800 Mc/sec event | 35 | 31 | 89 |
| | Null | 5 | 3 | 60 |
| 1+ | With 2800 Mc/sec event | 17 | 8 | 47 |
| | Null | 8 | 3 | 38 |
| 1 | With 2800 Mc/sec event | 61 | 27 | 44 |
| | Null | 77 | 9 | 12 |
| (?) | With 2800 Mc/sec event | 3 | 2 | ..... |
| | All flares with 2800 Mc/sec event | 122 | 74 | 61 |
| | All nulls | 91 | 16 | 18 |
| | Total flares | 213 | 90 | 42 |
| Subflares | With 2800 Mc/sec event | 33 | 3 | 9 |
| | Null | 140 | 5 | 4 |
| | Total subflares | 173 | 8 | 5 |

The flares in this study again exhibit the well-established fact that SID's occur more frequently with flares of importance 2 and 3 than with flares of importance 1. Ionospheric disturbances were reported for only 5 per cent of the brightenings here classified as subflares.

### E. POSITION OF FLARE ON SOLAR DISK

The position of the flare on the disk apparently plays a part in determining both the type and the magnitude of the associated 2800 Mc/sec event. Three lines of evidence indicate that the "gradual rises and falls" and the "postburst increases" are affected by the position of the flare on the disk. The purely burst-type events seem to be independent of this influence.

1. "Gradual rises and falls" and the *relatively* large "postburst increases" occur more often when the flare is close to the central meridian than when it is near the limb. Let the 2800 Mc/sec flare-associated events be divided into two groups, the first to include all cases in which the energy excess of the burst is greater than that of the postburst increase; the second to include all "gradual rises and falls" and all cases in which the energy excess of the burst is less than that of the "postburst increase." We then find that the flares associated with the events in group 1 show a relatively uniform distribution on the solar disk out to central meridian distances as great as 70° but that those associated with group 2 have a high concentration toward the central part of the disk (see Fig. 11). Closeness of the flare to the central meridian apparently favors the occurrence of a "gradual rise and fall" or of a "postburst increase" that is large in comparison to the burst itself.

2. The flares associated with "gradual rises and falls" and "postburst increases" with very great values of energy excess at 2800 Mc/sec show a high central concentration. On the other hand, the flares with strictly burstlike events of high energy excess exhibit no

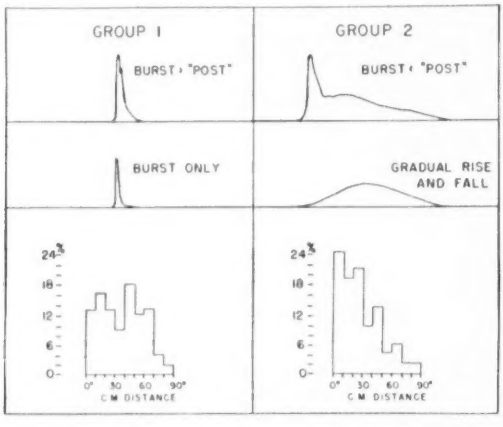


FIG. 11.—Comparison of position of flare on solar disk with form of associated 2800 Mc/sec disturbance.

obvious departure from uniform distribution on the disk. Bursts with very large values of the energy excess were associated with flares near the limb as well as near the central meridian (see Fig. 12).

3. For flares of importance 2 and 3 the energy excess of the "gradual rises and falls" and "postburst increases" tends to be greater for flares close to the central meridian than for flares closer to the limb. There is no such dependence on position for the strictly burst-type events associated with these flares (see Fig. 13).

## IV. PROPORTION OF OUTSTANDING 2800 MC/SEC EVENTS THAT ARE FLARE-ASSOCIATED

Up to this point, consideration has been focused on the presence or absence and the characteristics of 2800 Mc/sec events at the time of known flares. Let the problem now be reversed and consider how many of the outstanding events or disturbances in solar radiation at 2800 Mc/sec are flare-associated. Simple comparison of the day-long radio records with the collected data for flares for the same period shows the very close asso-

ciation of the two phenomena (see Fig. 14). Each of the bursts on the 2800 Mc/sec records here shown occurs at the start of a solar flare.

In order to test more closely the association between flares and 2800 Mc/sec bursts, we have examined the complete published list of outstanding disturbances at 2800 Mc/sec from March, 1947, through June, 1952. During this period 418 outstanding events were recorded at Ottawa. Flares or subflares were observed at the times of 193 of these, and SID's occurred concomitantly with 88 more (see Table 5). There remain 137 cases for which there are no known flares or SID's. For the times of 130 of these disturbances no observations were being made at the McMath-Hulbert Observatory. For the 131st case, we observed a large and fast ejection with a brightening at the solar limb. This could have been the limb aspect of a flare. Observations were in progress at the McMath-

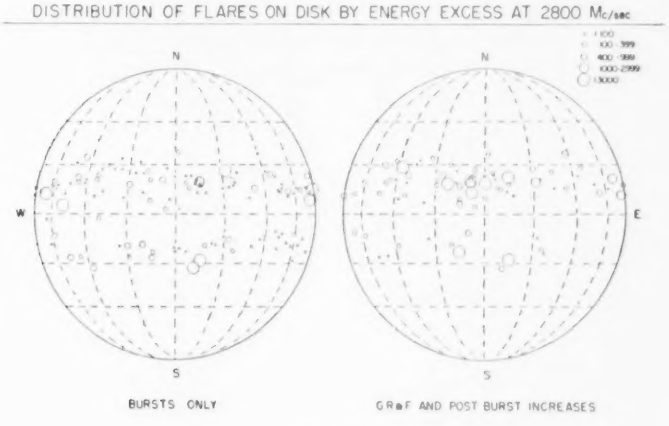


FIG. 12

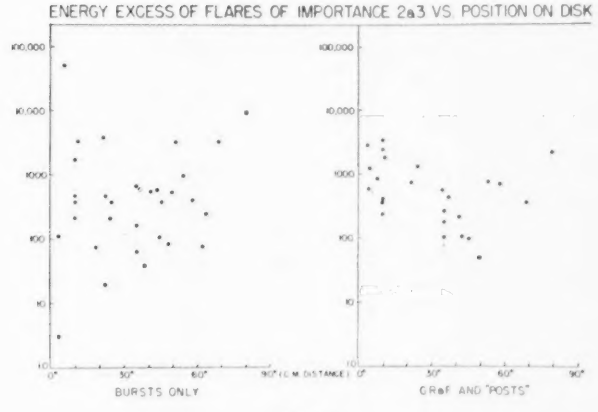


FIG. 13

Hulbert Observatory for the times of the 6 final cases, all small single bursts. There were no flares or brightenings in the solar regions being photographed. Thus, for 98.6 per cent of the outstanding disturbances at 2800 Mc/sec, there was either an observed flare, an SID, or no observation. Accordingly, at the present time, there is strong evidence that there is an outstanding event or disturbance in 2800 Mc/sec solar radiation only when a flare or subflare is in progress.

## V. CONCLUSIONS

1. Study of records of 2800 Mc/sec solar radiation at the times of 386 *Hα* flares and subflares shows that 57 per cent of the flares and 19 per cent of the subflares were accompanied by some form of disturbance on the 2800 Mc/sec records. The percentage of

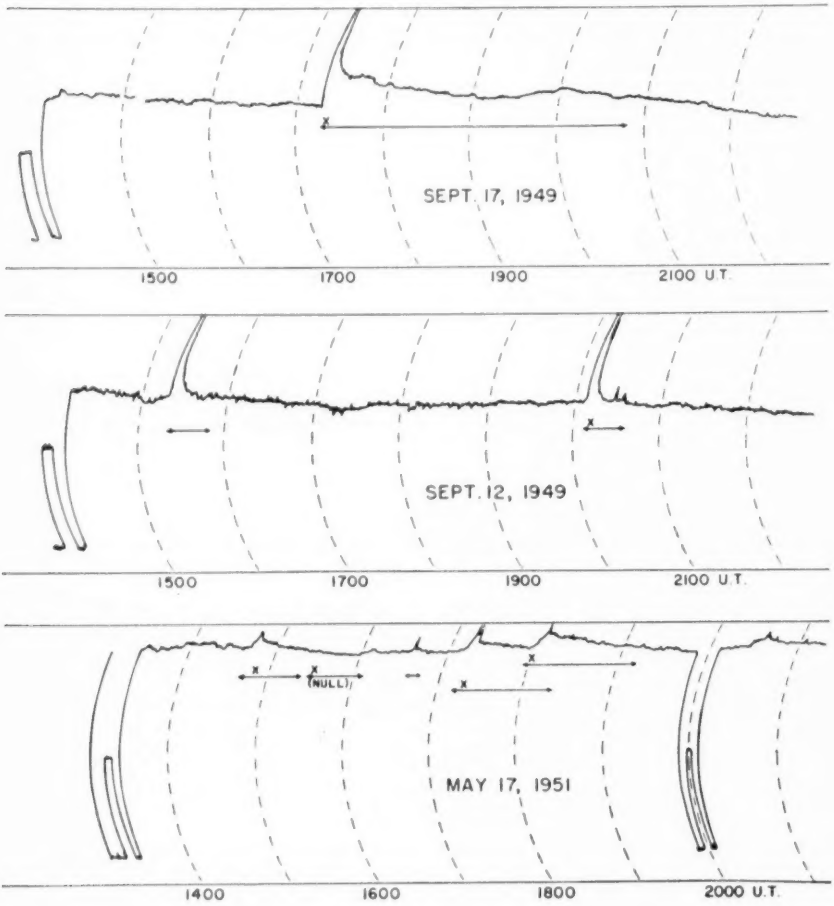


FIG. 14.—Association between observed *Hα* flares and disturbances on records of 2800 Mc/sec solar radiation. Arrow shows duration of flare. Cross indicates time of flare maximum.

flares with associated distinctive events at 2800 Mc/sec increased rapidly with increase in the importance of the *Hα* flare. On the average, the energy excess of the associated 2800 Mc/sec event increases with flare importance, but the scatter of values is very great.

2. The "null" cases are associated primarily with the "subflares" and flares of importance 1. There were, however, 6 flares of importance 2 or 3 for which there was no associated disturbance on the 2800 Mc/sec records.

TABLE 5

SUMMARY OF FLARES AND SID'S OBSERVED AT THE TIMES OF ALL REPORTED OUTSTANDING DISTURBANCES AT 2800 MC/SEC

| Year | Total 2800 Mc/sec Events | Number Associated with: | | | | Events without Known Flare or SID | |
|---|---|---|---|---|---|---|---|
| | | Flare and SID | Flare Only | SID Only | Flare or SID | Total No. | No Observations at McMath-Hulbert Obs. for Corresponding Times |
| 1947 (March) | 56 | 17 | 1 | 26 | 44 | 12 | 12 |
| 1948 | 61 | 16 | 4 | 25 | 45 | 16 | 14 |
| 1949 | 101 | 37 | 9 | 20 | 66 | 35 | 33 |
| 1950 | 78 | 31 | 11 | 10 | 52 | 26 | 25 |
| 1951 | 107 | 30 | 32 | 7 | 69 | 38 | 36 |
| 1952 (June) | 15 | 2 | 3 | | 5 | 10 | 10 |
| Total | 418 | 133 | 60 | 88 | 281 | 137 | 130 |

3. Flare-associated events at 2800 Mc/sec fall into two principal categories: (*a*) *single bursts*, which may be either simple or complex and which may or may not be followed by a "postburst increase"; (*b*) "gradual rises and falls of flux." Considerations of time relationships and the magnitude of the energy excesses suggest that the "postburst increases" and the "gradual rises and falls" of flux may represent the same physical phenomenon.

4. In general, the sudden, flare-associated bursts at 2800 Mc/sec start at the same time as the *Hα* flares, attain maximum before the *Hα* flares, and are over just as the *Hα* flares start to fade. On the average, the "gradual rises and falls" also start with the *Hα* flares, but their maximum occurs either with that of the flares or later.

5. Sudden ionospheric disturbances accompanied 61 per cent of the flares with associated 2800 Mc/sec events and only 18 per cent of the "null" cases.

6. Flares associated with "gradual rises and falls" and "postburst increases" of large energy excess show a high concentration toward the central part of the solar disk. The flares with large, strictly burstlike events at 2800 Mc/sec exhibit no obvious departure from uniform distribution on the solar disk.

7. Consideration of all outstanding disturbances recorded on the 2800 Mc/sec records at Ottawa between March 27, 1947, and June 30, 1952, provides strong evidence that there is an outstanding event or sudden disturbance on 2800 Mc/sec solar radiation only when a flare or subflare is in progress.

The authors acknowledge with pleasure the assistance and co-operation of their colleagues at the National Research Council of Canada and the McMath-Hulbert Observatory of the University of Michigan.

# INTENSITY MEASURES OF CALCIUM *PLAGES* FOR COMPARISON WITH 10.3-CENTIMETER SOLAR RADIATION OCTOBER 16, 1951

HELEN W. DODSON
McMath-Hulbert Observatory
University of Michigan
*Received November 19, 1953*

ABSTRACT

Photometric studies of $K_{232}$ spectroheliograms for October 16, 1951, are compared with Covington's records of the positions of 10.3-cm (2800 Mc/sec) emissive regions on the sun for the same date. There were three emissive regions at 10.3 cm, and there were three maxima in the east-west distribution of calcium *plage* intensity on the solar disk. Sunspots were observed in only two of the three regions.

Most of the studies comparing variations in solar radiation at radio frequencies with solar activity observed photographically and visually have used sunspots as the basic indicators of activity observed in the optical region. This practice probably developed initially because sunspot data constituted the most readily available compilations of information relating to solar activity. It has been continued because these studies have been successful in showing that there is a high coefficient of correlation between sunspot area and the flux at certain high radio frequencies.[1] The magnitude of the flux changes in phase with variations in the total area of sunspots on the disk. Furthermore, Covington's observations during the partial eclipse of November 23, 1946, indicated clearly that there is a close association between the position of the source of 2800 Mc/sec solar radiation and the regions on the sun where sunspots are located.[2]

It seems probable that as studies of the sun at radio frequencies progress, it will be desirable to consider parameters of solar activity other than sunspots. The calcium *plages* are obvious features for consideration. The calcium *plage* usually forms before the appearance of the associated spot and continues after the spot has disappeared. There are many *plages* in which spots do not become visible; but we do not, at our observatory, have any observations of a spot without at least some trace of a bright, associated *plage*. In general, the area of the *plage* increases with spot area, but at a different rate. The range of variation in the area of the *plage* is greater than that of the spots. Finally, repeated intercomparisons of *plage* and coronal data have shown that the positions of the calcium *plages*, both with and without spots, are closely associated with the principal regions of strong monochromatic coronal emission.[3] This association is of special interest for the problem under consideration, since both theoretical and observational results place the source of radio radiation from the sun in regions located thousands of kilometers above the photosphere.

The excellent data now being secured by Covington and Broten with the 150-foot array of the Radio Observatory of the National Research Council of Canada may make it possible to judge the relative merits of spots and *plages* as indicators of the regions emitting 10.3-cm (2800 Mc/sec) radiation. Covingto has prepared for analysis his radion data for October 16, 1951. For the same date, we have prepared isophotes of the $K_{232}$

[1] Covington, *Proc. Inst. Radio Eng.*, **36**, 454, 1948; *J.R.A.S. Canada*, **45**, 15, 1951; Lehany and Yabsley, *Australian J. Sci. Res. A*, **2**, 48, 1949.

[2] Covington, *Nature*, **159**, 405, 1947.

[3] Dodson and Mohler, *Observatory*, **73**, 116, 1953.

(λ 3934) spectroheliograms. A $K_{232}$ spectroheliogram and a spot map for this date are shown in Figure 1.

The photometric measures were carried out with a microdensitometer using a 1P21 cell as the light-sensitive element. The measures were made point by point across a projected solar image 222 mm in diameter. Intensity measures were recorded for a network of points separated by 2 mm in the image—or 12,000 km on the solar disk. Isophotes were derived for intensity values 1.1, 1.3, 1.5, . . . , 2.3 times the intensity of the undisturbed $K_{232}$ background. The isophotes so derived are shown in Figure 1.

In order to make the measures directly comparable with the data available for 2800 Mc/sec, the quantity, Area (intensity $-1$), has been integrated along chords cutting the solar disk in the north-south direction, i.e., in a direction perpendicular to the terrestrial horizon. This calculation provides a measure of the radiation at λ 3934 due to departures from a *plage*less sun. Figure 2 shows the distribution from east to west of such excess solar radiation, for various lower limits of the intensity, on October 16, 1951. In this calculation the unit of area is that of a square, 2 mm on a side, in the projected solar image. The unit of intensity is that of the undisturbed $K_{232}$ background, near the center of the projected solar image (slit-widths = 0.4 A).

Data for the 2800 Mc/sec radiation are presented in strips 1.°5 in width (65,000 km on the sun). The position and magnitude of the sources of excess radiation at 2800 Mc/sec on October 16, 1951, as determined by Covington, are shown by the dotted histogram superposed on the bottom diagram of Figure 2. To facilitate the comparison of the *plage* and radio data, we have further combined our *plage* measures into integrated values for vertical north-south strips 1.°5 in width. The measures in this form are shown in the accompanying article by Covington and Broten.[4] The pertinent facts are summarized in Table 1.

## DISCUSSION

Comparison of the location and extent of the 2800 Mc/sec emissive regions as measured by Covington[4] with the foregoing measurements of the calcium *plages* indicates the following features.

1. There are three emissive regions at 2800 Mc/sec, and there are three maxima in the east-west distribution of *plage* intensity on the solar disk. The *plage* maxima and the radio-emissive regions occur in very similar, but not identical, "strips" of the solar disk. The *plage* maxima as here computed are wider than the radio-emissive regions; but in both studies the two limbward regions are of comparable width and distinctly wider than the central one.

2. On October 16, 1951, there were sunspots in the central and western *plages*, but none was observed in the eastern *plage*.

3. The radio data show three *isolated* emission regions. In order to change the integrated *plage* measures from three "maxima" to three separate regions, it is necessary to limit the measures to those parts of the *plage* for which the intensity is at least 1.5 × the intensity of the undisturbed background (see Fig. 2). When this is done or when the measures are restricted still further to the most intense regions, the similarity between the distribution of the calcium *plages* and the designated radio-emission regions is strengthened. The calcium regions become comparable in width to the radio regions and agree more closely in position and relative magnitudes.

4. The 2800 Mc/sec emissive regions and the calcium *plages* are markedly similar in position. However, the two outer radio-emissive regions appear to lie slightly closer to the limb of the sun than do the *plages*. A difference of this kind might be expected as a result of projection, if the radio-emissive regions are located in the corona above the calcium *plages*.

[4] Covington and Broten, *Ap. J.*, **119**, 569, 1954.

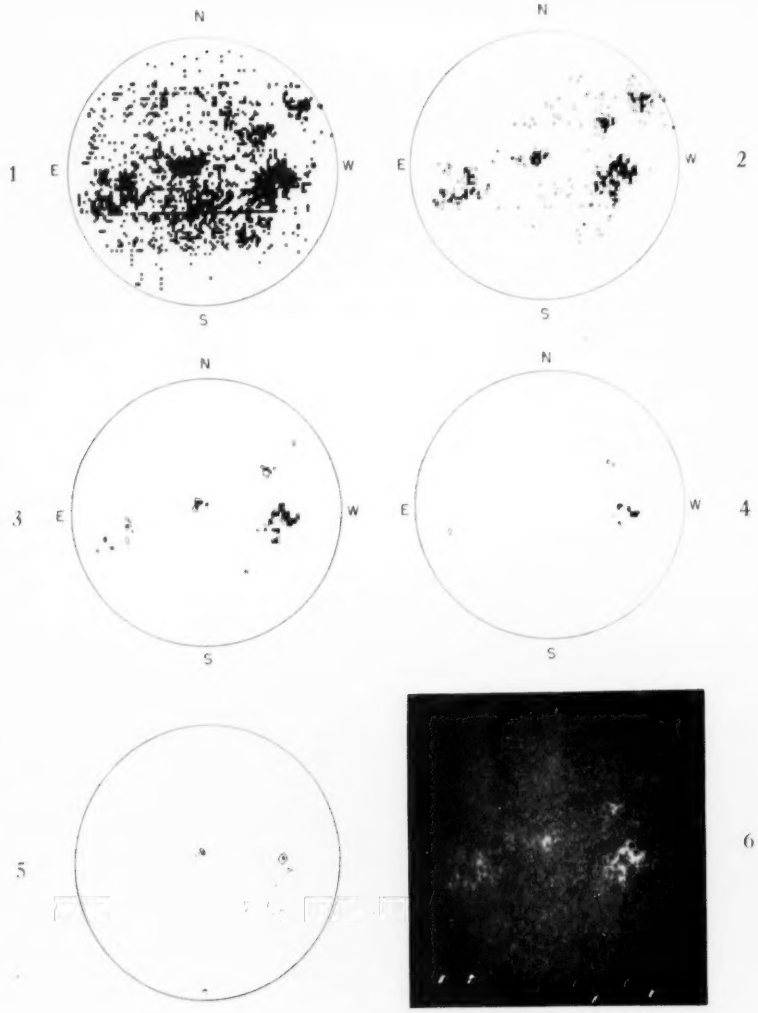


FIG. 1.—Isophotes of calcium *plages*, October 16, 1951. *1*, intensity $\gtrsim$ 1.1. *2*, intensity $\gtrsim$ 1.3 (*open*); $\gtrsim$ 1.5 (*filled*). *3*, intensity $\gtrsim$ 1.7 (*open*); $\gtrsim$ 1.9 (*filled*). *4*, intensity $\gtrsim$ 2.1 (*open*); $\gtrsim$ 2.3 (*filled*). *5*, sunspots, October 16, 1951. *6*, $K_{232}$ spectroheliogram, October 16, 1951. All disks have same orientation; directions refer to horizon system of co-ordinates at noon.

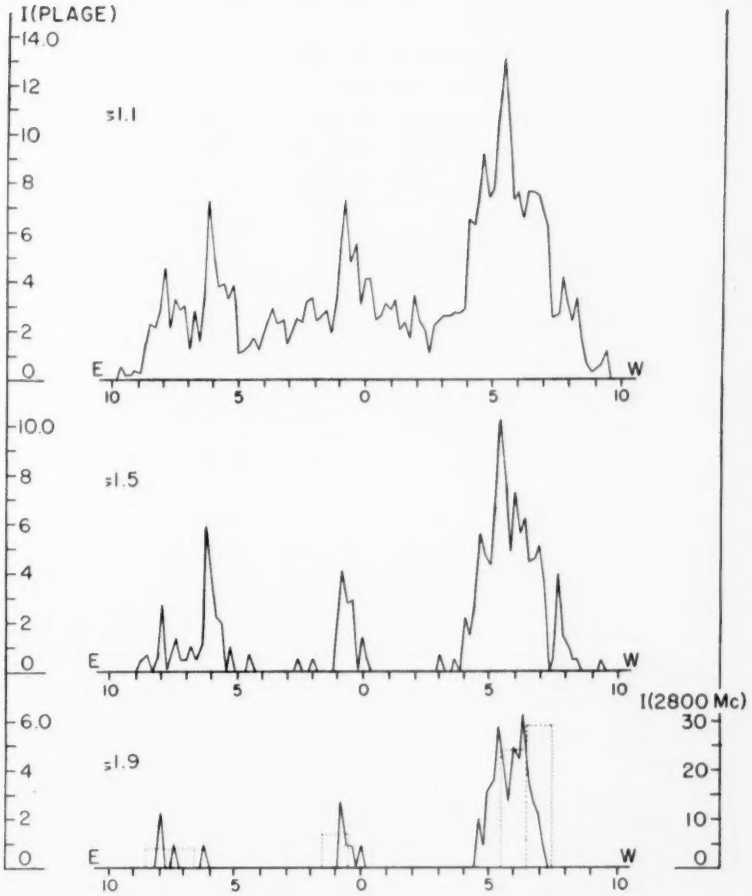


FIG. 2.—East-west distribution of λ 3934 radiation in excess of that from *plage*less sun. *Top*, intensity ≤ 1.1 × undisturbed disk; *center*, ≤ 1.5 ×; *bottom*, ≤ 1.9 ×. Intensity unit for *plage* radiation is area of square, 12,000 km on side at center of disk, multiplied by intensity in excess of that of undisturbed $K_{232}$ disk, i.e., area (intensity − 1). Units for abscissae are strips 1°.5 in width. Dotted histogram shows radio emission at 2800 Mc/sec. See article by Covington (this issue, p. 569).

5. If there is a contribution to the 2800 Mc/sec radiation from the areas associated with the faint and almost uniformly distributed calcium regions with intensity less than 1.5 × that of the undisturbed disk, it has apparently not been recognized as excess radiation. The distribution of these faint calcium regions on the sun can be seen by intercomparison of the top and central curves in Figure 2.

TABLE 1

COMPARISON OF CALCIUM *Plages* AND 2800 MC/SEC EMISSIVE REGIONS

| | Eastern Region | Central Region | Western Region |
|---|---|---|---|
| | Calcium *Plages* | | |
| 1. *Intensity* ≥ *1.1* × *background:* | | | |
| Distance from center (min. of arc) | 10.2*E* | 0.9*E* | 9.2*W* |
| Width, east-west (min. of arc) | 5.5 | 2.3 | 7 |
| Σ area (intensity − 1) | 84 | 82 | 182 |
| Σ in units of western region | 0.46 | 0.45 | 1.00 |
| 2. *Intensity* ≥ *1.5* × *background:* | | | |
| Distance from center (min. of arc) | 10.0*E* | 0.9*E* | 9.0*W* |
| Width, east-west (min. of arc) | 4 | 2 | 6 |
| Σ area (intensity − 1) | 25 | 15 | 98 |
| Σ in units of western region | 0.25 | 0.15 | 1.00 |
| 3. *Intensity* ≥ *1.9* × *background:* | | | |
| Distance from center (min. of arc) | 10.5*E* | 0.8*E* | 9.0*W* |
| Width, east-west (min. of arc) | 3 | 1.5 | 4 |
| Σ area (intensity − 1) | 4.0 | 5.4 | 46.9 |
| Σ in units of western region | 0.09 | 0.12 | 1.00 |
| | 2800 Mc/Sec Emissive Regions | | |
| Distance from center (min. of arc) | 11.25*E* | 1.5*E* | 9.75*E* |
| Width, east-west (min. of arc) | 3 | 1.5 | 3 |
| Total flux ($10^{-22}$ watts/m²/cps) | 6.1 | 5.3 | 40 |
| Total flux in units of western region | 0.15 | 0.13 | 1.00 |

The author wishes to acknowledge with pleasure the privilege of collaborating in these studies with Mr. Covington and other members of the staff of the National Research Council at Ottawa.

# BRIGHTNESS OF THE SOLAR DISK AT A WAVE LENGTH OF 10.3 CM*

A. E. Covington and N. W. Broten
National Research Council of Canada, Radio and Electrical Engineering Division
Ottawa, Canada
*Received December 1, 1953*

ABSTRACT

A slotted wave-guide array, 150 feet long, has been constructed for operation at a wave length of 10.3 cm and produces a fan-shaped radiation pattern with a resolving power of 0°.130 in the narrow dimension. The sun is scanned by the earth's rotation and the resulting drift-curves can be interpreted in terms of a radio disk with bright regions that partake of the solar rotation. Analysis for 1952 shows that the radio disk has a bright ring at the limb of the photospheric disk with an intensity twice that of the central region. The equivalent temperature of the center of the radio sun is 21,800° K, while the radius of the radio disk is 1.15 times that of the visible sun. The radio-emissive regions have been located within strips, and the analysis for one day, October 16, 1951, shows that there were one intense and two weaker radio spots. Comparison with sunspot data assembled by the Naval Observatory shows that sunspots can be associated with the intense radio spot and with one of the adjacent weaker radio spots, but none can be found for the third. Comparison with spectroheliograms taken at the McMath-Hulbert Observatory shows that a distinct *plage* can be associated with each of the three radio-emissive regions.

## INTRODUCTION

The early observations of solar radio noise were made with various antennae capable of collecting energy in broad beams which covered considerably more than the optical disk. This made it impossible to locate the emitting regions by direct observations, and consequently newer antennae have been made with increased resolving power. The receiving pattern of any antenna is found according to the principles of well-known wave theory; and in the case of a paraboloidal reflector the angular opening of the pattern to the half-power points is determined to a first approximation by the ratio of wave length to diameter. The original radiotelescope used in Ottawa by the National Research Council was made with a 4-foot paraboloidal reflector and was operated at a wave length of 10.7 cm.[1] In this particular case the resolving power was measured and found to be about 7°.

A slotted wave-guide antenna with an aperture in the long dimension of about 450 wave lengths has now been constructed and produces a fan-shaped beam with sufficient resolving power in one dimension that the emission from the radio sun may be examined in narrow strips. The use of strips is indicated by the rectangular outline of the radiation pattern, which has angular openings to the half-power points of $\frac{1}{8}°$ and 22°.5. The radiotelescope appears as a V-shaped trough, 150 feet long, 18 inches wide, and $12\frac{1}{2}$ inches deep, with the slotted rectangular wave guide in the bottom (see Fig. 1). The horn can be rotated about its long axis, which is held in a level east-west direction so that the radiotelescope is used in the manner of a meridian telescope, and celestial objects drift through the narrow part of the receiving pattern. The maximum of the beam in the narrow cross-section does not fall on the meridian but squints to the east by an amount that is determined by the operating wave length. This feature is characteristic of a nonresonant array and results in the maximum of the radiation pattern describing a small circle to the east of the zenith when the horn is rotated about its long axis. A superheterodyne

* Paper presented to the spring meeting of Union Radio Scientifique Internationale held in Washington, D.C., April, 1953.

[1] A. E. Covington, *Proc. I.R.E.*, **36**, 454, 1948.

receiver is used, with simultaneous reception occurring on the upper and lower side bands. Corresponding to the wave length of these two side bands, there are two receiving beams separated by 1°.5 (see Fig. 2). Observations are taken by allowing the sun to drift through the narrow part of the two beams and by recording on an Esterline-Angus meter the varying intensity of the radio waves as a function of time. As yet, the variation of squint angle with frequency has not been exploited.

## RECEIVING PATTERN

The fan-shaped receiving pattern can be described conveniently as being composed of two independent variations in perpendicular directions. The pattern in the narrow direction is of most concern and is determined by the phase and amplitude of the energy contributions from 510 slots which have been placed uniformly along the wave guide every 3.500 inches. The slots are collectors and have been designed[2] so that each one delivers

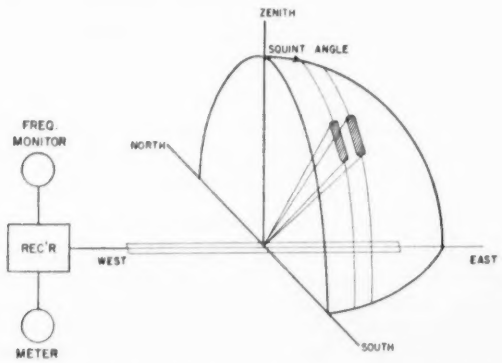


FIG. 2.—Orientation of long array with respect to the compass

the same energy amplitude to the receiver. The phase difference between the contributions from adjacent slots is determined by the angle of incidence, $\theta$, of a plane wave front, the distance, $d$, between slot centers, the guide wave length, $\lambda_g$, and the free-space wave length, $\lambda$, of the radiation. The vector sum from the $n$ slots determines a voltage-receiving pattern and is given by equation (1):

$$V = \frac{\sin n\{\pi (d/\lambda)[(\lambda/\lambda_g) - \sin \theta] - (\pi/2)\}}{n \sin\{\pi (d/\lambda)[(\lambda/\lambda_g) - \sin \theta] - (\pi/2)\}}. \tag{1}$$

The maximum in the receiving pattern occurs when the incident wave fronts arrive at an angle given by the formula

$$\sin \theta_1 = \lambda \left(\frac{1}{\lambda_g} - \frac{1}{2d}\right), \tag{2}$$

where $\theta_1$ is the squint angle measured from the normal of the array.

The array, a nonresonant type, operates with the guide wave length different from twice the spacing between slot centers ($\lambda_g \neq 2d$), so that its input impedance will remain nearly constant over a large band width. When operated in the condition such that

[2] H. Gruenberg, "A Waveguide Array for Solar Noise Studies," submitted for publication, *Trans. I.R.E.* (Professional Group on Antennas and Propagation).

FIG. 1.—View of slotted wave guide array for operation on $\lambda = 10.3$ cm. 450 wave length aperture

$\lambda_g = 2d$, the squint angle is zero, and the impedance of each slot adds in phase to produce a large mismatch to the receiver input. At near-by wave lengths, this input impedance rapidly drops to a minimum value and remains relatively constant over a broad band of wave lengths about the design wave length of 10.3 cm. Tests have shown that operating conditions are satisfactory over a total band of wave lengths from 10.0 to 10.9 cm.

The theoretical angle of squint, as calculated by equation (2), varies with wave length. For example,

$$\theta_1 = 9°7' \text{ for } \lambda = 10.0 \text{ cm}, \qquad \theta_1 = 6°57'.5 \text{ for } \lambda = 10.3 \text{ cm},$$

$$\theta_1 = 2°25' \text{ for } \lambda = 10.9 \text{ cm}.$$

These values can be checked by using the sun as an external signal generator. Astronomical considerations give the position of the sun, and, by assuming that the radio and optical disks have the same centers, the actual angle of squint can be measured. The results show that there is an unexpected westerly displacement of the beam by $\frac{1}{4}°$ for all wave lengths. This requires the introduction of a hitherto unknown reactance in the equivalent circuit of the slot collectors.[2] Corrections have been applied to the squint angle for the thermal expansion of the wave guide and for atmospheric refraction at different elevations. The corrections amount to only a few minutes of arc and are of secondary importance, since the accidental errors are of the same magnitude.

In order to obtain the maximum amount of information about the distribution of temperature on the solar disk, the exact variations of the narrow receiving pattern must be known accurately. Since considerable design knowledge exists concerning the slots, some consideration can be given to the theoretical pattern. The shape of the receiving pattern is given by equation (1), which has a maximum value when the incident wave arrives at an angle given by equation (2). A change in wave length progressively alters the phase of each slot contribution, so that the maximum shifts to a new angle without altering the receiving pattern of the array. This feature can be shown readily in a new form of equation (1), which is expressed in terms of an angular increment, $\Delta\theta$, from a reference squint angle, and a frequency increment, $\Delta f$. The more suitable frequency increment replaces a wave-length increment which is measured from the wave length associated with the reference angle. Since the receiver is a power detector, the receiving pattern is expressed as a power pattern and is given by equation (3):

$$P(\Delta\theta, \Delta f) = P_0 \frac{\sin^2 (a\Delta\theta - b\Delta f)}{(a\Delta\theta - b\Delta f)^2}, \tag{3}$$

where $a$ and $b$ are constants containing the reference frequency, squint angle, and array dimensions. For a wave length of 10.3 cm (2920 Mc/sec) and its associated squint angle of 6°57'.5, $a = 1372.5$ per degree, and $b = 35.6$ per megacycle. Expressed in another way, the pattern shifts 0°.026 per megacycle. Since thermal radiations have a continuous spectrum, a band of frequencies will be detected by the receiver, and the effective receiving pattern, $P'(\Delta\theta)$, is found by integration:

$$P'(\Delta\theta) = \int P(\Delta\theta, \Delta f) B(\Delta f)\, d(\Delta f), \tag{4}$$

where $B(\Delta f)$ is the receiver-power band pass centered about the reference frequency, $f_0$. This equation shows that undesirable broadening of the pattern occurs (reduction in antenna gain) with increasing width of the receiver band pass. On the other hand, the average power received from a source with a continuous spectrum increases in proportion to the integrated receiver band width, while the ratio of noise-signal: residual-noise-fluctuations increases as the square root of the band width. For the present case, when the receiver band pass has the form associated with resonant circuits, the optimum half-

power band width is about 4.5 Mc/sec, and the beam width is 0°.168. This represents an increase of 40 per cent from the initial beam-width value of 0°.116. A narrower band pass of 1.5 Mc/sec was found to give sufficient signal from the sun and has been used, with a consequent minimum amount of broadening. The band shape was measured experimentally, and the calculated pattern showed a half-power beam width of 0°.125. The resultant receiving pattern is shown in Figure 3, the indicated points referring to the average value in an interval of 1'.5.

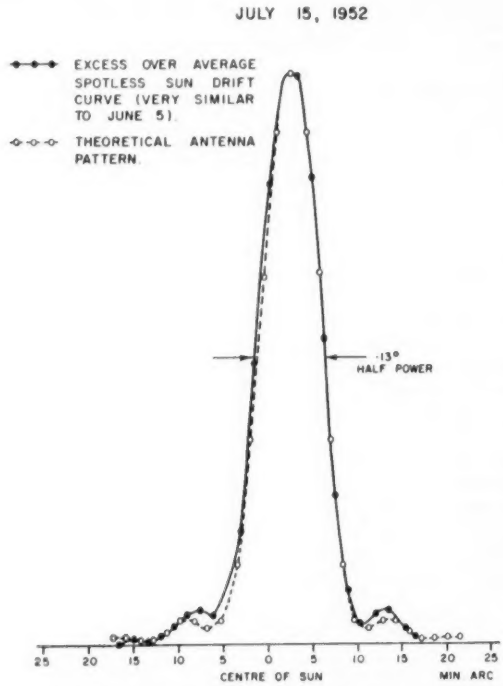
JULY 15, 1952
EXCESS OVER AVERAGE SPOTLESS SUN DRIFT CURVE (VERY SIMILAR TO JUNE 5).
THEORETICAL ANTENNA PATTERN.
.13°
HALF POWER
25 20 15 10 5 0 5 10 15 20 25
CENTRE OF SUN
MIN. ARC

FIG. 3.—Comparison of antenna pattern with radio-spot drift-curves

In normal practice the radiation pattern is checked by transmission of energy at various angles to a receiving point sufficiently far removed that the Fraunhofer pattern is effectively measured. By application of the reciprocity theorem, it may be shown that the receiving pattern is the same as this radiation pattern. For the 150-foot array the receiving point in the far field is about 25 miles distant, and difficulties are encountered in carrying out the tests. The theoretical pattern was partially checked by making use of the radio emission from a certain sunspot region, which was assumed to have an emissive area small in comparison to the theoretical beam width. This interpretation of the size of the emissive regions is based upon eclipse observations, which have shown that the radio emission of certain sunspot regions is confined to areas which are, at most, only twice as large as the optical area.[3]

On July 15, 1952, one suitable spot presented itself, and a comparison between the

[3] A. E. Covington, *Nature*, **159**, 405, 1947.

theoretical and the observed pattern is shown in Figure 3. The radio-spot drift-curve is broader between the half-power points by less than 5 per cent, shows somewhat higher side lobes, and provides an upper limit to the antenna beam width. In the analysis of the results, two antenna patterns have been used; one with the theoretical pattern and another with the theoretical pattern broadened by 5 per cent (see Table 1). The latter provides the better fit to the drift-curve of the assumed point source. The two patterns were used to show how a given error in the antenna pattern would affect the calculated

TABLE 1

ANTENNA PATTERNS

| Curve Number* | Strip Number | | | | | | | | | | | | | | | |
|---|---|---|---|---|---|---|---|---|---|---|---|---|---|---|---|---|
| | 0 | 1 | 2 | 3 | 4 | 5 | 6 | 7 | 8 | 9 | 10 | 11 | 12 | 13 | 14 | 15 |
| 1 | 1.000 | 0.898 | 0.648 | 0.360 | 0.144 | 0.044 | 0.028 | 0.039 | 0.039 | 0.024 | 0.009 | 0.007 | 0.013 | 0.014 | 0.010 | 0 |
| 2 | 1.000 | 0.912 | 0.676 | 0.400 | 0.180 | 0.060 | 0.027 | 0.035 | 0.042 | 0.032 | 0.015 | 0.007 | 0.008 | 0.014 | 0.014 | 0.008 |

* Curve No. 1 = theoretical pattern for an observed I-F band pass of 1.5 Mc/sec; curve No. 2 = above pattern broadened 5 per cent at the half-power point; and strip width = 1.'5.

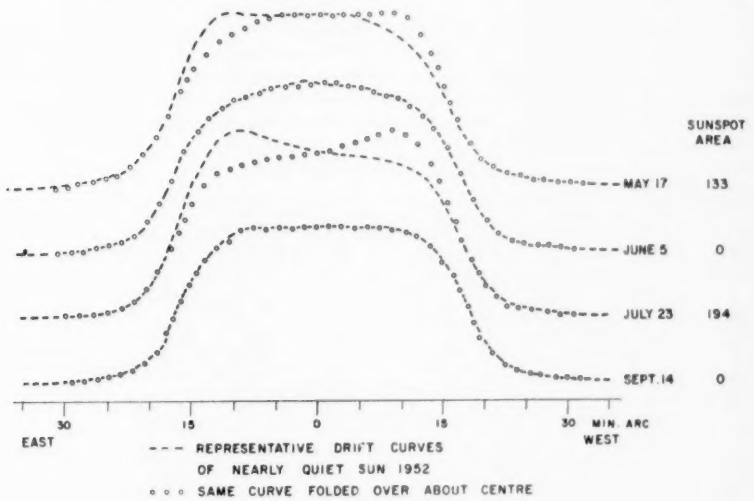


FIG. 4.—Selected solar drift-curves

solar brightness. In interpreting the results, preference was given to the broader antenna pattern, which has a half-power beam width of 0°.130. In order to find the radio-spot emission, the total emission on July 15 was referred to the spotless sun, which occurred on June 5, 1952 (see Fig. 4). This curve is very similar to an average curve, which will be discussed later.

The antenna pattern in the north-south direction is broad and is determined by the narrow opening of the horn. The particular size was determined by convenience, and the radiation pattern has been found experimentally to have a half-power width of 22°.5.

The amount of power actually radiated (or received) by an antenna in the direction of the maximum of its pattern ($p_{max}$) can be compared to the average value of the total

power radiated by the same antenna. This ratio is called the directive gain, $G_0$, and is given by the equation

$$G_0 = \frac{p_{\max}}{(1/4\pi)\int p(\theta, \phi)\, d\omega} = \frac{4\pi}{\int g(\theta, \phi)\, d\omega}, \tag{5}$$

where $g(\theta, \phi)$ is the normalized gain with a peak value of unity and $d\omega$ is an element of solid angle. The inclusion of ohmic losses in the antenna reduces this maximum to a lower value. The gain measured at the input to the antenna includes these losses and is called the "effective gain." The normalized pattern has been measured, and the evaluation of the integral leads to a measure of the directive gain.

For a fan-shaped beam, where one dimension is much narrower than the other, the gain function, $g(\theta, \phi)$, can be separated into two functions: $g_1(\phi)$ in the north-south direction and $g_2(\theta)$ in the east-west direction. The gain function, $g_2(\theta)$, is the normalized value of equation (3) or equation (4), as the case may be. The integration of these two functions gives a measure of the angular openings, $\Phi$ and $\Theta$, of an equivalent beam with uniform gain. Thus

$$G_0 = \frac{4\pi}{\int g_1(\phi)\, d\phi \int g_2(\theta)\, d\theta} = \frac{4\pi}{\Phi\Theta}. \tag{6}$$

In the case of the long array, $\Phi$ is the beam width in the north-south direction and equals 0.393 radians (or 22°.5); $\Theta$ is the beam width in the east-west direction and equals 0.00256 radians (or 0°.130); and $G_0$ is the maximum antenna gain and equals 12,500. The antenna gains measured in this manner may be higher than the actual value, since there may be undetected lobes of the pattern away from the main beam.

## ANTENNA CONSTRUCTION

The fundamental structure for supporting the radiotelescope is an iron shaft which rotates in forty-six bearings firmly fastened to a concrete pier. This pier is reinforced with iron and provides the necessary strength and rigidity for the array. It is 14 inches thick, 160 feet long, and extends below the surface of the ground to the underlying bedrock, which is about 2 feet below the surface. Provision was made so that each of the bearings could be adjusted and placed in a level and straight line by sighting through a transit. Forty-six castings are positioned on the iron shaft, spaced every 40 inches, and placed opposite a bearing. These castings have two arms projecting radially outward in the form of a **V**, with the sides meeting at 60°. Sheets of metal are fastened between these arms, so that a trough is formed, somewhat longer than the slotted length of the wave guide.

The 150-foot length of brass wave guide is a standard rectangular guide of 3 × 1.5 inches in outside dimensions and 0.080 inches in wall thickness, and is composed of 10-foot sections which were selected for uniformity of cross-section. The individual lengths of the wave guide have 33 slots cut into the broad side and are soldered together, so that one continuous length is produced. This is placed in the bottom of the trough, with the broad side facing outward, and is seated in rectangular grooves which were milled in the castings. Clips hold the wave guide in place. The receiver end of the wave guide is firmly fastened to three castings, while the remaining part is free to slide through the grooves. This allows for differential thermal expansion between the horn and the wave guide. In Ottawa, where the temperature ranges from +90° to −20° F, a mean variation in guide length of 1.5 inches has been recorded. This has no harmful effect on the radiation pattern and merely alters the squint angle by 4′. The whole horn assembly can be rotated and held at any elevation by a system of chains connected to sixteen of the castings, which have been provided with a special track. The chains are operated together by a worm-gear mechanism located in the receiver house.

### RECEIVER

The receiver and associated power supplies are placed in a small building located at the end of the array. A stable superheterodyne receiver[4] has been used as a detector of radio noise without employing the high-speed switching between antenna and reference resistance that was introduced by Dicke. This type of receiver has the advantage of utilizing all the energy collected by the antenna, as well as being simple and easily attached to the movable horn. The long-term stability is not so great as in the comparison system, but it has been found to be sufficient for observing the two transits of the sun, which are separated by about 6 minutes of time. These transits correspond to receiving energy in two different beams with squint angles corresponding to two different frequencies. These are the upper and lower side bands of the superheterodyne receiver, which are separated by twice the frequency of the intermediate-frequency amplifier. In this case the separation is 60 Mc/sec, and the beams are separated by an angle of 1°.5.

The superheterodyne receiver is composed of a local oscillator, a broad-band crystal mixer, an intermediate-frequency amplifier, a second detector, and a direct-current amplifier. The local oscillator power is produced by a reflex klystron and is injected into the wave-guide mixer by means of a directional coupler. A portion of the local oscillator power is fed to a high-$Q$ resonant cavity ($Q = 4000$). Before each transit the frequency of the local oscillator is manually adjusted for maximum output current from the resonant cavity, which is tuned to a frequency of 2950 Mc/sec or a wave length of 10.16 cm. The stability of the klystron is such that the frequency is maintained to within $\pm 0.1$ Mc/sec for periods exceeding that required for a transit. The intermediate-frequency amplifier has a band pass of 1.5 Mc/sec and operates on a center frequency of 30 Mc/sec. The constancy of these two frequencies determines the constancy of the squint angle. Both the local oscillator and the intermediate-frequency amplifier derive their voltages from well-regulated B+ power supplies, which are supplied with well-regulated 110 volts a.c. In addition, the intermediate-frequency amplifier has been provided with a network to compensate for any changes in mutual conductance due to residual heater voltage changes. The noise generated in the receiver is one hundred times greater than the desired signal, and consequently the voltage output of the second detector is predominantly related to the receiver noise. The average value of the receiver noise is represented by the direct-current component and can be canceled out by applying a voltage equal in magnitude but of opposite polarity. This is derived from a regulated voltage source, which is placed in series with the diode load. The signal appears as a differential d.c. voltage and is further amplified by a d.c. amplifier. The low-frequency component of the receiver noise is always present and can be reduced to a certain value by employing a long time-constant response in the recorder or d.c. amplifier. The over-all time response has been set to about 1 second.

### ANTENNA RADIATION RESISTANCE AND ITS TEMPERATURE

The radio receiver has sufficient sensitivity to detect the thermal noise voltages generated in any resistance which is connected to its input. The magnitude of the open-circuit r.m.s. voltage and the absolute temperature of the resistor are related by Nyquist's formula,[5]

$$\overline{V^2} = 4kTR\Delta f \,, \tag{7}$$

where $\overline{V^2}$ is the mean-square noise voltage; $k$ is Boltzmann's constant and equals $1.37 \times 10^{-23}$ watts/° K; $T$ is the absolute temperature of the resistor; $R$ is the resistance in ohms; and $\Delta f$ is the band width in cycles per second. The maximum power one is able to transfer from this resistance to the receiver occurs when the antenna radiation resistance is

[4] N. W. Broten, *Proc. I.R.E.*, **40**, 834, 1952.

[5] *Phys. Rev.*, **32**, 110, 1928.

matched to the receiver input resistance. This power is called the "available power" and is equal to $kT\Delta f$. Because of this ability to detect thermal radiation, the receiver is sometimes called a "radiometer," and the output current is measured in terms of power ($kT\Delta f$), or in equivalent units of temperature, $T$. The sensitivity can be found readily in an absolute manner by noting the output current and the temperature of the input resistor after the latter is heated to various values. In all measurements involving the substitution of various resistors for the antenna, it is necessary to maintain the match in order to have the same power transfer.

When the antenna is connected to the receiver, two resistances are placed in the input circuit—one representing the ohmic losses in the antenna system and the other representing the radiation resistance of the antenna. The latter takes account of the fact that the antenna will radiate an electromagnetic wave if suitable power is applied to its terminals; or, conversely, it will generate a voltage across its terminals when excited by incident radiation. The ohmic resistance of the antenna not only reduces the received power but also emits a thermal noise power associated with its temperature. The effective temperature of these two resistances, as measured by the radiometer, is given by the equation

$$T_e = (1 - a)\, T_1 + aT_2 , \tag{8}$$

where $a$ is the fractional ohmic losses in the antenna system, $T_1$ is the temperature of the antenna radiation resistance, and $T_2$ is the temperature of the ohmic losses.

The thermal voltages induced in the antenna from an external source may be said to originate in the radiation resistance of the antenna, whereby it assumes a temperature given by the general equation[6]

$$T_1 = \frac{1}{4\pi} G_0 \int t(\theta, \phi)\; g(\theta, \phi)\; d\omega , \tag{9}$$

where $T_1$ is the temperature of the antenna radiation resistance; $t(\theta, \phi)$ is the temperature distribution of a distant object in directions $\theta$ and $\phi$; $G_0$ is the maximum antenna gain; $g(\theta, \phi)$ is the normalized antenna gain in directions $\theta$ and $\phi$; and $d\omega$ is the element of the solid angle. Nonthermal sources can be given an equivalent temperature at a particular wave length, and the manner of the treatment will be the same.

The solution of this equation is determined by the ratio of the angular size of the distant source in relation to the angular dimensions of the antenna receiving pattern. Three cases of particular interest will be discussed.

1. If a source with uniform temperature distribution completely fills the antenna pattern, the temperature of the radiation resistance becomes equal to the temperature of the source. This follows from equations (9) and (5). Thus if

$$t(\theta, \phi) = t , \qquad T_1 = t . \tag{10}$$

This condition is fulfilled when the long array or the 4-foot reflector points toward the "empty" sky, which has a uniform temperature very close to absolute zero at these wave lengths. The condition is also fulfilled during the calibration of the 4-foot reflector when the dipole at the focus is placed in a "radio black box" which is at ambient temperature.

2. If the angular size of the source is much smaller than the antenna pattern, as is the case for the 4-foot reflector pointing toward the sun or the long array pointing toward certain radio-emissive regions, the gain function, $g(\theta, \phi)$, is relatively constant over the source and is equal to unity. Thus the temperature of the radiation resistance reaches a value given by

$$T_1 = \frac{G_0}{4\pi} \int t(\theta, \phi)\, d\omega . \tag{11}$$

[6] R. E. Burgess, *Proc. Phys. Soc. London*, **53**, 293, 1941.

The drift-curve resulting from a rotation of the earth with the antenna fixed in position is obviously the radiation pattern in a particular direction with a maximum value given by equation (11).

The magnitude of the radiation can also be expressed as a flux density in units of watts/meter$^2$/cps band width. This is deduced from the antenna temperature, from the power available according to Nyquist's theorem, and from a knowledge of the effective area, $A$, of the antenna given by

$$A = \frac{G_0 \lambda^2}{4\pi}.$$

Thus the flux density equals

$$\frac{kT_1 \Delta f}{A \Delta f} = \frac{k}{\lambda^2} \int t(\theta, \phi)\, d\omega \text{ watts/meter}^2\text{/cps}. \tag{12}$$

The customary factor 2 has been omitted from this equation, since the antenna accepts only one polarization of the radiation.

3. The third case arises when the angular size of the source is greater than the beam width of the antenna pattern. Detailed information will be obtained only when the antenna is directed to different parts of the object. Scanning an object produces a variation of the radiation-resistance temperature, and a new integral equation can be derived which will take this into account. When the long array scans the sun in the $\chi$-direction (i.e., the east-west direction), the gain variation, $g(\phi)$, in the north-south direction can be set to unity over the half-degree solar disk since the radiation pattern in that direction is 22°.5. With these modifications, the temperature of the radiation resistance for a given $\chi$ is given by

$$T_1(\chi) = \frac{G_0}{4\pi} \int\int t(\chi + \theta, \psi + \phi)\, g(\theta)\, d\theta d\phi, \tag{13}$$

where $\chi$ and $\psi$ are position angles of the maximum of the antenna pattern referred to the center of the sun; $\theta$ and $\phi$ are variables about the maximum of the antenna pattern; and $t(\chi + \theta, \psi + \phi)$ is the temperature of an element at the indicated angular positions.

Integration of equation (13) with respect to $d\chi$ produces another equation which contains, among other factors, the integral of temperature $\times$ angle on the right-hand side. This latter integral is also given by equation (11) and is determined experimentally when one measures the temperature of the radiation resistance and the gain of the 4-foot reflector. Elimination of this integral results in a relationship between the observable quantities for the two antennae:

$$\int T_1(\chi)\, d\chi = G_0 \Theta \frac{T_1'}{G_0'}, \tag{14}$$

where $T_1'$ is the temperature of the radiation resistance of the 4-foot reflector; $G_0'$ is the gain of the 4-foot reflector; $G_0$ is the gain of the long array; and $\Theta$ is the equivalent beam width of the long array in the east-west direction. The various expressions for $T_1$, $T(\chi)$, and $\int T(\chi) d(\chi)$ can be read from the drift-curve only after the ohmic emission and loss have been considered according to equation (8).

In reading a drift-curve it is very convenient to refer th amplitude of the drift-curve at any given point to the base line which extends to either side. This base line represents the receiver output when the antenna is pointing toward the empty sky, where $T_1 = t_{sky}$. Operationally, it represents zero or near-zero output in the recording meter. This value is obtained by adjusting the "bucking-out" voltage to equal the receiver-noise output when the sun is not in view. When the sun is in the radiation pattern, the signal

causes the output meter to register a new level. The difference in effective temperatures between this new level and the base line will be given by the equation

$$\Delta T_e(\chi) = (1-a)[T_3(\chi) - T_4(\chi)], \tag{15}$$

where $T_3(\chi)$ is the temperature of the radiation resistance of the long array when looking at the sun and sky, and $T_4(\chi)$ is the temperature of the radiation resistance of the long array when looking at the sky. In this form the emission from the ohmic losses ($aT_2$) does not appear because it is a constant present in both levels. The quantity $T_4(\chi)$ represents the emission from the sky and can be separated approximately into two parts, one part from a disk the same size as the radio sun and a second part from the remaining portions of the sky covered by the antenna pattern. The second part does not need to be determined when the difference is found between the two integrals. Other observations[7] have shown that the sky has an equivalent temperature of 8° K, so that the integration of this amount over the equivalent disk produces a small quantity in comparison to the same integration of the high-temperature radio sun. These considerations lead to the neglect of $T_4(\chi)$; hence from equations (13) and (15) the final equation for solution may be written

$$\Delta T_e(\chi) = (1-a)\frac{G_0}{4\pi}\int t(\chi+\theta, \psi+\phi)\, G(\theta)\, d\theta d\phi . \tag{16}$$

Before attempting a solution for the unknown temperature distribution across the sun, the radiometer must be calibrated to find $\Delta T_e$, and $(1-a)$—the fraction of energy reaching the radiometer—must also be found. Estimates of the gain of the antenna ($G_0$) have already been made.

The output of the radiometer, $\Delta T_e$, can be compared to the radio noise from a fluorescent lamp which is injected into the wave guide by means of a directional coupler. This reference signal has been calibrated and contains both upper and lower side bands of noise, acting simultaneously. In the drift-curves, the side-band responses are separated in time, and sometimes a difference in the amplitudes of the two transits appears. This has been attributed to matching problems which are primarily in the mixer. In making a comparison with the test signal, this matching problem can be minimized by using the total deflection of the two transits. The calibration of the fluorescent lamp and directional coupler can be made without changing the matching conditions, if the same superheterodyne receiver is used in the calibration of the noise sources as is used to obtain the drift-curve. The amplitude of a test signal of 200° C is comparable to the amplitude of the quiet-sun drift-curve at the center. The residual fluctuations of the radiometer are of the order of 5° C.

The fraction of energy ($a$) dissipated in the ohmic losses is not known accurately and appears somewhat variable, owing to changing losses in the wave-guide slot-covering during rainy periods, when drops of water collect on the covers. From comparison with dry periods, dampness appears to cause only a loss in gain and does not affect the directivity of the antenna. Estimates indicate that the losses are about 35 per cent in fair weather. This includes a 10 per cent loss in a resistance which terminates the far end of the wave guide.

Because of the uncertainty in the ohmic losses, this calibration is used only for coarse adjustment of the radiometer sensitivity. It may be used, however, to find the effective antenna gain $(1-a)G_0$, once the absolute solar flux is known from other measurements. Calculations based either upon equation (14), modified to include ohmic losses, or upon equation (16), after the temperature distribution across the sun has been found, give an effective antenna gain of 7300. A critical analysis of the results involving the directive gain and the ohmic losses is given elsewhere.[2]

[7] A. E. Covington and W. J. Medd, unpublished results on absolute measurement of solar flux.

Another estimate of the ohmic losses was made from a measurement of $T_1$ when the antenna points to the sky. The absolute determination of $T_1$ now involves a source external to the fluorescent lamp and is readily provided by inserting a wave-guide attenuator at ambient temperature between the antenna and the radiometer. Unfortunately, small differences in match between the wave-guide antenna and attenuator introduce a large error signal.

Because of the difficulties in obtaining the absolute values of $\alpha$ and $G_0$, the amplitudes of the daily drift-curves were normalized with respect to the daily temperatures of the antenna radiation resistance of the 4-foot reflector, according to equation (14), modified to include ohmic losses. The gain of the radiometer need not be determined, since it can be included in the constant of proportionality. Thus each daily drift-curve is compared to a standard drift-curve by the use of a scale factor based upon the proportionality of area and temperature. The errors in temperature measurement of the 4-foot radiotelescope are now reflected into the drift-curve. The accidental errors are believed to be about $\pm 2.5$ per cent for a single reading.

## OBSERVATIONAL DATA

The long array and radiometer were put into regular operation in October, 1951, and, except for a few unavoidable interruptions, have been in continuous service since. By the end of 1952, there were 270 daily records available. Each record consists of the two transits corresponding to the upper and lower side bands of the radiometer with the local oscillator operated on $\lambda = 10.16$ cm and is made on an Esterline-Angus recording meter with a time scale of 1.5 inches per minute. In order to relate the transits of the radio sun and the optical sun, time signals from the Dominion Observatory are recorded on the margin of the chart by an additional pen.

For convenience in handling the data, the drift-curve time scale is divided into intervals corresponding to 1.5 (6 seconds time). This is done by means of a set of curves which automatically apply two corrections, so that the same time scale will apply to all the curves. The first correction is for the varying angular rate of motion of the sun due to its declination north or south of the equator, and the second is to place the sun at the unit astronomical distance. The average ordinate of each interval of the drift-curve is read off with reference to the sky level on either side of the sun. The sum of these ordinates gives the daily area under the drift-curve, which is adjusted with reference to the daily radio flux as measured by the 4-foot reflector. When adjusted in this manner, the difference between the first and second transits was negligible in all cases of the spotless sun, and two drift-curves were averaged sometimes, in order to reduce possible errors.

These values of daily radio-flux density are not identical with those reported to the *Quarterly Bulletin on Solar Activity*. They have been modified by a correction placing the sun at unit astronomical distance and also by a new determination of the sky temperature in which 8° K replaces the original determination of 50° K. The gain of the 4-foot reflector has been remeasured[7] at $\lambda = 10.7$ cm and shows good agreement with the value of 700 originally obtained.

Two components of solar radio emission have been identified from eclipse records and from the analysis of the daily flux-density readings obtained from the 4-foot reflector. One is a constant emission from the background of the whole disk, and the other is a slowly varying emission from certain regions containing sunspots. (A third component—bursts of solar noise—has not been observed with the long array and will not be discussed.) Both components can be recognized in the drift-curves; but, because of the relatively poor resolving power, the identification is best made at certain times when emphasis is placed upon one or the other component. The emission from the background, or the "quiet"-sun emission, is best seen when there is no solar activity, while the radio sunspot emission is necessarily superimposed upon the disk emission and is easily recognized when a very strongly emitting radio spot is present. These two components of solar radio

noise will be studied separately after a method of selecting suitable drift-curves for the quiet sun has been devised.

Since both components of solar noise are measured simultaneously with the 4-foot reflector, it is reasonable to regard days of minimum radio flux as days with a minimum number of radio sunspots and as most suitable for investigating the brightness distribution of the radio disk. The selected days should also be spotless. In general, these two criteria—minimum daily flux and zero sunspot area—will be somewhat related, since a correlation coefficient of 0.85 has been found between the radio-flux variations and the sunspot area. Both have been used to find drift-curves suitable for studying the quiet sun, and only 4 suitable days were found in the previously mentioned period of 270 days.

During the same period, additional data about the quiet sun can be found from other considerations which are not so exclusive as those already considered. On certain days

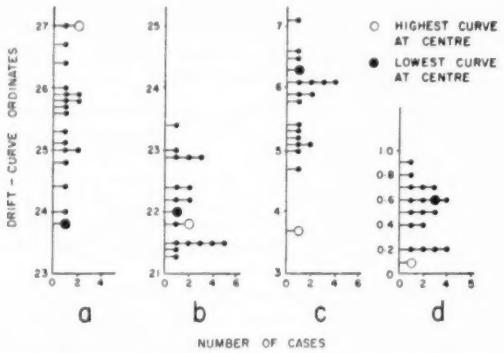


FIG. 5.—Distribution of drift-curve ordinates from the center of the radio sun: *a*, 0′; *b*, 12′; *c*, 19′.5; *d*, 27′, respectively.

it is possible to find sunspot activity on half the disk, while the remaining half is free from activity and thus presents an undisturbed surface. If the squint angle were known exactly, then from tabulated positions of the sun it would be possible to find the center of the drift-curve and so use half of it in a study of the quiet sun. However, the squint angle is evaluated from the same curves, and consequently the center of the radio sun was found by using the center of the drift-curve with respect to its base. This required a check to insure that radio and optical spots were one-quarter of the solar diameter from the eastern and western limbs. By selecting solar disks with activity on one side only, fifteen additional curves were obtained.

Four typical drift-curves are shown in Figure 4. The dashed curve refers to the observed drift-curve, while the curve shown by the open circles refers to the same drift-curve reflected about its center. The emission from the radio sunspots on May 17 and July 23 appears as a separation of the lines. Drift-curves on June 5 and September 14 occurred when the optical sunspot area was zero and the daily flux was very close to the yearly minimum. Comparison of the original and reflected curves shows that the two curves fall upon each other and indicate the apparent absence of a radio spot. However, the curves for the two days are slightly different in shape; the curve for June 5 has a rounded center, while the curve for September 14 has square shoulders. It may be reasonable to assume that the curves differ in shape on these days of zero sunspot area because of broad radio-emitting areas, whose emission cannot be subtracted from the curves by the above reflection method. The chronological order of the curves shown in

Figure 4 and the apparent degree of limb brightening, as shown by the squareness of the shoulders, do not bear any relationship to each other, in view of the observation that the drift-curve of June 8 is almost identical to that of September 14 and the curve for September 11 is very similar in shape to the curve for June 5.

When these methods were used for the selection of curves which would give the basic emission from the spotless sun, nineteen curves were found; they are representative of six solar-rotation periods. These curves are very similar in form and amplitude, and their relationships are best displayed by showing the distribution of the half-curves at various distances from the center (see Fig. 5). The two curves that have the highest and lowest values at the center are identified by solid and open circles, respectively. The errors due to reading the records are relatively small in comparison to the error of normalization, which is directly related to the accidental errors in the calibration of the 4-foot reflector.

TABLE 2

DRIFT-CURVES FROM QUIET-SUN ANALYSIS

| Curve Number* | Strip Number | | | | | | | | | | | |
|---|---|---|---|---|---|---|---|---|---|---|---|---|
| | 0 | 1 | 2 | 3 | 4 | 5 | 6 | 7 | 8 | 9 | 10 | 11 |
| 1 | 25.54 | 25.53 | 25.44 | 25.28 | 25.04 | 24.67 | 24.17 | 23.40 | 22.11 | 20.11 | 16.99 | 13.08 |
| 2 | 24.40 | 24.40 | 24.34 | 24.24 | 24.10 | 23.82 | 23.34 | 22.74 | 21.44 | 19.16 | 15.88 | 11.90 |

| Curve Number | Strip Number | | | | | | | | | | |
|---|---|---|---|---|---|---|---|---|---|---|---|
| | 12 | 13 | 14 | 15 | 16 | 17 | 18 | 19 | 20 | 21 | 22 |
| 1 | 9.08 | 5.68 | 3.17 | 1.84 | 1.12 | 0.77 | 0.50 | 0.30 | 0.20 | 0.10 | 0 |
| 2 | 8.10 | 4.72 | 2.32 | 1.32 | 0.76 | 0.42 | 0.18 | 0.10 | 0 | 0 | 0 |

* Curve No. 1 = average drift-curve, average from 19 drift-curves; curve No. 2 = lower envelope drift-curve, average of 5 lowest points; and strip width = 1.°5.

A composite quiet-sun drift-curve, consisting of the lowest regions which appeared on different days and at different distances from the center, can be found from the lower envelope to the distributions shown at each abscissa. If only the lowest points are considered, too much weight is given to the accidental calibration error. In order to reduce this error, the average of the five lowest points at each abscissa was found and was taken as the lower envelope drift-curve. This is shown in Table 2. In addition, the average drift-curve was found from the nineteen drift-curves and is also shown in this table.

### ANALYSIS FOR BRIGHTNESS VARIATION ACROSS THE SOLAR DISK

Without knowing the values of $\alpha$ and $G_0$, only the relative distribution of temperature can be found by solving the integral equation (16). The method of scanning the solar surface with a fan-shaped beam gives no information about the temperature distribution in the other direction, so that the equation can be solved only by assuming definite distributions in the directions at various angles to the scan. In the present case the unknown distributions were assumed to have radial symmetry about the center of the disk.

The solution of the integral equation was effected by replacing it with a set of linear

equations with 13 unknown variables and by solving the resulting set. This representation is based upon a geometrical construction, in which the solar field was divided into 13 rings, with an angular width of 1.'5 and centered on the solar disk. To each ring was assigned an unknown temperature. Correspondingly, the antenna pattern was divided into strips 1.'5 wide, and the relative gain was found for each strip. With this geometrical pattern as a basis, a set of coefficients can be calculated for the set of linear equations. The temperature on the fourteenth ring was made zero and serves as a boundary condition that satisfactorily includes all the information on the drift-curve.

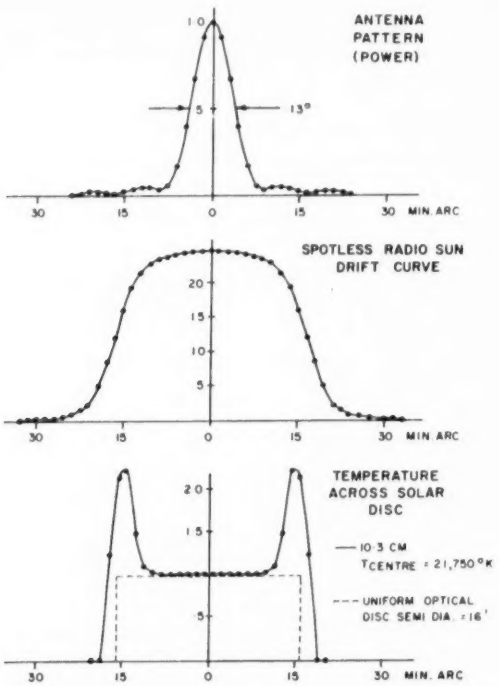


FIG. 6

A graphical representation of the antenna pattern with a beam width of 0.°130, the lower envelope drift-curve, and the solution of the integral equation are shown in Figure 6. In this figure each point represents the average value of the function in a ring or strip with a width of 1.'5. Numerical values for this and three other cases are shown in Tables 1, 2, and 3. The four solutions have been calculated in order to show the effect of possible known errors in both the drift-curve and the antenna pattern. The solutions represent all the combinations of two drift-curves (one found from the average of all the points and the other consisting of the mean of the five lowest points), together with two antenna patterns (the theoretical and the same pattern broadened by 5 per cent). All these solutions are similar and show the effect of systematic errors. Case No. 2 of Table 3 is the preferred solution, since it is based upon the best approximation to the quiet sun (lower

envelope–curve) and uses the broadened antenna pattern which is based upon the spot drift-curve of July 15, 1952. The sought-for distribution of radio brightness across the spotless sun exhibits a brightening to the limb with a maximum value of twice that of the center. This ring exists just at the limb of the photospheric disk, and the radius of the radio sun is 1.15 times that of the optical disk.

TABLE 3

TEMPERATURE DISTRIBUTION OF THE QUIET SUN

| Case Number | Ring Number | | | | | | | | | | | | |
|---|---|---|---|---|---|---|---|---|---|---|---|---|---|
| | 1 | 2 | 3 | 4 | 5 | 6 | 7 | 8 | 9 | 10 | 11 | 12 | 13 |
| 1 | 1.00 | 1.00 | 1.00 | 1.01 | 1.02 | 1.03 | 1.04 | 1.11 | 1.41 | 2.11 | 2.06 | 1.41 | 0 |
| 2 | 1.00 | 1.00 | 1.00 | 1.01 | 1.01 | 1.01 | 1.01 | 1.07 | 1.52 | 2.23 | 2.44 | 0.95 | 0 |
| 3 | 1.00 | 1.00 | 1.01 | 1.02 | 1.02 | 1.03 | 1.04 | 1.05 | 1.23 | 1.95 | 2.17 | 1.71 | 0 |
| 4 | 1.00 | 1.00 | 1.00 | 1.00 | 1.00 | 1.00 | 1.00 | 1.00 | 1.28 | 1.99 | 2.16 | 1.66 | 0 |
| 5 | 1.00 | 1.00 | 1.01 | 1.02 | 1.04 | 1.07 | 1.11 | 1.16 | 1.25 | 1.42 | 2.12 | 1.54 | 0.30 |

| Case No. | $T_{center}$ °K | $2\int xI(x)dx$ | Fraction Uneclipsed | Per Cent Error of Area |
|---|---|---|---|---|
| 1 | 21,800 | 1.82 | 0.23 | 1.48 |
| 2 | 21,800 | 1.82 | .19 | 1.61 |
| 3 | 22,800 | 1.84 | .26 | 1.33 |
| 4 | 23,000 | 1.82 | .25 | 1.26 |
| 5 | 24,500 | 1.80 | 0.28 | |

Case No.

1. . . Theoretical antenna pattern with drift-curve of lowest 5 points
2. . . Broadened antenna pattern with drift-curve of lowest 5 points
3. . . Theoretical antenna pattern with average drift-curve
4. . . Broadened antenna pattern with average drift-curve
5. . . Theoretical temperature distribution derived from Hagen's results

The solution to the set of equations was found by successive approximations, in which the error between the observed curve and a reconstructed curve was successively reduced by adjusting the temperature of a single ring. This method makes use of Seidel's approximation to the least-squares solution[8] and involves the use of the normal equations. The minimum value of the sum of the errors squared is given by the least-squares solution and was approached in a series of approximations. This process was stopped when the resulting deviations of the reconstructed, from the observed, curve were of the order of the accidental error in the drift-curves. When closer approximations are made, the temperatures of the rings are adjusted according to the accidental errors in the drift-curves. Furthermore, in the approximation, adjacent values of temperature were adjusted simultaneously in such a manner that the over-all curve was smooth without any large fluctuation of temperature between adjacent rings.

The degree of approximation of a solution is indicated by the area inclosed between the observed and the reconstructed drift-curves, which may be expressed as a percentage of the area under the observed curve. These percentage areas are shown in Table 3. The

[8] E. T. Whittaker and G. Robinson, *The Calculus of Observations* (London: Blackie & Son, Ltd., 1944), p. 255.

reconstructed curve varies positively and negatively about the observed curve, and there are several crossing points. These variations are of the same magnitude as the accidental errors which are believed to be about $\pm\frac{1}{4}$ of the central difference between the average and the lower envelope drift-curves.

Since the rings are a small fraction of the beam width, it is possible to introduce a certain type of fluctuation of temperature into the solution with negligible change in the over-all error. This is done by simultaneously increasing the temperature of one ring and decreasing the temperature of an adjacent ring by a corresponding amount. The error introduced by one change is largely canceled by the second change. It is thus possible to sharpen the peak or to introduce a temperature into the thirteenth ring by making such changes. The magnitude can be as much as 30 per cent before the deviations are comparable to the accidental errors. A similar increase in the error is introduced by adding only 10 per cent to the peak or to the outer ring. These alternative distributions produced by a reciprocal change of temperature or by a single increase in the outer ring contain certain features that are too fine to be resolved within the attainable accuracy of measurement. They should be regarded as possibilities most easily resolved by using a larger antenna. The position of a point source can be located to an accuracy that is a small fraction of the beam width of the antenna pattern. Thus the small fractional intervals of 1.5 were used as a unit of angle in order to locate the antenna pattern with respect to the center of the sun. It has also enabled the shape of the radiation pattern to be used in the analysis.

## TEMPERATURE AT THE CENTER OF DISC

The magnitude of the temperature at the center of the radio disk can be calculated by means of equation (11) from the relative brightness of the disk and from the total radiation measured by the 4-foot reflector. The introduction of a radial temperature distribution, $t(x)$, allows equation (11) to be written in the following form:

$$T_1' = \frac{G_0'}{4\pi}(\pi R_0^2)\, t_c 2\int x t(x)\, dx\,, \tag{17}$$

where $R_0$ is the radius of the photospheric disk and is 16′; $x$ is an angular variable measured in terms of $R_0$; $T_1'$ is the temperature of the radiation resistance of the 4-foot reflector; $t_c$ is the temperature at the center of the radio disk; and $G_0'$ is the gain of the 4-foot reflector. The integral $2\int x\, t(x)\, dx$ is the ratio of the integrated flux from the radio disk to the flux from a disk at uniform temperature which has the same size as the photosphere. The values of these integrals are shown in Table 3. The observations with the long array have been made with the local oscillator set to a wave length of 10.16 cm, while the readings with the 4-foot reflector have been taken with the local oscillator set at 10.7 cm. Some studies of the solar spectrum in this region would indicate that the antenna temperature of the 4-foot reflector is essentially the same at 10.16 as at 10.7 cm. The antenna gain, however, is increased from that measured at 10.7 cm, since it varies inversely as $\lambda^2$. A value of 755 has been calculated for its operation at 10.3 cm, which is the wave length of the side band used for most of the present observations. The temperature of the radiation resistance of the 4-foot reflector, associated with the lower envelope drift-curve, is 161° K (24.4 arbitrary divisions at the center of the drift-curve). Using these values and the preferred brightness distribution, the temperature at the center of the sun can be calculated from equation (17). A value of 21,800° K has been obtained. Central temperatures for the other three solutions are shown in Table 3.

## COMPARISON WITH A MODEL OF THE SOLAR ATMOSPHERE

The existence of a bright ring on the radio disk at decimeter wave lengths was realized from theoretical considerations[9] after experiments had shown that the sun had an equiva-

[9] D. F. Martyn, *Nature*, **158**, 632, 1946.

lent temperature of $10^{6}$° K in the meter wave-length band. This brightening arises from the greater thickness of the bright coronal layers when viewed at the limb. All theoretical studies have been based upon thermal emission from the electron gas in the solar atmosphere; but, in arriving at the brightening to the limb, various details of the problem are treated differently,[10, 11] so there may be minor differences in the results. In order to make a comparison with theory, a brightening to the limb has been obtained from the work of Hagen.[11] The curve of limb brightening (for a wave length of 10.6 cm) is shown in

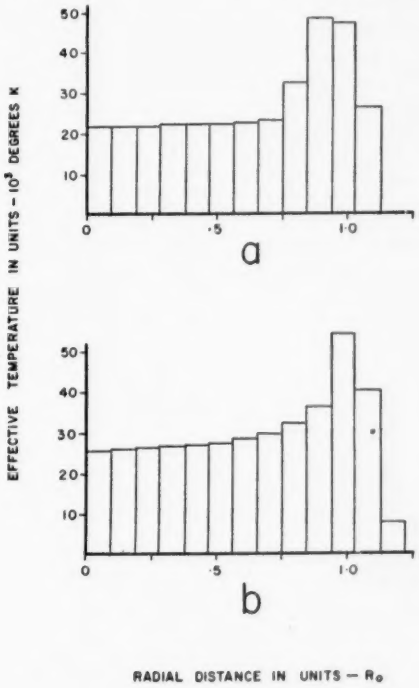


FIG. 7.—Brightness distribution across the solar disk in intervals of 1′.5: *a*, observed at 10.3 cm; *b*, calculated according to Hagen's model, 10.6 cm.

Figure 7. The average value of temperature in rings 1′.5 wide has been shown in order to allow a comparison with the observed results, which are shown on the same basis. The averaging of a temperature over 1′.5 greatly reduces the peak value of the bright ring seen just at the limb of the optical disk. Without averaging, the ratio of peak-to-center temperature is 3.8:1, while after averaging the ratio is 2.1:1.

An inspection of the observed and the theoretical curves shows good agreement (Fig. 7). The observed central temperatures at 10.3 cm lie within the range 21,800°–23,000° K, while the calculated temperature at 10.6 cm is 26,000° K. There is brightening to the limb; the observed ratio of peak temperature to center temperature lies between 2.1 and 2.6, while the calculated ratio is 2.1.

A detailed comparison between the observed and theoretical curves can be made on

[10] S. F. Smerd, *Australian J. Sci. Res.*, *A*, **3**, 34, 1950.

[11] J. P. Hagen, *Ap. J.*, **113**, 547, 1951.

two independent grounds, one based upon the magnitude of the temperature at the center and the other based upon the relative shape of the curves. The errors in the absolute temperature measurement are directly related to the errors of measurement involved in the 4-foot reflector and are known to be of the order of $\pm 5$ per cent. In the preferred solution the central temperature of 21,800° K is about 15 per cent lower than the theoretical value of 24,500° K. This latter value is the modified central temperature for comparison at a wave length of 10.3 cm. The central temperature of 23,000° K, given by the average drift-curve (case No. 4), shows better agreement and differs from the theoretical value by only 6 per cent.

The relative temperature distributions can be compared by constructing a drift-curve from the theoretical distribution and then adjusting the area under this curve to equal that of the observed drift-curve. The percentage area inclosed between the theoretical drift-curve constructed by using the broadened antenna pattern and the observed curve has been found and is 4.7 per cent for the lower envelope and 1.9 per cent for the average curve. Since the accidental errors give a percentage area which is only slightly less than the last quantity, it follows that the relative temperature distributions given by case No. 4 and the theoretical curve give reconstructed drift-curves that fit equally well to the observed average drift-curve. Furthermore, it has already been shown that the central temperatures for these two distributions lie within the experimental error, so that these two brightenings may be considered the same in all respects.

The preferred distribution differs from case No. 4, in that both the magnitude of the central temperature and the area expressing the differences in the shape are about three or four times greater than the accidental errors. The difference between the average drift-curve and the lower envelope drift-curve is of some significance and may be interpreted in terms of broad radio-emissive regions that are not associated with sunspots.

Eclipse observations provide another means of examining limb brightening, and a convenient parameter for comparison is the fraction of radiation left over at the middle of the eclipse. During the eclipse of September 12, 1950, Hagen, Haddock, and Reber[12] observed a fraction of 0.17 at a wave length of 10.7 cm. Similar fractions can be obtained from the four derived distributions in which an imaginary moon has the same size as the photospheric disk. The results are shown in Table 3.

Asymmetry in the solar atmosphere may be related to the solar axis of rotation and would modify the brightness variation that has been derived under the assumption of spherical symmetry. Some information on this symmetry should be obtained, because the direction of scanning the sun changes from along the equator in the solstitial months to an angle of 26° in the equinoctial months. In this series of observations there are insufficient spotless-sun drift-curves to give any information on this variation.

## ANALYSIS OF RADIO-EMISSIVE REGIONS

The excess emission above the spotless solar drift-curve is interpreted in terms of bright regions that are on the solar disk. In the period from October, 1951, to the end of 1952, practically all the daily drift-curves show some excess. The excess for July 15, 1952, has already been shown and was used to produce a measure of the receiving pattern. This excess drift-curve is the narrowest recorded to date and the one most similar to the theoretical antenna pattern. It has been assumed that the associated radio-emissive region formed an effective point source; thus the spot drift-curve has been taken as an upper limit of the antenna pattern and forms the basis for analyzing all other observations.

The excess curve for October 16, 1951, taken shortly after the array was initially placed in operation, is shown in Figure 8 and was obtained as an excess over the average drift-curve for 1952. This drift-curve is slightly higher than the composite drift-curve using the lowest five points, and its use may be in keeping with the higher quiet sun

[12] J. P. Hagen, F. T. Haddock, and G. Reber, *Sky and Telescope*, **10**, 111, 1951.

that has been indicated by the flux intercept for zero sunspot area in a correlation study.

The variations of intensity in the excess drift-curve that are introduced by the antenna pattern can be removed by solving the appropriate integral equation (eq. [16]) by the same method as was used for the quiet sun. However, in this case the radio emission is found from north-south strips 1'.5 wide, rather than in rings. The three peaks of the excess curve for October 16 are well separated, so that the solution of the integral equation should be simply related to the original curve. Three radio-emissive regions have

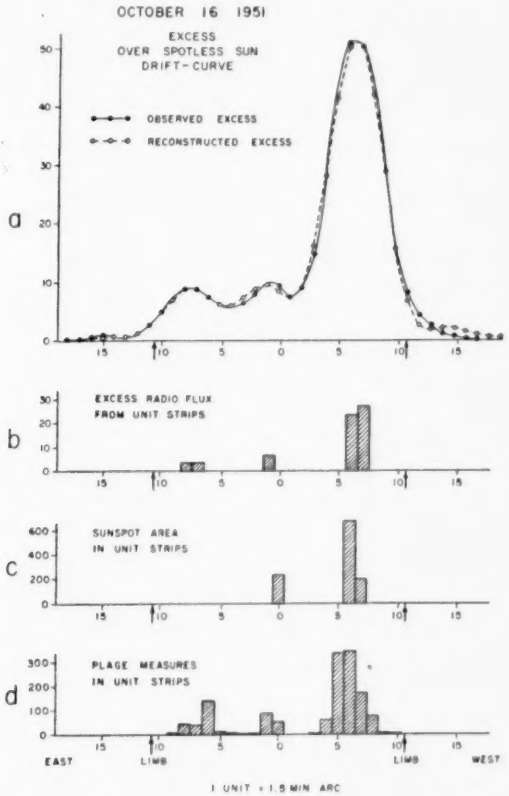


FIG. 8.—Bright features on solar radio disk, October 16, 1951: *a*, drift-curve; *b*, radio spots in a strip; *c*, sunspot area in a strip; *d*, plage measures in a strip.

been found, and the relative flux density in strips is shown in the histogram below the excess drift-curve. The finite width of the brightest region is significant and is related to the half-power width of the excess drift-curve. It is noticeably greater than that for July 15, 1952. The greatest error in this analysis lies in determining the middle spot, since it is blended with the two outer spots. The three radio spots satisfy the excess drift-curve to within the limits set by the receiver noise. This is shown by noting the error between this drift-curve and a reconstructed drift-curve which has been made by passing the antenna pattern over the deduced radio spots (see Fig. 8).

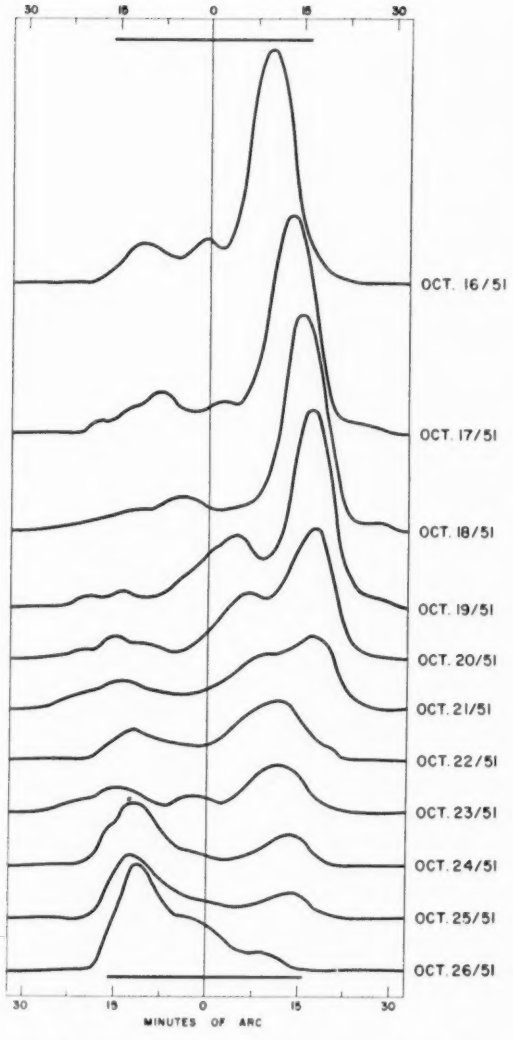


FIG. 9.—Rotation of bright features, October 16–26, 1951

The radio flux from the bright regions has been analyzed as originating in strips considerably longer than the requirements of any physical picture. In order to obtain some estimate of the equivalent radio temperature of these regions, it is reasonable to assume in this simple case that the regions have the same extent in the north-south direction as they do in the east-west direction. Equivalent square areas have been assigned on this basis, and the calculated equivalent temperatures are shown in Table 4. These high temperatures are in agreement with the results obtained from the eclipse observations. Various theoretical interpretations[13] have been given to the origin of this radiation.

In the visible region of the electromagnetic spectrum, the disturbed solar surface presents complex phenomena whose details can be easily seen, while in the radio spectrum only average values over large areas are at present measured. Solar activity has long been studied, and one measure of it is provided in the areas of the sunspots. These are published by the Naval Observatory in Washington and have been used in one comparison

TABLE 4*

CHARACTERISTICS OF RADIO-EMISSIVE REGIONS

| | Region 1 | Region 2 | Region 3 |
|---|---|---|---|
| Center of spot (minutes of arc) | 11.25E | 1.5E | 9.75W |
| Total flux (2 pols.) ($10^{-22}$ watts/meter$^2$/cps) | 6.1 | 5.3 | 40 |
| Width east-west (minutes of arc) | 3 | 1.5 | 3 |
| Assumed square area (square minutes of arc) | 9 | 2.25 | 9 |
| Average equivalent temperature (° K) | $3.0\times10^6$ | $10.5\times10^6$ | $20\times10^6$ |
| Sunspot area (millionths) of hemisphere | 0 | 254 | 932 |
| Sunspot center (minutes of arc) | ..... | 0 | 9 |

* Co-ordinates of north-south strips measured along a celestial latitude from center of sun.

of the optical features with radio features. The sunspot area in strips has been found and plotted below the radio-flux histogram. Comparison shows that two separate regions containing sunspots can be associated with two of the radio-emissive regions, while no such region can be identified for the third radio region on the eastern limb. However, this unique region has been identified[14] with a *plage* region on spectroheliograms taken at the McMath-Hulbert Observatory and points to the necessity of considering such features. A selected measure of the calcium *plages* has been plotted in Figure 8, and three *plage* regions can be identified with the three radio regions.

The excess drift-curves for 10 successive days (Fig. 9) show the subsequent development of these regions, as well as the effect of solar rotation. The brightest region of October 16 gradually shifts and disappears with diminishing amplitude on the western limb; and after a few days a new source appears on the eastern limb. In addition to these gradual changes, a sudden change appears on October 19, and there is a new region of radio noise on the solar disk. This has its maximum intensity in the region between the smaller radio sources, which were first noticed on October 16.

The authors wish to express their thanks to their associates in the Radio and Electrical Engineering Division and, in particular, to Dr. G. A. Miller for his unfailing interest in, and encouragement of, this undertaking. The mechanical design of the array was undertaken by Mr. H. E. Parsons and Mr. Z. Mordasewicz and was executed under their supervision in our model shop. Dr. Helen W. Dodson of the McMath-Hulbert Observatory has kindly provided the calcium *plage* data before publication.

[13] J. F. Denisse, *Ann. d'ap.*, **13**, 181, 1950; M. Waldemeier and H. Mueller, *Zs. f. Ap.*, **27**, 58, 1950; and J. H. Piddington and H. C. Minnet, *Australian J. Sci. Res.*, A, **4**, 131, 1951.

[14] Helen W. Dodson, *Ap. J.*, **119**, 564, 1954.

# A REVISED ANALYSIS OF THE SOLAR SPECTRUM FROM 2990 TO 2635 A

N. L. Wilson, R. Tousey, J. D. Purcell, and F. S. Johnson
U.S. Naval Research Laboratory, Washington, D.C.
AND
C. E. Moore
National Bureau of Standards, Washington, D.C.
*Received December 17, 1953*

## ABSTRACT

New solar spectra from 2990 to 2635 A, obtained from spectrographs flown in rockets on February 9, 1950, September 3, 1952, and December 15, 1952, are presented and analyzed. Lines as close as 0.3 A were observed. Nearly 500 lines are recorded and are attributed to 1054 atomic lines. The detailed spectral-intensity distribution-curve is presented instead of the customary visual-intensity estimates. The effect of instrumental blending is illustrated by comparing a long-wave-length region of the rocket spectrum with the high-resolution *Utrecht Atlas* curve, after averaging the latter over appropriate wave-length intervals.

## INTRODUCTION

Since publication in 1949 of the analysis of the early rocket ultraviolet solar spectra obtained by the Naval Research Laboratory,[1] improved spectra have been obtained, extending the wave-length range to about 2100 A and with three to four times increased resolution. A new and more detailed analysis is thus made possible and will be published in two or more parts. The present paper covers the spectrum from 2990 to 2635 A. A separate report on the absolute intensity distribution is also in preparation.[2]

## THE SPECTROGRAPH

The spectra upon which the present analysis is based were obtained from three different rocket flights: Viking 3, February 9, 1950; Aerobee 11, September 3, 1952; and Viking 9, December 15, 1952. The solar altitudes at the time of firing were 32°, 26°, and 23°, respectively.

The spectrograph flown in each rocket used a concave diffraction grating of 40 cm radius of curvature and approximately 15,000 lines per inch in a near-normal incidence mounting. In two of the instruments Johns Hopkins University gratings were used; the third grating was a "tripartite" from the Bausch and Lomb Optical Company, ruled in three sections, each blazed for about 1500 A. In each spectrograph, two cassettes were provided, each carrying ten strips of film on facets of a drum and providing for ten or twenty exposures as desired. In Viking 3 the two cassettes were located on opposite sides of the central image and received the first-order spectra. In Aerobee 11 and Viking 9, both cassettes were located on the same side of the central image; the one was placed so as to receive the first-order spectrum from 550 A to about 2500 A, and the other intercepted the second-order spectrum from 2500 A to longer wave lengths. In the latter case the overlapping first order of wave lengths greater than 5000 A did not record because of the lack of sensitivity of the film from this wave length toward the red.

In each spectrograph, sunlight was admitted through an open slit, of the type described by Johnson, Purcell, Tousey, and Watanabe,[3] employing mirror jaws to expand

[1] E. Durand, J. J. Oberly, and R. Tousey, *Ap. J.*, **109**, 1, 1949.
[2] Unpublished material.
[3] *J. Geophys. Res.*, **57**, 157, 1952.

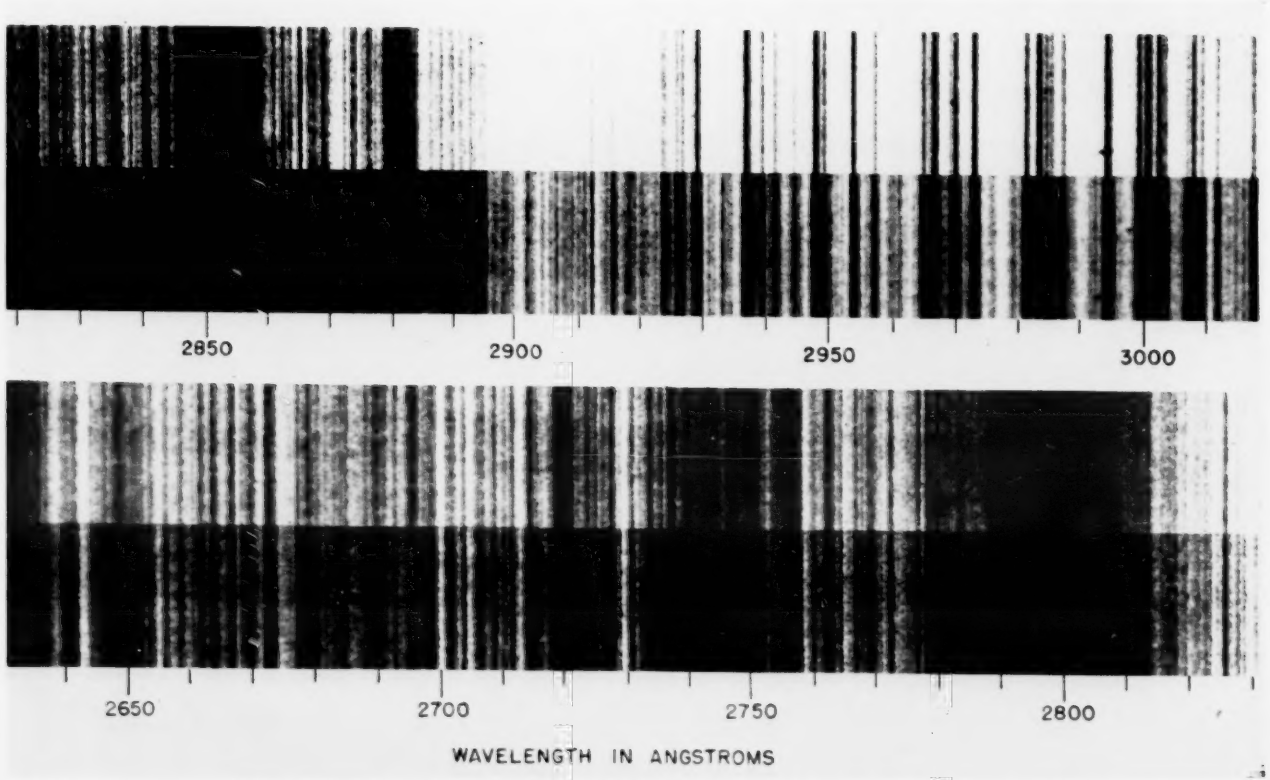


FIG. 1*a*.—The solar spectrum photographed with a 30-cm radius, 15,000 lines per inch, grating spectrograph from a rocket. February 9, 1950, altitude 66–70 km, dispersion 43.7 A/mm.

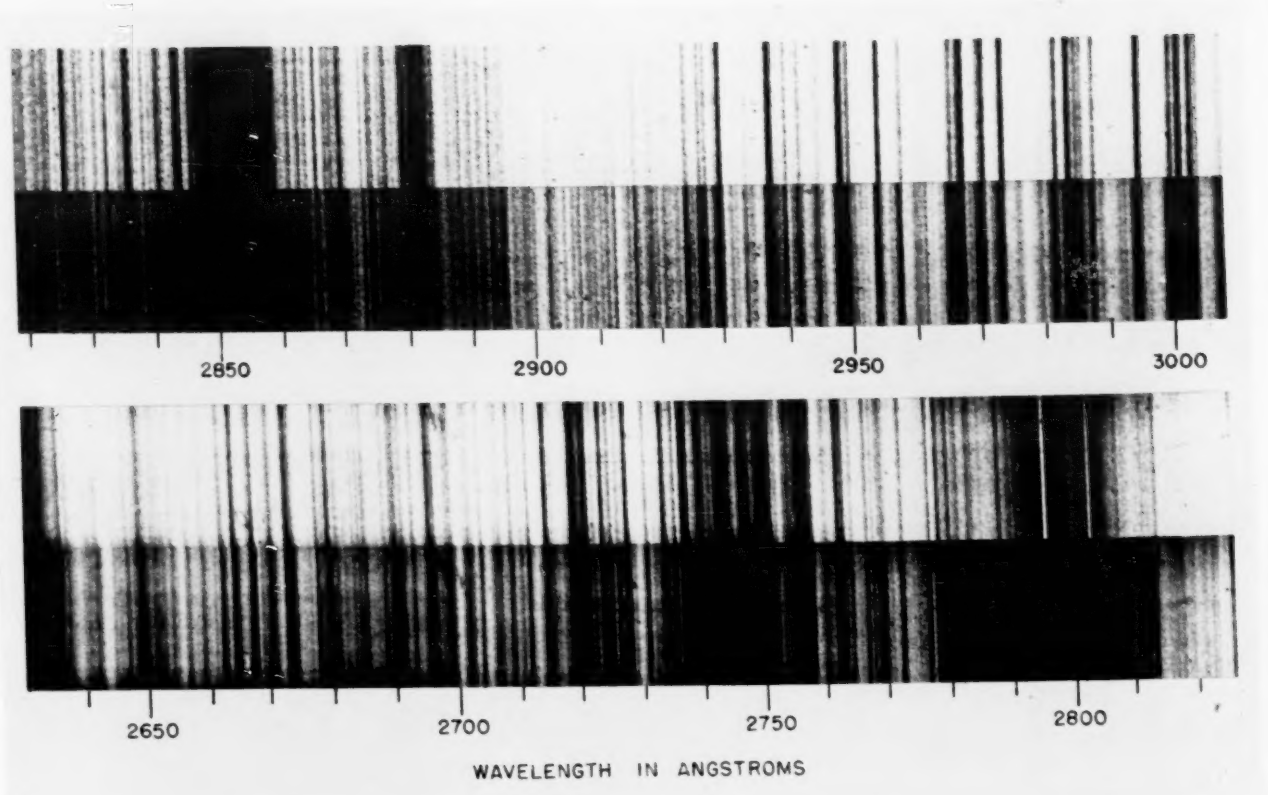


FIG. 1*b*.—The solar spectrum photographed with a 40-cm radius, 15,000 lines per inch, grating spectrograph from a rocket, September 3, 1952, altitude 56–68 km, dispersion 20.2 A mm in the second order.

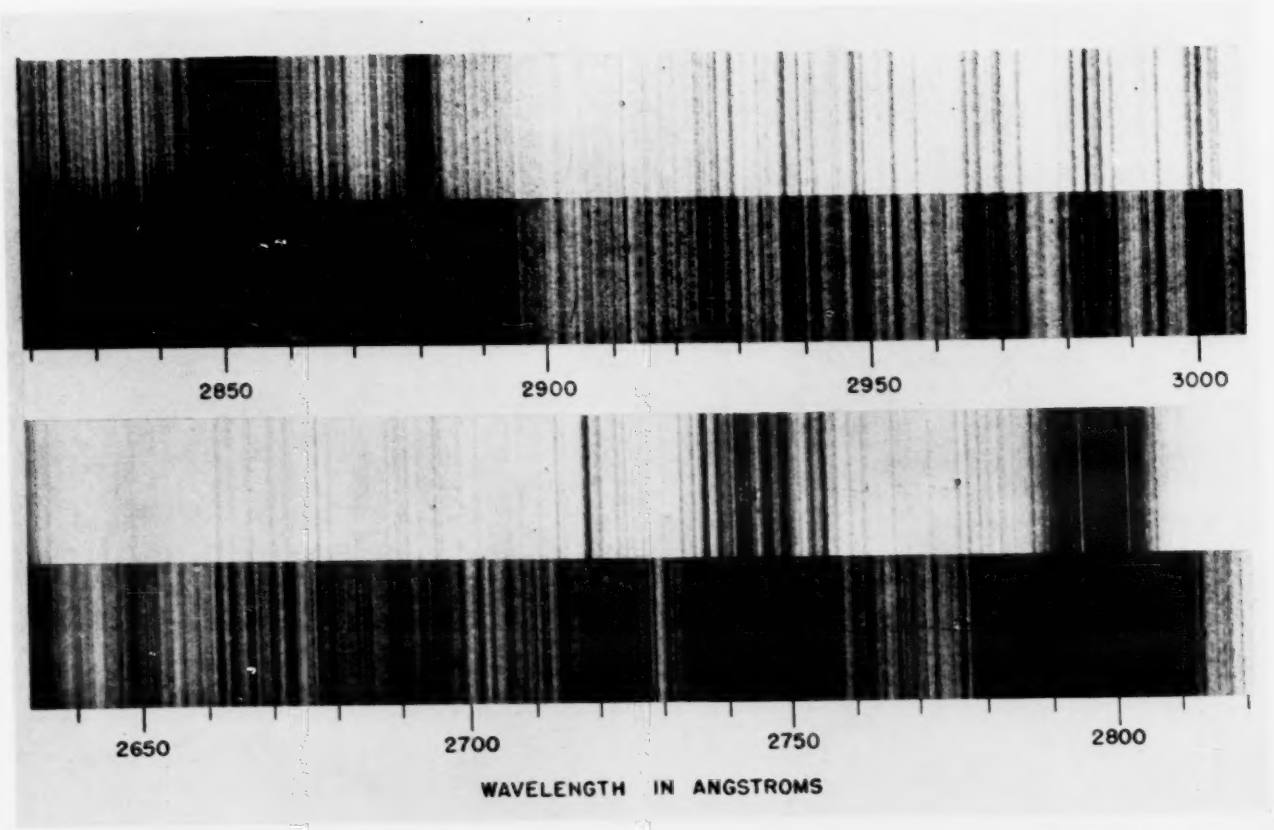


FIG. 1c.—The solar spectrum photographed with a 40-cm radius, 15,000 lines per inch, grating spectrograph from a rocket, December 15, 1952, altitude 158–163 km, dispersion 21.6 A mm in the second order.

the field of view. In the case of Viking 3, the patch of sunlight transmitted by the slit swept across the grating once during each revolution of the rocket about its long axis. In the other two rockets the spectrograph was mounted on the turntable of a one-axis sun-following device, driven by a photoelectrically actuated servo-system; this caused the patch of sunlight to stay on the grating during the entire exposure, in spite of the roll of the rocket, and made possible more dense exposures. The slit-width used in each instrument was 15 $\mu$.

## THE SPECTRA

Although many exposures were made on each flight, only the four spectra showing the greatest resolution over the wave-length range 3000–2630 A were used in the present paper. Reproductions of three of these, each printed at two densities, are presented in Figure 1. Spectrum *a*, for Viking 3, was made on Eastman type IV-O film and was exposed intermittently for 16 seconds over an altitude interval of 56–66 km above sea-level. The effective exposure was approximately 0.2 second. This is a first-order spectrum, with a dispersion of 43.7 A/mm. Another exposure from the same flight and almost identical to *a* was also measured; this was made on Eastman SWR film, and the altitude interval was 66–70 km above sea-level. Spectrum *b*, from Aerobee 11, has a high density, owing to the use of a sun-follower; it is a second-order spectrum of dispersion 20.2 A/mm on Eastman IV-O film; the total exposure was of the order of 14 seconds, and the altitude range covered was 56–68 km above sea-level. However, the sun-follower was hunting, so that the effective exposure was only 4 seconds. Spectrum *c* was also photographed from Viking 9 with a sun-follower, using IV-O film and the second order. The exposure of 4.5 seconds covered 158–163 km, and the sun-follower kept the spectrograph pointed at the sun for an effective exposure of 3 seconds; the dispersion was 21.6 A/mm. In spectra *a* and *b* some lines as close as 0.4 A were resolved, while in *c* the minimum observed separation was 0.3 A.

The primary purpose of the Viking 9 experiment was to extend the spectrum as far as possible below 2000 A. High resolution above 2500 A, as provided by the second-order camera, was of secondary importance. The particular grating used was chosen because of its high first-order speed below 2000 A and low stray-light intensity; unfortunately, it produced Rowland ghosts, which were quite appreciable in the second order. First-order spectra were secured to 1850 A, and showed the best resolution yet obtained below 2500 A. The second-order spectra also attained a new height in resolution but were troubled by ghosts. Close examination of Figure 1, *c*, shows that the contrast in this spectrum is noticeably reduced, presumably by ghosts, and the intense *Mg* II emission lines at 2800 A are accompanied by ghosts located 2 A to the violet. It was therefore necessary to determine to what further extent, if any, spurious lines had been introduced.

An attempt was made to correct a 100 A portion of the solar intensity-curve of the Viking 9 spectrum for the effect of ghosts. The spacing and intensities of the ghosts, relative to the parent-line, were determined for the 2478 A carbon line from exposures made with a carbon arc before flight. The correction was made by subtracting the curve from itself twice, after displacing and reducing it to correspond to the two principal ghosts and retaining full detail. The contrast of the spectrum was increased as a result and became approximately the same as other spectra, photographed with ghost-free gratings. The intensity of lines relative to neighboring lines changed somewhat, but their positions did not change within the limits of our wave-length accuracy. The ghosts of the *Mg* II emission lines were completely removed by this procedure. With the exception of a few very weak lines, no absorption lines were added or removed by the process of ghost correction, and this led us to believe that the additional resolution in Viking 9 was not a spurious effect due to ghosts. In most cases the additional lines not observed in other spectra seemed to be supported by the identifications. The spectra from Viking 9 were not used for detailed intensity measurements.

### WAVE LENGTHS

The wave-length determinations were made from comparator readings of the positions of the spectral lines. Twenty of the least-blended strong lines distributed over the region 3000–2635 A were selected as wave-length standards in setting up the wave-length equation. They are listed in Table 1.

In the case of the first-order spectrum a linear wave-length equation was sufficiently exact. Correction-curves for departure from linear dispersion were applied to the two second-order spectra. Since the spectra were recorded on a film base, it was necessary to take care that shrinkage effects due to relative-humidity changes did not occur during the measurements.

TABLE 1

STANDARD LINES

| Multiplet No. | Spectrum | Laboratory (A) | Multiplet No. | Spectrum | Laboratory (A) |
|---|---|---|---|---|---|
| R30 | *Fe* I | 2999.512 | R 1 | *Mg* II | 2802.698 |
| 1 | *Fe* I | 2966.901 | 1 | *Mg* II | 2795.523 |
| 1 | *Fe* I | 2957.365 | 6 | *Mg* I | 2782.974 |
| 5 | *Mn* II | 2933.051 | 6, 7 | *Mg* I | 2781.418 |
| 60 | *Fe* II | 2926.584 | 6, 6 | *Mg* I | 2779.832 |
| 1 | *Fe* I | 2912.158 | 6, 7 | *Mg* I | 2776.695 |
| 43 | *Si* I | 2881.595 | 5 | *Fe* I | 2720.902 |
| 43 | *Fe* I | 2845.595 | 63 | *Fe* II | 2714.414 |
| 44 | *Fe* I | 2838.120 | 8 | *Cr* II | 2658.59 |
| 44 | *Fe* I | 2813.288 | 52 | *Fe* I | 2635.808 |

### INTENSITIES

Density-curves of the three films were made with a Leeds and Northrup microphotometer. The tracings were converted to curves of relative intensity by a photographic method devised by Purcell[4] and to be described in full elsewhere. Briefly, the method involves moving an 80 A-long segment of the density trace past an illuminated slit so that all points representing equal density are in contact with the slit at one time. The speed of the motion is varied and is determined by the density-log intensity-curve for the film. Sensitized paper placed on top of and in contact with the microphotometer tracing is also moved perpendicularly past the slit, but at a uniform speed. The resulting contact print thus has its density scale distorted into an intensity scale. Since the contrast of the film varied slightly with wave length, a different characteristic curve was used for each 80 A segment. The characteristic curves were determined from exposures made just before flight on film from the same roll and developed at the same time as the flight film. The light-source used was a carbon arc, whose spectral intensity distribution was known from measurements of Packer and Lock.[5]

The solar spectral irradiance-curve shown in Figure 2 is from Viking 3, except for a few angstroms near 2800 A and at 2852 A, where the film density went to zero and the curve of Aerobee 11 was used. However, throughout the entire region the curves from these two flights agreed very well in contrast and detail. Viking 3 was chosen for presentation because it seemed to show very slightly more resolution. The second half of the curve is plotted on an expanded intensity scale, so as not to lose detail.

The intensity scale of Figure 2 is in absolute units. The determination of the absolute

[4] *J. Opt. Soc. Amer.*, **42**, 880, 1952 (abstr.).

[5] *J. Opt. Soc. Amer.*, **42**, 879, 1952 (abstr.)

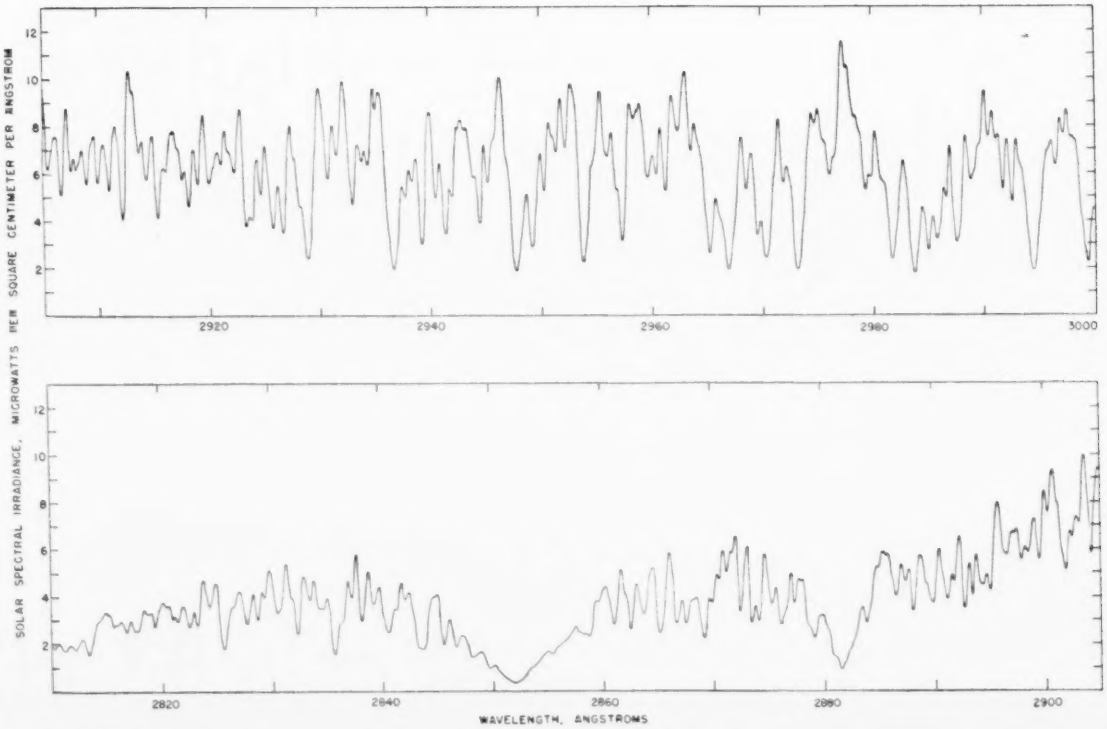


FIG. 2.—The solar spectral irradiance, derived mainly from the spectrum of Fig. 1, *a*. The energy units are based on a scale compatible with a solar constant value of 2.00 cal $min^{-1}$ $cm^{-2}$.

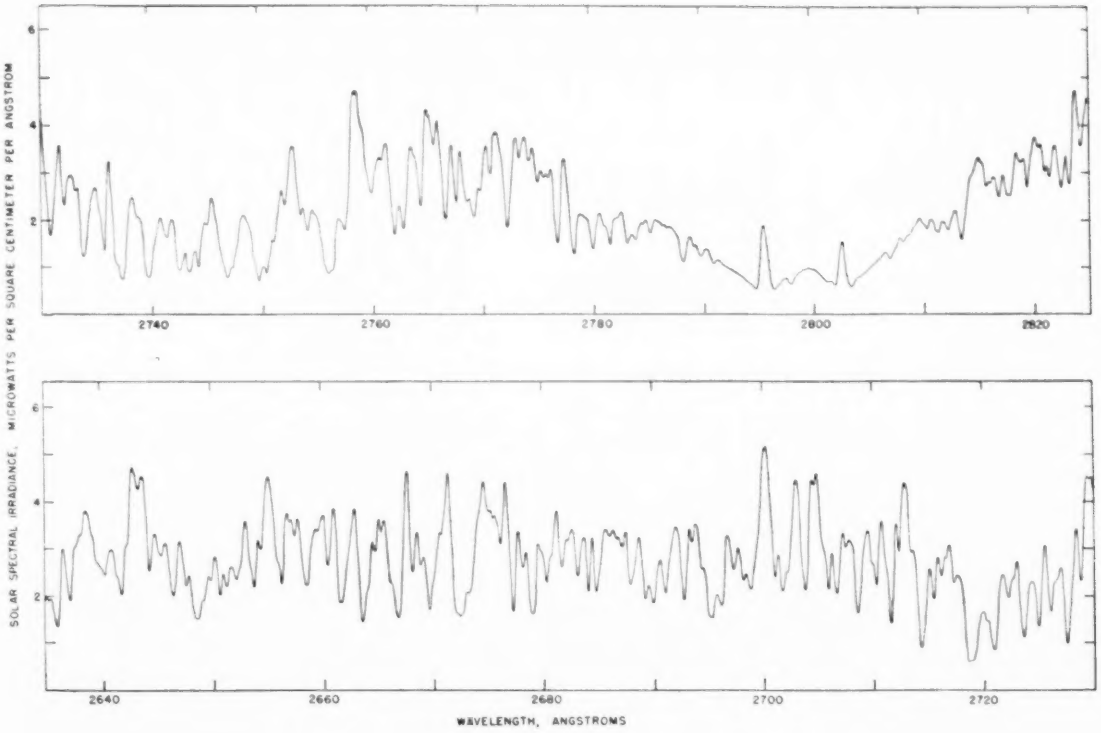


FIG. 2.—*Continued*

energy scale is described in detail by Johnson.[6] In brief, a new curve of solar intensity distribution was obtained by a piecing-together process from the best average rocket data[2] from 2200 to 3400 A; new data from 3100 to 6000 A obtained from Mount Lemmon, Arizona;[7] and, to longer wave lengths, the Smithsonian curve as presented by Moon.[8] The level for the composite curve was adjusted so that the area underneath gave the solar constant. The value of the solar constant used was 2.00 cal $cm^{-2}$ $min^{-1}$ and resulted from a reconsideration of the zero air-mass corrections based on the rocket data in the ultraviolet and a 6000° K black-body-curve in the infrared.

In general, the spectral intensity-curve of the sun falls more and more below a 6000° K black body, the farther one goes into the ultraviolet. There is, however, an intense peak at 2977 A, where the solar curve exceeds the 6000° K level by 3 per cent, and the peak at 2913 A just reaches this level. With greater instrumental resolution, most of the peaks would be expected to rise somewhat higher.

### THE INTERPRETATION OF A BLENDED SPECTRUM

The extreme natural crowding of lines in the ultraviolet combined with the low resolving power of the rocket spectrograph produce a blended spectrum. No lines are entirely free from blending, and, as a result, a completely definitive analysis is impossible. For example, a comparison of the rocket-curve near 3340 A with the Rowland table[9] showed an average of nine contributing lines to each of our observed "lines." This blending increases at shorter wave lengths. In much of the spectrum the problem is one more nearly of synthesis than of analysis.

The extent of the possible analysis can best be explained by comparing our spectrum with the far more highly resolved spectrum of the *Utrecht Atlas*[10] over a wave-length range where they overlap. The region selected was from 3365–3374 A and is shown in Figure 3. The comparison was made by reducing the resolution of the Utrecht curve until it became approximately equal to that of the rocket-curve. This was done through an averaging process; the ordinates, read every millimeter (approximately 0.05 A), from the *Atlas* curve, were added over the selected averaging interval and divided by its length. These averages were computed every millimeter along the *Atlas* curve.

Figure 3, *a*, shows the *Atlas* curve and the averages computed for three intervals. The 0.65 A curve corresponds to the band width of the 15 $\mu$ slit used in the first-order Viking 3 spectrum. It can be seen that the profile of the average curve is very sensitive to the length of the averaging interval and may be greatly altered by varying its "resolution." For example, in an extreme case, the maxima and minima between 3372 and 3373 A become completely reversed as the averaging interval is increased from 0.45 to 0.85 A. Furthermore, a minimum of an average curve may differ in wave length from its strongest contributors by as much as half a band width, while a fairly strong atomic line, 3370.3 A, for example, may even fall close to a maximum of the average curve, depending on the strength and distribution of its neighbors.

In general, therefore, the wave-length measurements from the three rocket films need not necessarily be expected to agree exactly with one another, since the instrumental resolution was not exactly the same. Furthermore, differences of as much as 0.2 A between the observed line positions and the locations of the principal contributors become plausible.

[6] Unpublished material.

[7] L. Dunkelman and R. Scolnik, *J. Opt. Soc. Amer.*, **42**, 876, 1952 (abstr.)

[8] *J. Franklin Inst.*, **230**, 583, 1940.

[9] C. E. St. John, C. E. Moore, L. M. Ware, E. F. Adam, and H. D. Babcock, *Revision of Rowland's Table of Solar Spectrum Wavelengths* ("Carnegie Institute of Washington Publications," No. 396 [Washington, D.C., 1928]).

[10] M. Minneart, G. F. W. Mulders, and J. Houtgast, *Photometric Atlas of the Solar Spectrum* (Amsterdam, 1940).

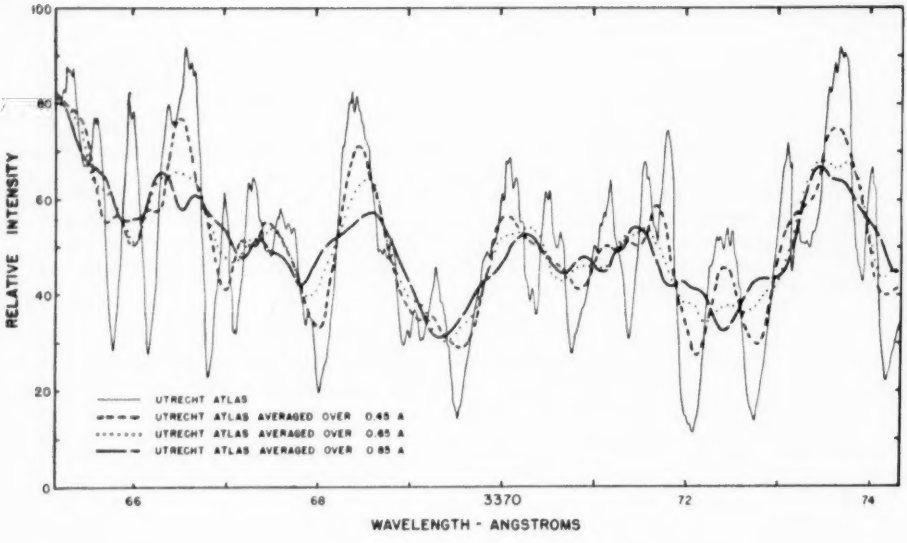


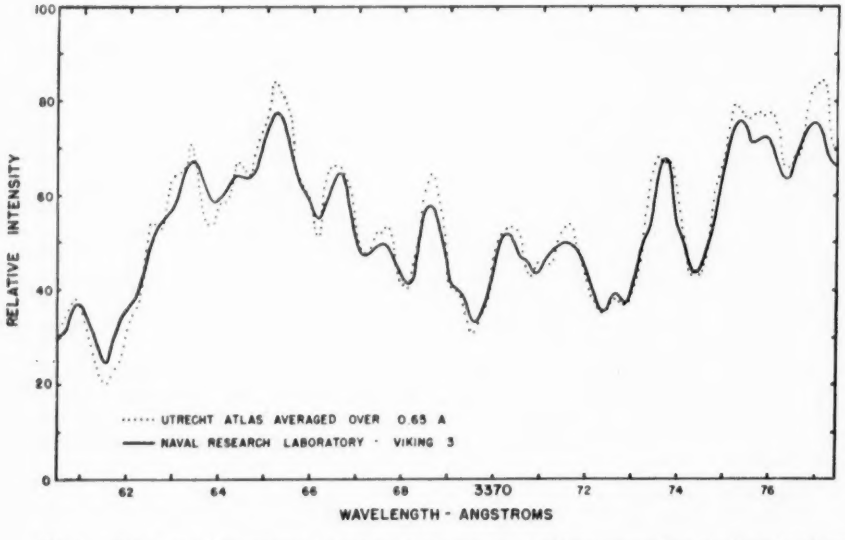


FIG. 3.—The effect of instrumental blending. In *a*, a portion of solar spectrum from the Utrecht *Atlas* is presented, together with the same curve "blended" by averaging it over three wave-length intervals. The blended curve depends strongly on the length of the averaging interval. In *b*, the Utrecht curve averaged over a 0.65 A interval is compared with the curve obtained from the Viking 3 spectrograph, which had a slit-width equivalent to 0.65 A.

The 0.85 A curve of Figure 3 between 3366 and 3367 A presents another paradoxical situation. The dip at 3366.5 A is clearly introduced through the averaging process and is due principally to the strong lines 0.3 and 0.4 A on either side of it. From simply looking at this average curve, one would not suspect that these lines contributed to this dip, since they lie beyond the two adjacent maxima of the average curve. Furthermore, the dip in the 0.85 A average curve at 3367.2 A has a greater contribution in the mathematical averaging process from the line at 3366.85 A, due to its greater depth, than from the much closer line at 3367.1 A. The existence of these various effects of blending should be kept in mind while examining the analysis of the rocket spectra.

The Utrecht curve averaged over the 0.65 A interval and the Viking 3 rocket-curve, resulting from a spectrograph with a slit-width equivalent to 0.65 A, are compared in Figure 3, *b*. The agreement in the number and the positions of the features is quite satisfactory, and many of the shoulders and inflections are very similar. Random variations introduced by the photographic process probably account for part of the residual differences. Also, the mathematical averaging process should probably have been weighted somehow, were it to correspond exactly to the instrumental averaging process introduced by the finite spectrographic slit-width and imperfect resolution of the photographic emulsion. The contrast in the two curves is very similar, and the agreement is certainly as close as can be expected from two completely different and independent determinations, each involving photographic photometry. Correction of the Viking 3 spectrum for Rowland ghosts, which appeared to total less than 2 per cent of the parent-line intensity, would have made the agreement a little closer. The contrast in the rocket spectrum above 3300 A was also reduced a little by interreflections between the film and a metalized filter located 2 mm in front, introduced to reduce the intensity for the longer wave lengths.

### THE IDENTIFICATION TABLE

The observed Fraunhofer lines and their identifications, in terms of probable contributing atomic lines, are presented in Table 2. The table departs from the conventional list in having the form of an expanded linear wave-length scale, with columns of 10 A each. The wave lengths for the three flights, from observations under the comparator, are entered at their proper scale positions and comprise the first, second, and third columns under the headings "V-3," "A-11," and "V-9." In place of the usual visual-intensity estimates we have chosen to present the actual spectral-intensity distribution-curve. This is a greatly expanded version of the Viking 3 curve of Figure 2 and is superimposed upon the table so as to match the Viking 3 observed wave lengths. Four different solar irradiance scales were used, as shown at the bottom of each column; the scale units are microwatts $cm^{-2}$ $A^{-1}$. This method of presenting the line intensities and making comparison with the atomic lines contributing to the absorption seems especially well adapted to the study of a spectrum containing so much blending. The comparison should be regarded in the light of the discussion of blending accompanying Figure 3, *a*.

The fourth through the seventh columns list the pertinent laboratory data on the atomic lines estimated to be the most prominent contributors to the absorption spectrum. These data are from the *Ultraviolet Multiplet Table*,[11] except for a few entries from the *Revised Multiplet Table*,[12] which are marked with an "R" preceding the multiplet number, and a few weak lines not appearing in either. The laboratory wave lengths given in the fourth column are entered as closely as possible to their proper positions on the wave-length scale of the table. A dash preceding the wave length indicates that it is considered the predominant contributor. It is left to the reader to decide on the relative

[11] Charlotte E. Moore, *An Ultraviolet Multiplet Table* (National Bureau of Standards Circ. 488 [Washington, D.C., 1950, 1952]), Secs. I and II.

[12] Charlotte E. Moore, *A Revised Multiplet Table of Astrophysical Interest* ("Contributions from the Princeton University Observatory," No. 20 [1945]).

## TABLE 2

### THE SOLAR SPECTRUM FROM 2990 TO 2635 A*

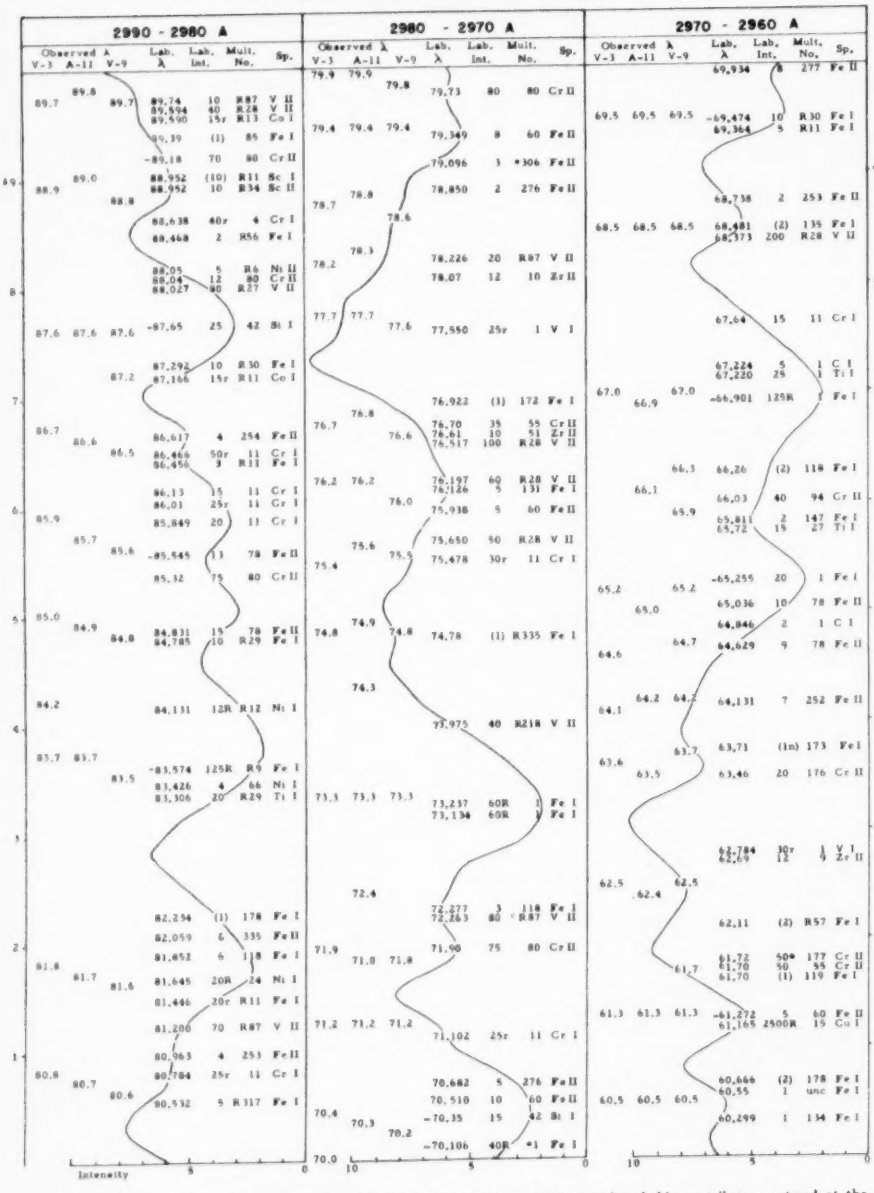


*The columns are in the form of a wave-length scale, with the observed lines and probable contributors entered at the proper positions. The superimposed curve is the trace of the Viking 3 spectrum, reduced to intensities; the scale is microwatts $cm^{-2} A^{-1}$.

TABLE 2—*Continued*

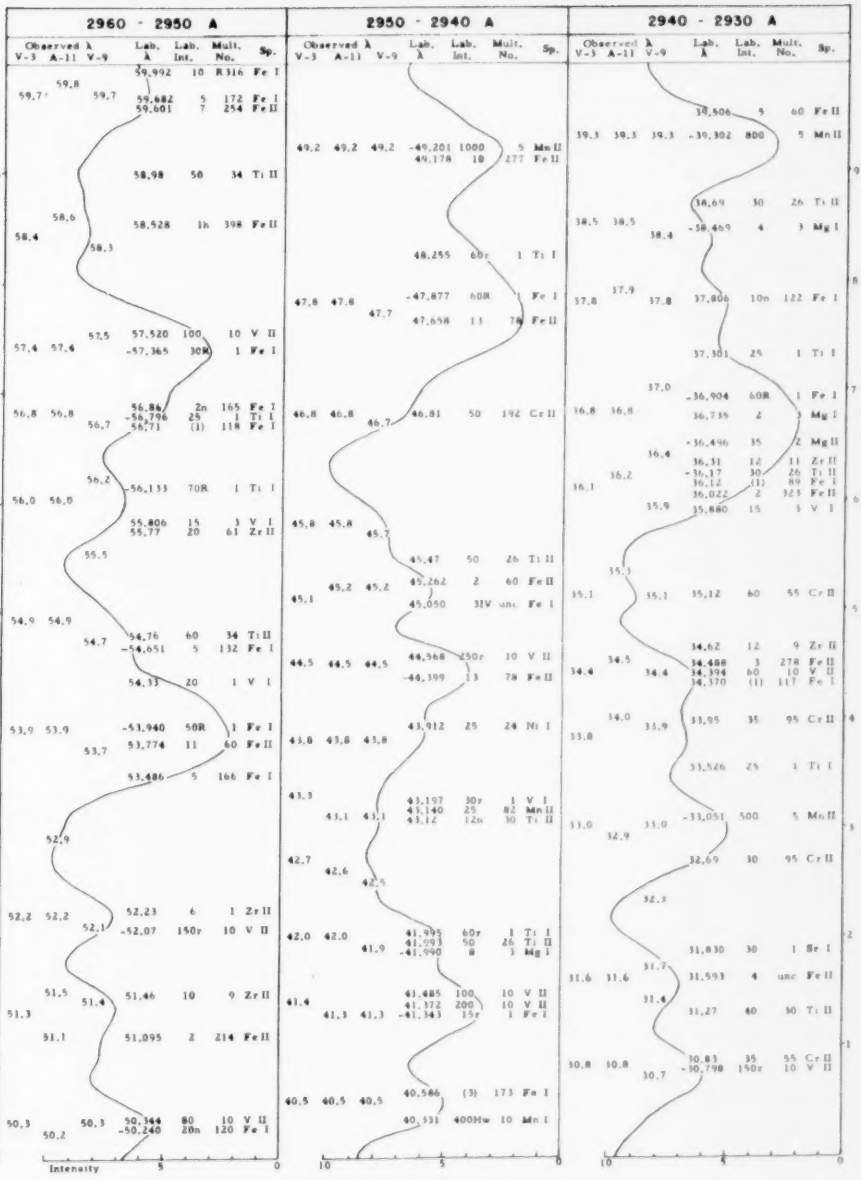

TABLE 2—*Continued*

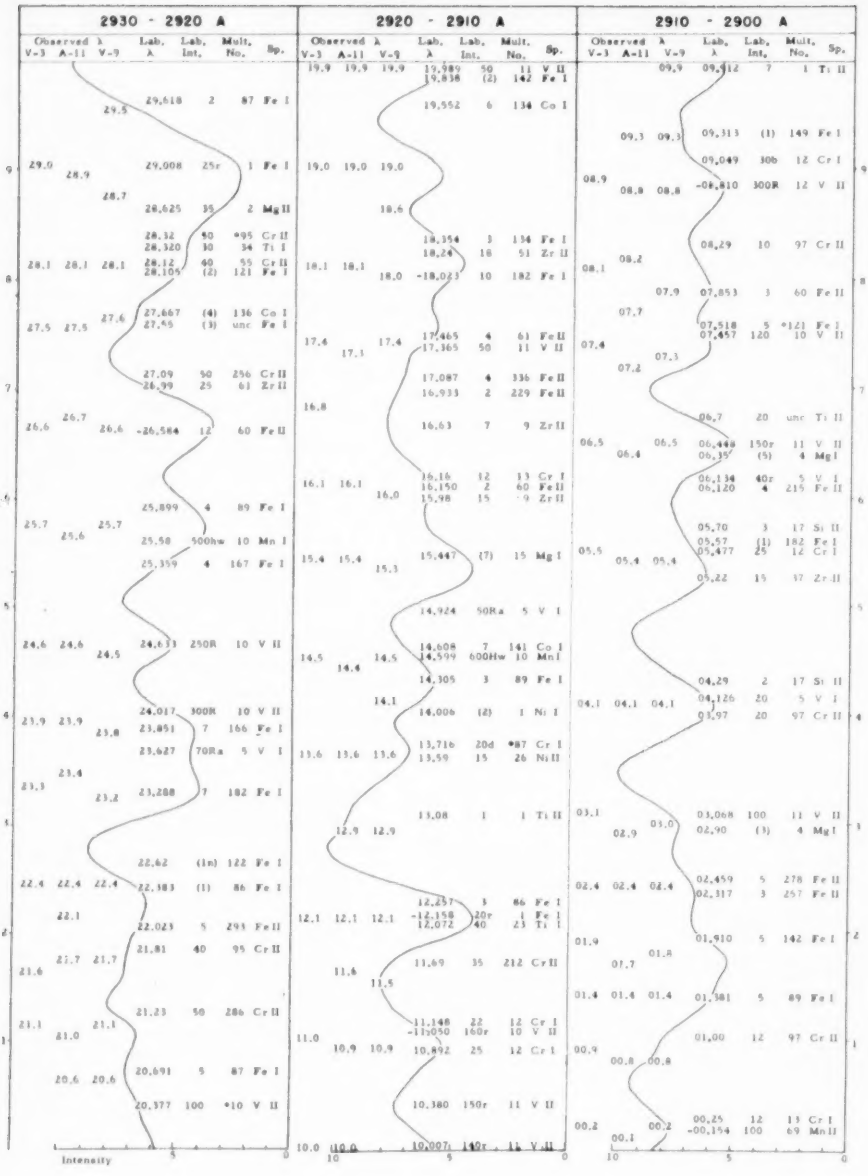

TABLE 2—*Continued*

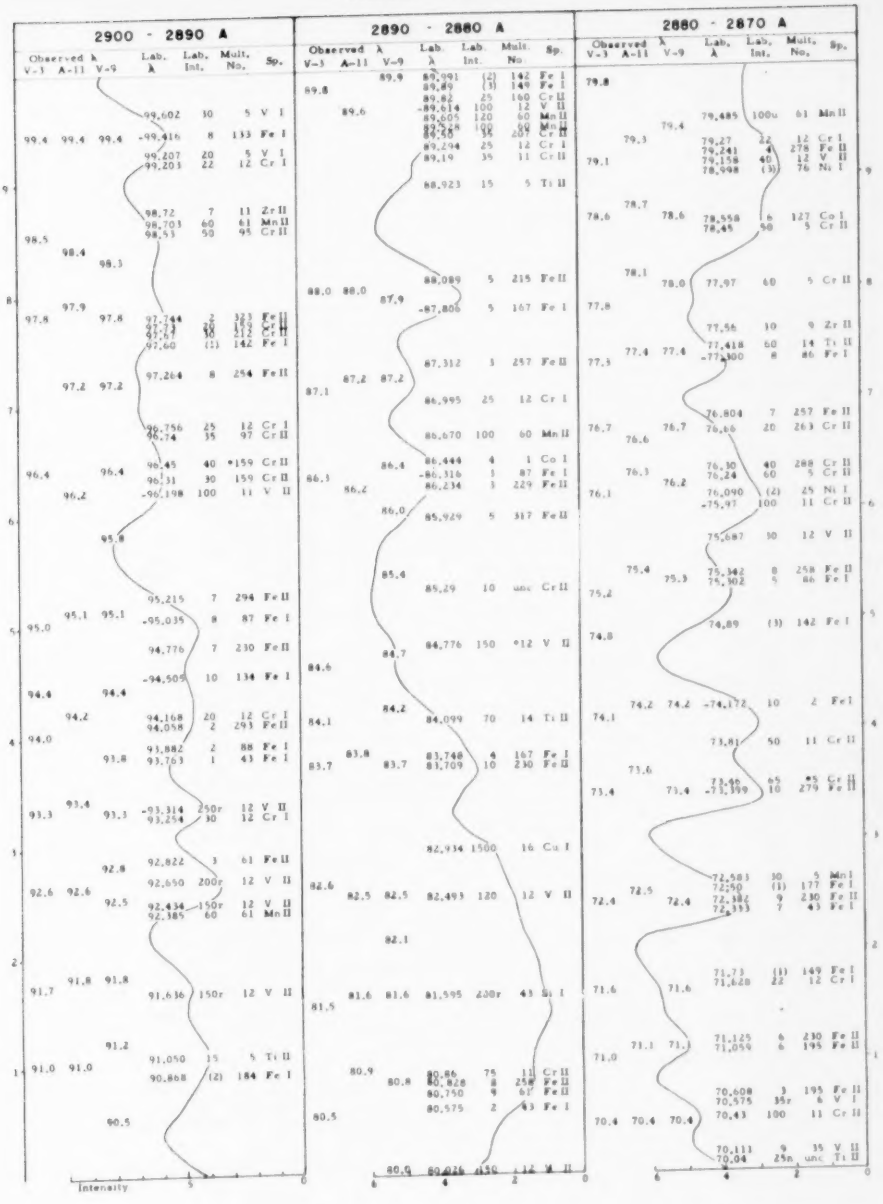

TABLE 2—*Continued*

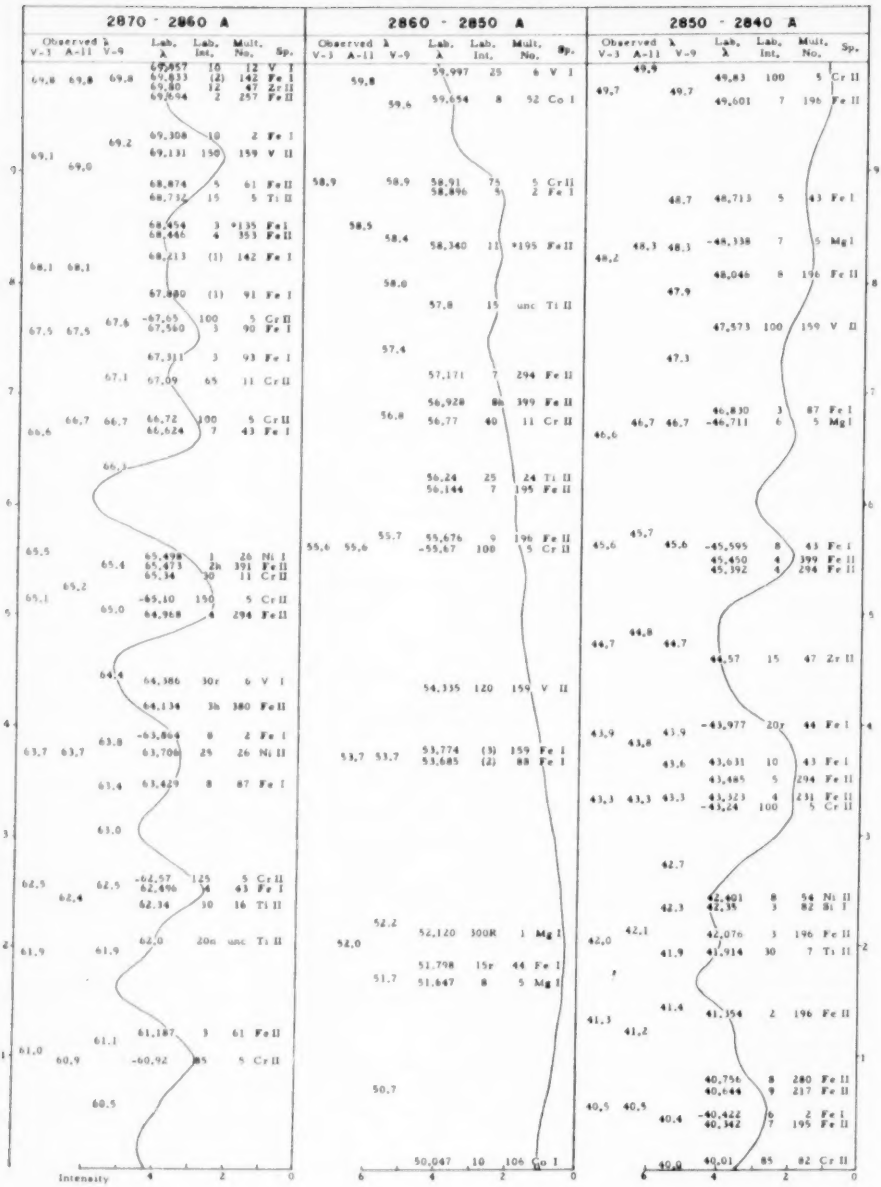

TABLE 2—*Continued*

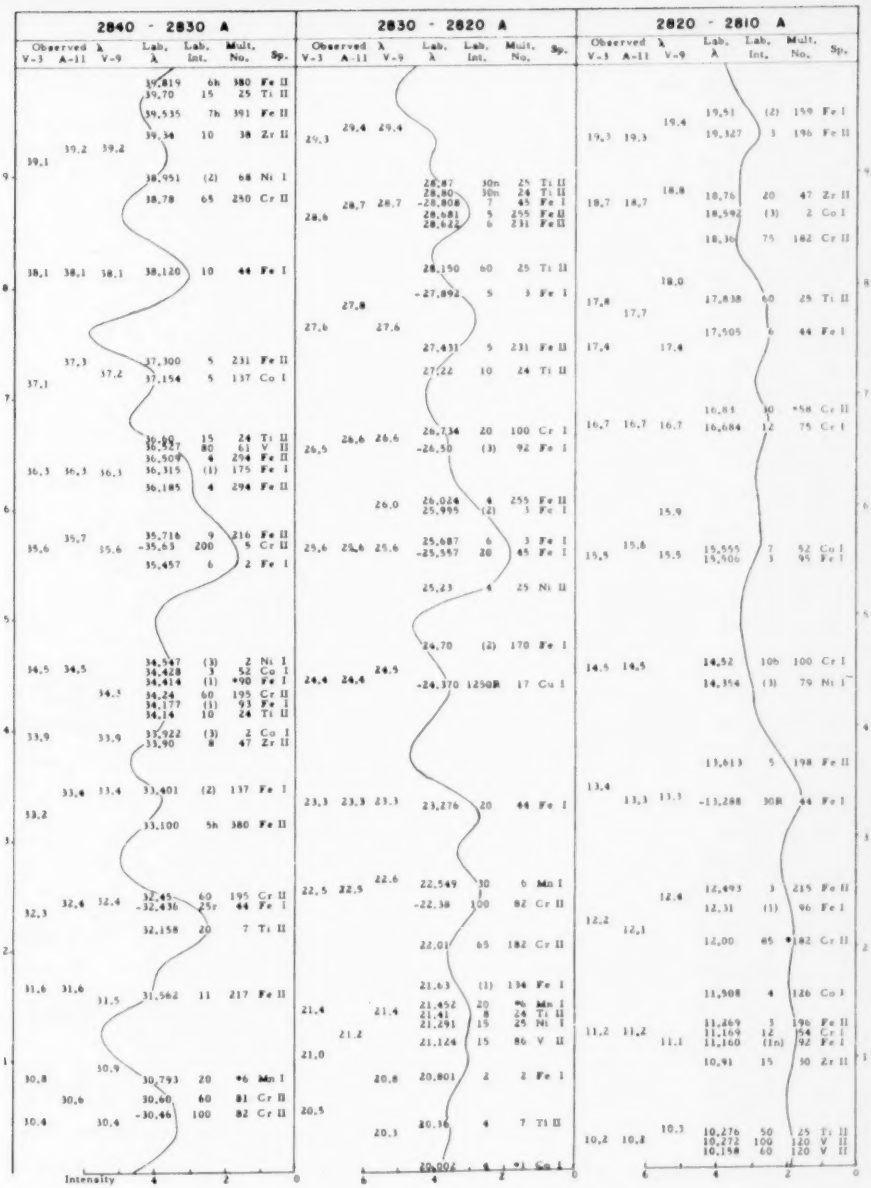

TABLE 2—*Continued*

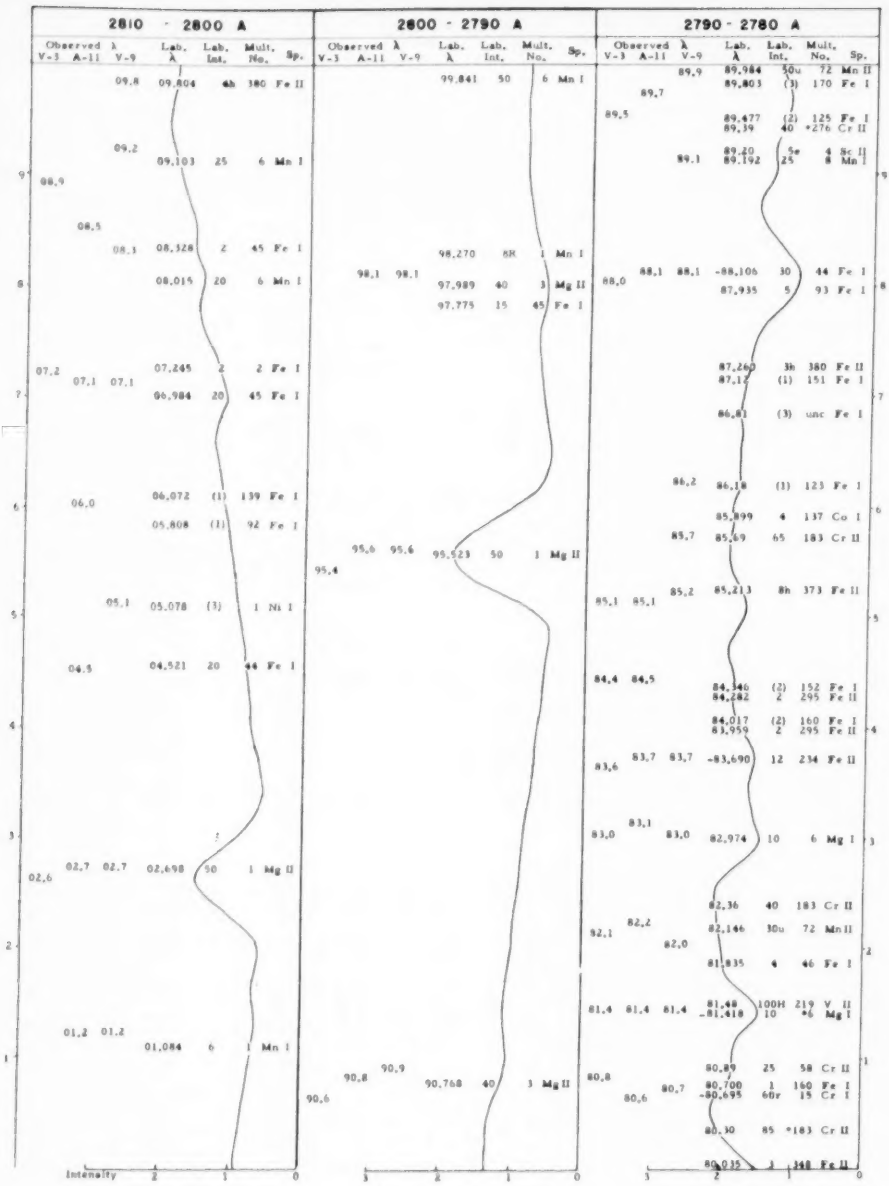

TABLE 2—*Continued*

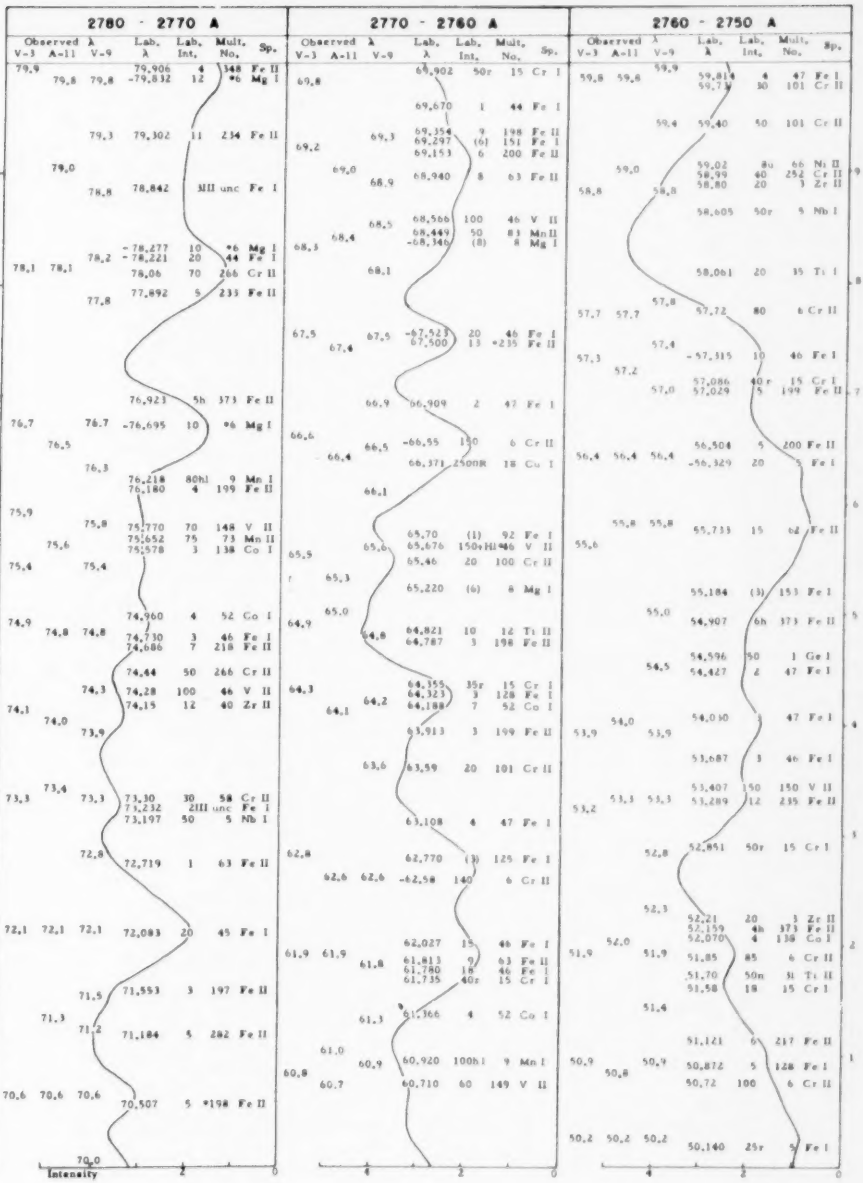

TABLE 2—*Continued*

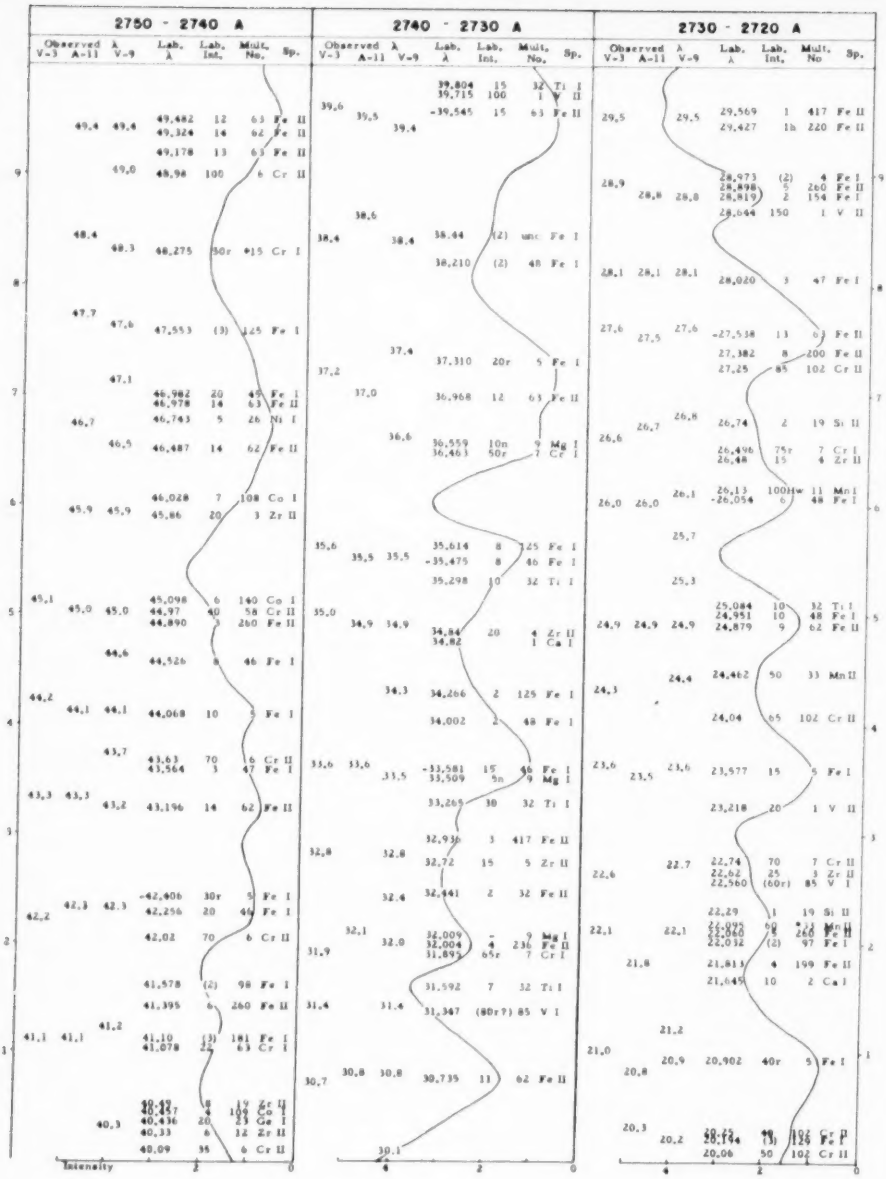

TABLE 2—*Continued*

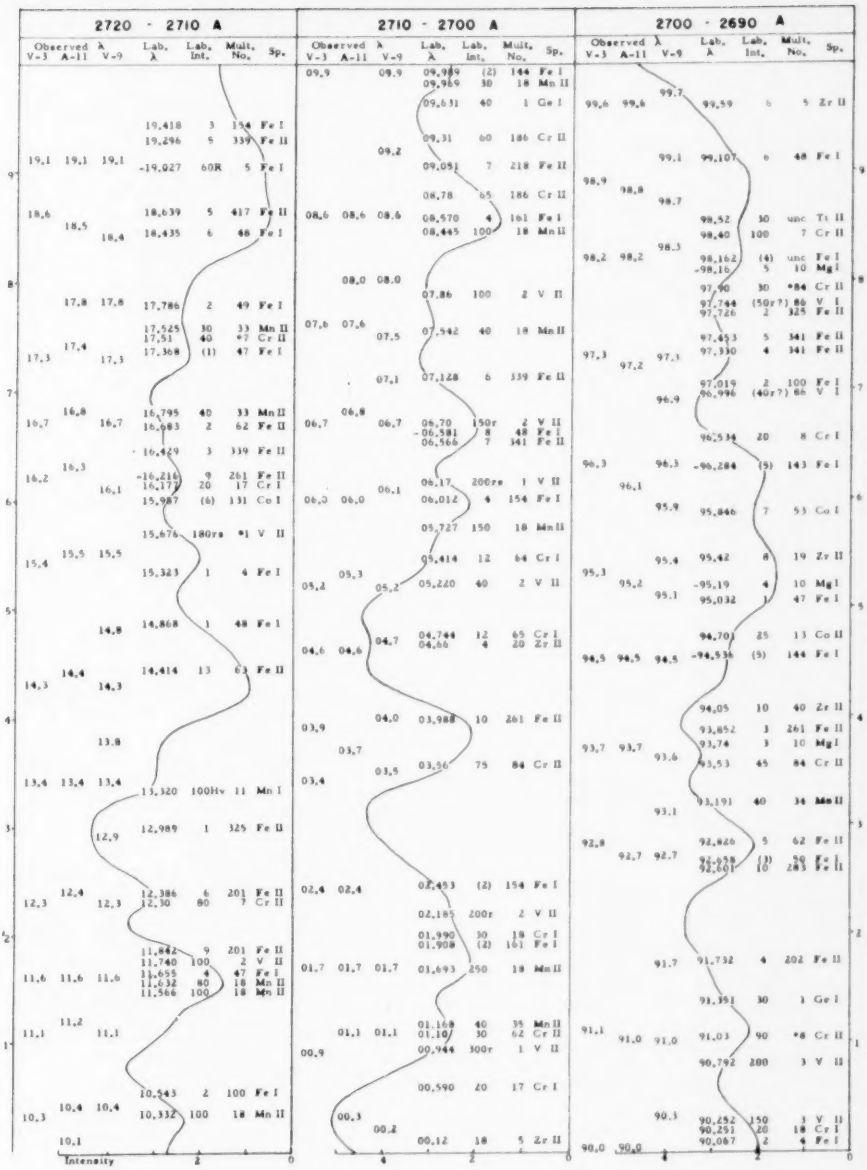

TABLE 2—*Continued*

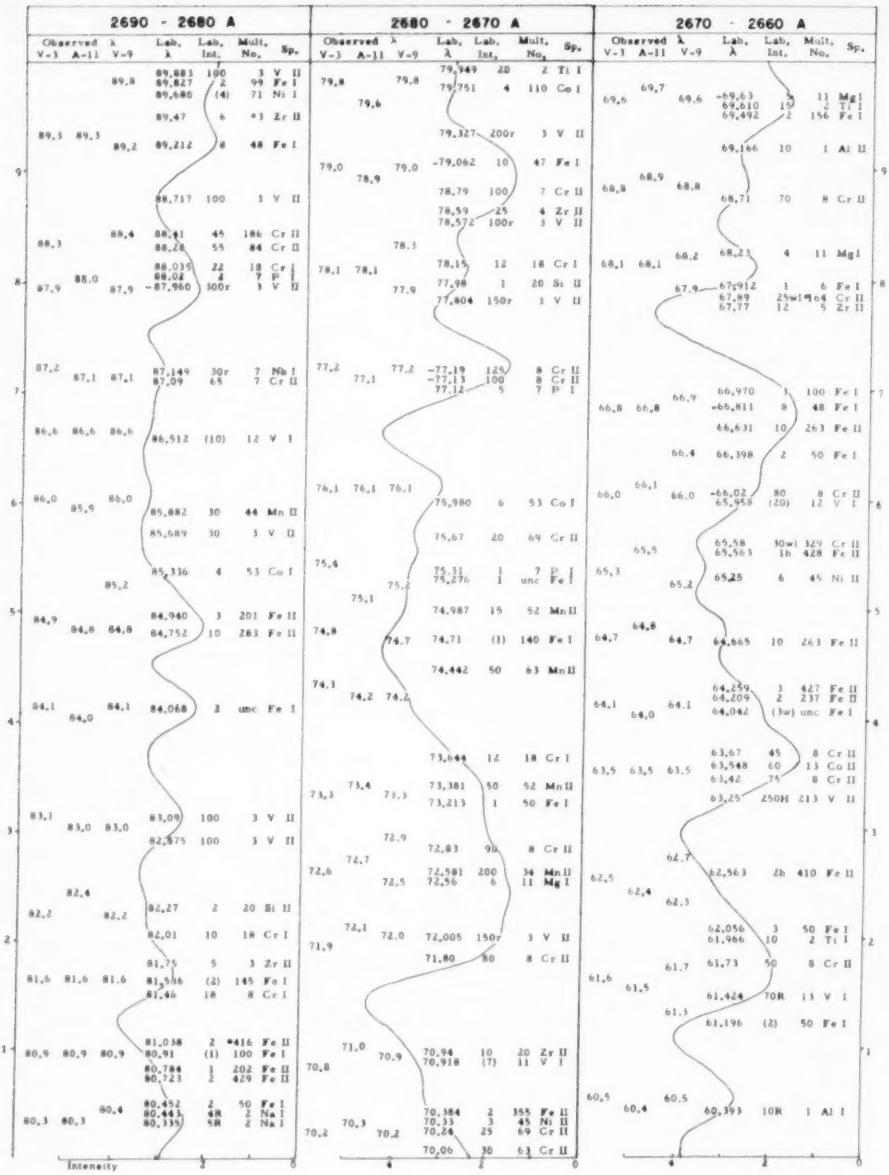

TABLE 2—*Continued*

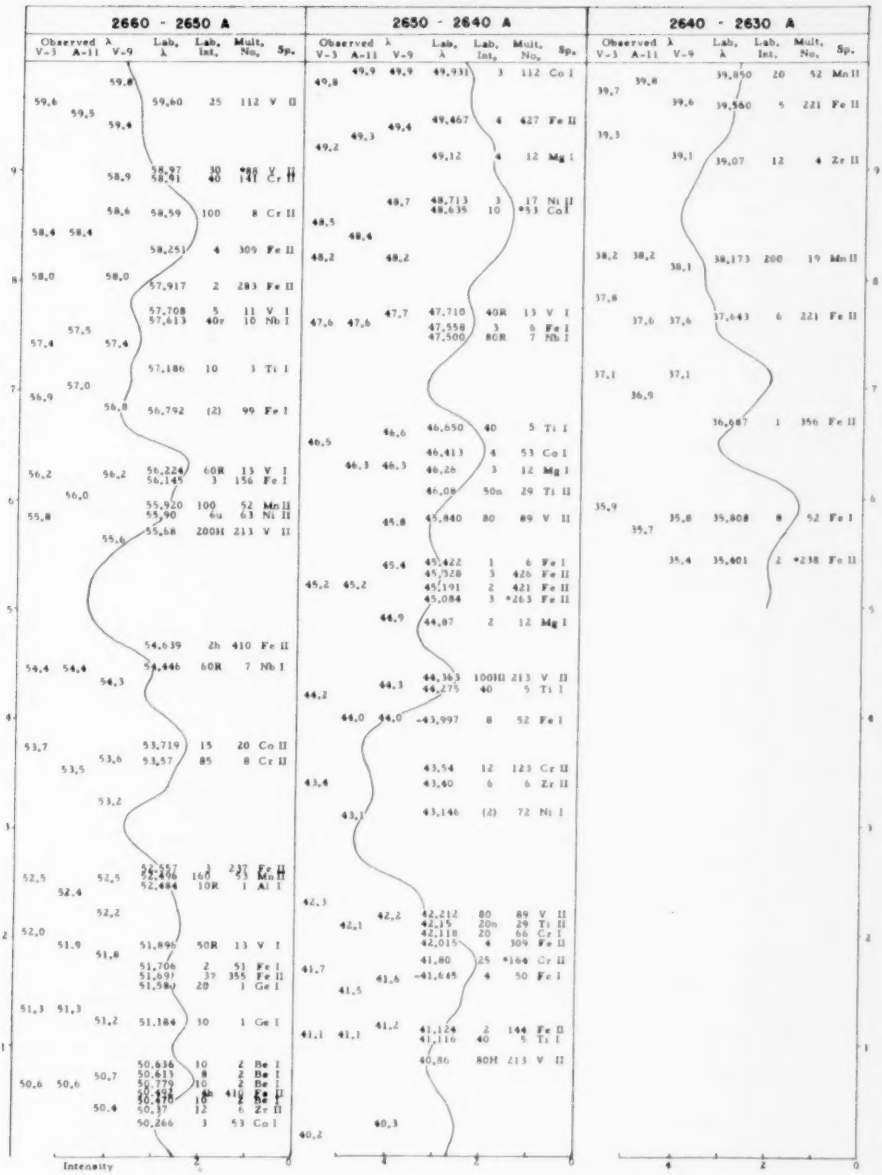

importance of the other contributors. The fifth column lists the laboratory intensities given in the *Revised Multiplet Table*. As indicated there, extreme caution must be exercised when comparing intensities between elements or different spectra of the same element. Within a single multiplet, however, the intensities have more significance. The sixth column gives the multiplet numbers; an asterisk in front indicates that the line is blended with another line in the same spectrum; and when the two lines are from different multiplets, only the lower multiplet number is given. The seventh column names the spectra from which the lines originate.

## IDENTIFICATION

The initial step toward identification was made with the aid of microphotometer traces of emission spectra of the following elements, most prominent in the solar atmosphere: *Mg, Al, Si, Ti, V, Cr, Mn, Fe, Co,* and *Ni*. The spectra were photographed with a spectrograph similar to the flight instrument. The leading multiplets were marked on the traces, and a comparison was made with the solar trace. With this as a guide, rough sets of minimum values of laboratory intensity and maximum values of low excitation potential for the first and second spectra of the above elements were established for the purpose of determining which lines of these elements might be expected to be significant in a solar spectrum at the present resolution.

Compilation of the identification table was begun by preparing, from the *Ultraviolet Multiplet Table*, a finding list of all fairly low-level lines of the above elements of intensity greater than the tentative minima established with the aid of the laboratory spectra. This list was compared with the list of observed wave lengths and the intensity trace of the solar spectrum in the form of Table 2. The various members of each multiplet were examined and compared with the intensity values indicated by the curve, the effects of blending described earlier being kept in mind. Many other lines of intensity below the tentative minima were added for spectra well represented in the sun, especially when the excitation potential was low and also when the solar absorption was weak.

Multiplets of all likely first and second spectra through niobium ($Z = 41$), where the *Ultraviolet Multiplet Table* at present ends, were carefully examined. For heavier elements, identifications would, at best, be dubious in the light of the faintness of their lines in the Rowland table and the serious blending in the rocket spectra. A search for the "raies ultimes"[13] and sensitive lines[14] of these elements that lie in our region led to no conclusive results. However, it should be mentioned that many of these spectra, especially the rare earths, are far from completely known in the laboratory. Future study of molecular absorption in this region is tempting but was felt to be unwarranted with the present resolution. Third spectra were also considered, but in this spectral range no probable contributors were found.

## NOTES ON THE IDENTIFICATION TABLE

Perusal of Table 2 will show that the positions of the lines observed on the three rocket firings are in agreement within 0.2 A or less, with some exceptions, where the blending situation is such that a line in one spectrum is split in another. In the Viking 3 spectrum, underexposure accounts for the absence of lines in three low-intensity regions near 2852, 2800, and 2750 A. The Viking 9 spectrum showed more lines than the other two; however, a number of lines were missing on this spectrum, owing to its abnormally low contrast.

The list of observed wave lengths in Viking 3 contains some entries which cannot readily be distinguished on the intensity-curve, although it was made largely from this spectrum, and there are places where the nature of the curve suggests the presence of a

[13] W. F. Meggers, *J. Opt. Soc. Amer.*, **31**, 39, 605, 1941.

[14] *M.I.T. Wavelength Tables* (New York: John Wiley & Sons, Inc., 1939).

line and none was observed under the comparator. We have listed only those features that were recorded consistently by more than one observer, and we consider the list to be more reliable than the curve with respect to the features and wave lengths. The curve, however, is the index of the intensity and nature of the wave-length entries. There is a residual uncertainty in the wave-length scale of the intensity trace of about 0.1 A, due to lack of precision in the microphotometer drive system; this, combined with the error in comparator setting of 0.1 A, accounts for the occasional observed lines which do not fall exactly at the minima of the intensity trace.

In many cases the identification of the observed lines is clear-cut, and there is no doubt that one particular line is the prominent contributor. At the other extreme there are confused regions with many weak lines, where the spacing and relative intensity of the contributors and their relation to the instrumental resolution determine the nature of the observed intensity-curve and the number of lines that can be seen. In these regions the observed number of lines and their wave lengths are more likely to differ in the three spectra. Between these extremes there are intermediate cases of all sorts. Predominant contributors are designated only where they were reasonably certain, and no further breakdown is given. In some cases the predominant contributor seems to lie quite far away from the observed line. This is believed to be a result of the instrumental blending, as explained by the previous discussion of the Utrecht curve and illustrated in Figure 3, *a*.

The four most conspicuous lines whose principal contributors have not been found lie at 2919, 2684, 2640, and 2637 A. There are, of course, numerous other inadequately identified features. The wing at 2860.5 A, which appears as a resolved line on the Viking 9 spectrum, coincides with a strong line of *As* I, an element not yet detected in the sun. However, the leading line of this multiplet, at 2780.22 A, is masked, and the identification, though tempting, cannot be confirmed without higher resolution.

A few other special cases of lines not included in the table should be mentioned. *O* I, though abundant, appears to be seriously blended, and its one multiplet in this region has not been included. *Ga* I, being masked, has also been omitted, although the rocket region is favorable for several strong lines. The "raie ultime" of *Pt* I lies at 2659.44 A; this may account for the line at 2659.4 A, resolved in Viking 9, though there is a weak line of *V* II at 2659.60 A. Another sensitive line of *Pt* I at 2830.295 A may be present as a contributor. There are six sensitive lines of *Ru* II reported[14] in this spectral range; the presence of the line at 2945.668 A is suggested by the unidentified line near 2945.8 A observed in all three spectra; the others are either masked or not observed.

Three lines of *P* I have been included in the table. The strongest of these, lying at 2677.2 A, is masked by *Cr* II. Another, at 2688.0 A, is blended with *V* II. The third, considered too weak for inclusion in the *Ultraviolet Multiplet Table*, lies at 2675.3 A in a flat region with several other weak lines and is certainly not prominent. The presence of this multiplet is considered likely, but it is completely masked, and its strength cannot be judged.

Beryllium, according to the Rowland tables, is represented by four weak lines. There are six *Be* I lines between 2650.470 and 2650.779 A, four of which are listed in Table 2. These lines, which, of course, lie too close together to be resolved by our spectrograph, coincide with an otherwise unsatisfactorily identified line of moderate intensity, present in all three spectra. A preliminary search for a *Be* I triplet at 2496 A and the "raie ultime" at 2348.612 A in the portion of the Viking 9 spectrum not yet analyzed was inconclusive. We therefore regard the presence of the six lines as likely but not definite.

Two previous analyses have been made of rocket ultraviolet spectra; the one by Durand, Oberly, and Tousey[1] in 1949 and the other by Hopfield and Clearman[15] in 1948 and revised by Clearman[16] in 1953. An indication of the improvement in resolution obtained in the present work is given by the numbers of observed lines in the region 2990–

[15] *Phys. Rev.*, **73**, 877, 1948.

[16] *Ap. J.*, **117**, 29, 1953.

2635 A. Durand, Oberly, and Tousey list 106 measured wave lengths with 247 identifications; Clearman gives 160 observed lines and 283 identifications; Table 2 lists 373 observed lines for Viking 3, 372 for Aerobee 11, and 488 for Viking 9 and attributes them to 1054 atomic lines.

In general, the analysis of Durand, Oberly, and Tousey is supported at its degree of resolution. There seems, however, to have been a consistent omission of weaker lines of *Mg* I, whose presence is confirmed by our greater resolution. Their analysis was based on an early manuscript copy of the *Ultraviolet Multiplet Table*, which accounts for the fact that most of the multiplet numbers, many of the laboratory intensities, and even some of the laboratory wave lengths are different from the corresponding entries in Table 2.

Clearman's analysis discriminates against noniron lines. We feel that other elements of the first long period in addition to iron may well be prominent. Chromium, especially, seems to have been underestimated, for no *Cr* II lines and only four *Cr* I lines are listed in the region covered here. The "raie ultime" of *Cr* II lies at 2835.63 A; although blended with two lines of *Fe*, it is considered by us to be the predominant contributor to the observed line at 2835.6 A; and, indeed, all 14 lines of the multiplet are clearly present. As a result of this underestimation of chromium and other noniron lines, Clearman was led to identify three lines in his spectrum as due solely to *P* I, multiplet 7. These lines, as discussed previously, are considered by us to be masked.

The *Mg* II doublet at 2802.698 and 2795.523 A and the emission cores have already been discussed in a note by Johnson, Purcell, Tousey, and Wilson.[17] The changes of 0.1 A in observed wave lengths of the three features noted within the absorption region are due to the fact that the wave lengths were previously calculated by using only the two emission lines as standards, while those in Table 2 used many standards covering the whole region. Some of the contributing atomic lines mentioned in the note are omitted because they are considered too weak to contribute significantly.

No attempt was made to measure any equivalent widths. Only the *Mg* II doublet at 2800 A, the "raie ultime" of *Mg* I at 2852 A, and the *Si* I line at 2882 A even approach showing any part of their true line shapes, because of instrumental and natural blending. Furthermore, the background level has not been determined. Therefore, it is left to the reader to choose his own background and estimate the shapes of the wings, if he wishes to do so.

The shapes of the *Mg* II emission cores are largely instrumental. Their areas were measured from the Aerobee 11 trace to be 0.7 and 1.2 microwatt $cm^{-2}$. The intensity ratio, computed from these values, is 1.7. This is considered satisfactory agreement with the theoretical ratio of approximately 2.0, in view of the uncertainty in estimating the local continuum and also because of the difficulties of applying photographic photometry to lines which do not have flat tops.

[17] *Ap. J.*, **117**, 238, 1953.

# THE APPLICATION OF AN OSCILLOSCOPIC MICROPHOTOMETER TO THE SPECTRAL CLASSIFICATION OF LATE-TYPE STARS*

WILLIAM R. HOSSACK
David Dunlap Observatory
*Received December 31, 1953*

ABSTRACT

A technique with an oscilloscopic microphotometer has been applied to the classification of late-type spectra photographed with dispersion 33 A/mm. This technique gives luminosity classifications having probable errors of the order of 0.15 of a luminosity class and spectral-type classifications having probable errors of about 0.2 of a spectral subclass. The speed of measurement is comparable to that of visual classification.

## INTRODUCTION

The method most widely used today for the classification of stars from examination of their spectra is that developed by Morgan and his associates and known under the names of the MKK[1] and MK[2] systems. This method involves visual comparison of the spectra but does not entail any attempt to estimate numerically or to measure the strengths of individual lines or features in the spectra. Young and Harper[3] have used numerical estimates of line strength in their system; and astronomers in Sweden[4] have used a recording microphotometer to measure line strengths in their system. However, the time and labor involved in these latter methods, when used with slit spectra of moderate dispersion, have put them at a disadvantage as compared with the speed of the visual-comparison system.

The method employed for classification, which will now be described, is as rapid as visual classification and is capable of greater precision. It involves making numerical measures of the strengths of certain lines without using the density calibration of the plate. For this purpose, use was made of a new type of instrument called an "oscilloscopic microphotometer," which has been described by the author in a recent paper.[5] This instrument is capable of presenting, upon an oscilloscope screen, spectrophotometric traces of two stellar spectra, derived from their separate spectrograms. The technique for obtaining the measures of line strength has been fully described in the earlier paper, and it may be summarized as follows: Two traces appeared on the oscilloscope screen, one corresponding to the spectrogram to be classified and the other to a standard spectrogram that always remained in the microphotometer carriage. Amplification controls made it possible to adjust the vertical magnitude of either trace. The pair of lines for which the ratio was to be estimated was compared with the same pair in the standard trace, and the first line of the pair was made to appear of equal depth in both traces by means of the amplification controls. If the second line of the pair in the trace of the

* *Communication from the David Dunlap Observatory*, No. 35.

[1] Morgan, Keenan, and Kellman, *An Atlas of Stellar Spectra with an Outline of Spectral Classification* ("Astrophysical Monographs" [1943]).

[2] Johnson and Morgan, *Ap. J.*, **117**, 313, 1953.

[3] *Pub. Dom. Ap. Obs. Victoria*, **3**, 3, 1927.

[4] See, e.g., Lindblad and Stenquist, *Stockholm Astr. iaktt. och. unders.* (*Stockholm Ann.*), Vol. **11**, No. 12, 1934; Lindblad, *Ap. J.*, **104**, 325, 1946.

[5] *J.R.A.S. Canada*, **47**, 195, 1953.

spectrogram to be examined then appeared deeper than in the trace of the standard, a scaled rheostat in series with the analyzing light of the microphotometer was used to cut down the light supplied to the optical system until this second line in the trace of the spectrogram to be examined appeared to have the same depth that it had had in the standard trace for full light. The setting of the rheostat, a number, was recorded. When the second line was stronger in the standard trace, a similar procedure was carried out, and the number was termed negative. The examination of a single plate in this manner yielded three or four numbers representing line ratios (in terms of the ratios in the standard star), which could be used as luminosity criteria, and two to five similar numbers, which could be used as spectral-type criteria.

In order to assay the value of these oscilloscopic line ratios in spectral-type and luminosity classification, it is necessary to compare them with some well-established system. The MK system of luminosity classes appeared preferable to any system of spectroscopic absolute magnitudes or parallaxes, because it is more widely used and because it is based on the spectrum alone and involves no calibration from spectrum to absolute magnitude. Calibration of the MK system, it is maintained, should be considered as a separate problem and should be continuously adjusted as our knowledge increases. It is unfortunate that the probable error of a particular estimate in the MK system is so difficult to estimate and cannot be accounted for in statistical problems. The luminosities in the MK system are seldom given to closer than half a luminosity class; and, indeed, many investigators show a decided preference for integral values because the standards usually have integral values. A scale with no such selection effect and with more continuous units, even involving no greater precision, would be preferable for statistical purposes.

Since the spectrograms employed by the writer were of dispersion 33 A/mm at 4340 A, four times that used in the MK work, a decimal system seemed feasible for luminosity classes and for subclasses of spectral type.

Line ratios sensitive to luminosity or spectral type were measured with the microphotometer, and from each such ratio an independent estimate of luminosity or spectral type was obtained. Averages were taken, and the internal probable error among the criteria was calculated.

In the following sections details of the determination of luminosity ratios and spectral-type ratios are treated separately, and an attempt is made to relate these ratios to the Roman numeral system of luminosity and spectral type. However, it should be emphasized that the problem of relating a continuous variable to a discretely varying quantity when observational errors are present in both is extremely difficult. Until measures are available on a series of MK standards, the true relation between the oscilloscopic ratios and the MK system cannot be established. Nevertheless, the data at hand do suffice to indicate the degree of precision of the oscilloscopic classification, which, it should be emphasized, is the principal purpose of this investigation.

## LUMINOSITY DETERMINATIONS

Eighty-seven spectrograms with fairly uniform plate densities, of K0- and K1-type stars were examined for luminosity. Seven of the spectrograms, with densities covering the range involved in the entire sample, were of the same star, in order that the effect of density upon the line-ratio values could be checked. The fact that density calibration was not used made this essential. A plate of $\tau$ CrB (MK: K0 III) was employed as a comparison plate in the microphotometer.

The following luminosity criteria in the 4045–4350 A range were examined: 4045/4077, 4077/4071, 4215/4202, 4226/4215, 4250/4215, 4233/4236, and 4260/4258. These criteria were selected from the MKK *Atlas* and from the *Handbuch der Astrophysik*.[6] The

[6] *Handbuch der Astrophysik*, **5**, No. 1, 455–472, 1932.

4045/4077, 4226/4215, and 4260/4258 criteria showed too large a density effect and were eliminated from further consideration.

In Figure 1 the ratios for three criteria are plotted as ordinates against the 4250/4215 criterion ratios as abscissae, each point representing a single plate. A visual classification of the spectra, using MKK standards, had been made in the course of another investigation by Mr. Ian Halliday, now of the Dominion Observatory. His classifications were accepted, and his visual luminosity classes are marked in Figure 1 opposite the corresponding ratio value. The correlation can be judged from Figure 1, and it will also be noted from Figure 1 (*bottom*) that the ratio 4233/4236 is very sensitive to luminosity in the I's and II's and insensitive below the III's.

Figure 2 serves to illustrate the problem involved in relating the oscilloscopic ratios to the system of visual luminosity classes. In Figure 2 the ratios for the 4250/4215 criterion are plotted as abscissae, and the corresponding visual luminosity classes as ordinates, each point representing a plate, as before. The problem is to predict, for a specific ratio value, the luminosity class which would have been obtained had the visual classification according to the MK system been done with no errors and on a continuous scale. A method suggested by Trumpler and Weaver[7] was used to obtain the relation between line ratio and luminosity class and resulted in the curve of Figure 2. The data were first corrected for observational errors; and the correction, of course, involved some arbitrary, but not unreasonable, assumptions, particularly in the case of visual classifications. The points shown in Figure 2 correspond to uncorrected data.

Curves were obtained in this way for all the luminosity criteria; and, after a decimal and therefore Arabic system of luminosity classes had been introduced, the curves were used to obtain a luminosity estimate for each measured ratio. Estimates were averaged for each spectrum, with the 4233/4236 ones being given much weight in luminosity classes 1 and 2 and no weight in classes 4 and 5. Results of the writer's classification are given in Table 1. Values are given to one-tenth of a luminosity class. The Halliday visual luminosities are also listed, together with Miss Roman's published estimates[8] for a few of the stars.

The standard deviation of luminosity obtained by using a single criterion was 0.34 of a luminosity class. This was equivalent to a probable error of the mean of three criteria of 0.13 of a luminosity class. It is to be noted that the line 4215 A is involved in two of the ratios and that they are therefore not entirely independent. It can be shown that, at worst, this would raise the probable error of the mean to 0.18 of a luminosity class.

The probable error of a mean luminosity from a single plate was obtained in a different manner by comparing the means of the seven plates used for density checking. This probable error turned out to be 0.16 of a luminosity class. Consequently, it can be assumed that the luminosities in the column of averages in Table 1 have probable errors of roughly 0.15 of a luminosity class. The use of more criteria would further reduce this in future work. Such a probable error justifies the use of a decimal system of luminosities. The precision makes the method useful for investigations such as those designed to obtain luminosity functions, calibrations to more precise absolute magnitudes, etc.

Table 1 shows $\tau$ CrB to be fainter than $\alpha$ UMa, although both are MK standard K0 III's. From Table 1, $\gamma$ Cep appears to be brighter than $\eta$ Cep, although they are both MK standard IV's. The difference in their spectral types, K1–K0, does not entirely account for this. It is well known that small discrepancies do exist in some similar MK standards. The present method could be used to calibrate the standards more precisely in terms of luminosity class. This would be valuable, since an investigator using a poor standard will incorporate into his work an unknown systematic error, which

[7] *Statistical Astronomy* (Berkeley and Los Angeles: University of California Press, 1953), p. 154.

[8] *Ap. J.*, **116**, 122, 1952.

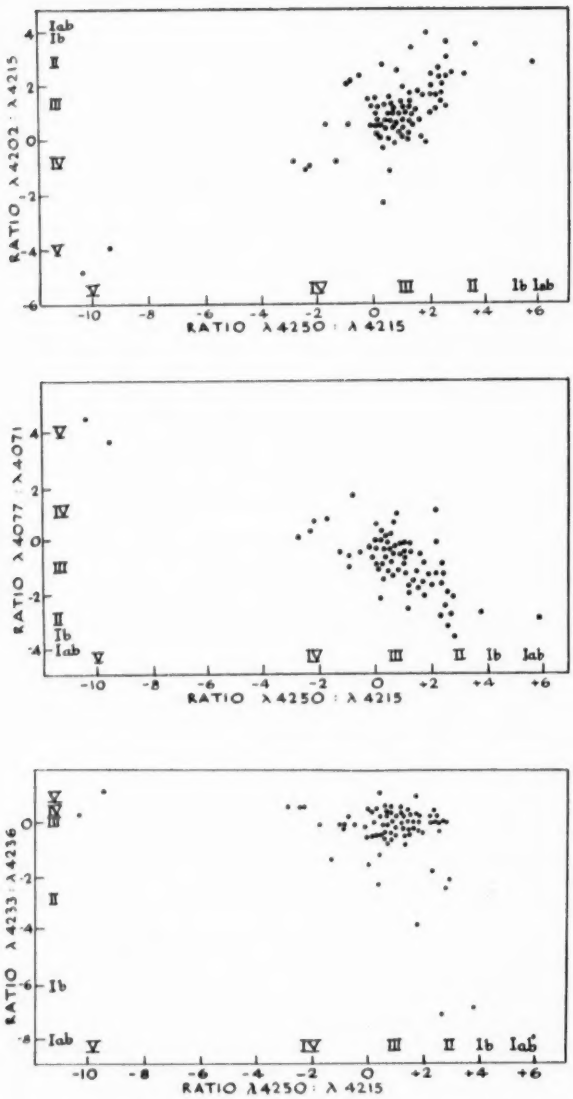


FIG. 1.—Ratios for three luminosity criteria plotted as ordinates against the λ 4250: λ 4215 luminosity criterion ratios as abscissae, each point representing a single plate.

will be important, even though his precision may be low. His random errors can be accounted for statistically, but not this systematic error. If, on the other hand, he uses several similar standards which are actually different, his precision cannot be anything but lowered.

### SPECTRAL-TYPE DETERMINATIONS

Forty-two spectra assigned visually to class III and having spectral types ranging from G5 to K5 from visual comparison with MK standards were examined on the oscilloscopic microphotometer for spectral type. Several spectrograms of HD 213389 were also measured as a check on the effects of plate density. The plate of $\tau$ CrB was again employed as the comparison plate in the microphotometer.

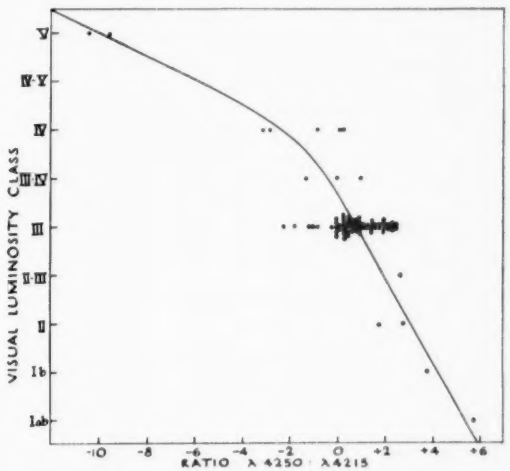


FIG. 2.—Ratios for the λ 4250:λ 4215 luminosity criterion plotted against visual luminosity class, each point representing a single plate. The relation between them is drawn in.

The following spectral-type criteria were examined: 4030–4034/4300, 4101/4096, 4226/4271, 4226/4290, 4260/4254, 4271/4274, 4290/4300, 4326/4226, and 4384/4340. These criteria were again selected from the MKK *Atlas* and the *Handbuch der Astrophysik*. The density effects were found to be large in some of these, and for final measurements the following were used: 4101/4144, 4340/4326, 4384/4340, 4260/4254, and 4290/4300. The first three are hydrogen criteria, and the last two metallic.

The ratios for some of the criteria are plotted against one another in Figure 3, *a* and *b*, where each point represents a plate. Halliday's corresponding visual values are again marked in, and the correlation between the ratios can easily be judged. According to Figure 3, the hydrogen criteria are much the best for G-type spectra; in K-type spectra the hydrogen lines are too weak to be measured accurately, and the metallic criteria are better.

The same method was employed to obtain the relation between line ratio and spectral type as was used in the previous section in relation to luminosity. Hydrogen ratios were used for classification, G5–G9. Metallic ratios were used for classification, K1–K5. All ratios were used for classification, G9–K1. Results of the oscilloscopic classification are

## TABLE 1

### Luminosity Estimates

| Star | 4077/4071 | 4233/4236 | 4202/4215 | 4250/4215 | Average | Halliday | Roman |
|---|---|---|---|---|---|---|---|
| HD 1419 | 2.6 | ..... | 2.8 | 2.6 | 2.7 | III | ..... |
| 2952 | 3.2 | ..... | 2.8 | 2.3 | 2.8 | III | ..... |
| 4372 | 3.4 | ..... | 3.9 | 4.1 | 3.8 | IV | ..... |
| 12897 | 3.4 | ..... | 3.0 | 3.4 | 3.3 | III | ..... |
| 15328 | 3.3 | ..... | 3.3 | 3.4 | 3.3 | III | ..... |
| 15464 | 3.4 | ..... | 3.2 | 3.0 | 3.2 | III | ..... |
| 28191 | 3.0 | ..... | 3.4 | 3.4 | 3.3 | III | ..... |
| 34810 | 2.3 | ..... | 2.9 | 2.2 | 2.5 | III | ..... |
| 35238 | 3.0 | ..... | 3.4 | 2.5 | 3.0 | III | ..... |
| 36040 | 3.0 | ..... | 3.4 | 3.4 | 3.3 | III | ..... |
| 41467 | 2.3 | ..... | 2.9 | 2.0 | 2.4 | III | ..... |
| 42466 | 2.4 | ..... | 2.9 | 2.9 | 2.7 | III | ..... |
| 44780 | 3.0 | ..... | 3.4 | 2.8 | 3.1 | III | ..... |
| 46178 | 3.2 | ..... | 2.7 | 2.7 | 2.9 | III | ..... |
| 46509 | 2.5 | ..... | 2.7 | 2.4 | 2.5 | III | ..... |
| 47220 | 3.1 | ..... | 3.1 | 2.7 | 3.0 | III | ..... |
| 47270 | 2.5 | ..... | 2.9 | 2.9 | 2.8 | III | ..... |
| 54825 | 2.3 | 2.2 | 2.2 | 2.2 | 2.2 | III | ..... |
| 63799 | 3.5 | ..... | 3.2 | 3.1 | 3.3 | III | ..... |
| 65066 | 3.3 | ..... | 3.3 | 2.8 | 3.1 | III | ..... |
| 65735 | 3.3 | ..... | 3.4 | 2.8 | 3.2 | III | ..... |
| 65757 | 3.2 | ..... | 3.2 | 3.5 | 3.3 | III–IV | ..... |
| 73599 | 3.4 | ..... | 3.6 | 3.4 | 3.5 | III | ..... |
| 77445 | 2.4 | ..... | 2.7 | 2.4 | 2.5 | III | ..... |
| 89268 | 3.0 | ..... | 3.3 | 2.7 | 3.0 | III | ..... |
| 103953 | 3.3 | ..... | 2.6 | 2.1 | 2.7 | III | ..... |
| 111591 | 3.3 | ..... | 2.8 | 2.8 | 3.0 | III | ..... |
| 116594 | 3.1 | ..... | 2.8 | 2.1 | 2.7 | III | ..... |
| 153226 | 3.4 | ..... | 3.7 | 4.1 | 3.7 | IV | ..... |
| 154391 | 3.0 | ..... | 3.4 | 3.1 | 3.2 | III | ..... |
| 162468 | 3.3 | 2.2 | 2.8 | 3.4 | 2.9 | III–IV | ..... |
| 166207 | 2.1 | ..... | 2.3 | 2.3 | 2.2 | III | ..... |
| 167304 | 3.0 | ..... | 3.5 | 3.0 | 3.2 | III | ..... |
| 169221 | 3.0 | ..... | 3.2 | 3.3 | 3.2 | III | ..... |
| 175743 | 3.3 | ..... | 3.5 | 3.5 | 3.4 | III | ..... |
| 176776 | 3.3 | ..... | 3.2 | 3.5 | 3.3 | III | ..... |
| 181597 | 3.3 | ..... | 3.4 | 3.4 | 3.4 | III | ..... |
| 182272 | 3.4 | ..... | 3.0 | 3.2 | 3.2 | III | ..... |
| 185436 | 2.5 | ..... | 2.4 | 3.1 | 2.7 | III | ..... |
| 194220 | 3.3 | ..... | 3.1 | 2.8 | 3.1 | III | ..... |
| 194616 | 2.4 | ..... | 2.9 | 2.1 | 2.5 | III | ..... |
| 195820 | 3.3 | ..... | 3.6 | 2.5 | 3.1 | III | ..... |
| 203630 | 3.0 | ..... | 3.7 | 3.0 | 3.2 | III | ..... |
| 203886 | 3.0 | ..... | 3.4 | 3.1 | 3.2 | III | ..... |
| 210026 | 4.0 | ..... | 2.5 | 2.4 | 3.0 | III | ..... |
| 212750 | 3.3 | ..... | 3.7 | 3.6 | 3.5 | III | ..... |
| 214265 | 3.0 | ..... | 3.7 | 3.7 | 3.5 | III | ..... |
| 218356 | 2.3 | 2.3 | 2.3 | 2.4 | 2.3 | II–III | ..... |
| 218416 | 3.3 | ..... | 2.6 | 2.5 | 2.8 | III | ..... |
| 218660 | 3.3 | ..... | 3.0 | 2.6 | 3.0 | III | ..... |
| 221364 | 3.2 | ..... | 3.0 | 3.0 | 3.1 | III | ..... |
| 221861 | ..... | 1*ab* | ..... | ..... | 1*ab* | 1*ab* | ..... |
| 224895 | 3.3 | ..... | 3.2 | 3.1 | 3.2 | III | ..... |
| $\zeta$ And | 2.4 | 2.5 | 3.0 | 3.5 | 2.8 | III | II |
| $\tau$ Psc | 3.4 | ..... | 3.2 | 3.4 | 3.3 | III | III–IV |
| $\xi$ And | 3.2 | ..... | 3.4 | 3.8 | 3.5 | III | III–IV |
| 49 And | 2.8 | ..... | 2.5 | 2.4 | 2.6 | III | III |
| 107 Psc | 4.9 | ..... | 4.9 | 4.9 | 4.9 | V | V |
| 39 Ari | 3.3 | ..... | 2.5 | 3.7 | 3.2 | III | III |

TABLE 1—*Continued*

| Star | 4077/4071 | 4233/4236 | 4202/4215 | 4250/4215 | Average | Halliday | Roman |
|---|---|---|---|---|---|---|---|
| 46 LMi | 3.8 | ..... | 3.4 | 4.1 | 3.8 | III | III |
| $\psi$ UMa | 3.3 | ..... | 3.0 | 3.5 | 3.3 | III | III |
| HR 4668 | 3.4 | ..... | 2.9 | 3.6 | 3.3 | III | III |
| HR 5361 | 3.2 | ..... | 2.7 | 3.9 | 3.3 | III | III |
| $\kappa$ CrB | 3.8 | ..... | 3.2 | 4.0 | 3.7 | III | III–IV |
| HR 6199 | 3.7 | ..... | 3.3 | 3.8 | 3.6 | III–IV | III |
| $\kappa$ Lyr | 3.1 | ..... | 2.1 | 2.7 | 2.6 | III | III |
| $o$ Dra | 2.9 | ..... | 2.8 | 3.0 | 2.9 | III–IV | II–III |
| $\epsilon$ Aql | 3.3 | ..... | 3.2 | 3.1 | 3.2 | III | III |
| HR 7468 | 3.7 | ..... | 3.2 | 3.5 | 3.5 | III | III |
| $\phi$ Cyg | 3.8 | ..... | 2.4 | 3.1 | 3.1 | III | III–IV |
| 12 Peg | ..... | 1*b* | ..... | ..... | 1*b* | 1*b*–II | 1*b* |
| 56 Peg | 2.4 | 2.5 | 2.2 | 2.8 | 2.5 | III | II pec. |
| $\alpha$ UMa | 2.9 | ..... | 3.3 | 3.2 | 3.1 | Standard K0 III | |
| $\tau$ CrB | 3.5 | ..... | 3.5 | 3.4 | 3.5 | Standard K0 III | |
| $\theta$ Her | 2.2 | 1*b*.9 | 2.1 | 2.5 | 2.0 | Standard K1 II | |
| $\theta$ Lyr | 2.0 | 2.5 | 2.1 | 2.0 | 2.2 | Standard K0 II | |
| $\sigma$ Dra | 5.1 | ..... | 5.3 | 5.1 | 5.2 | Standard K0 V | |
| $\eta$ Cep | 4.1 | ..... | 4.0 | 3.7 | 3.9 | Standard K0 IV | |
| $\zeta$ Cep | ..... | 1*b* | ..... | ..... | 1*b* | Standard K1 1*b* | |
| $\gamma$ Cep | 3.0 | ..... | 3.4 | 3.4 | 3.3 | Standard K1 IV | |
| HD 213389 (check) | 2.9 | ..... | 2.5 | 2.9 | 2.8 | No correlation with density | |
| | 2.8 | ..... | 2.8 | 2.8 | 2.8 | | |
| | 3.8 | ..... | 2.8 | 3.4 | 3.3 | | |
| | 3.0 | ..... | 3.1 | 3.4 | 3.2 | | |
| | 3.3 | ..... | 2.6 | 3.3 | 3.1 | | |
| | 3.6 | ..... | 2.3 | 2.3 | 2.7 | | |
| | 3.1 | ..... | 2.6 | 2.7 | 2.8 | | |

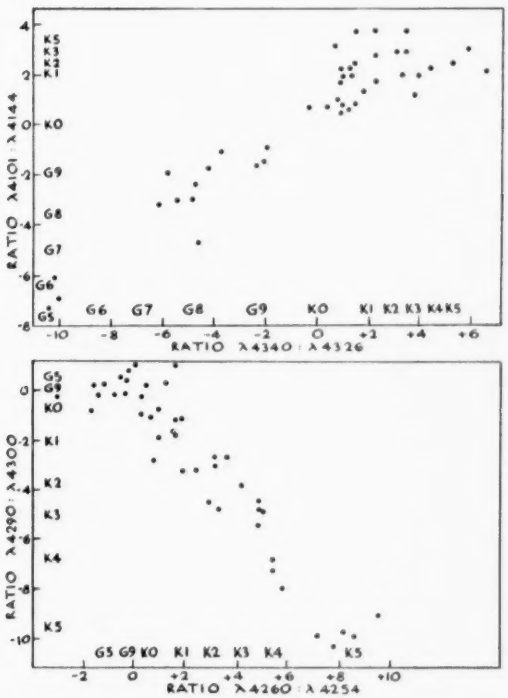


FIG. 3.—Plots of corresponding ratios for hydrogen spectral-type criteria, each point representing a single plate (*top*); plots of corresponding ratios for metallic spectral-type criteria, each point representing a single plate (*bottom*).

given in Table 2. Halliday's visual classifications are also listed, together with Miss Roman's estimates for a few of the stars.

The standard deviation of a spectral type obtained by using a single criterion was 0.43 of a spectral subclass. This was equivalent to a probable error of the mean of 0.17 of a spectral subclass. The probable error of the mean from plate-to-plate considerations of HD 213389 was 0.15 of a spectral subclass. These probable errors of the mean demonstrate a precision warranting the tenth spectral subclass units employed.

TABLE 2

SPECTRAL-TYPE DETERMINATIONS

| Star | 4101/4144 | 4340/4326 | 4384/4340 | 4260/4254 | 4290/4300 | Average | Halliday | Roman |
|---|---|---|---|---|---|---|---|---|
| HR 152 | ..... | ..... | ..... | K5.2 | K4.8 | K5.0 | K5 | K5 |
| $\zeta$ And | G8.2 | G7.9 | G8.1 | K1.8 | K2.2 | Pec. | K1 | K1 |
| $\eta$ And | G8.7 | G7.7 | G8.1 | K1.1 | G9.4 | Pec. | G9 | G8 |
| $\epsilon$ Pis | G8.8 | G8.4 | G8.7 | ..... | ..... | G8.6 | G8 | K0 |
| $\eta$ Pis | G8.4 | G8.1 | G8.2 | ..... | ..... | G8.2 | G8 | G8 |
| 51 And | ..... | ..... | ..... | K3.4 | K3.1 | K3.2 | K3 | K3 |
| 39 Ari | ..... | ..... | ..... | K1.7 | K0.7 | K1.2 | K1 | K0 |
| $\lambda$ Leo | ..... | ..... | ..... | K4.8 | K5.0 | K4.9 | K5 | K5 |
| $\mu$ Leo | ..... | ..... | ..... | K2.6 | K2.0 | K2.3 | K3 | K2 |
| $\psi$ UMa | ..... | ..... | ..... | K1.1 | K0.5 | K0.8 | K1 | K1 |
| 11 Com | G8.9 | G9.0 | G8.5 | ..... | ..... | G8.8 | G8 | G8 |
| HR 6388 | ..... | ..... | ..... | K3.4 | K3.4 | K3.4 | K4 | K3 |
| $\xi$ Her | G8.9 | G9.1 | G9.1 | ..... | ..... | G9.0 | G9 | K0 |
| HR 6791 | G8.0 | G7.5 | G7.8 | ..... | ..... | G7.8 | G9 | K0 pec. |
| $\epsilon$ Aql | K1.2 | K1.0 | K1.3 | G9.9 | G9.8 | K0.6 | K0 | K2 |
| 53 Dra | G8.1 | G8.1 | G8.3 | ..... | ..... | G8.2 | G9 | G8 |
| HR 7956 | ..... | ..... | ..... | K2.4 | K2.4 | K2.4 | K3 | K3 |
| HR 8475 | ..... | ..... | ..... | K1.7 | K0.8 | K1.2 | K2 | K2 |
| 66 Peg | ..... | ..... | ..... | K2.7 | K2.5 | K2.6 | K4 | K3 |
| HD 167 | G9.1 | G8.6 | G8.2 | ..... | ..... | G8.5 | G9 | ..... |
| 6953 | ..... | ..... | ..... | K4.9 | K4.8 | K4.9 | K5 | ..... |
| 7647 | ..... | ..... | ..... | K4.7 | K5.2 | K5.0 | K5 | ..... |
| 7724 | ..... | ..... | ..... | K2.0 | K2.9 | K2.4 | K2 | ..... |
| 11613 | ..... | ..... | ..... | K3.5 | K3.2 | K3.4 | K3 | ..... |
| 14373 | ..... | ..... | ..... | K2.1 | K2.3 | K2.2 | K2 | ..... |
| 15453 | K0.2 | K0.0 | G9.7 | K0.6 | K0.6 | K0.2 | K2 | ..... |
| 18700 | ..... | ..... | ..... | K4.4 | K5.1 | K4.8 | K5 | ..... |
| 23838 | G5.5 | G5.1 | G6.4 | ..... | ..... | G5.7 | G7 | ..... |
| 39429 | ..... | ..... | ..... | K3.7 | K4.0 | K3.8 | K4 | ..... |
| 62407 | ..... | ..... | ..... | K3.7 | K4.2 | K4.0 | K4 | ..... |
| 63435 | G5.3 | G4.9 | G5.7 | ..... | ..... | G5.3 | G5 | ..... |
| 65522 | ..... | ..... | ..... | K3.9 | K4.5 | K4.2 | K4 | ..... |
| 173920 | G6.0 | G5.0 | G5.0 | ..... | ..... | G5.3 | G5 | ..... |
| 182272 | K0.0 | K0.2 | K0.2 | K0.1 | K0.6 | K0.2 | K0 | ..... |
| 191814 | G7.0 | G8.2 | G6.8 | ..... | ..... | G7.3 | G7 | ..... |
| 194220 | K0.3 | K0.6 | G9.8 | K0.4 | K0.0 | K0.2 | K0 | ..... |
| 210026 | K0.0 | K0.6 | K0.3 | G9.5 | G9.9 | K0.1 | K0 | ..... |
| 213644 | ..... | ..... | ..... | K1.6 | K1.3 | K1.4 | K2 | ..... |
| 218416 | K1.5 | K1.9 | K0.7 | K0.5 | G9.5 | K0.8 | K2 | ..... |
| 218660 | ..... | ..... | ..... | K1.6 | K1.3 | K1.4 | K1 | ..... |
| 224895 | ..... | ..... | ..... | K0.9 | K2.0 | K1.4 | K1 | ..... |
| $\rho$ Boo | ..... | ..... | ..... | K3.2 | K2.7 | K3.0 | Standard KO III | ..... |
| | G9.2 | G8.9 | G7.8 | K2.7 | K2.2 | Pec. | ..... | ..... |
| | G9.0 | G9.5 | G8.0 | K3.0 | K2.8 | Pec. | ..... | ..... |
| HD 213389 (check) | G9.0 | G9.6 | G8.7 | K2.4 | K2.3 | Pec. | ..... | ..... |
| | G9.0 | G9.5 | G8.6 | K2.6 | K2.4 | Pec. | ..... | ..... |
| | G9.0 | G9.5 | G8.7 | K2.6 | K1.4 | Pec. | ..... | ..... |
| | G9.3 | G8.9 | G8.5 | K2.8 | K2.0 | Pec. | ..... | ..... |

Three spectra showing too strong hydrogen lines were discovered in the spectral-type investigation. These were the spectra of $\zeta$ And, $\eta$ And, and HD 213389. Their metallic ratios gave one value for the spectral type, and their hydrogen ratios a decidedly earlier one. The effect could not be accounted for on grounds of different luminosities, and it turned out that all three are spectroscopic binaries listed in Moore and Neubauer's catalogue.[9] $\eta$ And is the only one of the three which is double-lined. Plates covering the different radial-velocity phases were available for HD 213389; from these the hydrogen lines show no change in appearance depending on phase, and the radial velocities for the hydrogen lines do not differ from those for the metallic lines in any way dependent on phase. They appear, on the average, however, from measurements of $H\gamma$ to have velocities about 5 km/sec more positive than those velocities obtained from the metallic lines. Other spectroscopic binaries are now being examined for the hydrogen-strong effect, and many appear to exhibit it. The oscilloscopic method yielded a quantitative estimate of this effect, namely, the difference in the spectral types given by the metallic and hydrogen criteria, respectively, as seen from the "peculiar" spectra of Table 2.

It is a pleasure to thank Dr. J. F. Heard for his valued assistance. Mr. Halliday, in addition to classifying the stars visually, provided the writer with much stimulating discussion during the course of the investigation.

[9] *Lick Obs. Bull.*, No. 521, 1948.

# PHOTOMETRIC AND SPECTROSCOPIC OBSERVATIONS OF STARS IN IC 348*

D. L. Harris, W. W. Morgan, and N. G. Roman
Yerkes and McDonald Observatories
*Received December 10, 1953*

ABSTRACT

Photoelectric observations of twelve stars in the cluster near o Persei have been made on the (*U*, *B*, *V*) system. Spectrograms for eight of these stars have been obtained; these allow classification on the two-dimensional Yerkes system. The parallax of the cluster is similar to that of the ζ Persei association. The most heavily reddened stars are the three involved in the brightest nebulosity; this indicates a density maximum in the same region and is thus qualitatively similar to the Trapezium region of the Orion Nebula.

The cluster in the nebula IC 348 consists of around a dozen probable members. It has been investigated by Gingrich,[1] Hubble,[2] and Greenstein,[3] among others. A recent investigation by Blaauw[4] indicates that the cluster is probably a part of the ζ Persei associa-

TABLE 1

STARS IN OMICRON PERSEI CLUSTER

| Star | *V* | *B*−*V* | *U*−*B* | MK | $E_{(B-V)}$ | $V_0$ | $(V_0-M_0)$ | $M_V$ |
|---|---|---|---|---|---|---|---|---|
| +31°643 | 8.51 | +0.70 | 0.00 | B5 V | +0.86 | (6.5)* | 7.8 | −1.4 |
| 4 | 9.92 | +0.48 | +0.33 | A0 V | + .48 | 8.5 | 8.0 | +0.6 |
| 5 | 10.02 | +0.52 | +0.35 | A2 V | + .46 | 8.6 | 7.4 | +0.7 |
| 12 | 10.20 | +0.88 | +0.66 | A2 III:† | + .82 | 7.7 | ..... | −0.2 |
| 11 | 10.62 | +0.96 | +0.72 | F0 m:‡ | + .63 | 8.7 | ..... | +0.4 |
| 3 | 11.35 | +0.74 | +0.21 | ..... | ..... | ..... | ..... | ..... |
| 9 | 11.58 | +0.99 | +0.56 | F2 (IV, V): | + .61 | 9.8 | ..... | +1.9 |
| 7 | 11.63 | +0.79 | +0.19 | ..... | ..... | ..... | ..... | ..... |
| 10 | 11.84 | +0.84 | +0.70 | A2 V | + .78 | 9.5 | 8.3 | +1.6 |
| 6 | 11.90 | +0.80 | +0.31 | F0 (III, V): | +0.47 | 10.5 | ..... | +2.6 |
| 13 | 12.90 | +1.63 | +1.02 | ..... | ..... | ..... | ..... | ..... |
| 8 | 13.43 | +1.23 | +0.65 | ..... | ..... | ..... | ..... | ..... |

* Close double: $V_0$ corrected by +0.6 mag.

† The wings of $H\gamma$, $H\delta$, and $H\epsilon$ are less pronounced than in No. 5. There is at present no accurate calibration for class A2 III in terms of luminosity; therefore, no value of $V_0 - M_0$ is given.

‡ Probably a metallic-line star of small amplitude. The type given is from the metallic lines. The region of the K line is underexposed.

tion. Two stars showing large proper motions relative to the remainder of the cluster are considered by him to be probably foreground objects.

Twelve of the stars in the neighborhood of the cluster were observed photoelectrically by Harris with the 82-inch reflector of the McDonald Observatory. Table 1 gives the photometric observations on the (*U*, *B*, *V*) system of Johnson and Morgan.[5] The numbers of the stars in the first column are those of Gingrich.

* *Contributions from the McDonald Observatory, University of Texas*, No. 235.

[1] *Ap. J.*, **56**, 139, 1922.

[2] *Ap. J.*, **56**, 181 and 404, 1922.

[3] *Ap. J.*, **107**, 376, 1948.

[4] *B.A.N.*, **11**, 412, 1952.

[5] *Ap. J.*, **117**, 313, 1953.

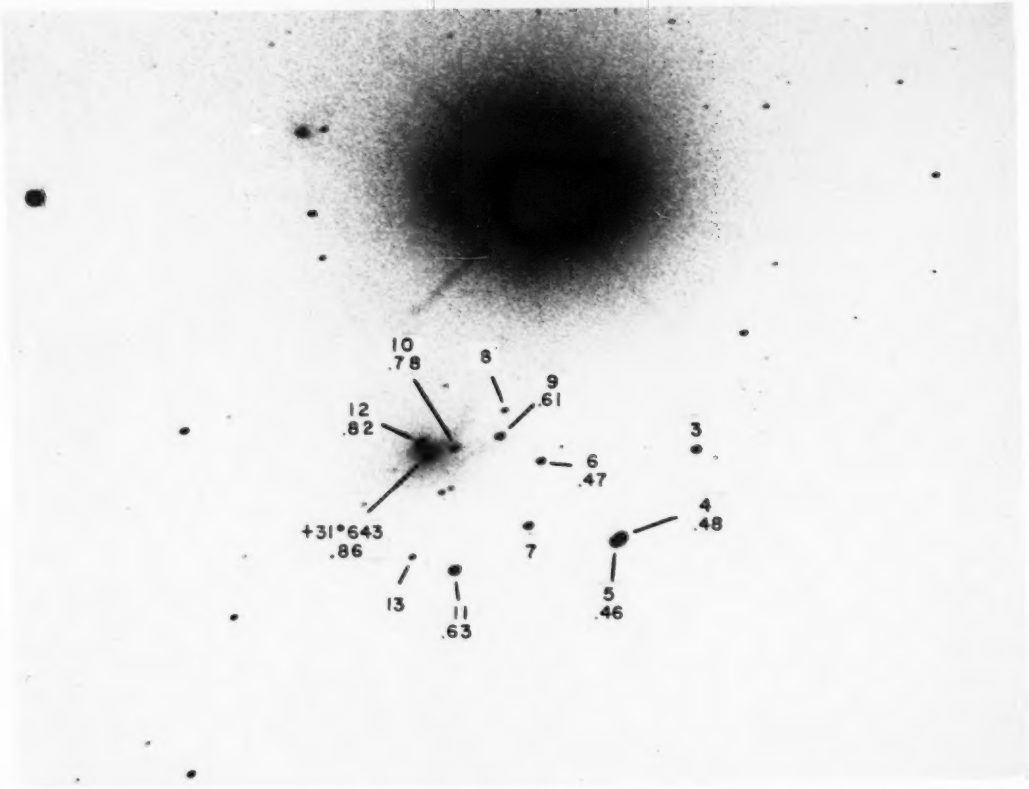


FIG. 1.—Region of IC 348 from 24-inch plate by G. Van Biesbroeck. Eastman 103*a*-O emulsion. North is at top; east is at left. The brightest star at top is $\sigma$ Persei. Stars observed are marked by the numbers from Gingrich's catalogue; the color excess is given below the catalogue number.

Slit spectrograms for eight of the cluster stars were obtained with the 82-inch telescope by Miss Roman; the spectral types on the revised Yerkes *Atlas* system are given in the fifth column of Table 1. The color excesses for these stars are listed in the sixth column; normal colors for the spectral type were taken from a paper by Morgan, Harris, and Johnson.[6] The seventh column of the table gives corrected apparent magnitudes; the eighth lists individual values of the true distance modulus for the four stars having luminosity classifications of highest weight. The last column gives the absolute magnitudes on the assumption that the true distance modulus is 7.9 mag.

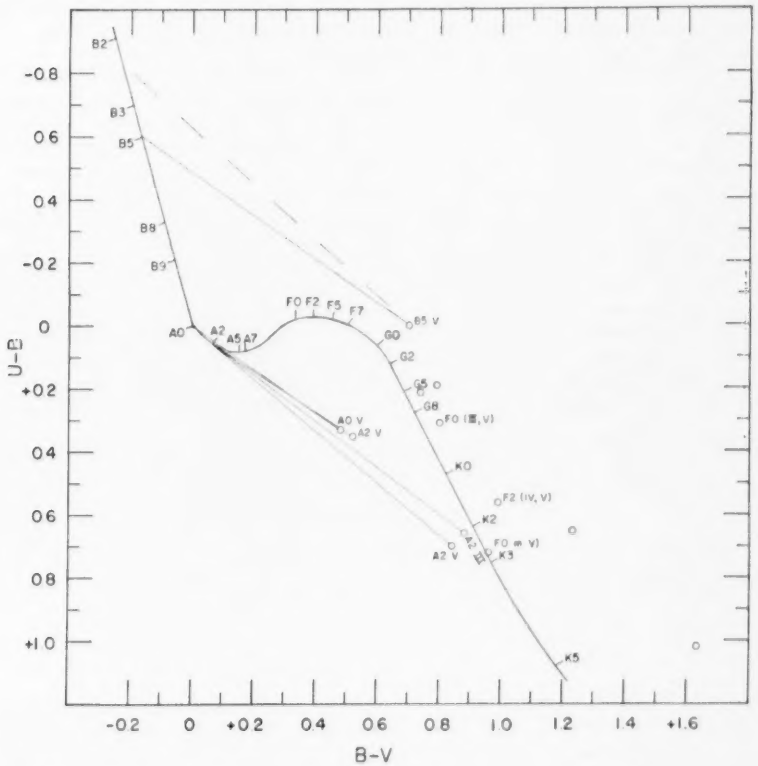


FIG. 2.—Two-color diagram of stars observed in IC 348. The continuous curve represents the position of a normal, unreddened main sequence; the spectral types are marked on this curve. Stars in IC 348 are plotted as open circles; spectral types are also given. The reddening lines are shown for cluster members of spectral type A2 and earlier. The dashed line represents the normal reddening slope found earlier by Morgan, Harris, and Johnson.

The mean of the four values of the true distance modulus is 7.9 mag.; this corresponds to a distance of around 380 parsecs; the distance of the cluster is therefore identical—within the errors of observation—with that of the $\zeta$ Persei association,[7] and there seems to be no reason to doubt that it is a physical part of the association.

The region of IC 348 is illustrated in Figure 1, which is from a plate obtained by G.

[6] *Ap. J.*, **118**, 92, 1953.

[7] *Ap. J.*, **118**, 318, 1953.

Van Biesbroeck with the 24-inch reflector of the Yerkes Observatory; an Eastman 103*a*-O plate was used. The stars observed are numbered according to Table 1; in addition, the value of the color excess is listed for each star for which spectrograms were available. It is interesting to note that the color excesses (and therefore the total absorptions) decrease fairly smoothly on passing outward from BD+31°643; this indicates that the density of the absorbing material is greatest near the latter star and decreases with increasing distance from it. We thus have a phenomenon similar to that found by Sharpless in the Orion Nebula.[8]

Figure 2 gives a two-color plot of the cluster stars, together with the position of a normal main-sequence.[5] Lines have been drawn connecting the positions of the five stars of earliest spectral type with their normal unreddened positions. The dashed line indicates the slope found earlier for the "reddening line."[6]

The two-color data allow some further information to be derived for the four stars for which spectra were not available. The conclusion of Blaauw that stars 3 and 7 are probably foreground objects is confirmed; they are probably G dwarfs having considerably lower color excesses than the cluster members. On the other hand, there is a possibility from the photometric observations that they may have spectral types either of class F or of late B; these possibilities, however, seem remote; when considered in connection with the large proper motions, it seems almost conclusive that they are foreground G dwarfs. Star 8 is probably a dwarf of type G5–G9, with a color excess similar to star 6.

The case of star 13 is more uncertain. If its type is near K0, its color excess is near +0.8 mag.; this would give a corrected apparent magnitude of 10.5 and a visual absolute magnitude of around +2.6. The star would then be a subgiant; this would cast serious doubts as to its cluster membership. If its spectral type is near F0, the color excess would be about 1.3 mag. and its absolute magnitude near +1.1. This is possible; however, it seems unlikely that the color excess could have this high value. The most likely possibility seems to be that it is a yellow giant or subgiant not connected with the cluster.

[8] *Ap. J.*, **116**, 251, 1952.

# THE SPACE MOTIONS OF AE AURIGAE AND $\mu$ COLUMBAE WITH RESPECT TO THE ORION NEBULA

A. Blaauw and W. W. Morgan
Yerkes Observatory
*Received January 19, 1954*

ABSTRACT

The B0 V star, $\mu$ Columbae, appears to move in the direction away from the Orion association, with the same speed, 127 km/sec, as the O9.5 V star, AE Aurigae, discussed by the authors in a previous paper. The motions of the two stars are, moreover, almost exactly opposite. The observational data suggest that the stars were formed in the same physical process 2.6 million years ago and that this took place in the neighborhood of the Orion Nebula.

## I. INTRODUCTION

In a previous paper[1] we have shown that the O9.5 V star AE Aurigae possesses a high space velocity, 128 km/sec, in the direction away from the Orion association, and we suggested that it probably originated there 2.7 million years ago. The evidence for its high velocity is supported by the peculiar structure of the emission nebula IC 405, surrounding AE Aurigae.

TABLE 1

OBSERVATIONAL DATA ON AE AURIGAE AND $\mu$ COLUMBAE

| | AE Aur | $\mu$ Col |
|---|---|---|
| $\alpha$, $\delta$ (1900) | $5^h9^m.7$, $+34°12'$ | $5^h42^m.3$, $-32°21'$ |
| $l$, $b$ | $139°.8$, $-0°.9$ | $204°.5$, $-25°.9$ |
| $m$, visual magnitude | 5.8 | 5.2 |
| $m_0$, magnitude corrected for interstellar absorption | 4.4 | ..... |
| Spectral type in revised system of Yerkes spectral atlas | O9.5 V | B0 V |
| Radial velocity (km/sec) and p.e. | $+59.3 \pm 0.7$ | $+109.9 \pm 2.1$ |
| $\mu_\alpha \cos\delta$ (unit $0''.0001$) | $-2 \pm 22$ | $+81 \pm 21$ |
| $\mu_\delta$ (unit $0''.0001$) | $+401 \pm 24$ | $-266 \pm 20$ |

Since that paper was written, we have found that the star $\mu$ Columbae, spectral type B0 V, possesses similar properties, in that it also moves away from the Orion region, with approximately the same space velocity, and must have originated there at about the same time as AE Aurigae. Moreover, the motion of $\mu$ Columbae is directed just opposite to that of AE Aurigae. The two stars present a phenomenon which has not been encountered before and which throws new light on the process which causes the expanding motions in the associations of O and B stars. In the present case there is strong reason to think that the point of origin of the two stars is located in the neighborhood of the Orion Nebula.

## II. THE OBSERVATIONAL DATA

Table 1 summarizes the observational data on the two stars. The proper motions are in the average of the systems of FK3 and N30, with precessional corrections applied.

[1] *B.A.N.*, No. 448, p. 76, 1953.

For AE Aurigae, as was described,[1] a solution was based on all available meridian observations, including some very recent ones. $\mu$ Columbae (HD 38666) appears both in the *General Catalogue* and in the recently published N30 catalogue (GC 7230, N30-1235); and for this star we made no new solution but combined the data given in the two catalogues. The catalogue values reduced to the fundamental system mentioned above, including the precessional corrections, are given in the accompanying tabulation.

| | $\mu_\alpha \cos\delta$ | $\mu_\delta$ |
|---|---|---|
| From *GC* | $+0''.0102 \pm 0''.0024$ (p.e.) | $-0''.0252 \pm 0''.0022$ (p.e.) |
| From N30 | $+0.0018 \pm 0.0041$ | $-0.0315 \pm 0.0041$ |

The star deserves further observation; for the present we adopt the weighted mean given in Table 1. The radial velocities of both stars are those given in Moore's catalogue (*Pub. Lick Obs.*, Vol. **18**, 1932). For $\mu$ Columbae no measure of the color excess is available as yet.

Figure 1 shows the position of the two stars in the sky with respect to the Orion group. Large dots and open circles are the stars brighter than apparent visual magnitude 3.5; solid dots represent the OB supergiants. It is interesting to note the isolated position at relatively high latitude of $\mu$ Columbae, which also belongs to this class.

Arrows indicate the directions of the proper motions of AE Aurigae and $\mu$ Columbae; their sizes correspond to the displacements in $4 \times 10^5$ years. These proper motions are the observed ones after elimination of the standard solar motion (20 km/sec toward R.A. 270°, Dec. +30°). The great circles defined by these proper motions have been traced backward in Figure 1; the shaded areas indicate the uncertainty in their directions corresponding to the probable errors of the proper motions. If the medium in which the two stars originated is at rest with respect to the standard of rest obtained by elimination of the standard solar motion, then this medium must now be located somewhere on the great circles traced backward from the proper motions. Or, rather, in view of the uncertainty in the directions of the proper motions, it will probably be located somewhere in the shaded areas. If the medium is not at rest in the reference system defined by elimination of the standard solar motion, it need not be on the backward-traced circles. For instance, in view of what will be said below, it may be that both stars originated in the cloud surrounding $\theta^2$ Orionis (the Trapezium stars). The position of this cloud east of the two shaded areas would then indicate a positive proper motion in right ascension for this cloud in the adopted reference system.

### III. THE SPACE MOTION OF $\mu$ COLUMBAE

It is of interest to estimate the amount and the direction of the space motion of $\mu$ Columbae. In the following computations in this section it will be assumed that the standard solar motion is eliminated. The "observed" radial velocity then is +90.0 km/sec and the total proper motion $0''.0282$. Assuming the visual absolute magnitude −3.9, in accordance with the provisional calibrations as given in *Astrophysics* (ed. J. A. Hynek), page 23, and neglecting interstellar absorption (which probably is quite low in this direction), we find a distance of 600 parsecs and a space velocity of 126 km/sec. That this motion is away from the Orion association not only in its projection on the sky but also in space can be shown as follows. Assuming for the Orion association a distance of 500 parsecs, as found by Sharpless,[2] we find that a velocity of 126 km/sec along the line connecting it with $\mu$ Columbae corresponds to a radial velocity of + 86 km/sec and a proper motion of $0''.0293$. Both are very close to the "observed" values. The distance

[2] *Ap. J.*, **116**, 25, 1952.

of $\mu$ Columbae from the center of the Orion association is about 320 parsecs; this would have been traveled with the speed of 126 km/sec in $2.5 \times 10^6$ years. This is almost equal to the age of AE Aurigae found in the previous paper: $2.7 \times 10^6$ years.

These results, together with the observation of the opposite directions of the space motions, suggest strongly that we are not dealing here with a chance phenomenon but that the two stars must have originated in the same physical process. The probable relation of the medium in which the process took place with the Orion Nebula makes the

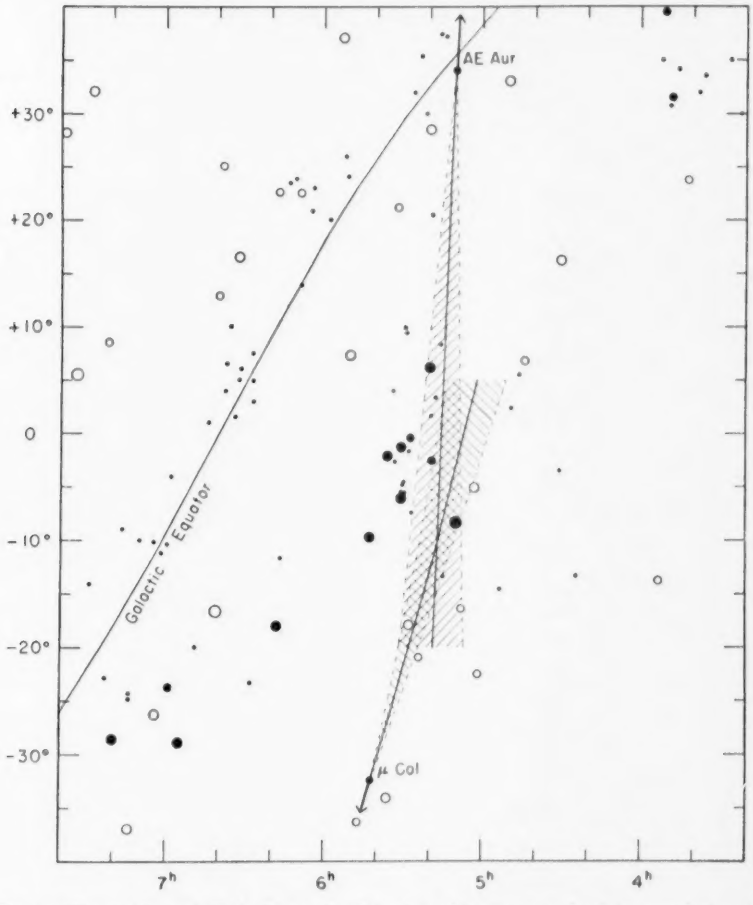


FIG. 1.—The positions of AE Aurigae and $\mu$ Columbae with respect to the Orion association. Arrows show the directions of their proper motions when corrected for the standard solar motion. The paths of the two stars with respect to the standard of rest thus defined are shown by the great circles traced backward from the proper motions. The shaded areas indicate the uncertainty in their directions. The sizes of the arrows correspond to the displacements in $4 \times 10^6$ years. Stars brighter than apparent magnitude 3.5 are represented by large dots (OB supergiants) and open circles. Small dots represent the fainter OB supergiants.

phenomenon particularly interesting. The relative importance of the process of the formation of the two stars may be illustrated by the following consideration. The average speed of the O and B stars in the Orion Nebula and its immediate neighborhood, as inferred from the radial velocities and proper motions, is about 8 km/sec. The stars $\mu$ Columbae and AE Aurigae therefore represent the same amount of kinetic energy as do about 500 stars in the Orion group, on the assumption that the masses are the same. Actually, the total number of stars with spectral types B9 and earlier in the subsystem around $\theta^1$ and $\theta^2$ Orionis is only about 100, and the average mass will be lower than that of AE Aurigae and $\mu$ Columbae.

## IV. THE HYPOTHESIS OF EQUAL AND OPPOSITE VELOCITIES

No explanation of the remarkable phenomenon of this pair of stars will be attempted in this paper. We shall, however, show how well the observations can be represented by the hypothesis that the stars were formed with exactly equal and opposite velocities with respect to the generating medium and shall discuss the probable present location of this medium.

On this hypothesis the medium must be located on the line connecting the two stars in space and at equal distances from the two. This means, in the first place, that it must be located on the great circle through the two stars. Part of this great circle is shown by the white dotted line in Figure 2, which represents a section of the Ross *Atlas* photograph of the Orion constellation. It shows that the great circle runs through the Orion Nebula, and computations show that it actually passes the Trapezium stars at an angular distance of only 23 minutes of arc. This corresponds to a projected distance of 3.3 parsecs at the distance of the Orion group. It strongly suggests that the origin of the stars is indeed in the Orion Nebula.

In order to see where exactly it would be located on the above hypothesis, we have proceeded as follows. For AE Aurigae we have adopted, as before, the distance of 525 parsecs given in our first paper. For $\mu$ Columbae the distance has been taken as an unknown. The present hypothesis, combined with the observed proper motions and radial velocities of the two stars, then allows a determination of the distance of $\mu$ Columbae, the direction and the distance of the origin of the two stars, the motion of the two stars with respect to it, and the space motion of this origin. The results of the solution are summarized in Table 2. In this table all observed and computed quantities are referred to the sun and not to the system of reference adopted in the previous section.

The distance of $\mu$ Columbae is found to be 675 parsecs, corresponding to $m_0 - M = 9.14$. With the adopted absolute magnitude $M_v = -3.9$ (see the preceding section), we find $m - M = 9.1$. There may be some interstellar absorption; and one might expect, therefore, a somewhat higher value for $m - M$ than 9.1. On the other hand, the adopted value of $M_v$ is also uncertain by at least a few tenths of a magnitude.

The velocity of the two stars with respect to their origin, 127 km/sec, and their distance from the origin, 337 parsecs, leads to an age of $2.6 \times 10^6$ years for the pair. The agreement between the observed and computed values of the $\mu_\delta$'s and the radial velocities is not surprising, as it is mainly these quantities which determine the relative speed of the stars, the distance of $\mu$ Columbae, and the motion and location of the point of origin. The agreement of the observed and computed values of $\mu_\alpha \cos \delta$ for both stars, on the other hand, is significant, in that it means that the two stars move with respect to each other along the connecting line.

The distance of the generating medium is found to be 502 parsecs; this is equal to the distance of the Orion association. The position of the generating medium (R.A. $5^h27^m8$, Dec. $-3°47'$ for 1900) is indicated by the cross in Figure 2. The motion of the generating medium is small, as shown in the lower part of Table 2. If we convert these data into the radial velocity and the components of proper motion, we get the values at the bottom of Table 2. For comparison, the mean proper motions and radial velocity of the stars in the

FIG. 2.—Section of the Ross atlas photograph of the Orion region. The white dotted line is part of the great circle connecting AE Aurigae and $\mu$ Columbae. The white cross indicates the position of the point of origin as found on the hypothesis of equal and opposite velocities of the two stars.

subsystem around $\theta^1$ and $\theta^2$ Orionis (12 stars in the region R.A. $5^h20^m$ to $5^h40^m$, Dec. $-4°$ to $-6°45'$) are also given, together with the quantities which would be observed for an object at the location of the Orion Nebula but showing only standard solar motion and galactic rotation. As could be foreseen, the space motion of the generating medium with respect to this assumed object is quite small. Of more interest is the question: Can it be identified with the Orion Nebula? The fact that its position is found to be a little

TABLE 2

SOLUTION BASED ON HYPOTHESIS OF EQUAL AND OPPOSITE VELOCITIES

QUANTITIES RELATING TO THE TWO STARS AE AURIGAE AND $\mu$ COLUMBAE

| | |
|---|---|
| Distance of $\mu$ Col | 675 parsecs |
| Distance from point of origin | 337 parsecs |
| Speed with respect to point of origin | 127 km/sec |
| Time elapsed since stars left point of origin | $2.6\times10^6$ years |

| | AE Aur | | $\mu$ Col | |
|---|---|---|---|---|
| | Obs. | Comp. | Obs. | Comp. |
| $\mu_\alpha \cos\delta$ and p.e. | $-0^s.0002\pm0^s.0022$ | $+0^s.0003$ | $+0^s.0081\pm0^s.0021$ | $+0^s.0077$ |
| $\mu_\delta$ | $+0.0401\pm.0024$ | $+0.0401$ | $-0.0266\pm0.0020$ | $-0.0271$ |
| Radial velocity | $+59.3\quad\pm0.7$ | $+59.7$ | $+109.9\quad\pm2.1$ | $+109.8$ |

QUANTITIES RELATING TO THE POINT OF ORIGIN

| | |
|---|---|
| Position (1900) | $\alpha=5^h27^m.8,\quad\delta=-3°47'$<br>$l=174°.8,\quad b=-17°.7$ |
| Distance | 502 parsecs |
| Motion with respect to the sun: | |
| Component $X$ ($\alpha=0°$, $\delta=0°$) | $-11.6$ km/sec |
| $Y$ ($\alpha=90°$, $\delta=0°$) | $+20.9$ km/sec |
| $Z$ ($\delta=90°$) | $-8.0$ km/sec |

DATA EXPRESSED IN "OBSERVED" QUANTITIES

| | $\mu_\alpha \cos\delta$ | $\mu_\delta$ | Radial Velocity (Km/Sec) |
|---|---|---|---|
| Motion of point of origin | $+0^s.0061$ | $-0^s.0028$ | $+19.5$ |
| Motion of subsystem around $\theta^1$, $\theta^2$ Ori | $+.0011\pm.0015$ | $+.0015\pm.0015$ | $+25.0\pm1.2$ |
| Standard solar motion plus galactic rotation | $+0.0020$ | $-0.0039$ | $+25.6$ |

north of the nebula is of little importance; a slightly different assumption with somewhat different velocities of the stars with respect to their origin, not violating the observed quantities, could easily bring this origin somewhat farther south. Somewhat more significant may be the difference in the motion in right ascension. The position of the nebula somewhat east of the line connecting the two stars would indicate a relative motion eastward with respect to the point of origin. The observed relative motion of the subsystem of stars around $\theta^1$ and $\theta^2$ Orionis, which may also be the motion of the nebula,

is in the opposite direction. The difference amounts to $0''.0050 \pm 0''.0015$ (p.e.). But the possibility of a systematic error in the relative motions in right ascension of a few thousandths of a second of arc is not entirely ruled out, and therefore it does not seem justified to discard the hypothesis that the origin of the stars was in the Orion Nebula.

In a more refined discussion we would also have to take into account the curvature of the paths of the two stars as a consequence of the gravitational field of force of the galaxy, i.e., principally the force $K(z)$ perpendicular to the plane. A rough estimate of its influence has been made on the assumption that $K(z)$ around the Orion association is the same as it is around the sun, according to Oort's paper in *B.A.N.*, No. 238, an assumption that will be only approximately true in view of the very presence of the cloud complex in and around Orion. It is found that this field of force has only slightly changed the path of the two stars. This is due to the short time the force has acted. For $\mu$ Columbae, for which the influence must have been greatest, the total deceleration is about 2.2 km/sec; the lag in distance $z$, 2 parsecs; and the deviation of the direction of its path less than 1°.

In conclusion, it can be said that the hypothesis described in the beginning of this section seems to describe the phenomenon remarkably well. The ages of 2.6 million years are quite reasonable, in view of what has been found for the expansion ages of similar stars in other near-by associations. The question of whether or not the formation of these two stars took place at the same time as the stars of the Orion association should be left open for the present.

The occurrence of early-type stars with these exceptionally high velocities leads us to expect the presence of a few such stars in high galactic latitudes. AE Aurigae and $\mu$ Columbae will reach distances of 1500 parsecs from the galactic plane, but it takes them about 50 million years to travel this distance, and by that time they may not be O or B0 stars any longer. The statistical study of such objects would present interesting possibilities for the study of their evolution, if they are numerous enough. The further discussion of this topic, however, is beyond the scope of the present paper.

*Note added in proof.*—After this paper was submitted for publication, the color of $\mu$ Columbae was measured with the 20-inch reflector of the Lowell Observatory by Dr. D. L. Harris, to whom we are indebted for permission to quote his results here. He also measured AE Aurigae and found the values given in the accompanying tabulation.

| | $V$ | $B-V$ | $U-B$ | Measured on |
|---|---|---|---|---|
| AE Aurigae | 5.94 | +0.23 | −0.72 | 2 nights |
| $\mu$ Columbae | 5.20 | −0.31 | −1.05 | 3 nights |

These measures show $\mu$ Columbae to be one of the bluest bright stars we know. In their table of intrinsic colors for main-sequence stars (*Ap. J.*, **117**, 346, 1953), Johnson and Morgan give for type B0 V, to which $\mu$ Columbae belongs, $B - V = -0.32$ and $U - B = -1.13$; and they indicate that both values are extrapolated and hence somewhat uncertain. These values are so close to the observed colors for $\mu$ Columbae that the total visual absorption almost certainly is less than 0.1 mag. This is a remarkable result for a star at the distance of 675 parsecs. It justifies the assumption of negligible absorption made in the above computations. For AE Aurigae, the new observation confirms the color excess adopted in our earlier discussion.

# THREE-COLOR PHOTOELECTRIC PHOTOMETRY OF HD 199140

MERLE F. WALKER*
Berkeley Astronomical Department, University of California
*Received November 2, 1953; revised December 30, 1953*

ABSTRACT

Photoelectric observations of HD 199140 in infrared, yellow, and ultraviolet light indicate that the temperature of the star varies by about 2000° K during the 5-hour period, maximum temperature coinciding with maximum light. Semiempirical tests of pulsation have been applied by combining these data with simultaneous observations of the radial velocity. Owing to the uncertainties in these tests, the correctness of the pulsation hypothesis remains undecided.

The cause of the variability of the $\beta$ Canis Majoris or $\beta$ Cephei stars has not yet been determined. However, at the present time it seems most likely that they are undergoing some type of pulsation. It is therefore of great interest to apply to these stars the semiempirical tests of pulsation which have been developed by Baade and others.[1] For this purpose it is necessary to have simultaneous observations of the variation in light, color, and velocity of the stars. Unfortunately, the two stars for which such observations have been obtained, 16 Lacertae[2] and $\nu$ Eridani,[3] do not show detectable variations in color when observed with the usual yellow-blue color base line.[4] Since in hot stars, such as these, the yellow-blue color is insensitive to small changes in temperature, it seemed likely that the temperature variation might be detected by the use of a longer color base line. Observations of HD 199140 obtained at Mount Hamilton in 1951 indicated that there was a yellow-blue color variation of 0.03 mag. While this result was not of sufficiently high accuracy to permit the application of the pulsation tests, it did indicate that this star would probably be the most favorable to study with an extended color base line. Accordingly, the star was observed at Mount Hamilton during the summer of 1952 with an infrared-sensitive photometer constructed by G. E. Kron.

HD 199140 was first observed on September 7, 1951, as part of a general program of simultaneous spectroscopic and photometric observations of the $\beta$ Canis Majoris stars. The photometric observations were obtained with the 12-inch Lick refractor, using the photometric equipment and yellow and blue filters already described in connection with the investigation of 16 Lacertae.[2] HD 198820 was used as the comparison star, and the observations were corrected for extension in the usual manner.[2] Simultaneous spectroscopic observations were made by D. H. McNamara with the two-prism spectrograph and a 12-inch camera on the 36-inch refractor. The dispersion of this combination is 37 A/mm at $H\gamma$.

The observations are shown in Figure 1. The topmost curve represents the blue-magnitude differences; and the middle curve, the color differences, HD 199140 *minus* HD 198820, reduced to no atmosphere. The bottom curve shows the velocity variation of the star. The abscissa of the curves is the Julian date.

As in the other $\beta$ Canis Majoris stars, maximum light occurs at the time of maximum contraction, and minimum light at the time of maximum dilation of the star on the

* Since October, 1952, Carnegie Fellow at the Mount Wilson and Palomar Observatories.

[1] S. Rosseland, *The Pulsation Theory of Variable Stars* (Oxford: Clarendon Press, 1949), chap. ix.

[2] M. F. Walker, *Ap. J.*, **116**, 106, 1952.

[3] M. F. Walker, *ibid.*, p. 391.

[4] The observations of these stars have been rediscussed recently by C. de Jager (*B.A.N.*, in press). Forming mean color-curves, he finds a small color variation, the stars being bluest when brightest.

pulsation hypothesis. As mentioned above, there is a color variation of 0.03 mag., the star being bluest when brightest. In addition, a stillstand occurred on the rising branch of the light-curve at the time when the velocity of the star had its maximum positive value, and a stillstand in velocity occurred at the time of maximum contraction of the star, when the brightness of the star was at its maximum. The stillstand in velocity was discovered earlier by R. M. Petrie,[5] while the color variation and the stillstand in light

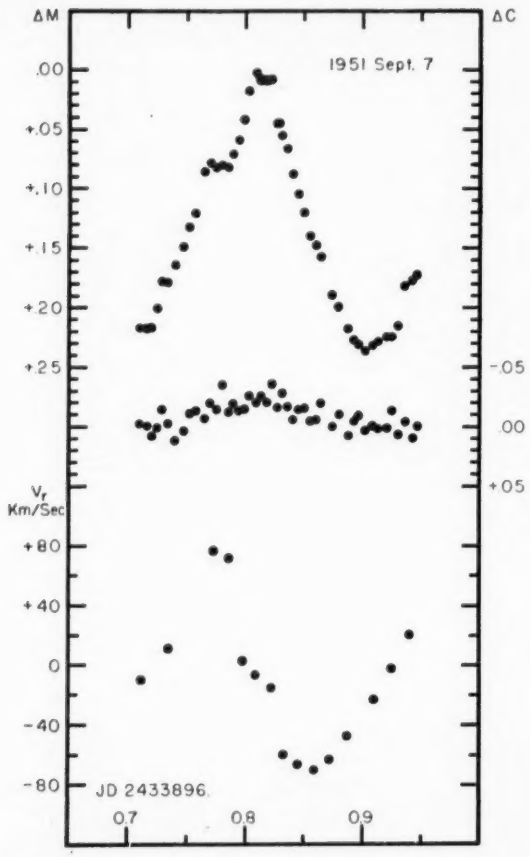


FIG. 1.—Simultaneous observations of the light, color, and velocity variations of HD 199140 in 1951. The topmost curve represents the blue-magnitude differences, and the middle curve color differences, HD 199140 *minus* HD 198820, reduced to no atmosphere. The bottom curve shows the velocity variation.

were discovered independently several days prior to my observations by V. B. Nikonov and E. K. Nikonova at Simeis.[6]

The 1952 photometric observations were made with the Crossley reflector. On three nights a photometer containing an unrefrigerated Continental Electric CE 25 A/B

[5] Private communication.

[6] *Pub. Crimean Ap. Obs.*, **9**, 135, 1952.

photocell was used. The photometer and amplifier have already been described by Kron.[7] A Brown recorder was used to register the output of the amplifier. The following filters were used: infrared, Wratten 88A (cemented); yellow, 2-mm Schott GG 7 plus 1-mm Schott BG 18 (cemented); ultraviolet, Corning 5840, standard optical thickness. The response-curves of the cell and filter combinations to an equal-energy source are shown in Figure 2. The sensitivity-curve of the CE 25 photocell was determined by Kron; the filter-curves were taken from the manufacturers' catalogues. The effective wave lengths of the three response-curves are 0.846, 0.549, and 0.358 $\mu$. The infrared and ultraviolet

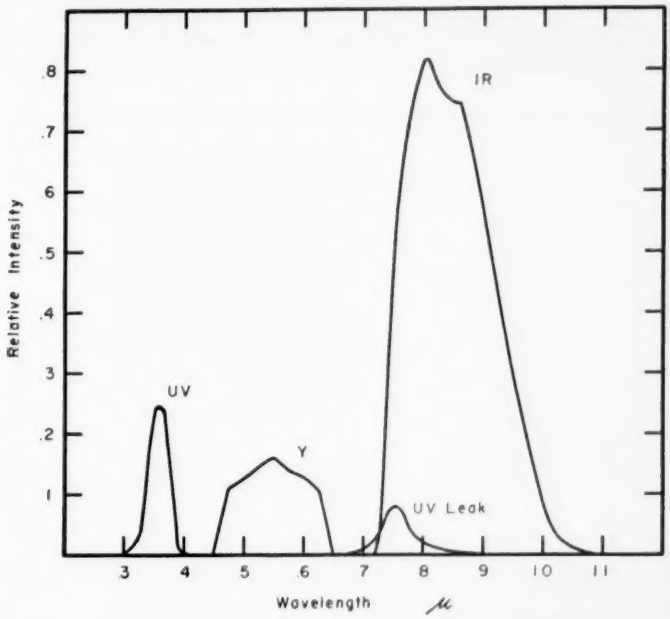


FIG. 2.—Response of CE 25 A/B photocell and infrared, yellow, and ultraviolet filters to an equal-energy source.

deflections were, owing to the blueness of the stars, nearly equal in size. Thus it was evident from the areas under the response-curves that no correction was necessary for the red leak of the ultraviolet filter.

Since there was no provision for refrigerating the photometer, the accuracy of the observations was limited by the thermal noise of the photocell. In an effort to secure more precise observations of the stillstand and of its variation in appearance with wave length, the star was observed on one night, September 7, using a photometer containing an unrefrigerated 1P21 photomultiplier tube and the same yellow and ultraviolet filters as were used before. The response-curves of the multiplier and filters to an equal-energy source are shown in Figure 3.[8] The effective wave lengths of the response-curves are 0.499 and 0.355 $\mu$.

[7] *Ap. J.*, **115**, 1, 1952.

[8] These are the cell and filters used in the observations of HD 199908; see M. F. Walker, *Pub. A.S.P.*, **65**, 39, 1953.

HD 198820 was again employed as the comparison star. The light-curves are presented in Figures 4 and 5. The ordinates are the magnitude difference, HD 199140 *minus* HD 198820, reduced to no atmosphere; the abscissae are Julian days. The infrared light-curves are at the top, followed by the yellow and ultraviolet light-curves. These magnitude differences have been left on the system defined by the telescope-filter-cell combination.

On two nights simultaneous spectroscopic observations were obtained by Petrie and his associates at Victoria, using the single-prism spectrograph on the 73-inch reflector, which gives a dispersion of 51 A/mm at $H\gamma$. Dr. Petrie has very kindly made his measurements of the radial velocity available to me in advance of the publication of his own spectroscopic investigation of HD 199140. They are presented in the lower portion of Figure 4. The circles represent velocities brought forward one cycle of the star, 0.201 day.

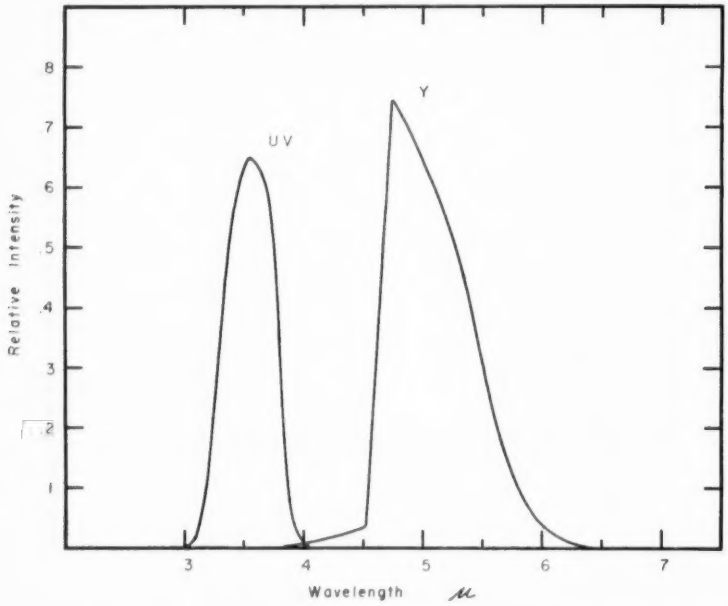


FIG. 3.—Response of 1P21 photomultiplier tube and yellow and ultraviolet filters to an equal-energy source.

The light-curves show very clearly the variation of amplitude with wave length. The amplitudes of the light-variations in the infrared and yellow are 0.5 and 0.6, respectively, of the amplitude in the ultraviolet. In addition, there is no detectable shift in the time of maximum or minimum light with wave length; maximum blueness of the star coincides, within the limit of observational error, with the time of maximum light.

The 1952 observations again show the stillstand in light, although not so clearly as does the light-curve obtained in 1951. The observations on August 8 and 9 seem to indicate that it was present in all three wave lengths, while those on September 2 and 7 suggest that it was not present in the ultraviolet. However, it was not very pronounced in any wave length on the latter dates, so that this conclusion is rather uncertain. It would

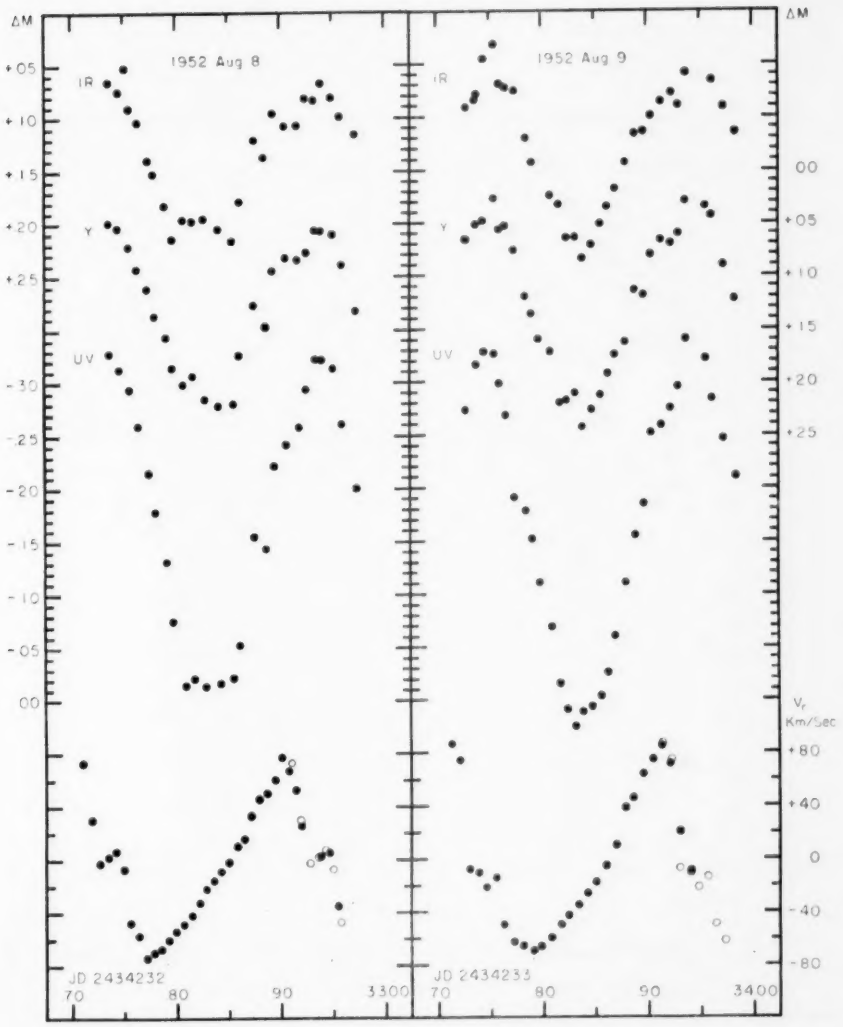


FIG. 4.—Simultaneous three-color light-curves and velocity-curves of HD 199140 in 1952. The infrared light-curves are given at the top of the figure, followed by the yellow and ultraviolet light-curves. The ordinates of these curves are the magnitude differences, HD 199140 *minus* HD 198820, reduced to no atmosphere. The velocity-curves are shown at the bottom of the figure. Circles represent velocities brought forward one cycle of the star.

appear that the stillstand is a fairly permanent feature of the light-curve but that it undergoes changes in size. This conclusion is borne out by the observations of Nikonov and Nikonova[8] and by those of R. P. Kraft.[9] We have as yet no explanation of this feature. It seems probable that it is related to the flare-up which O. J. Eggen observed in this star in 1947.[10]

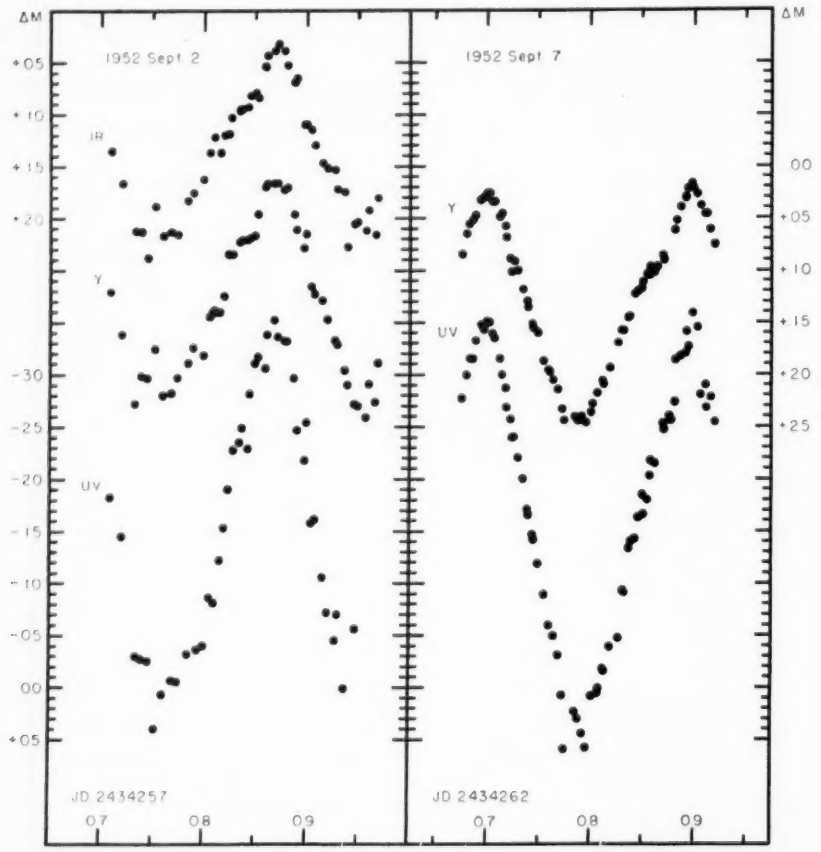


FIG. 5.—Photometric observations of HD 199140 in 1952. The infrared light-curve is given at the top of the figure, followed by the yellow and ultraviolet light-curves. The observations on September 2 were obtained with a CE 25 A/B photocell; those on September 7 were made with a 1P21 photomultiplier tube.

Petrie's 1952 observations of the radial velocity show the stillstand in velocity with great clarity. Again, we have no explanation of this irregularity. It is interesting to note in passing that we should expect an interval of constant velocity[11] if the satellite theory, proposed at one time by O. Struve,[12] were correct.

[9] *Pub. A.S.P.*, **65**, 45, 1953.

[10] *A.J.*, **53**, 197, 1948.

[11] O. Struve, *Pub. A.S.P.*, **64**, 20, 1952.

[12] *Ibid.*, **63**, 249, 1951.

Petrie[13] finds that the sharpest line profiles occur at the time of maximum expansion of the star. This implies that the $P_2$ period, with which the variation in line profile is associated, must dominate in this star. It is evident from an inspection of the present light-curves, together with those of Nikonov and Nikonova[6] and of Kraft,[9] that small changes in the amplitude of the light-variation do occur. There is not yet enough observational material to enable us to say whether these result from changes in the amplitude of the $P_2$ variation or whether a second $P_1$ oscillation, having a much smaller amplitude, is also present.

The observed heliocentric maxima of HD 199140 are given in Table 1. The observa-

TABLE 1

OBSERVED MAXIMA OF HD 199140

| Helioc. JD | Helioc. JD | Helioc. JD |
|---|---|---|
| 2433 896.816 | 2434 233.946 | 2434 262.700 |
| 2434 232.940 | 257.870 | 263.898 |

TABLE 2

OBSERVED LIGHT-VARIATION OF HD 199140

| DATE JD 2434 | LIGHT VARIATION (MAG.) | | |
|---|---|---|---|
| | IR 0.846 $\mu$ | Y 0.549 $\mu$ | UV 0.358 $\mu$ |
| 232.9 | 0.130 | 0.162 | 0.305 |
| 233.9 | .185 | .210 | .335 |
| 257.8 | 0.180 | .207 | .340 |
| 262.8* | ..... | 0.200 | 0.392 |
| Calc. for black body at 20,000° K, $\Delta T = 2400°$ | 0.161 | 0.219 | 0.300 |

* The effective wave lengths on this date are 0.499 $\mu$ and 0.355 $\mu$ (see text).

tions do not extend over a long enough interval to make possible any significant improvement in the value of $P_2 = 0.201028$ day found by Petrie[14] for the variation in radial velocity.

If we plot the observed ranges of the light-variation against the reciprocal of the effective wave length, we find that the three amplitudes agree fairly well with the light-variation which we would observe with our cell and filters if a black body at 20,000° K changed its temperature by 2400°. The observed and calculated light-variations are listed in Table 2. In the wave-length region covered by the observations, the light-variation resulting from the change in temperature of the black body is essentially linear in $1/\lambda$. However, there is some tendency for the observed light-variations to be nonlinear, the yellow amplitude falling below a line drawn through the infrared and ultraviolet amplitudes. It is not possible to say, from the existing material, whether this nonlinearity is real or, if it is, whether it results from an abnormally small amplitude in the yellow or an abnormally large one in either the infrared or the ultraviolet. We might expect the ultraviolet amplitude to be abnormally large, owing to the change in the continuous hydrogen absorption produced by the variation in temperature.

[13] *J.R.A.S. Canada*, **40**, 149, 1946.

[14] *Pub. A.A.S.*, **9**, 53, 1938.

The observed temperature variation of 2400° agrees both with Petrie's[14] observation that the spectral class of the star changes by one subdivision during the 5-hour period and with the conclusions of Nikonov and Nikonova,[6] who arrived at a value of 2000° from their observations of the color variation. However, if the star is pulsating, the observed light-variation will be made up of the change in brightness resulting from the change in radius as well as that arising from the change in temperature. From the phase relationship between the light- and velocity-curves, it is evident that the contributions from changes in radius and in temperature must be out of phase by 180°. Consequently, the plot of observed light-variation against reciprocal wave length ought to be parallel

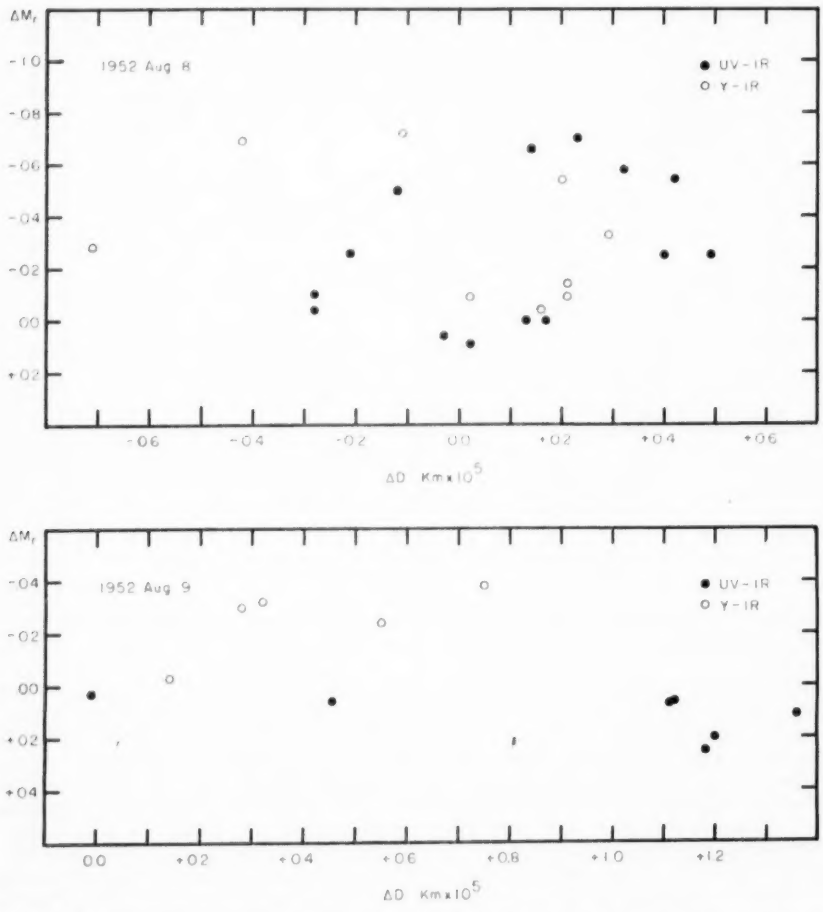


FIG. 6.—Semiempirical tests of pulsation in HD 199140, using Wesselink's method of points of equal color. The ordinates are the change in brightness resulting from a change in radius; the abscissae are the displacement of the surface of the star. Dots represent points of equal ultraviolet-infrared color; circles represent points of equal yellow-infrared color.

to the curve for some change in temperature but should lie below the computed temperature-curve by an amount which is $-\Delta m_r$, the light-variation produced by the change in radius.

Assuming a coefficient of limb darkening of 0.54, the total change in radius, obtained by integrating the velocity-curves, was $6.5 \times 10^5$ km on August 8 and $5.0 \times 10^5$ km on August 9. Since $-\Delta m_r = 2.17\ \Delta R/R$,[1] a negative displacement of 0.01 mag. would correspond to a radius of about $1.3 \times 10^8$ km, while a displacement of 0.10 mag. would correspond to $1.3 \times 10^7$ km. If the infrared, yellow, and ultraviolet amplitudes are given equal weight, the observed light-amplitudes, as pointed out above, agree fairly well with those calculated for a temperature variation of 2400°, so that $\Delta m_r = 0$. If we consider only the infrared and yellow amplitudes, $\Delta m_r \geq 0$, so that the radius of the star would have to be zero or negative. If we omit the infrared amplitude, the yellow and ultraviolet amplitudes fall parallel to and below the computed curve for $\Delta T = 5000°$. For these two colors, the values of $\Delta m_r$ would be $-0.25$ mag. on August 8 and $-0.20$ mag. on August 9, giving radii of $5.6 \times 10^6$ km and $5.4 \times 10^6$ km, respectively. However, there seems to be no reason for supposing that the infrared observations are less reliable than the others, and, as mentioned earlier, there is some reason to suspect that the ultraviolet range is abnormally large. Consequently, we cannot attach too much significance to this result and should probably conclude that the assumption of black-body conditions does not lead to a satisfactory confirmation of the pulsation hypothesis.

To avoid the assumption of black-body conditions, we may employ the test devised by A. J. Wesselink,[15] where we suppose that there exists a single-valued relationship between the color and the effective temperature of the star. Then the change in brightness between two phases when the star has the same color is that produced by the change in radius. The displacement of the surface of the star during the same interval, $\Delta D$, is obtained by integrating the velocity-curve. If the pulsation hypothesis is correct, a plot of $\Delta D$ against $\Delta m_r$ for a succession of such points of equal color should yield a straight line whose slope would be proportional to the radius of the star. This test has been carried out, using the simultaneous observations of light and velocity obtained on August 8 and 9. Both ultraviolet-infrared and yellow-infrared colors were used. Times of equal color do not coincide in these two color systems. However, this is probably the result of observational error. The results of the test are shown in Figure 6; the points scatter all over the diagram for August 8 and tend to lie along the $\Delta D$ axis in the August 9 diagram. It is evident that this test also does not confirm the pulsation hypothesis.

One reason why we might expect this test to fail is that the light-variations are very nearly symmetric about maximum light and, as mentioned earlier, that the contributions to the light-variation from the change in radius and the change in temperature are 180° out of phase. It is obvious that under these conditions this test becomes indeterminate. In addition, there is the possibility that the relationship between the color and effective temperature in this star is not single-valued.

Owing to the uncertainties involved in these tests, the correctness of the pulsation hypothesis must be left undecided. Even if the results of these tests could be interpreted as showing that radial pulsations do not occur, this still does not necessarily mean that the concept of pulsation is basically wrong. There remains the possibility that some type of nonradial oscillation could produce the observed phenomena.

It is a pleasure to thank Dr. C. D. Shane for permission to use the Lick telescopes, and Dr. G. E. Kron for the use of one of his infrared-sensitive photometers. I am especially indebted to Dr. R. M. Petrie for obtaining the simultaneous spectroscopic observations at Victoria and for permitting me to use his results in this paper. I am also grateful to Dr. D. H. McNamara for making available to me his simultaneous observations of the radial velocity made in 1951, and to Dr. H. H. Voigt and Mr. A. Poveda for assisting me at the Crossley reflector.

[15] *B.A.N.*, **10**, 91, 1946.

# THE TRANSFER OF RADIATION BY AN EMITTING ATMOSPHERE. III

HENRY G. HORAK*
University of Kansas
*Received December 30, 1953*

ABSTRACT

The transfer of radiation by a plane-parallel atmosphere containing a uniform distribution of emission sources is considered for the following cases: (*a*) scattering according to the Rayleigh phase function and (*b*) Rayleigh scattering. The exact expressions for the emergent intensity are derived for finite atmospheres. The solutions in the $n$th approximation for any depth $\tau$ are also given. Polarization calculations are made for an atmosphere of optical thickness $\tau_1 = 0.20$.

## I. INTRODUCTION

We shall continue the discussion of the transfer of radiation by an emitting atmosphere which was begun in a previous paper.[1] We shall restrict the discussion to the finite, plane-parallel atmosphere with a uniform distribution of energy sources. Two types of conservative scattering will be considered, viz.: (*a*) scattering according to the Rayleigh phase function $\frac{3}{4}(1+\cos^2\Theta)$, and (*b*) Rayleigh scattering, in which the polarization of the scattered light is taken into account.

## II. SCATTERING ACCORDING TO RAYLEIGH'S PHASE FUNCTION

The fundamental equation for the emergent intensity has already been derived in *E.A.* I (eq. [10]) by using two invariance principles. This equation is the following:

$$I(0,+\mu) = \mathfrak{I}(0,+\mu) - e^{-\tau_1/\mu}\mathfrak{I}(0,-\mu) + \frac{1}{2}\int_0^1 S(\tau_1;\mu,\mu')\,\mathfrak{I}(0,-\mu')\frac{d\mu'}{\mu'} - \frac{1}{2}\int_0^1 T(\tau_1;\mu,\mu')\,\mathfrak{I}(0,-\mu')\frac{d\mu'}{\mu'}. \tag{1}$$

Again we shall apply this equation combined with certain relations derived by Chandrasekhar[2] in his study of diffuse reflection.

In the case of scattering according to Rayleigh's phase function we have the following relations (*R.T.*, p. 220):

$$p^{(0)}(\mu,\mu') = \tfrac{3}{4}[1+\mu^2\mu'^2+\tfrac{1}{2}(1-\mu^2)(1-\mu'^2)];$$

$$\mathfrak{I}(\tau,\mu) = \tfrac{3}{16}\Big[(3-\mu^2)\int_{-1}^{+1} I(\tau,\mu')\,d\mu' + (3\mu^2-1)\times\int_{-1}^{+1} I(\tau,\mu')\,\mu'^2 d\mu'\Big] + \epsilon; \tag{2}$$

$$S(\tau_1;\mu,\mu') = \tfrac{3}{8}\frac{\mu\mu'}{\mu+\mu'}\{\tfrac{1}{3}[\psi(\mu)\psi(\mu') - \chi(\mu)\chi(\mu')] + \tfrac{8}{3}[\phi(\mu)\phi(\mu') - \zeta(\mu)\zeta(\mu')]\};$$

$$T(\tau_1;\mu,\mu') = \tfrac{3}{8}\frac{\mu\mu'}{\mu-\mu'}\{\tfrac{1}{3}[\chi(\mu)\psi(\mu') - \psi(\mu)\chi(\mu')] + \tfrac{8}{3}[\zeta(\mu)\phi(\mu') - \phi(\mu)\zeta(\mu')]\},$$

* Visiting professor at the Yerkes Observatory during August, 1952.

[1] Horak, *Ap. J.*, **116**, 477, 1952; hereafter referred to as "*E.A.* I."

[2] *Radiative Transfer* (Oxford: Clarendon Press, 1950); hereafter referred to as "*R.T.*"

where

$$\begin{aligned}
\psi(\mu) &= (3-\mu^2) + \frac{1}{2}\int_0^1 (3-\mu'^2)\, S(\tau_1;\, \mu,\, \mu')\, \frac{d\mu'}{\mu'}, \\
\phi(\mu) &= \mu^2 + \frac{1}{2}\int_0^1 \mu'^2 S(\tau_1;\, \mu,\, \mu')\, \frac{d\mu'}{\mu'}, \\
\chi(\mu) &= (3-\mu^2)\, e^{-\tau_1/\mu} + \frac{1}{2}\int_0^1 (3-\mu'^2)\, T(\tau_1;\, \mu,\, \mu')\, \frac{d\mu'}{\mu'}, \\
\zeta(\mu) &= \mu^2 e^{-\tau_1/\mu} + \frac{1}{2}\int_0^1 \mu'^2 T(\tau_1;\, \mu,\, \mu')\, \frac{d\mu'}{\mu'}.
\end{aligned} \tag{3}$$

Using equations (2), it is possible to write equation (1) in the form

$$\begin{aligned}
I(0,+\mu) = \left[\tfrac{3}{8}J(0) - \tfrac{1}{8}K(0) + \frac{\epsilon}{3}\right][\psi(\mu) - \chi(\mu)] \\
+ \left[K(0) + \frac{\epsilon}{3}\right][\phi(\mu) - \zeta(\mu)],
\end{aligned} \tag{4}$$

where

$$J(0) = \frac{1}{2}\int_0^1 I(0,\, \mu)\, d\mu \tag{5}$$

and

$$K(0) = \frac{1}{2}\int_0^1 I(0,\, \mu)\, \mu^2 d\mu. \tag{6}$$

Next we must evaluate $J(0)$ and $K(0)$. This can be done by multiplying through equation (4) by $\frac{1}{2}$ and $\frac{1}{2}\mu^2$, respectively, and integrating over the range of $\mu$. We obtain two simultaneous linear equations for the unknowns $J(0)$ and $K(0)$. Solving, we obtain

$$J(0) = \frac{\epsilon}{3\Delta}[-a-b+\tfrac{9}{8}(aB-bA)], \tag{7}$$

$$K(0) = \frac{\epsilon}{3\Delta}[-A-B+\tfrac{3}{8}(aB-bA)], \tag{8}$$

where

$$\begin{aligned}
\Delta &= -1 - \tfrac{1}{8}A + B + \tfrac{3}{8}[a - (aB - bA)], \\
a &= \frac{1}{2}\int_0^1 [\psi(\mu) - \chi(\mu)]\, d\mu, \qquad b = \frac{1}{2}\int_0^1 [\phi(\mu) - \zeta(\mu)]\, d\mu, \\
A &= \frac{1}{2}\int_0^1 [\psi(\mu) - \chi(\mu)]\, \mu^2 d\mu, \qquad B = \frac{1}{2}\int_0^1 [\phi(\mu) - \zeta(\mu)]\, \mu^2 d\mu.
\end{aligned} \tag{9}$$

The next step is to evaluate $a$, $b$, $A$, and $B$, making use of the following relations (*R.T.*, p. 226):

$$\begin{aligned}
\psi(\mu) &= (3 - c_1\mu)\, X(\mu) - c_2\mu\, Y(\mu), \qquad \phi(\mu) = \mu[q_1 X(\mu) - q_2 Y(\mu)], \\
\chi(\mu) &= (3 + c_1\mu)\, Y(\mu) + c_2\mu X(\mu), \qquad \zeta(\mu) = \mu[q_2 X(\mu) - q_1 Y(\mu)], \\
q_1 &= \tfrac{3}{16}(3a_1 - c_1a_2 - c_2\beta_2), \qquad q_2 = \tfrac{3}{16}(3\beta_1 + c_1\beta_2 + c_2a_2), \\
c_1 + c_2 &= \frac{(a_2 - \beta_2)\,\tau_1 + 6(a_1 - \beta_1)}{(a_1 + \beta_1)\,\tau_1 + 2(a_2 + \beta_2)}, \qquad c_1 - c_2 = \frac{a_2 + \beta_2}{a_1 - \beta_1}.
\end{aligned} \tag{10}$$

In these expressions $X(\mu)$ and $Y(\mu)$ are the "standard solutions" (*R.T.*, p. 222) defined in terms of the characteristic function $\Psi(\mu) = \frac{3}{16}(3 - \mu^2)$, and the $\alpha$'s and $\beta$'s are, respectively, moments of $X(\mu)$ and $Y(\mu)$. It follows that

$$\begin{aligned} a &= \tfrac{3}{2}(\alpha_0 - \beta_0) - \tfrac{1}{2}(c_1 + c_2)(\alpha_1 + \beta_1), \qquad b = \tfrac{1}{2}(q_1 - q_2)(\alpha_1 + \beta_1), \\ A &= \tfrac{3}{2}(\alpha_2 - \beta_2) - \tfrac{1}{2}(c_1 + c_2)(\alpha_3 + \beta_3), \qquad B = \tfrac{1}{2}(q_1 - q_2)(\alpha_3 + \beta_3). \end{aligned} \tag{11}$$

Further simplification does not seem to be possible. In particular, the coefficient of $\mu$ in the final expression for the emergent intensity does not vanish, as in the case of the asymmetric phase function (cf. *E.A.* I, eq. [47]). Thus equation (4) is the final result, with $J(0)$ and $K(0)$ given by equations (7) and (8).

The solution of the equation of transfer in the $n$th approximation can be obtained by Chandrasekhar's method.[3] The equation of transfer appropriate to the problem may be written

$$\mu \frac{dI(\tau, \mu)}{d\tau} = I(\tau, \mu) - \frac{3}{16}\left\{(3 - \mu^2)\int_{-1}^{+1} I(\tau, \mu)\, d\mu + (3\mu^2 - 1) \times \int_{-1}^{+1} I(\tau, \mu)\, \mu^2 d\mu\right\} - \epsilon. \tag{12}$$

It can be shown that the intensity at any optical depth $\tau$ is given by

$$I(\tau, +\mu) = I(\tau_1 - \tau, -\mu) = T(\tau, \mu) - e^{-(\tau_1 - \tau)/\mu} T(\tau_1, \mu), \tag{13}$$

where

$$T(\tau, \mu) = \sum_{\alpha = \pm 1}^{\pm(n-1)} \frac{L_\alpha (3 - \mu^2)}{1 + \mu k_\alpha} e^{-k_\alpha \tau} + L_0(\tau + \mu) + L_n - \epsilon\left(\tfrac{3}{2}\tau^2 + 3\tau\mu + \tfrac{10}{3}\mu^2\right). \tag{14}$$

The $k_\alpha$'s are $2n - 2$ distinct nonzero roots of the characteristic equation

$$1 = \frac{3}{8}\sum_{j=1}^{n} \frac{a_j (3 - \mu_j^2)}{1 - \mu_j^2 k^2}, \tag{15}$$

where $a_j$ and $\mu_j$ are, respectively, the Gaussian weights and divisions. The $L$'s are determined from the boundary conditions, which may be written

$$T(0, -\mu_i) = T(\tau_1, +\mu_i) = 0 \qquad (i = 1, \ldots, n). \tag{16}$$

## III. RAYLEIGH SCATTERING

In this section we shall discuss the problem of Rayleigh scattering by an emitting atmosphere of finite optical thickness. It will be assumed that the energy sources emit natural light and that the only polarization which arises is due to scattering. The radiation field will be axially symmetric and can be completely characterized by two intensities $I_l$ and $I_r$, which refer to the light which vibrates, respectively, in the meridian plane and perpendicular to it. It is convenient to use matrix notation, in which case $I_l$ and $I_r$ represent the two components of the vector $\boldsymbol{I}$.

The fundamental equation for the emergent intensity (eq. [1]) becomes the following for polarized light:

$$\boldsymbol{I}(0, \mu) = \boldsymbol{\mathfrak{I}}(0, +\mu) - e^{-\tau_1/\mu}\boldsymbol{\mathfrak{I}}(0, -\mu) + \frac{1}{2}\int_0^1 \boldsymbol{S}(\tau_1; \mu, \mu')\, \boldsymbol{\mathfrak{I}}(0, -\mu')\, \frac{d\mu'}{\mu'} - \frac{1}{2}\int_0^1 \boldsymbol{T}(\tau_1; \mu, \mu')\, \boldsymbol{\mathfrak{I}}(0, -\mu')\, \frac{d\mu'}{\mu'}. \tag{17}$$

[3] Cf., e.g., Chandrasekhar, *Ap. J.*, **106**, 172, 1947.

Furthermore, we have the following relations (*R.T.*, p. 43, eq. [227]; pp. 249 ff.):

$$\boldsymbol{P}(\mu, \mu') = \frac{3}{4}\begin{bmatrix} 2(1-\mu^2)(1-\mu'^2)+\mu^2\mu'^2 & \mu^2 \\ \mu'^2 & 1 \end{bmatrix},$$

$$\mathfrak{J}(\tau, \mu) = \frac{1}{2}\int_{-1}^{1} \boldsymbol{P}(\mu, \mu')\boldsymbol{I}(\tau, \mu')\,d\mu' + \frac{\epsilon}{2}\begin{bmatrix} 1 \\ 1 \end{bmatrix},$$

$$\boldsymbol{S}(\tau_1; \mu, \mu') = \frac{3}{4}\begin{bmatrix} S_{ll} & S_{lr} \\ S_{rl} & S_{rr} \end{bmatrix} = \frac{3}{4}\frac{\mu\mu'}{\mu+\mu'} \times \left\{ \begin{bmatrix} \psi(\mu) & \sqrt{2}\,\phi(\mu) \\ \chi(\mu) & \sqrt{2}\,\zeta(\mu) \end{bmatrix} \right.$$

$$\left. \times \begin{bmatrix} \psi(\mu') & \chi(\mu') \\ \sqrt{2}\,\phi(\mu') & \sqrt{2}\,\zeta(\mu') \end{bmatrix} - \begin{bmatrix} \xi(\mu) & \sqrt{2}\,\eta(\mu) \\ \sigma(\mu) & \sqrt{2}\,\theta(\mu) \end{bmatrix} \begin{bmatrix} \xi(\mu') & \sigma(\mu') \\ \sqrt{2}\,\eta(\mu') & \sqrt{2}\,\theta(\mu') \end{bmatrix} \right\}, \tag{18}$$

$$\boldsymbol{T}(\tau_1; \mu, \mu') = \frac{3}{4}\begin{bmatrix} T_{ll} & T_{lr} \\ T_{rl} & T_{rr} \end{bmatrix} = \frac{3}{4}\frac{\mu\mu'}{\mu-\mu'} \times \left\{ \begin{bmatrix} \xi(\mu) & \sqrt{2}\,\eta(\mu) \\ \sigma(\mu) & \sqrt{2}\,\theta(\mu) \end{bmatrix} \right.$$

$$\left. \times \begin{bmatrix} \psi(\mu') & \chi(\mu') \\ \sqrt{2}\,\phi(\mu') & \sqrt{2}\,\zeta(\mu') \end{bmatrix} - \begin{bmatrix} \psi(\mu) & \sqrt{2}\,\phi(\mu) \\ \chi(\mu) & \sqrt{2}\,\zeta(\mu) \end{bmatrix} \begin{bmatrix} \xi(\mu') & \sigma(\mu') \\ \sqrt{2}\,\eta(\mu') & \sqrt{2}\,\theta(\mu') \end{bmatrix} \right\},$$

where

$$\begin{aligned}
\psi(\mu) &= \mu^2 + \frac{3}{8}\int_0^1 \frac{d\mu'}{\mu'}\,[\mu'^2 S_{ll} + S_{lr}], \\
\phi(\mu) &= (1-\mu^2) + \frac{3}{8}\int_0^1 \frac{d\mu'}{\mu'}\,(1-\mu'^2)\,S_{ll}, \\
\chi(\mu) &= 1 + \frac{3}{8}\int_0^1 \frac{d\mu'}{\mu'}\,[\mu'^2 S_{rl} + S_{rr}], \\
\zeta(\mu) &= \frac{3}{8}\int_0^1 \frac{d\mu'}{\mu'}\,(1-\mu'^2)\,S_{rl}, \\
\xi(\mu) &= \mu^2 e^{-\tau/\mu} + \frac{3}{8}\int_0^1 \frac{d\mu'}{\mu'}\,[\mu'^2 T_{ll} + T_{lr}], \\
\eta(\mu) &= (1-\mu^2)\,e^{-\tau_1/\mu} + \frac{3}{8}\int_0^1 \frac{d\mu'}{\mu'}\,(1-\mu'^2)\,T_{ll}, \\
\sigma(\mu) &= e^{-\tau_1/\mu} + \frac{3}{8}\int_0^1 \frac{d\mu'}{\mu'}\,[\mu'^2 T_{rl} + T_{rr}], \\
\theta(\mu) &= \frac{3}{8}\int_0^1 \frac{d\mu'}{\mu'}\,(1-\mu'^2)\,T_{rl}.
\end{aligned} \tag{19}$$

Substituting equations (18) in equation (17), we obtain the final expressions for $I_l(0, \mu)$ and $I_r(0, \mu)$:

$$I_l(0, \mu) = \tfrac{3}{2}\,[J_l(0) - K_l(0) + \tfrac{1}{3}\epsilon]\,[\phi(\mu) - \eta(\mu)]$$
$$+ \tfrac{3}{4}\,[J_r(0) + K_l(0) + \tfrac{2}{3}\epsilon]\,[\psi(\mu) - \xi(\mu)]$$

$$I_r(0,\mu) = \tfrac{3}{2}\,[J_l(0) - K_l(0) + \tfrac{1}{3}\epsilon]\,[\zeta(\mu) - \theta(\mu)] + \tfrac{3}{4}\,[J_r(0) + K_l(0) + \tfrac{2}{3}\epsilon]\,[\chi(\mu) - \sigma(\mu)]\,, \tag{21}$$

where

$$J_l(0) = \frac{1}{2}\int_0^1 I_l(0,\mu)\,d\mu\,,$$

$$J_r(0) = \frac{1}{2}\int_0^1 I_r(0,\mu)\,d\mu\,, \tag{22}$$

$$K_l(0) = \frac{1}{2}\int_0^1 I_l(0,\mu)\,\mu^2 d\mu\,.$$

It remains to evaluate the quantities $J_l(0)$, $J_r(0)$, and $K_l(0)$. This can be done by multiplying through each of equations (20) and (21) by $\frac{1}{2}$ and $\frac{1}{2}\mu^2$ and integrating over the range of $\mu$. This yields four linear equations involving the unknowns $J_l(0)$, $J_r(0)$, $K_l(0)$, $K_r(0)$; however, we need only the first three of these. We obtain the simultaneous system

$$\boldsymbol{MX} = \boldsymbol{L}\,, \tag{23}$$

where

$$\boldsymbol{M} = \begin{bmatrix} 1-\frac{3}{2}a & -\frac{3}{4}b & \frac{3}{2}(a-\frac{1}{2}b) \\ -\frac{3}{2}c & 1-\frac{3}{4}d & \frac{3}{2}(c-\frac{1}{2}d) \\ -\frac{3}{2}A & -\frac{3}{4}B & 1+\frac{3}{2}(A-\frac{1}{2}B) \end{bmatrix}, \quad \boldsymbol{X} = \begin{bmatrix} J_l(0) \\ J_r(0) \\ K_l(0) \end{bmatrix}, \quad \boldsymbol{L} = \frac{\epsilon}{2}\begin{bmatrix} a+b \\ c+d \\ A+B \end{bmatrix}, \tag{24}$$

and

$$a = \frac{1}{2}\int_0^1 [\phi(\mu) - \eta(\mu)]\,d\mu\,, \qquad b = \frac{1}{2}\int_0^1 [\psi(\mu) - \xi(\mu)]\,d\mu\,,$$

$$A = \frac{1}{2}\int_0^1 [\phi(\mu) - \eta(\mu)]\,\mu^2 d\mu\,, \qquad B = \frac{1}{2}\int_0^1 [\psi(\mu) - \xi(\mu)]\,\mu^2 d\mu\,, \tag{25}$$

$$c = \frac{1}{2}\int_0^1 [\zeta(\mu) - \theta(\mu)]\,d\mu\,, \qquad d = \frac{1}{2}\int_0^1 [\chi(\mu) - \sigma(\mu)]\,d\mu\,.$$

The solution of system (23) for $\boldsymbol{X}$ is

$$\boldsymbol{X} = \boldsymbol{M}^{-1}\boldsymbol{L}\,. \tag{26}$$

The elements of $\boldsymbol{M}^{-1}$ can be found, provided that we know $a$, $b$, $A$, $B$, $c$, and $d$. These latter may be obtained in terms of the moments of the $X$- and $Y$-functions by using the relations given in *R.T.*, page 269, equation (183). The following results are derived:

$$\begin{aligned} a &= \tfrac{1}{2}\,\{(\alpha_0 - \beta_0) + (\nu_4 - \nu_3)\,(\alpha_1 + \beta_1)\}\,, \\ b &= \tfrac{1}{2}\,[(\nu_1 - \nu_2)\,(\alpha_1 + \beta_1)]\,, \\ A &= \tfrac{1}{2}\,[(\alpha_2 - \beta_2) + (\nu_4 - \nu_3)\,(\alpha_3 + \beta_3)]\,, \\ B &= \tfrac{1}{2}\,[(\nu_1 - \nu_2)\,(\alpha_3 + \beta_3)]\,, \\ c &= \tfrac{1}{4}\,(\nu_1 - \nu_2)\,[(A_1 + B_1) - 2Q\,(A_2 - B_2)]\,, \\ d &= \tfrac{1}{2}\,\{(A_0 - B_0) + (u_3 - u_4)\,[(A_1 + B_1) - 2Q\,(A_2 - B_2)]\}\,. \end{aligned} \tag{27}$$

Here $\alpha_n$ and $\beta_n$ are the moments of $X_l$ and $Y_l$, and $A_n$ and $B_n$ are the moments of $X_r$ and $Y_r$. The constants $\nu_1$, $\nu_2$, $\nu_3$, $\nu_4$, $u_3$, $u_4$, and $Q$ are determined by formulae (184), (185), and (186) of *R.T.* (p. 269).

In performing a computation it seems simplest to compute, first, $a$, $b$, $A$, $B$, $c$, and $d$, and then to form the matrix $\boldsymbol{M}$, which can be inverted by numerical methods. Finally, the matrix $\boldsymbol{L}$ can be formed, whereupon $\boldsymbol{X}$ is obtained by equation (26); $J_l(0)$, $J_r(0)$, and $K_l(0)$ must all be positive.

Next we shall obtain the solution of the two equations of transfer in the $n$th approximation. The equations of transfer appropriate to the problem are the following:

$$\mu \frac{dI_l(\tau,\mu)}{d\tau} = I_l(\tau,\mu) - \frac{3}{8}\left\{2\int_{-1}^{+1} I_l(\tau,\mu)(1-\mu^2)\,d\mu + \mu^2\int_{-1}^{+1} I_l(\tau,\mu)(3\mu^2-2)\,d\mu + \mu^2\int_{-1}^{+1} I_r(\tau,\mu)\,d\mu\right\} - \tfrac{1}{2}\epsilon, \tag{28}$$

$$\mu \frac{dI_r(\tau,\mu)}{d\tau} = I_r(\tau,\mu) - \frac{3}{8}\left\{\int_{-1}^{+1} I_l(\tau,\mu)\,\mu^2 d\mu + \int_{-1}^{+1} I_r(\tau,\mu)\,d\mu\right\} - \tfrac{1}{2}\epsilon. \tag{29}$$

The solution of the homogeneous parts of these equations has already been given by Chandrasekhar,[4] and it is necessary for us to consider merely the effect of the particular integrals. It can be shown that the solution for the radiation field at any depth $\tau$ is given by

$$I_l(\tau,\mu) = I_l(\tau_1-\tau,-\mu) = T_l(\tau,\mu) - e^{-(\tau_1-\tau)/\mu}T_l(\tau_1,\mu), \tag{30}$$

$$I_r(\tau,\mu) = I_r(\tau_1-\tau,-\mu) = T_r(\tau,\mu) - e^{-(\tau_1-\tau)/\mu}T_r(\tau_1,\mu), \tag{31}$$

where

$$T_l(\tau,\mu) = \sum_{\alpha=\pm 1}^{\pm n} M_\alpha(1-k_\alpha\mu)\,e^{-k_\alpha\tau} + \sum_{\beta=\pm 1}^{\pm(n-1)} \frac{L_\beta(1-\mu^2)}{1+\mu\kappa_\beta}\,e^{-\kappa_\beta\tau} + L_0(\tau+\mu) + L_n + \epsilon(1-\tfrac{3}{4}\tau^2-\tfrac{3}{2}\tau\mu-\tfrac{5}{2}\mu^2), \tag{32}$$

$$T_r(\tau,\mu) = L_0(\tau+\mu) + L_n - \sum_{\alpha=\pm 1}^{\pm n} M_\alpha\frac{(k_\alpha^2-1)}{1+\mu k_\alpha}\,e^{-k_\alpha\tau} + \epsilon(-\tfrac{3}{4}\tau^2-\tfrac{3}{2}\tau\mu-\tfrac{3}{2}\mu^2). \tag{33}$$

The $k_\alpha$'s are $2n$ distinct nonvanishing roots of the characteristic equation

$$\tfrac{4}{3} = \sum_{j=1}^{n}\frac{a_j(1-\mu_j^2)}{1-\mu_j^2k^2}, \tag{34}$$

and the $\kappa_\beta$'s are $2n-2$ distinct nonvanishing roots of the characteristic equation

$$\tfrac{2}{3} = \sum_{j=1}^{n}\frac{a_j(1-\mu_j^2)}{1-\mu_j^2\kappa^2}, \tag{35}$$

where $a_j$ and $\mu_j$ are, respectively, the Gaussian weights and divisions. The $L$'s and $M$'s are determined from the boundary conditions, which may be written

$$T_l(0,-\mu_i) = T_r(0,-\mu_i) = T_l(\tau_1,+\mu_i) = T_r(\tau_1,+\mu_i) = 0 \qquad (i=1,\ldots,n). \tag{36}$$

[4] *Ap. J.*, **106**, 184 ff., 1947.

## IV. COMPUTATIONS AND FINAL REMARKS

The emergent radiation field has been calculated for a finite Rayleigh-scattering atmosphere of thickness $\tau_1 = 0.20$. The results are given in Table 1. The degree of polariza-

TABLE 1

RAYLEIGH SCATTERING: $\tau_1 = 0.20$

| $\mu$ | $I_l(0, \mu)/\epsilon$ | $I_r(0, \mu)/\epsilon$ | $\delta(\mu)$ | $\mu$ | $I_l(0, \mu)/\epsilon$ | $I_r(0, \mu)/\epsilon$ | $\delta(\mu)$ |
|---|---|---|---|---|---|---|---|
| 0.00 | 0.69 | 0.63 | −0.045 | 0.60 | 0.20 | 0.19 | −0.040 |
| .02 | .71 | .64 | − .054 | 0.70 | .17 | .16 | − .032 |
| .04 | .72 | .64 | − .057 | 0.80 | .15 | .14 | − .023 |
| .06 | .70 | .63 | − .059 | 0.90 | .13 | .13 | − .012 |
| .10 | .63 | .56 | − .060 | 1.00 | 0.12 | 0.12 | −0.000 |
| .20 | .46 | .41 | − .058 | | | | |
| .30 | .35 | .32 | − .056 | | | | |
| .40 | .28 | .26 | − .052 | $J_l(0)/\epsilon = 0.152$ | | $J_r(0)/\epsilon = 0.139$ | |
| 0.50 | 0.24 | 0.22 | −0.047 | $K_l(0)/\epsilon = 0.029$ | | | |

tion given in the last column is defined by

$$\delta(\mu) = \frac{I_r(0, \mu) - I_l(0, \mu)}{I_r(0, \mu) + I_l(0, \mu)}. \tag{37}$$

Dr. Chandrasekhar has kindly provided me with tables of the various functions necessary for carrying out these calculations. I wish to thank the University of Kansas for a research grant which enabled me to work on this paper during the summer of 1952.

# MAGNETOHYDRODYNAMIC WAVES UNDER THE ACTION OF THE CORIOLIS FORCE

B. LEHNERT*
Yerkes Observatory
*Received January 11, 1954*

ABSTRACT

In the sun, magnetohydrodynamic waves with wave lengths larger than about a hundredth of the solar radius will be strongly influenced by the Coriolis force if a dipole field with a polar strength of less than 25 gauss is assumed. For small amplitudes, a plane Alfvén wave will be split up into two circularly polarized, transverse waves, traveling with velocities $C_1$ and $C_2$ in the direction of the wave normal and with moduli $|C_1| > |V_a| > |C_2|$, where $V_a = V \cos \psi$, $\boldsymbol{V} = \boldsymbol{B}(\mu\rho)^{-1/2}$ being the Alfvén velocity and $\psi$ the angle between the wave normal and the magnetic field, $\boldsymbol{B}$. Further, there is no equipartition between the kinetic and the magnetic energies. These facts will modify Alfvén's theory of sunspots as far as the periods are concerned; and disturbances of large linear dimensions will be distorted, owing to dispersion. Alfvén's conclusions based on the geometry of the solar magnetic field and his hypothesis on the creation of disturbances due to the presence of instability regions in the solar core are not affected by the discussion of this paper.

## I. INTRODUCTION

The Coriolis force, which usually plays no important role in physical phenomena on a laboratory scale, may often have a dominating influence on phenomena in cosmic physics. This has been pointed out by Chandrasekhar[1] on the basis of his investigations on the effect of the Coriolis force on problems of thermal instability[2] and on the stability of a viscous flow in the presence of a magnetic field.[3] In an earlier work on magneto-turbulence[4] it was concluded that the force is important for a large range of wave numbers of disturbances in the interior of the sun.

## II. AN ESTIMATE OF THE CORIOLIS FORCE

In the theory of turbulence just mentioned, the relative importance of the action on turbulent intensity by an angular velocity, $\boldsymbol{\Omega}$, and an external magnetic field,[5] $\boldsymbol{B}$, is given by the ratio

$$\chi_0 = \frac{\Omega\,(\mu\rho)^{1/2}}{\kappa B}, \tag{1}$$

where $\mu$ is the absolute permeability, $\rho$ is the density of the medium, and $\kappa$ is the wave number, which is supposed to be parallel with $\boldsymbol{B}$. It is easily seen from dimensional considerations that $\chi_0$ represents the ratio between the Coriolis force, $f_C$, and the electromagnetic force, $f_m$:

$$\boldsymbol{f}_C = ?\rho\boldsymbol{v} \times \boldsymbol{\Omega} = \rho\Omega_c\, v_c 2\boldsymbol{v}' \times \boldsymbol{\Omega}' \tag{2}$$

and

$$\boldsymbol{f}_m = (\operatorname{curl} \boldsymbol{h}) \times \boldsymbol{B} = \frac{B_c^2}{\mu L_c} (\operatorname{curl}' \boldsymbol{h}') \times \boldsymbol{B}'. \tag{3}$$

* Now at the Department of Electronics, Royal Institute of Technology, Stockholm, Sweden.

[1] George Darwin lecture for 1953 (in press *M.N.*).

[2] *Proc. Roy. Soc. London*, *A*, **217**, 306, 1953.

[3] *Ibid.*, **216**, 293, 1953.

[4] B. Lehnert, *Quart. Appl. Math.* (in press).

[5] MKSA units are used throughout this paper.

The primed variables in these equations are dimensionless and $B_c$, $\Omega_c$, $L_c = 2\pi/\kappa_c$, and $v_c = L_c/T_c = \Omega_c L_c$ are characteristic values of the actual configuration and state of motion. We get

$$\left|\frac{f_C}{f_m}\right| = \chi_0^2 G' , \tag{4}$$

where $G'$ is a function of the dimensionless variables only.

An estimate of the forces on a whirl-ring according to the theory of sunspots by Alfvén[6] and Walén[7] gives essentially the same result. In the absence of the Coriolis force, a ring-shaped disturbance[8] (Fig. 1) in an incompressible liquid with high electrical conductivity will travel along the magnetic field with a velocity

$$V = B\,(\mu\rho)^{-1/2} ; \tag{5}$$

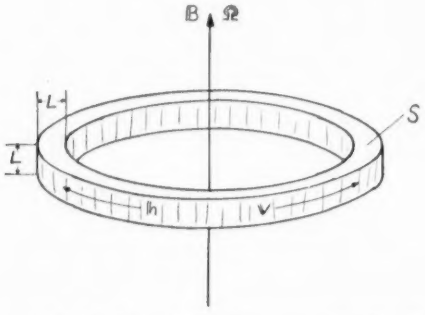


FIG. 1.—Ring-shaped magnetohydrodynamic disturbance traveling along the lines of a magnetic field of strength $\boldsymbol{B}$. An angular velocity, $\boldsymbol{\Omega}$, is introduced parallel to $\boldsymbol{B}$.

and the particle velocity, $\boldsymbol{v}$, and induced magnetic field, $\mu\boldsymbol{h}$, are related by

$$\boldsymbol{v} = -\boldsymbol{h}\left(\frac{\mu}{\rho}\right)^{1/2} ; \qquad \tfrac{1}{2}\rho v^2 = \tfrac{1}{2}\mu h^2 . \tag{6}$$

Assume the front area of the ring to be equal to $S$. The increase in momentum per unit time due to matter being taken in at the front of the ring and accelerated to the velocity $v$ is

$$f_m = \rho v V S , \tag{7}$$

which is also equal to the electrodynamic force on the front of the ring. Now, if an angular velocity, $\boldsymbol{\Omega}$, is introduced perpendicular to the plane of the ring, the Coriolis force becomes

$$f_C = 2\rho\Omega v S L , \tag{8}$$

$L$ being the height of the ring (see Fig. 1). The ratio of the forces becomes

$$\frac{f_C}{f_m} = \frac{\Omega\,(\mu\rho)^{1/2}}{B/2L} . \tag{9}$$

[6] *Ark. f. mat., astr. o. fys.*, Vol. **29B**, No. 2, 1942; and *Nature*, **150**, 405, 1942.

[7] *Ark. f. mat., astr. o. fys.*, Vol. **30A**, No. 15, 1944.

[8] The plane of the ring has been chosen perpendicular to the field, in order to simplify the calculation.

If we assume $L$ to be a hundredth of the solar radius, $R_0 = 6.96 \times 10^8$ meters, and choose some intermediate values, $\Omega = 2 \times 10^{-6}$ sec$^{-1}$, $V = 2$ meters/sec corresponding to a dipole field with a polar strength of about 25 gauss (figures from Alfvén, *Cosmical Electrodynamics* [London: Oxford University Press, 1950], chap. v), we find $f_c/f_m \approx 14$. Hence, *for disturbances larger than a hundredth of the solar radius the Coriolis force plays a dominant role if the polar strength is less than 25 gauss.* The next section gives a quantitative proof of this statement in the case of small amplitudes.

## III. PLANE WAVES FOR SMALL AMPLITUDES

### 1. DEDUCTION OF THE WAVE VELOCITY

With our present knowledge of the physical constants of the sun and the expected order of magnitude of particle velocity, $\boldsymbol{v}$, and induced magnetic field, $\mu\boldsymbol{h}$, we may, with good approximation, treat the interior of the sun as an incompressible liquid with infinite electrical conductivity and neglect the displacement current. We start with the fundamental equations,

$$\operatorname{curl} \boldsymbol{h} = \boldsymbol{i}; \qquad \operatorname{curl} \boldsymbol{E} = -\mu \frac{\partial \boldsymbol{h}}{\partial t}, \tag{10}$$

$$\boldsymbol{E} + \mu \boldsymbol{v} \times (\boldsymbol{H} + \boldsymbol{h}) = 0, \tag{11}$$

$$\operatorname{div} \boldsymbol{h} = \operatorname{div} \boldsymbol{v} = 0, \tag{12}$$

and

$$\rho \left[ \frac{\partial \boldsymbol{v}}{\partial t} + (\boldsymbol{v} \cdot \nabla)\, \boldsymbol{v} + 2\boldsymbol{\Omega} \times \boldsymbol{v} + \boldsymbol{\Omega} \times (\boldsymbol{\Omega} \times \boldsymbol{r}) \right] = \mu \boldsymbol{i} \times (\boldsymbol{H} + \boldsymbol{h}) - \nabla p, \tag{13}$$

where $\boldsymbol{E}$ is the electric field, $\mu\boldsymbol{H}$ a homogeneous magnetic field constant in time, $\boldsymbol{\Omega}$ the angular velocity of the medium, $\boldsymbol{r}$ the radius vector from the origin on the axis of rotation, and $p$ the pressure. The reduction of the system of equations is analogous to the deductions by Walén[7] and Lundquist[9] and will not be given here in detail. An elimination of $\boldsymbol{i}$ and $\boldsymbol{E}$ gives

$$\frac{\partial \boldsymbol{h}}{\partial t} = (\boldsymbol{H} \cdot \nabla)\, \boldsymbol{v} + \operatorname{curl} (\boldsymbol{v} \times \boldsymbol{h}), \tag{14}$$

$$\frac{\partial \boldsymbol{v}}{\partial t} = \frac{\mu}{\rho} (\boldsymbol{H} \cdot \nabla)\, \boldsymbol{h} + 2\boldsymbol{v} \times \boldsymbol{\Omega} - \nabla \Phi - \frac{\mu}{\rho} \boldsymbol{h} \times \operatorname{curl} \boldsymbol{h} + \boldsymbol{v} \times \operatorname{cur} \boldsymbol{v}, \tag{15}$$

and

$$\Phi = \phi_0 + \phi = \frac{p}{\rho} + \phi_c + \frac{\mu}{\rho} (\boldsymbol{H} \cdot \boldsymbol{h}) + \frac{\rho v^2}{2}, \tag{16}$$

where $\phi_c$ is the centrifugal potential and $\phi_0$ is the static value of $\Phi$. Consider plane waves propagated in the $z$-direction (say), so that all quantities vary as $\exp(i\alpha)$, where

$$\alpha = \kappa z + \omega t = \kappa (z + Ct); \qquad \omega = \kappa C. \tag{17}$$

In equation (17), $\kappa$ is the wave number, $C$ is the velocity of propagation, and $\omega$ is the frequency. From equations (12) we obtain

$$\frac{\partial v_z}{\partial z} = \frac{\partial h_z}{\partial z} = 0, \tag{18}$$

which shows that the waves are *transverse;* and we have

$$\boldsymbol{v} = (v_x, v_y, 0); \qquad \boldsymbol{h} = (h_x, h_y, 0). \tag{19}$$

[9] *Ark. f. fys.*, **5**, 338, 1952.

In the following we will carry out the discussion for small amplitudes, so that the second-order terms may be neglected; equations (14) and (15), written in terms of components, take the form

$$\frac{\partial h_x}{\partial t} - H_z \frac{\partial v_x}{\partial z} = 0\,, \qquad \frac{\partial h_y}{\partial t} - H_z \frac{\partial v_y}{\partial z} = 0\,,$$

$$\frac{\partial v_x}{\partial t} - \frac{\mu}{\rho} H_z \frac{\partial h_x}{\partial z} - 2\Omega_z v_y = 0\,, \qquad \frac{\partial v_y}{\partial t} - \frac{\mu}{\rho} H_z \frac{\partial h_y}{\partial z} + 2\Omega_z v_x = 0\,, \tag{20}$$

and

$$2\,(\Omega_y v_x - \Omega_x v_y) - \frac{\partial \phi}{\partial z} = 0\,.$$

With the notation of equation (17), these expressions are equivalent to the linear system of equations[10]

$$\begin{vmatrix} i\omega & 0 & -i\kappa H_z & 0 & 0 \\ 0 & i\omega & 0 & -i\kappa H_z & 0 \\ -\frac{\mu}{\rho} H_z i\kappa & 0 & i\omega & -2\Omega_z & 0 \\ 0 & -\frac{\mu}{\rho} H_z i\kappa & 2\Omega_z & i\omega & 0 \\ 0 & 0 & -2\Omega_y & 2\Omega_x & i\kappa \end{vmatrix} \begin{vmatrix} h_x \\ h_y \\ v_x \\ v_y \\ \phi \end{vmatrix} = 0\,, \tag{21}$$

which has a vanishing determinant if

$$\left[\omega^2 - \frac{\mu}{\rho} H_z^2 \kappa^2\right]^2 - 4\omega^2 \Omega_z^2 = 0\,. \tag{22}$$

The solutions are

$$\pm \omega_{1,\,2} = \pm \kappa C_{1,\,2} = \pm \{\Omega_z \pm [\Omega_z^2 + (\kappa V_z)^2]^{1/2}\}^{1/2}; \qquad \boldsymbol{V} = \boldsymbol{H}\left(\frac{\mu}{\rho}\right)^{1/2}, \tag{23}$$

where $\Omega_z$ and $V_z$ are the components of the angular velocity, $\boldsymbol{\Omega}$, and the Alfvén velocity, $\boldsymbol{V}$, in the direction of $\boldsymbol{\kappa}$. The wave velocity in this direction becomes

$$C_{1,\,2} = \pm V_z [(1+\chi^2)^{1/2} \pm \chi]\,, \qquad \text{where } \chi = \frac{\Omega_z}{\kappa V_z}, \tag{24}$$

the normal of the wave front making the angles $\psi$ and $\varphi$ with the magnetic field and the angular velocity, respectively;

$$V_z = V \cos\psi\,; \qquad \Omega_z = \Omega \cos\varphi\,, \tag{25}$$

In Figure 2 the values of the wave velocities $C_1$ and $C_2$ are given for disturbances in the sun with wave lengths in the range $0.5\text{–}5 \times 10^{-4}$ of the solar radius. The parameter $\chi$, which corresponds to the ratio between the Coriolis force and the electrodynamic force, is equal to, or larger than, unity in a large part of the range. It is evident that $|C_1|$ and $|C_2|$ *differ appreciably from* $|V_z|$ *when the wave length exceeds a hundredth of the solar radius.*

[10] This is a special case of Chandrasekhar's results (*Ap. J.*, **118**, 7, 1953).

2. PROPERTIES OF THE WAVES

When equation (23) is satisfied, it follows from equations (21) that

$$v_y = \pm i v_x \tag{26}$$

and

$$h_x = \frac{\kappa H_z}{\omega} v_x ; \qquad h_y = \frac{\kappa H_z}{\omega} v_y . \tag{27}$$

Thus the particle velocity and the induced magnetic field are

$$\boldsymbol{v}(z, t) = v_{1x}(1, i, 0)\, e^{i(\kappa z \pm \omega_1 t)} + v_{2x}(1, -i, 0)\, e^{i(\kappa z \pm \omega_2 t)} = \boldsymbol{v}_1 + \boldsymbol{v}_2 \tag{28}$$

and

$$\boldsymbol{h}(z, t) = \left(\frac{\rho}{\mu}\right)^{1/2} \left[\frac{V_z}{C_1} \boldsymbol{v}_1 + \frac{V_z}{C_2} \boldsymbol{v}_2\right]. \tag{29}$$

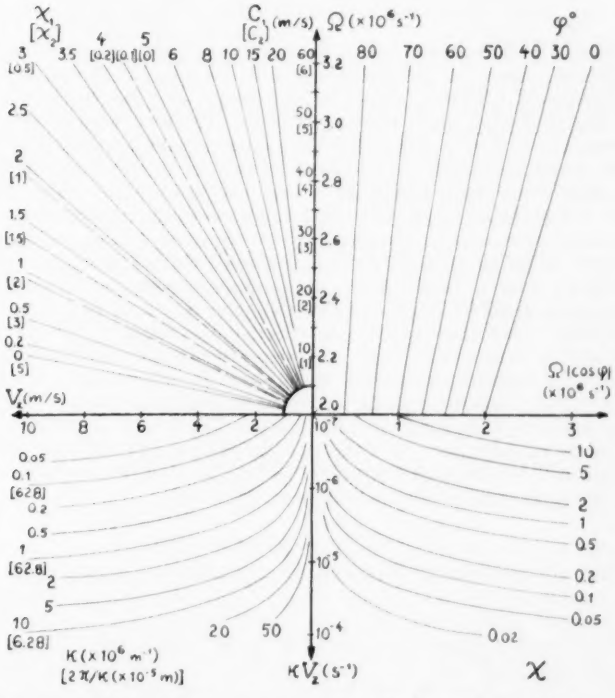


FIG. 2.—Plane magnetohydrodynamic waves for small amplitudes in the sun: $\Omega$ is the angular velocity (*right-hand side of upper co-ordinate axis*), and $V_z = H_z(\mu/\rho)^{1/2} = V \cos\psi$ is the velocity of the Alfvén wave in the direction of the wave normal, which forms the angle $\psi$ with the sun's magnetic field, $\boldsymbol{B} = \mu \boldsymbol{H}$, where $\boldsymbol{V} = \boldsymbol{H}(\mu/\rho)^{1/2}$ is chosen within the range given by Alfvén (*Cosmical Electrodynamics*, chap. v). Further, $\varphi$ is the angle between $\boldsymbol{\Omega}$ and the wave number $\boldsymbol{\kappa}$ and $\chi$ is a parameter given by equation (24) with indices 1 and 2, corresponding to $C_1$ and $C_2$, which are the wave velocities of the two circularly polarized solutions given by equation (24) and shown by the left-hand side of the upper co-ordinate axis. All figures within brackets in the upper left-hand quadrant refer to the solution $C_2$; dashed lines refer only to $\chi_2$ (and $C_2$), whereas lines with two figures refer to both $\chi_1$ and $\chi_2$. The sun's radius is equal to $6960 \times 10^5$ meters. Values are given for the wave length, $2\pi/\kappa$, by figures within brackets in the lower left-hand quadrant.

The solution, therefore, represents *two circularly polarized, transverse waves with the field vectors rotating in opposite directions*. The wave velocities are $C_1$ and $C_2$, where $|C_1| > |V_z| > |C_2|$ and $V_z$ is the velocity of the wave front in the direction of $\boldsymbol{\kappa}$ in the absence of the angular velocity, $\boldsymbol{\Omega}$.

A special type of wave is obtained if we assume the equivalent strings to be removed from their equilibrium position and released with zero initial velocity at time $t = 0$ in the $xy$-plane. The particle velocity is the real value, given by equation (28),

$$\boldsymbol{u}(0, 0) = Re\,[\boldsymbol{v}(0, 0)] = 0\,; \qquad v_{1x} + v_{2x} = 0\,. \tag{30}$$

For waves with normals in the negative $z$-direction (say), we get

$$\boldsymbol{u} = v_{1x}(\cos a_1, -\sin a_1, 0) - v_{1x}(\cos a_2, \sin a_2, 0) = \boldsymbol{u}_1 + \boldsymbol{u}_2\,; \tag{31}$$

this reduces to

$$\boldsymbol{u} = 2\,v_{1x}\,[\sin\,\kappa\,(z + V_z t)]\,(\sin\,\Omega_z t, -\cos\,\Omega_z t, 0) \tag{32}$$

for small values of $\chi$. The case $\chi = 0$ corresponds to a plane-polarized Alfvén wave. For small values of $\chi$, equation (32) shows that the wave velocity remains approximately unaltered, whereas the "plane" of polarization precesses with the frequency $\Omega_z$.

The foregoing results are easily understood if, for simplicity, we assume $\boldsymbol{V}$ and $\boldsymbol{\Omega}$ to be parallel with $\boldsymbol{\kappa}$ (i.e., $\psi = \varphi = 0$). Then the vectors $\boldsymbol{u}_1$ and $\boldsymbol{u}_2$ rotate in anticlockwise and clockwise directions, respectively, when observed in the direction of the positive $z$-axis. The accelerations $2\boldsymbol{u}_1 \times \boldsymbol{\Omega}$ and $2\boldsymbol{u}_2 \times \boldsymbol{\Omega}$ act, respectively, in the same and in the opposite direction as the restoring electromagnetic force of the equivalent elastic strings representing the magnetic field. Consequently, the apparent tension will be greater for the $\boldsymbol{u}_1$-wave and smaller for the $\boldsymbol{u}_2$-wave than for the Alfvén wave and $|C_1| > V > |C_2|$. On the other hand, when $\varphi$ tends to $\pi/2$, the contribution from Coriolis force to the tension of the strings decreases to zero, and both $|C_1|$ and $|C_2|$ tend to $V$. The situation is somewhat similar to the classical Zeeman effect, if the restoring force acting on an oscillating charge is represented by the restoring force of the magnetic-field lines and the Lorentz force is represented by the Coriolis force. The state of motion described by equation (32) would, in such a case, be analogous to the Larmor precession.

Finally, we conclude from equation (29) that *there is generally no equipartition beween the kinetic and the magnetic energies* in the waves. Solutions (28) and (29) do not satisfy equations (14) and (15) for large amplitudes as long as $\chi$ differs from zero, since there remains an uncompensated nonlinear term in equation (15).

### 3. DISTURBANCES OF ARBITRARY FORM

An arbitrary traveling disturbance may be obtained from a superposition of plane waves:

$$\boldsymbol{v}(\boldsymbol{r}, t) = \int_{-\infty}^{+\infty}\!\!\int\!\!\int [\boldsymbol{v}_1(\boldsymbol{\kappa})\, e^{i\omega_1(\boldsymbol{\kappa})t} + \boldsymbol{v}_2(\boldsymbol{\kappa})\, e^{i\omega_2(\boldsymbol{\kappa})t}]\, e^{i\boldsymbol{\kappa}\boldsymbol{r}} d\kappa_x d\kappa_y d\kappa_z\,. \tag{33}$$

At time $t = 0$, the disturbance has the forms

$$\boldsymbol{v}(\boldsymbol{r}, 0) = \int_{-\infty}^{+\infty}\!\!\int\!\!\int [\boldsymbol{v}_1(\boldsymbol{\kappa}) + \boldsymbol{v}_2(\boldsymbol{\kappa})]\, e^{i\boldsymbol{\kappa}\boldsymbol{r}} d\kappa_x d\kappa_y d\kappa_z \tag{34}$$

and

$$\boldsymbol{v}(\boldsymbol{\kappa}) = \boldsymbol{v}_1(\boldsymbol{\kappa}) + \boldsymbol{v}_2(\boldsymbol{\kappa}) = (2\pi)^{-3} \int_{-\infty}^{+\infty}\!\!\int\!\!\int \boldsymbol{v}(\boldsymbol{r}, 0)\, e^{-i\boldsymbol{\kappa}\boldsymbol{r}} dx dy dz\,. \tag{35}$$

A simple example of these formulae is given if we put $v_{1z}(\boldsymbol{\kappa}) = v_{2z}(\boldsymbol{\kappa}) = 0$ and study a disturbance which is made up of circularly polarized waves with particle velocities in the $xy$-plane, where we have chosen

$$\boldsymbol{\kappa} = (0, 0, \kappa) \tag{36}$$

for all these waves. From equation (26) we get

$$v_{1y}(\boldsymbol{\kappa}) = i v_{1x}(\boldsymbol{\kappa}) \qquad \text{and} \qquad v_{2y}(\boldsymbol{\kappa}) = -i v_{2x}(\boldsymbol{\kappa}) ; \tag{37}$$

and from equation (35) we deduce

$$v_{1x}(\boldsymbol{\kappa}) = \tfrac{1}{2}[v_x(\boldsymbol{\kappa}) - i v_y(\boldsymbol{\kappa})] ; \qquad v_{2x}(\boldsymbol{\kappa}) = \tfrac{1}{2}[v_x(\boldsymbol{\kappa}) + i v_y(\boldsymbol{\kappa})] . \tag{38}$$

Equation (33) now assumes the special form

$$\begin{aligned} \boldsymbol{v}(\boldsymbol{r}, t) = \int_{-\infty}^{+\infty} (2\pi)^{-3} \iiint_{-\infty}^{+\infty} \{ &\tfrac{1}{2}(1, i, 0)[v_x(\boldsymbol{r}', 0) - i v_y(\boldsymbol{r}', 0)] e^{i\omega_1(\boldsymbol{\kappa})t} \\ &+ \tfrac{1}{2}(1, -i, 0)[v_x(\boldsymbol{r}', 0) + i v_y(\boldsymbol{r}', 0)] e^{i\omega_2(\boldsymbol{\kappa})t} \} e^{-i\kappa z'} dx' dy' dz' e^{i\kappa z} d\kappa . \end{aligned} \tag{39}$$

For small values of $\chi$ the frequencies are

$$\omega_1 \approx \kappa V_z + \Omega_z ; \qquad \omega_2 \approx \kappa V_z - \Omega_z . \tag{40}$$

Hence

$$\begin{aligned} \boldsymbol{v}(\boldsymbol{r}, t) \approx \int_{-\infty}^{+\infty} (2\pi)^{-3} \iiint_{-\infty}^{+\infty} \{ &\tfrac{1}{2}(1, i, 0)[v_x(\boldsymbol{r}', 0) - i v_y(\boldsymbol{r}', 0)] e^{i\Omega_z t} \\ &+ \tfrac{1}{2}(1, -i, 0)[v_x(\boldsymbol{r}', 0) - i v_y(\boldsymbol{r}', 0)] e^{-i\Omega_z t} \} e^{i\kappa V_z t - i\kappa z'} dx' dy' dz' e^{i\kappa z} d\kappa . \end{aligned} \tag{41}$$

Let

$$\boldsymbol{v}_A(\boldsymbol{r}, t) = (2\pi)^{-3} \int_{-\infty}^{+\infty} \boldsymbol{v}(\boldsymbol{\kappa}) e^{i\kappa(z + V_z t)} d\kappa ; \qquad \boldsymbol{u}_A(\boldsymbol{r}, t) = Re[\boldsymbol{v}_A(\boldsymbol{r}, t)] ; \tag{42}$$

this is the solution for $\chi = 0$. The real part of equation (41) becomes

$$\boldsymbol{u}(\boldsymbol{r}, t) = (u_{Ax} \cos \Omega_z t + u_{Ay} \sin \Omega_z t, -u_{Ax} \sin \Omega_z t + u_{Ay} \cos \Omega_z t, 0) . \tag{43}$$

Thus the disturbance is propagated with unaltered shape and with the same velocity as in the case where the angular velocity is absent. At the same time, the whole configuration precesses around the direction of $\boldsymbol{\kappa}$ with a frequency $\Omega \cos \varphi$, where $\varphi$ is the angle between the angular velocity and the normal of the wave front. However, *as soon as the main part of the spectrum, which builds up the disturbance, occurs in a region of wave numbers corresponding to $\chi \geqslant 1$, a given initial form will be strongly distorted due to dispersion* after having been propagated for a short time.

## IV. THE JOULE LOSSES

An estimate of the importance of the Joule losses is easily obtained if the term $(1/\mu\sigma)\nabla^2 \boldsymbol{h}$ ($\sigma$ is the electrical conductivity) is introduced in the right member of equation (14). The treatment follows the same lines as in Section III, and equation (22) is replaced by

$$[i\omega(i\omega + a) - V_z^2 (i\kappa)^2]^2 + 4(i\omega + a)^2 \Omega_z^2 = 0 ; \qquad a = \frac{\kappa^2}{\mu\sigma} , \tag{44}$$

which has the solutions

$$\pm \omega_{1,2} = \pm \Omega_z + i\,\frac{a}{2} \pm \left( \kappa^2 V_z^2 + \Omega_z^2 \pm i a \Omega_z - \frac{a^2}{4} \right)^{1/2}. \tag{45}$$

The wave length of interest in connection with sunspots will hardly be smaller than a hundredth of the solar radius, so that we may suppose that $\kappa_{\max} = 10^{-5}$ meter$^{-1}$. The conductivity may be supposed to exceed the value $\sigma_{\min} = 10^5$ ohm$^{-1}$ meter$^{-1}$ (see Alfvén, *Cosmical Electrodynamics*, chap. v), giving $a_{\max} = 4 \times 10^{-10}$ sec$^{-1}$. With a smallest value of $V$ equal to about 1 meter/sec, a minimum damping distance, $V/(2a)$ (where the wave has been damped to $1/e$ of its initial value), of about three times the solar radius is obtained for the Alfvén wave ($\chi = 0$) traveling in the direction of the magnetic field. Further, we have

$$\left[ \frac{a}{2\kappa V} \right]_{\max} \approx 4 \times 10^{-3}. \tag{46}$$

Consequently, Alfvén's statement that the losses are negligible for waves in the sun can be extended to solutions (45).

## V. CONCLUSIONS REGARDING THE THEORY OF SUNSPOTS

The discussion of the previous sections has shown that the Coriolis force plays an important role for magnetohydrodynamic waves in the sun which have wave lengths larger than a hundredth of the solar radius if the polar strength of the dipole field is less than 25 gauss. This has been shown quantitatively for waves of small amplitudes, but it can hardly be expected that the effect of the angular velocity will turn out to be negligible for waves of finite amplitudes. If the conclusions in this paper are right, then many important points in Alfvén's theory on sunspots[11] may have to be changed. Thus the calculations of the time of propagation of waves in the discussion of the sunspot cycle may have to be modified. Further, disturbances of large dimensions will probably be distorted because of dispersion. However, there are also many important parts of the theory of sunspots which remain unaltered, such as the symmetry of the patterns on the northern and southern hemispheres and the progression of the sunspot zone from high to low latitudes, as explained by the geometry of a field from a magnetic dipole in the sun. The creation of disturbances due to the presence of instability regions in the solar core, as assumed by Alfvén and supported by the statistical works of Galvenius and Wold[12] and Whittle[13] are not affected by this discussion.

The author wishes to express his thanks to Professor S. Chandrasekhar for suggesting these investigations and for many valuable and stimulating discussions. The author is also indebted to Professor H. Alfvén for a positive criticism of the paper. This work has been supported by grants from Statens Naturvetenskapliga Forskningsråd and the Royal Institute of Technology, Stockholm.

[11] *Cosmical Electrodynamics*, chap. v.
[12] *Ark. f. mat., astr. o. fys.*, Vol. **34A**, No. 24, 1947.
[13] In preparation.

# ANALYSIS OF COUNTS OF THE EXTRAGALACTIC NEBULAE IN TERMS OF A FLUCTUATING DENSITY FIELD. II

D. NELSON LIMBER
Yerkes Observatory
*Received June 24, 1953; revised December 30, 1953*

## ABSTRACT

In this paper the theory recently developed by the writer for the analysis of counts of the extragalactic nebulae in terms of a fluctuating density field has been applied to the counts obtained by Shane and Wirtanen at the Lick Observatory. The observational data have been reduced to the forms required for this analysis, and the corresponding theoretical functions have been obtained for several sets of values for the parameters involved. The comparison of the theory with the observations indicates that the effects of fluctuations in the absorption within our own Galaxy can be neglected in a first approximation; further, the theoretical expectations for the case in which there is a dispersion of 2 mag. in the absolute magnitudes of the nebulae are found to be in best accord with the observations. The mean square of the deviations in the space density of the nebulae from the mean is found to be about twenty-five times the square of the mean density. The value for the microscale, $r_0$, characterizing the "eddy" distribution of the nebulae and the value for the mean density of the nebulae in space, $\bar{\rho}$, are both dependent upon the particular values used for the limiting apparent magnitude of the counts, $m_0'$, the mean absolute magnitude of the nebulae, $M_0$, and the optical half-thickness of the galaxy, $\bar{\tau}_{1/2}$; for given values of these quantities it is shown how the corresponding values of $r_0$ and $\bar{\rho}$ can be deduced on the basis of the theory. From a straightforward analysis of the counts as they are given, the value $\bar{\tau}_{1/2} = 0.76$ is obtained. If this value is taken as that which is appropriate to the observational material and if the best available values for $m_0'$ and $M_0$ are used, it is found that $r_0 = 3.0 \times 10^6$ parsecs and $\bar{\rho} = 6.0 \times 10^{-19}$ nebulae per cubic parsec.

## I. INTRODUCTION

In a previous paper[1] the writer has developed a method for analyzing the counts of the extragalactic nebulae in terms of a fluctuating density field for the nebulae in space. In the present paper the counts obtained by C. D. Shane and C. A. Wirtanen at the Lick Observatory are analyzed according to the proposed model. Here—as in Paper I—we shall consider an idealized model such that the absolute magnitude, $M$, the apparent magnitude, $m$, and the distance, $r$, for a particular nebula are related in the following way:

$$M = m + 5 - 5 \log_{10} r - 2.5\tau \log_{10} e \,, \tag{1}$$

where $\tau$ is the optical thickness of the Galaxy in the direction considered. We shall further assume that the universe of those nebulae which are recorded in the counts is static in time and homogeneous with respect to the absolute magnitudes and the spatial-distribution properties of the nebulae within it. Deviations from the conditions of these assumptions most certainly exist; and, if well determined, the effects introduced by such deviations could be taken into account at the expense of some mathematical simplicity. However, it is felt that such deviations are not yet well enough known to warrant their inclusion. It is further felt that in the proposed type of statistical treatment such refinements are hardly justified in any case.

## II. THE OBSERVATIONAL DATA AND THEIR REDUCTION TO THE REQUIRED FORMS

*The counts.*—The counts to be analyzed in this paper are those of C. D. Shane and C. A. Wirtanen.[2] This material is discussed by them in a paper which is in preparation.[3]

[1] D. N. Limber, *Ap. J.*, **117**, 134, 1953; this paper will be referred to hereafter as "Paper I."

[2] I am greatly indebted to Professor Shane for making available to me the results of this work in the form of a master-chart of the counts themselves, together with valuable auxiliary material.

[3] See also the discussion of these observations which is given in the paper by J. Neyman, E. L. Scott, and C. D. Shane, *Ap. J.*, **117**, 92, 1953.

For our purposes it is sufficient to note that the observations consist of counts of the extragalactic nebulae to a given limiting apparent magnitude for each square degree of the sky between $11^h48^m$ and $18^h10^m$ in right ascension and between $-23^\circ$ and $+23^\circ$ in declination. The counts were made from $6^\circ \times 6^\circ$ plates, which were so taken that strips $1^\circ$ wide on the four edges of each plate overlap with the adjacent plates. The limiting apparent magnitude has been tentatively given by Professor Shane as 18.4 on Hubble's scale of nebular magnitudes; however, there is as yet some uncertainty in this figure.

*The raw observational values for* $\overline{N}^2$ *and* $\overline{NN}_\phi$.—In order to take into account most directly the effects of the absorption within our own Galaxy, the parallels of galactic latitude for each degree of latitude from $+20^\circ$ through $+77^\circ$ were drawn on the master-chart. The number of nebulae per square degree for every degree of arc along these parallels was then determined by means of four-point linear interpolation among the entries on the master-chart. We shall let $N$ denote the number of nebulae per square degree at a particular point, and we shall let $NN_\phi$ be the product of the numbers of nebulae at two points separated by an angle $\phi$ along a parallel of galactic latitude. From the interpolated values for $N$, the values for $\overline{N}^2$ and $\overline{NN}_\phi$ ($\phi = 0^\circ, 1^\circ, 2^\circ, 3^\circ, 4^\circ$, and $5^\circ$) were obtained for each of the parallels drawn.

The calculation of the values for $\overline{NN}_\phi$ was carried out in the following manner. Consider a given parallel $n$ degrees in length. The number of nebulae per square degree for each degree along such a parallel was recorded separately on each of two strips. In order to obtain $\overline{NN}_\phi$ for this parallel, one strip was displaced $\phi$ degrees with respect to the other, and then the values on the two strips which were adjacent after the displacement were multiplied together, and the mean value of these products was obtained. It is apparent that the data within $\phi$ degrees of the ends of the strips are used only once in the evaluation of $\overline{NN}_\phi$, in contrast with the overlapping portions of the strips, where each entry enters twice—once from each strip. In order to correct for this, let the value for $\overline{NN}_\phi$, when corrected for the inhomogeneity due to the end-points, be expressed as

$$(\overline{NN}_\phi)_{\text{homog}} = \frac{1}{n}\left[(n-\phi)(\overline{NN}_\phi)_{\text{calc}} + \phi(\overline{NN}_\phi)_{\text{end}}\right], \tag{2}$$

where $(\overline{NN}_\phi)_{\text{calc}}$ is the value uncorrected for the end-point errors, and $(\overline{NN}_\phi)_{\text{end}}$ is a fictitious $\overline{NN}_\phi$ corresponding to the $\phi$ degrees of data at the ends of the strips. If $(\overline{N}^2)_{n-\phi}$ and $(\overline{N}^2)_\phi$ are used to denote the values of $\overline{N}^2$ for those portions of the strips which overlap and for those portions which do not overlap, respectively, then the expression which has been assumed for the evaluation of $(\overline{NN}_\phi)_{\text{end}}$ can be written

$$\frac{(\overline{NN}_\phi)_{\text{end}}}{(\overline{N}^2)_\phi} = \frac{(\overline{NN}_\phi)_{\text{calc}}}{(\overline{N}^2)_{n-\phi}}. \tag{3}$$

The end-point corrections obtained in this way have been applied to each of the values of $\overline{NN}_\phi$ for all the galactic parallels chosen. While it is evident that such a correction does not provide an exact reduction to homogeneity, trial comparisons with a method of successive approximations indicate that it is sufficiently accurate for the present purposes.

Next, the results for the individual parallels obtained in the manner described were combined to form a series of overlapping normal points in galactic latitude. The data on the ranges in galactic latitude for these normal points are given in Table 1, where the weight which has been assigned to each of the normal points is the total number of degrees measured along those of the chosen parallels which contribute to the given normal point. The values for $\overline{N}^2$ and $\overline{NN}_\phi$—corrected for the errors in the end-points—are given in Table 2.

*The reduction of the raw observational values for* $\overline{NN}_\phi$ *to the required forms.*—The values for $\overline{N}^2$ and $\overline{NN}_\phi$ appearing in Table 2 have been calculated from values of $N$ which have been obtained from interpolation among the entries on the master-chart. In order to

emphasize the interpolation origin for these values, the Gothic letter $\mathfrak{N}$, which has been used for them above, will be reserved for them alone.

Let us denote by the use of the "open" $\mathfrak{N}$ those values which pertain to the $1^\circ \times 1^\circ$ squares on the master-chart. If $\mathfrak{N}_T$ is used to denote the true number of nebulae in such a square which are brighter than the selected limiting apparent magnitude of the counts and if $\mathfrak{N}_0$ is used to denote the corresponding value which is actually given on the master-chart, then the error $\delta$ for a particular entry on the master-chart is defined by the relation

$$\mathfrak{N}_0 = \mathfrak{N}_T + \delta \,, \tag{4}$$

TABLE 1

NORMAL POINTS AND THEIR GALACTIC-LATITUDE RANGES

| Normal Point | Weight | Galactic-Latitude Range | Normal Point | Weight | Galactic-Latitude Range |
|---|---|---|---|---|---|
| $\mathfrak{N}_1$ | 549 | $20^\circ \leqslant b < 30^\circ$ | $\mathfrak{N}_6$ | 671 | $50^\circ \leqslant b < 60^\circ$ |
| $\mathfrak{N}_2$ | 571 | $26^\circ \leqslant b < 36^\circ$ | $\mathfrak{N}_7$ | 579 | $56^\circ \leqslant b < 66^\circ$ |
| $\mathfrak{N}_3$ | 676 | $32^\circ \leqslant b < 42^\circ$ | $\mathfrak{N}_8$ | 486 | $62^\circ \leqslant b < 72^\circ$ |
| $\mathfrak{N}_4$ | 813 | $38^\circ \leqslant b < 48^\circ$ | $\mathfrak{N}_9$ | 394 | $68^\circ \leqslant b \leqslant 77^\circ$ |
| $\mathfrak{N}_5$ | 767 | $44^\circ \leqslant b < 54^\circ$ | | | |

TABLE 2

OBSERVATIONAL VALUES FOR $\overline{\mathfrak{N}^2}$ AND $\overline{\mathfrak{N}\mathfrak{N}_\phi}$ CORRECTED ONLY FOR END-POINT INHOMOGENEITIES

| Normal Point | $\overline{\mathfrak{N}^2}$ | $\overline{\mathfrak{N}\mathfrak{N}_1}$ | $\overline{\mathfrak{N}\mathfrak{N}_2}$ | $\overline{\mathfrak{N}\mathfrak{N}_3}$ | $\overline{\mathfrak{N}\mathfrak{N}_4}$ | $\overline{\mathfrak{N}\mathfrak{N}_5}$ | $\overline{\mathfrak{N}^2}$ |
|---|---|---|---|---|---|---|---|
| $\mathfrak{N}_1$ | 339.6 | 318.5 | 299.8 | 286.0 | 282.8 | 278.1 | 274.0 |
| $\mathfrak{N}_2$ | 722.8 | 698.1 | 661.4 | 642.7 | 634.5 | 626.1 | 633.2 |
| $\mathfrak{N}_3$ | 1631 | 1575 | 1516 | 1491 | 1483 | 1474 | 1446 |
| $\mathfrak{N}_4$ | 3617 | 3452 | 3276 | 3168 | 3100 | 3055 | 3012 |
| $\mathfrak{N}_5$ | 4534 | 4310 | 4108 | 3975 | 3874 | 3799 | 3796 |
| $\mathfrak{N}_6$ | 4259 | 4106 | 4021 | 3973 | 3945 | 3942 | 3908 |
| $\mathfrak{N}_7$ | 5254 | 5097 | 4963 | 4911 | 4872 | 4851 | 4861 |
| $\mathfrak{N}_8$ | 5586 | 5427 | 5271 | 5215 | 5172 | 5162 | 5200 |
| $\mathfrak{N}_9$ | 5514 | 5363 | 5206 | 5173 | 5156 | 5152 | 5172 |

where $\delta$ includes (1) the error in the plate limit for the particular $6^\circ \times 6^\circ$ plate, (2) the memory error on the given plate, and (3) the true counting error.

In terms of this notation, the fact that a particular interpolated value $\mathfrak{N}$ is a weighted mean of the four nearest master-chart entries can be expressed by means of the equation

$$\mathfrak{N} = \sum_k \omega_k \mathfrak{N}_{0,k} = \sum_k \omega_k [\mathfrak{N}_{T,k} + \delta_k] \,, \tag{5}$$

where $\omega_k$ is the appropriate weight for the $k$th of the contributing master-chart entries. From this equation it follows that (cf. eq. [12])

$$\overline{\mathfrak{N}\mathfrak{N}_\phi} = \sum_k \sum_l \bar{\omega}_{kl} [(\overline{\mathfrak{N}_{T,k}\mathfrak{N}_{T,l}}) + \overline{\delta_k \delta_l}] \,, \tag{6}$$

$$\bar{\omega}_{kl} \equiv \overline{\omega_k \omega_l} \,.$$

If we now introduce a function $F_\phi$, defined by the relation

$$F_\phi \equiv \sum_k \sum_l \tilde{\omega}_{kl} \overline{\delta_k \delta_l}, \tag{7}$$

then equation (6) can be written in the more useful form

$$\sum_k \sum_l \tilde{\omega}_{kl} (\overline{\mathbf{N}_{T,k} \mathbf{N}_{T,l}}) = (\overline{\mathbf{N}\mathbf{N}}_\phi - F_\phi). \tag{8}$$

Finally, a correction must be made for the smoothing effect introduced by the grouping of the counted numbers of nebulae into totals for $1^\circ \times 1^\circ$ squares. To do this, let the italic $N$ be used to denote the true area density of the nebulae for small subregions of the $1^\circ \times 1^\circ$ squares. (For purposes of reference the several notations for the several types of area densities which have been adopted are collected and defined in Table 3.) Let each

TABLE 3

NOTATIONS EMPLOYED FOR THE SEVERAL TYPES OF AREA DENSITIES

| Notation | Definition |
|---|---|
| $\mathbf{N}$ | Area density from interpolation among the master-chart entries |
| $\mathbf{N}_0$ | Observed area density for $1^\circ \times 1^\circ$ squares of the master-chart |
| $\mathbf{N}_T$ | True area density for $1^\circ \times 1^\circ$ squares of the master-chart |
| $N$ | True area density for small subregions of $1^\circ \times 1^\circ$ squares of the master-chart |

$1^\circ \times 1^\circ$ square on the master-chart be subdivided into $n$ of these small subregions. We then have

$$\mathbf{N}_T = \sum_{i=1}^{n} W_i N_i, \tag{9}$$

where the weight $W_i$ of the $i$th subregion is simply the area of that region. From equation (9) it follows that

$$\overline{\mathbf{N}_T \mathbf{N}_{T,\phi}} = \sum_i \sum_j \overline{W_{ij}} \overline{N_i N_j}, \tag{10}$$

$$\overline{W_{ij}} = \overline{W_i W_j}.$$

The values of $\overline{N_i N_j}$ can then be expressed in terms of the observed values for $\overline{\mathbf{N}\mathbf{N}}_\phi$ by combining equations (8) and (10). We obtain, in this way,

$$\sum_k \sum_l \tilde{\omega}_{kl} \left[ \sum_i \sum_j \overline{W_{ij}} \overline{N_i N_j} \right] = (\overline{\mathbf{N}\mathbf{N}}_\phi - F_\phi). \tag{11}$$

In the work to follow, the quantities $\tilde{\omega}_{kl}$, $\overline{W_{ij}}$, and $F_\phi$ will first be evaluated. Having obtained these, we shall then have, for each set of observational values $\overline{\mathbf{N}\mathbf{N}}_\phi$, $\phi = 0^\circ$, $1^\circ$, $2^\circ$, $3^\circ$, $4^\circ$, and $5^\circ$, six linear equations from which to determine the behavior of $\overline{NN}_\phi$. Since for a particular value of $\phi$ in equation (11) the quantities $\overline{N_i N_j}$ are known in terms of $\overline{NN}_{\phi'}$, the observational material permits the determination of six parameters describing the behavior of $\overline{NN}_\phi$ as a function of $\phi$. These parameters will be taken to be the values of $\overline{NN}_\phi$ for $\phi = 0^\circ$, $1^\circ$, $2^\circ$, $3^\circ$, $4^\circ$, and $5^\circ$, and these are the values which must be used in comparing theory and observation. The several steps outlined above for the determination of $\overline{NN}_\phi$ will now be considered in turn.

(i) *The evaluation of* $\overline{\mathbf{N}_T\mathbf{N}_{T,\phi}}$ *in terms of* $\overline{\mathbf{N}\mathbf{N}}_\phi$.—Let us examine equation (4) and its implications in some detail. If the relation

$$\bar{\delta} = 0 \tag{12}$$

be taken as a partial definition of $\delta$—and hence of the plate limit—we then have, from equation (4),

$$\begin{aligned}\overline{\mathbf{N}_T\mathbf{N}_{T,\phi}} &= \overline{(\mathbf{N}_0 - \delta)(\mathbf{N}_{0,\phi} - \delta_\phi)} \\ &= \overline{\mathbf{N}_0\mathbf{N}_{0,\phi}} - \overline{\delta\,\delta_\phi}\,.\end{aligned} \tag{13}$$

Thus the values for $\overline{\delta\delta}_\phi$ must be determined in order to express $\overline{\mathbf{N}_0\mathbf{N}_{0,\phi}}$ in terms of $\overline{\mathbf{N}_T\mathbf{N}_{T,\phi}}$. Preliminary values for $\overline{\delta\delta}_\phi$ can be obtained from the following considerations.

As noted in the earlier discussion, the data are such that each $6^\circ \times 6^\circ$ plate overlaps $1^\circ$ with the adjacent plates on every side. Hence on each of the plates twenty of the thirty-six $1^\circ \times 1^\circ$ squares for which $\mathbf{N}_0$ values are given overlap with $1^\circ \times 1^\circ$ squares on adjacent plates. We are thus provided with two determinations of $\mathbf{N}_0$ for those squares covered by the overlapping portions of two plates, and it is from this material that we must obtain estimates of $\overline{\delta\delta}_\phi$.

Consider a particular overlap for two adjacent plates, and let $\mathbf{N}_0$ denote the value given on the master-chart for the number of nebulae in a particular $1^\circ \times 1^\circ$ square on the overlapping strip of one of these plates; let $\mathbf{N}_0'$ denote the corresponding value for the same $1^\circ \times 1^\circ$ square on the other plate. For such an overlap let us consider the functions

$$\begin{aligned}2\,\mathfrak{I}_\phi &\equiv \mathbf{N}_0\mathbf{N}_{0,\phi} + \mathbf{N}_0'\mathbf{N}_{0,\phi}' \\ &\equiv (\mathbf{N}_T + \delta)(\mathbf{N}_{T,\phi} + \delta_\phi) + (\mathbf{N}_T + \delta')(\mathbf{N}_{T,\phi} + \delta_\phi')\end{aligned} \tag{14}$$

and

$$\begin{aligned}2\,\mathfrak{L}_\phi &\equiv \mathbf{N}_0\mathbf{N}_{0,\phi}' + \mathbf{N}_{0,\phi}\mathbf{N}_0' \\ &\equiv (\mathbf{N}_T + \delta)(\mathbf{N}_{T,\phi} + \delta_\phi') + (\mathbf{N}_{T,\phi} + \delta_\phi)(\mathbf{N}_T + \delta')\,.\end{aligned} \tag{15}$$

Taking the mean value over the overlaps for adjacent plates and making the reasonable assumption that $\delta$ and $\delta'$ are not correlated,

$$\overline{\delta\,\delta'}_\phi = \overline{\delta'\delta}_\phi = 0\,, \tag{16}$$

we obtain

$$2\,\overline{\mathfrak{I}}_\phi = 2\overline{\mathbf{N}_T\mathbf{N}_{T,\phi}} + 2\,\overline{\delta\,\delta}_\phi \tag{17}$$

and

$$2\,\overline{\mathfrak{L}}_\phi = 2\overline{\mathbf{N}_T\mathbf{N}_{T,\phi}}. \tag{18}$$

The expression for $\overline{\delta\delta}_\phi$ in terms of the observational data, then, is

$$\overline{\delta\,\delta}_\phi = \overline{\mathfrak{I}}_\phi - \overline{\mathfrak{L}}_\phi\,. \tag{19}$$

Thus equation (19) enables us to determine the preliminary values of $\overline{\delta\delta}_\phi$ for $\phi = 0^\circ$, $1^\circ$, $2^\circ$, $3^\circ$, $4^\circ$, and $5^\circ$.

In this way $\overline{\delta^2}$, $\overline{\delta\delta}_1$, and $\overline{\delta\delta}_3$ have been determined from an analysis of each of the overlaps on the master-chart between $+20^\circ$ and $+77^\circ$ in galactic latitude. The overlapping strips were then grouped according to their galactic latitudes and were assembled into the same overlapping intervals in galactic latitude as are given in Table 1. Mean values for $\overline{\delta^2}$, $\overline{\delta\delta}_1$, and $\overline{\delta\delta}_3$ were then calculated from these data for each of the normal points,

and these values were reduced to the values appropriate to the particular normal points as follows: Let $(\overline{\delta\delta}_\phi)_0$ be the value of $\overline{\delta\delta}_\phi$ obtained from the overlap material corresponding to a given one of the normal points, and let $(\overline{\delta\delta}_\phi)_R$ be its value when reduced in such a way that it characterizes the material for the normal point as a whole and not simply the overlap material. Then if $(\overline{\mathbf{N}}_0^2)_0$ and $(\overline{\mathbf{N}}_0^2)_N$ are used to denote the observed values of $\overline{\mathbf{N}}_0^2$ for the overlap material and for the normal point as a whole, respectively, the expression which has been assumed for the evaluation of $(\overline{\delta\delta}_\phi)_R$ can be written

$$\frac{(\overline{\delta\,\delta}_\phi)_R}{(\overline{\delta\,\delta}_\phi)_0} = \frac{(\overline{\mathbf{N}}_0^2)_N}{(\overline{\mathbf{N}}_0^2)_0}. \tag{20}$$

The approximate validity of this correction has been verified by studying the individual values of $\overline{\delta\delta}_\phi$ as functions of $\overline{\mathbf{N}}_0^2$ for the corresponding overlaps.

From the reduced values of $\overline{\delta\delta}_1$ and $\overline{\delta\delta}_3$ for each of the normal points, the values for $\overline{\delta\delta}_2$, $\overline{\delta\delta}_4$, and $\overline{\delta\delta}_5$ have been calculated by means of linear interpolation and extrapolation. The reduced values for $\overline{\delta\delta}_\phi$ obtained in this manner are given in Table 4. It will be noted

TABLE 4

REDUCED VALUES OF $\overline{\delta\delta}_\phi$

| Normal Point | $\overline{\delta^2}$ | $\overline{\delta\delta}_1$ | $\overline{\delta\delta}_2$ | $\overline{\delta\delta}_3$ | $\overline{\delta\delta}_4$ | $\overline{\delta\delta}_5$ |
|---|---|---|---|---|---|---|
| $\mathfrak{N}_1$ | 53.7 | 26.4 | 21.8 | 17.2 | +12.6 | + 8.0 |
| $\mathfrak{N}_2$ | 63.5 | 20.9 | 10.4 | 0.0 | −10.4 | −20.8 |
| $\mathfrak{N}_3$ | 82.6 | 29.5 | 22.5 | 15.6 | + 8.6 | + 1.6 |
| $\mathfrak{N}_4$ | 109.8 | 46.8 | 31.4 | 15.9 | + 0.4 | −15.1 |
| $\mathfrak{N}_5$ | 97.4 | 24.8 | 15.2 | 5.5 | − 4.2 | −13.9 |
| $\mathfrak{N}_6$ | 88.5 | 23.6 | 19.3 | 14.9 | +10.6 | + 6.3 |
| $\mathfrak{N}_7$ | 148.2 | 51.9 | 41.0 | 30.1 | +19.3 | + 8.4 |
| $\mathfrak{N}_8$ | 178.1 | 75.1 | 56.5 | 38.1 | +19.6 | + 1.1 |
| $\mathfrak{N}_9$ | 149.1 | 57.4 | 44.5 | 31.6 | +18.7 | + 5.8 |

that the procedure employed in obtaining the reduced values for $\overline{\delta\delta}_4$ and $\overline{\delta\delta}_5$ gives rise to negative values for these quantities for several of the observational normal points. Physically, one would not expect negative values for these quantities, and an approximation which asymptotically approached zero would seem to have been required. However, when the effects of the plate-jump correction have been considered, it will be found that the corrections $\overline{\delta\delta}_4$ and $\overline{\delta\delta}_5$ become insignificant in any case, so that a further refinement is not justified. The use of linear interpolation for $\overline{\delta\delta}_2$ should be sufficiently accurate for the present purposes.

It may be well to remark at this point that wherever values for $\overline{\delta\delta}_\phi$ occur for non-integral values of $\phi$ in the reduction process, they have been expressed in terms of the two nearest entries for integral values of $\phi$ by means of the linear relation

$$\overline{\delta\,\delta}_{\phi+x} = (1-x)\,\overline{\delta\,\delta}_\phi + x\,\overline{\delta\,\delta}_{\phi+1} \qquad (0 \leqslant x \leqslant 1), \tag{21}$$

$$\phi = 0^\circ,\ 1^\circ,\ 2^\circ,\ 3^\circ, \quad \text{and} \quad 4^\circ.$$

The reduced values given in Table 4 are not as yet final, however, for there are two further corrections which must be applied in order to obtain the values appropriate to the problem at hand. We first note that the calculations to this point have given those values of $\overline{\delta\delta}_\phi$ which pertain to single observations on the master-chart. However, at the positions of the overlapping of two (or of four) of the $6^\circ \times 6^\circ$ plates, mean values of the

two (or four) observational values were used as the corresponding master-chart entries. Thus if $\delta$ is the error of an individual observation, then we have, for the errors in master-chart entries which are the means of two and of four individual observations,

$$\delta_{II} = \tfrac{1}{2}(\delta' + \delta'') \tag{22^1}$$

and

$$\delta_{IV} = \tfrac{1}{4}(\delta' + \delta'' + \delta''' + \delta''''), \tag{22^2}$$

respectively. Hence

$$\overline{\delta_{II}^2} = \tfrac{1}{4}(\overline{\delta'^2} + \overline{\delta''^2}) = \tfrac{1}{2}\overline{\delta^2}, \tag{23^1}$$

and

$$\overline{\delta_{IV}^2} = \tfrac{1}{16}(\overline{\delta'^2} + \overline{\delta''^2} + \overline{\delta'''^2} + \overline{\delta''''^2}) = \tfrac{1}{4}\overline{\delta^2}. \tag{23^2}$$

A consideration of the nature of the overlappings of the $6^\circ \times 6^\circ$ plates shows that, for each such plate, (1) sixteen of its $1^\circ \times 1^\circ$ squares do not overlap with those of adjacent plates; (2) sixteen of its $1^\circ \times 1^\circ$ squares overlap with those of one other plate; and (3) the remaining four $1^\circ \times 1^\circ$ squares—at the corners of the plate—overlap with those of three adjacent plates. Upon weighting $\overline{\delta^2}$, $\overline{\delta_{II}^2}$, and $\overline{\delta_{IV}^2}$ according to these frequencies of occurrence, we find that the value of $\overline{\delta^2}$ which is relevant to our observational material is 0.694 times that for the individual values given in Table 4.

There is a similar correction to $\overline{\delta\delta_\phi}$ for $\phi \neq 0$. Here when one of the two points entering into a $\overline{\delta\delta_\phi}$ product falls on a $1^\circ \times 1^\circ$ square where four plates overlap, then, regardless of the position of the other point—so long as it falls upon at least one of the plates contributing to the overlap—the value of $\overline{\delta\delta_\phi}$ is one-quarter its value where both points represent single observations. Similarly, when one of the two points falls on a $1^\circ \times 1^\circ$ square where two plates overlap, then, so long as the other point falls on one of the two plates contributing to that overlap and does not fall on one of those squares where four plates overlap, $\overline{\delta\delta_\phi}$ will be one-half its value where both points represent single observations. Finally, where neither of the contributing points falls on any overlapping square, no correction is required. A consideration of the situation for $\phi = 1^\circ$ shows that the appropriate correction factor in this case is about 0.67, while for larger values of $\phi$ it continues to decrease and asymptotically approaches the value 0.546. In view of the effect of the plate-jump correction to be discussed in the next paragraph, no significant accuracy is lost in taking 0.694 as the correction factor to be applied to all the values of $\overline{\delta\delta_\phi}$ given in Table 4; and this has been done in the present reductions.

We must now consider the effect upon $\overline{\delta\delta_\phi}$ of steps from one plate to another. It is clear that the values of $\overline{\delta\delta_\phi}$ which are given in Table 4—even when corrected by the factor 0.694—can no longer be used as they stand, since in only a fraction, $a_\phi$, of the total number of situations do both $\delta$ and $\delta_\phi$ fall on the same plate. Thus, in the general case,

$$\begin{aligned} \overline{\mathbf{N}_0\mathbf{N}_{0,\phi}} &= \overline{\mathbf{N}_T\mathbf{N}_{T,\phi}} + \overline{\delta\,\delta_\phi} \\ &= \mathbf{N}_T\mathbf{N}_{T,\phi} + a_\phi(\overline{\delta\,\delta_\phi})_c + (1 - a_\phi)(\overline{\delta\,\delta_\phi})_u, \end{aligned} \tag{24}$$

where $(\overline{\delta\delta_\phi})_c$ is the appropriate value of $\overline{\delta\delta_\phi}$ when both $\delta$ and $\delta_\phi$ fall on the same plate, while $(\overline{\delta\delta_\phi})_u$ is the value of $\overline{\delta\delta_\phi}$ when $\delta$ and $\delta_\phi$ fall on different plates. It is clear that $(\overline{\delta\delta_\phi})_c$ corresponds exactly to the expressions given in Table 4 when that material has been corrected according to the work of the preceding paragraphs; and it also seems valid to assume that

$$(\overline{\delta\,\delta_\phi})_u = 0. \tag{25}$$

Hence we need simply determine $a_\phi$ for the different chosen parallels in order to correct the values of Table 4 for this effect. In order to do this, we shall let $1/\Lambda$ be the number

of degrees between jumps from one plate to the next for a particular case. Then if the first point considered lies on that part of the plate within $1/\Lambda - \phi$ degrees of the low-galactic-longitude end, the second point—at a distance $\phi$ degrees from the first—will fall on the same plate; whereas if the first point lies within $\phi$ degrees of the high-longitude end of the plate, the second point will fall on another plate. Thus, for this particular case,

$$(1 - a_\phi) = \frac{\phi}{1/\Lambda} \qquad (\phi \leqslant 1/\Lambda), \tag{26}$$

$$(1 - a_\phi) = 1 \qquad (\phi \geqslant 1/\Lambda).$$

Taking the mean value over the length of the galactic parallel and passing to the limit $\phi \to 0^\circ$, we obtain

$$(1 - a_\phi) = \bar{\Lambda}\phi \qquad (\phi \to 0^\circ). \tag{27}$$

In the evaluation of the average number of plate-jumps per degree, $\bar{\Lambda}$, along the different parallels, it was found adequate to treat the material in two parts: $b \leqslant 39^\circ$, and $b \geqslant 40^\circ$, where $b$ has been used to denote the galactic latitude. The values of $\bar{\Lambda}$ for these two cases have been determined and have been used in equation (27) to obtain the corresponding asymptotic expressions for $(1 - a_\phi)$—and hence for $a_\phi$—which are valid for small values of $\phi$. Further, for $\phi \gtrsim 7^\circ$, $a_\phi$ must be zero; and as $\phi \to 7^\circ$, $a_\phi$ must approach zero asymptotically. These asymptotes for $\phi \to 0^\circ$ and $\phi \to 7^\circ$ have been plotted, and connecting curves whose forms were based upon physical considerations have been drawn in for the two cases. From these curves the values of $a_\phi$ for the two cases have been determined, and the results are given in Table 5. Since the $\overline{\delta\delta}_\phi$ corrections are critical

TABLE 5

VALUES OF $a_\phi$ ENTERING INTO THE PLATE-JUMP CORRECTION

| $\phi$ | $b \leqslant 39^\circ$ | $b \geqslant 40^\circ$ | Mean | $\phi$ | $b \leqslant 39^\circ$ | $b \geqslant 40^\circ$ | Mean |
|---|---|---|---|---|---|---|---|
| 1° | 0.71 | 0.73 | 0.72 | 4° | 0.14 | 0.19 | 0.17 |
| 2° | .48 | .52 | .50 | 5° | 0.05 | 0.10 | 0.08 |
| 3° | 0.29 | 0.34 | 0.32 | | | | |

only for $\overline{\delta^2}$, $\overline{\delta\delta}_1$, and, to a lesser degree, $\overline{\delta\delta}_2$, the errors introduced by this procedure should be small. The mean values given in Table 5 have actually been used in correcting all the values of $\overline{\delta\delta}_\phi$, since the differences between the values for the two cases are smaller than the uncertainties arising from other sources.

Upon applying the correction factor 0.694 and the plate-jump corrections to the data of Table 4, we obtain the desired corrected values for $\overline{\delta\delta}_\phi$. These are given in Table 6.

We next turn to the determination of the interpolation weights $\bar{\omega}_{kl}$ which occur in equations (6), (7), (8), and (11). We proceed by considering a particular interpolated point on the master-chart. Let it fall within that $1^\circ \times 1^\circ$ square whose corners are the centers of the master-chart entries $P_1$, $P_2$, $P_3$, and $P_4$. For definiteness, let $P_1$ and $P_2$ be the upper left- and right-hand points of this square, and let $P_3$ and $P_4$ be the lower left- and right-hand points, respectively. Suppose, further, that the interpolated point lies at a distance $x$ to the right of the line through $P_1$ and $P_3$ and at a distance $y$ below the line through $P_1$ and $P_2$, $x$ and $y$ being measured in degrees. Then, since the original interpolations for $\boldsymbol{N}$ were obtained by the linear four-point process, weights corresponding to this same interpolation process must be used in determining $\bar{\omega}_{kl}$. It can be readily shown that in this case the interpolated value for $\boldsymbol{N}$ is given in terms of the master-chart

entries by means of the relation

$$\boldsymbol{N} = (1 - x - y + xy)\,\boldsymbol{N}_{0,1} + (x - xy)\,\boldsymbol{N}_{0,2} + (y - xy)\,\boldsymbol{N}_{0,3} + (xy)\,\boldsymbol{N}_{0,4}\,, \quad (28)$$

which is simply equation (5) with $\omega_k$ expressed in terms of $x$ and $y$. Similarly, a neighboring interpolated value $\boldsymbol{N}_\phi$ can be expressed in terms of its particular $x$ and $y$ values, $x_\phi$ and $y_\phi$, relative to the centers of the four master-chart points nearest it. Given the fact that two interpolated points lie $\phi$ degrees apart on a line making an angle $\theta$ with the horizontal (or vertical) axis determined by the array of master-chart entries, then $x_\phi$ and $y_\phi$ are determined in terms of $x$ and $y$; and hence the value for $\omega_{k,\phi}$ is determined by that for $\omega_k$. Upon averaging over all the relevant $x$ and $y$ values, we then obtain the desired values for $\bar{\omega}_{kl}$. The integrations which are required in this averaging process are all readily evaluated in terms of standard integrals, and exact results can be obtained

TABLE 6

FINAL VALUES FOR $\overline{\delta\delta}_\phi$

| Normal Point | $\overline{\delta^2}$ | $\overline{\delta\delta}_1$ | $\overline{\delta\delta}_2$ | $\overline{\delta\delta}_3$ | $\overline{\delta\delta}_4$ | $\overline{\delta\delta}_5$ |
|---|---|---|---|---|---|---|
| $\mathfrak{N}_1$ | 26.5 | 13.2 | 7.6 | 3.8 | +1.5 | +0.4 |
| $\mathfrak{N}_2$ | 27.3 | 10.4 | 3.6 | 0.0 | −1.2 | −1.2 |
| $\mathfrak{N}_3$ | 36.5 | 14.7 | 7.8 | 3.5 | +1.0 | +0.1 |
| $\mathfrak{N}_4$ | 51.5 | 23.4 | 10.9 | 3.5 | 0.0 | −0.8 |
| $\mathfrak{N}_5$ | 39.1 | 12.4 | 5.3 | 1.2 | −0.5 | −0.8 |
| $\mathfrak{N}_6$ | 35.9 | 11.8 | 6.7 | 3.3 | +1.2 | +0.3 |
| $\mathfrak{N}_7$ | 65.1 | 26.0 | 14.2 | 6.7 | +2.3 | +0.5 |
| $\mathfrak{N}_8$ | 83.2 | 37.5 | 19.6 | 8.5 | +2.3 | +0.1 |
| $\mathfrak{N}_9$ | 67.5 | 28.7 | 15.4 | 7.0 | +2.2 | +0.3 |

without great difficulty. For the work of this paper these calculations for $\bar{\omega}_{kl}$ were carried out for the following cases: (1) $\phi = 0°$; (2) $\phi = 1°$, $2°$, and $3°$ for both $\theta = 0°$ and $\theta = 45°$—the extreme cases; and (3) $\phi = 4°$ and $5°$ for $\theta = 0°$. Now the different combinations of master-chart entries, which have thus far been expressed only formally by means of subscripts $k$ and $l$ in the notations $\bar{\omega}_{kl}$, $\overline{\boldsymbol{N}_{T,k}\boldsymbol{N}_{T,l}}$, and $\overline{\delta_k\delta_l}$, can be characterized sufficiently for the purposes of this paper simply by the values for the separations in degrees of the pairs of entries making up these various combinations. Thus, for example, $\bar{\omega}_{\sqrt{5}}$, $\overline{\boldsymbol{N}_T\boldsymbol{N}_{T,\sqrt{5}}}$, and $\overline{\delta\delta}_{\sqrt{5}}$ will be taken to refer to pairs of master-chart entries which are separated by $\sqrt{5}°$, i.e., these pairs of entries are separated by $2°$ along one of the axes determined by the array of master-chart entries and by $1°$ along the other. Table 7 contains the results of the calculations for $\bar{\omega}_{kl}$ in terms of these separations.

It will be noted that the weights given in Table 7 apply not only to $\overline{\boldsymbol{N}_{T,k}\boldsymbol{N}_{T,l}}$ but also to $\overline{\delta_k\delta_l}$ in equation (6). Thus, in order to determine the functions $F_\phi$ which have been defined in equation (7) and which are required in equations (8) and (11), the weights given in Table 7 have been applied to the $\overline{\delta\delta}_\phi$ data of Table 6. Since the $\overline{\delta\delta}_\phi$ corrections are most sensitive for the lower latitudes, where $\theta = 45°$ is a good approximation to the actual situation, we shall use from Table 7 the values for $\theta = 45°$ where these are given ($\phi = 1°$, $2°$, and $3°$). The resulting values of $F_\phi$ for the nine normal points in galactic latitude are given in Table 8. Thus, using the results given in Tables 7 and 8, we can determine the values of $\overline{\boldsymbol{N}_T\boldsymbol{N}_{T,\phi}}$ in terms of those for $\overline{\boldsymbol{N}\boldsymbol{N}_\phi}$ by means of equation (8). Instead of explicitly evaluating $\overline{\boldsymbol{N}_T\boldsymbol{N}_{T,\phi}}$ at this stage, however, we shall first remove the effects of the smoothing errors which enter because of the finite size of the $1° \times 1°$ squares. When this has been done, an explicit solution for $\overline{\boldsymbol{N}\boldsymbol{N}_\phi}$ will be determined through equation (11).

## TABLE 7

VALUES OF $\tilde{\omega}_{kl}$ FOR THE RELEVANT SEPARATIONS

| $\tilde{\omega}_{kl}$ | Separation of the Interpolated Points | | | | | | |
|---|---|---|---|---|---|---|---|
| | $\phi = 0°$ | $\phi = 1°$ | | | $\phi = 2°$ | | |
| | | $\theta = 0°$ | $\theta = 45°$ | Mean | $\theta = 0°$ | $\theta = 45°$ | Mean |
| $\tilde{\omega}_0$ | 0.445 | 0.111 | 0.118 | 0.114 | 0 | 0.001 | 0.001 |
| $\tilde{\omega}_1$ | .444 | .500 | .410 | .455 | 0.111 | .035 | .073 |
| $\tilde{\omega}_{\sqrt{2}}$ | 0.111 | .222 | .357 | .290 | .056 | .282 | .169 |
| $\tilde{\omega}_2$ | 0 | .111 | .041 | .076 | .444 | .028 | .236 |
| $\tilde{\omega}_{\sqrt{5}}$ | 0 | 0.056 | .070 | .063 | .222 | .450 | .336 |
| $\tilde{\omega}_{2\sqrt{2}}$ | 0 | 0 | 0.004 | 0.002 | 0 | .180 | .090 |
| $\tilde{\omega}_3$ | 0 | 0 | 0 | 0 | .111 | .001 | .056 |
| $\tilde{\omega}_{\sqrt{10}}$ | 0 | 0 | 0 | 0 | 0.056 | .013 | .034 |
| $\tilde{\omega}_{\sqrt{13}}$ | 0 | 0 | 0 | 0 | 0 | 0.010 | 0.005 |

| $\tilde{\omega}_{kl}$ | Separation of the Interpolated Points | | | | |
|---|---|---|---|---|---|
| | $\theta = 0°$ | $\phi = 3°$ | | $\phi = 4°$ | $\phi = 5°$ |
| | | $\theta = 45°$ | Mean | $\theta = 0°$ | $\theta = 0°$ |
| $\tilde{\omega}_{\sqrt{2}}$ | 0 | 0.013 | 0.006 | 0 | 0 |
| $\tilde{\omega}_2$ | 0.111 | 0 | .056 | 0 | 0 |
| $\tilde{\omega}_{\sqrt{5}}$ | .056 | .148 | .101 | 0 | 0 |
| $\tilde{\omega}_{2\sqrt{2}}$ | 0 | .426 | .213 | 0 | 0 |
| $\tilde{\omega}_3$ | .444 | 0 | .222 | 0.111 | 0 |
| $\tilde{\omega}_{\sqrt{10}}$ | .222 | .053 | .138 | .056 | 0 |
| $\tilde{\omega}_{\sqrt{13}}$ | 0 | .305 | .153 | 0 | 0 |
| $\tilde{\omega}_4$ | .111 | 0 | .056 | .444 | 0.111 |
| $\tilde{\omega}_{\sqrt{17}}$ | 0.056 | 0 | .028 | .222 | .056 |
| $\tilde{\omega}_{3\sqrt{2}}$ | 0 | 0.055 | 0.027 | 0 | 0 |
| $\tilde{\omega}_5$ | 0 | 0 | 0 | .111 | .444 |
| $\tilde{\omega}_{\sqrt{26}}$ | 0 | 0 | 0 | 0.056 | .222 |
| $\tilde{\omega}_6$ | 0 | 0 | 0 | 0 | .111 |
| $\tilde{\omega}_{\sqrt{37}}$ | 0 | 0 | 0 | 0 | 0.056 |

## TABLE 8

VALUES OF $F_\phi$ FOR THE NINE OBSERVATIONAL NORMAL POINTS

| Normal Point | $F_0$ | $F_1$ | $F_2$ | $F_3$ | $F_4$ | $F_5$ |
|---|---|---|---|---|---|---|
| $\mathfrak{N}_1$ | 23.7 | 14.5 | 7.7 | 4.0 | +1.6 | +0.4 |
| $\mathfrak{N}_2$ | 25.1 | 12.5 | 3.1 | 0.4 | −1.0 | −1.2 |
| $\mathfrak{N}_3$ | 33.4 | 17.8 | 8.0 | 3.8 | +1.2 | +0.1 |
| $\mathfrak{N}_4$ | 46.4 | 26.2 | 11.4 | 4.2 | +0.4 | −0.8 |
| $\mathfrak{N}_5$ | 36.7 | 17.0 | 5.7 | 1.7 | −0.3 | −0.8 |
| $\mathfrak{N}_6$ | 33.7 | 16.2 | 6.8 | 3.5 | +1.5 | +0.3 |
| $\mathfrak{N}_7$ | 59.7 | 31.8 | 14.5 | 7.1 | +2.6 | +0.5 |
| $\mathfrak{N}_8$ | 75.1 | 42.8 | 20.2 | 9.2 | +2.8 | +0.1 |
| $\mathfrak{N}_9$ | 61.4 | 33.9 | 15.8 | 7.6 | +2.6 | +0.3 |

(ii) *The evaluation of* $\overline{NN}_\phi$ *in terms of* $\overline{\mathbf{N}_T\mathbf{N}}_{T,\phi}$.—Since the dimensions of the fundamental area for which the observations are given, the $1^\circ \times 1^\circ$ square, are comparable with the relevant range of separations $\phi$ for the combinations $\overline{\mathbf{N}_T\mathbf{N}}_{T,\phi}$, it is evident that the quantities $\overline{\mathbf{N}_T\mathbf{N}}_{T,\phi}$ should not be used for the true values $\overline{NN}_\phi$. The true values can be obtained from the values for $\overline{\mathbf{N}_T\mathbf{N}}_{T,\phi}$ by evaluating the kernels with which the true values are convolved in the formation of the different $\overline{\mathbf{N}_T\mathbf{N}}_{T,\phi}$ combinations. For the purposes of the present application it has been felt sufficient to obtain the approximate kernels by a subdivision of the $1^\circ \times 1^\circ$ squares into sixteen $\frac{1}{4}^\circ \times \frac{1}{4}^\circ$ squares. Then for each of the relevant $\overline{\mathbf{N}_T\mathbf{N}}_{T,\phi}$ combinations, the separations, $\phi'$, of the various combinations of subsquares have been calculated. Since, as has been mentioned earlier, only six parameters describing the dependence of $\overline{NN}_\phi$ on $\phi$ can be determined from the observational values $\overline{NN}_\phi$ for $\phi = 0^\circ$, $1^\circ$, $2^\circ$, $3^\circ$, $4^\circ$, and $5^\circ$, the values of $\overline{NN}_{\phi'}$ for the different values of $\phi'$ have had to be expressed in terms of a six-parameter representation

TABLE 9

VALUES OF $\overline{W}_{ij}$ FOR THE RELEVANT SEPARATIONS

| Separation of Master-Chart Entries | $\overline{W}_0$ | $\overline{W}_1$ | $\overline{W}_2$ | $\overline{W}_3$ | $\overline{W}_4$ | $\overline{W}_5$ | $\overline{W}_6$ | $\overline{W}_7$ |
|---|---|---|---|---|---|---|---|---|
| $0^\circ$ | 0.500 | 0.499 | 0.001 | 0 | 0 | 0 | 0 | 0 |
| $1^\circ$ | 0.113 | .691 | .196 | 0 | 0 | 0 | 0 | 0 |
| $\sqrt{2}^\circ$ | 0 | .286 | .690 | 0.024 | 0 | 0 | 0 | 0 |
| $2^\circ$ | 0 | .138 | .684 | .178 | 0 | 0 | 0 | 0 |
| $\sqrt{5}^\circ$ | 0 | 0.059 | .614 | .324 | 0.003 | 0 | 0 | 0 |
| $2\sqrt{2}^\circ$ | 0 | 0 | .051 | .769 | .180 | 0 | 0 | 0 |
| $3^\circ$ | 0 | 0 | .146 | .684 | .170 | 0 | 0 | 0 |
| $\sqrt{10}^\circ$ | 0 | 0 | .082 | .649 | .268 | 0.001 | 0 | 0 |
| $\sqrt{13}^\circ$ | 0 | 0 | 0.009 | .390 | .570 | .031 | 0 | 0 |
| $4^\circ$ | 0 | 0 | 0 | .149 | .684 | .167 | 0 | 0 |
| $\sqrt{17}^\circ$ | 0 | 0 | 0 | .100 | .659 | .241 | 0 | 0 |
| $3\sqrt{2}^\circ$ | 0 | 0 | 0 | 0.001 | .469 | .524 | 0.006 | 0 |
| $5^\circ$ | 0 | 0 | 0 | 0 | .150 | .685 | .165 | 0 |
| $\sqrt{26}^\circ$ | 0 | 0 | 0 | 0 | 0.150 | .685 | .165 | 0 |
| $6^\circ$ | 0 | 0 | 0 | 0 | 0 | .150 | .685 | 0.165 |
| $\sqrt{37}^\circ$ | 0 | 0 | 0 | 0 | 0 | 0.150 | 0.685 | 0.165 |

for $\overline{NN}_\phi$. For this purpose the dependence of $\overline{NN}_\phi$ on $\phi$ has been represented by that polygonal function whose straight-line segments are joined at $\phi = 1^\circ$, $2^\circ$, $3^\circ$, and $4^\circ$ and whose six parameters are taken to be the values of $\overline{NN}_\phi$ for $\phi = 0^\circ$, $1^\circ$, $2^\circ$, $3^\circ$, $4^\circ$, and $5^\circ$. In this way, for each of the relevant combinations $\overline{\mathbf{N}_T\mathbf{N}}_{T,\phi}$, the values of $\overline{NN}_{\phi'}$ for the individual combinations of pairs of the subregions have been expressed in terms of $\overline{NN}_\phi$, $\phi = 0^\circ$, $1^\circ$, $2^\circ$, $3^\circ$, $4^\circ$, and $5^\circ$; and the results for the two hundred and fifty-six combinations of subsquares have been combined to give an expression of the form

$$\overline{\mathbf{N}_T\mathbf{N}}_{T,\phi} = \sum_{\phi''=0^\circ}^{5^\circ} \overline{W}_{\phi''}\,\overline{NN}_{\phi''} . \tag{29}$$

It should be pointed out in this connection that wherever the values $\overline{NN}_6$ and $\overline{NN}_7$ have arisen, they have been expressed in terms of $\overline{NN}_4$ and $\overline{NN}_5$ by means of the relation

$$\overline{NN}_7 \cong \overline{NN}_6 \cong \tfrac{1}{3}\,[4\,\overline{NN}_5 - \overline{NN}_4] . \tag{30}$$

This is only an approximation; and yet, because of the fact that $\overline{NN}_\phi$ is, in this range, fast approaching its asymptotic value for large $\phi$, the errors introduced are small.

The explicit results for the quantities $\overline{W}_{ij}$ appearing in equation (29) are given in Table 9 for all the relevant combinations of $\overline{\mathbf{N}_T\mathbf{N}}_{T,\phi}$.

(iii) *The evaluation of $\overline{NN}_\phi$ in terms of $\overline{NN}_\phi$.*—For the galactic latitudes greater than 40° it would be an excellent approximation to the true situation if, for $\phi = 1°$, 2°, and 3°, the values given in Table 7 for the means between those for the cases $\theta = 0°$ and $\theta = 45°$ were adopted in the reduction process. For the galactic latitudes less than 40°, the values given for the case of $\theta = 45°$ would provide a better approximation; and yet an examination of Table 7 clearly indicates that a single set of values should be quite adequate for reducing the results for all values of the galactic latitude. In the choice between the two sets of relations for this purpose, the fact that the observational material for the higher latitudes provides the better statistical sample lends some slight support to a preference for the use of the mean values appearing in Table 7. For this reason, when the results from Tables 7 and 9 are used in equation (11), it is these mean values in Table 7 which have been used; and the six linear equations which are represented by equation (11) can then be written in matrix notation in the following way:

$$\begin{vmatrix} 0.272 & 0.561 & 0.164 & 0.003 & 0 & 0 \\ .109 & .469 & .380 & .042 & 0 & 0 \\ 0.009 & .152 & .514 & .286 & 0.039 & 0 \\ 0 & 0.015 & .161 & .519 & .270 & 0.035 \\ 0 & 0 & 0.021 & .200 & .500 & .279 \\ 0 & 0 & 0 & 0.022 & 0.128 & 0.850 \end{vmatrix} \begin{vmatrix} \overline{N^2} \\ \overline{NN}_1 \\ \overline{NN}_2 \\ \overline{NN}_3 \\ \overline{NN}_4 \\ \overline{NN}_5 \end{vmatrix} = \begin{vmatrix} \overline{N^2} - F_0 \\ \overline{NN}_1 - F_1 \\ \overline{NN}_2 - F_2 \\ \overline{NN}_3 - F_3 \\ \overline{NN}_4 - F_4 \\ \overline{NN}_5 - F_5 \end{vmatrix} \tag{31}$$

The values of the quantities $\overline{NN}_\phi$ are just the values given in Table 2, while the values of the functions $F_\phi$ are given in Table 8. We thus have a matrix equation of this type for each of the observational normal points. In theory, these could be solved separately. However, because of the limited nature of the statistical sample from which each of the observational normal points is obtained, the observational values for $(\overline{NN}_\phi - F_\phi)$ do not define entirely smooth functions for the separate normal points. In the solution of the six linear equations for the six unknowns, these irregularities enter critically and are greatly magnified in the resulting solutions for $\overline{NN}_\phi$, giving rise in some cases to situations in which $\overline{NN}_\phi$ has one or more minima for $\phi < 5°$. To avoid this difficulty, the procedure adopted has been to combine the observational material for the normal points $\mathfrak{N}_1$, $\mathfrak{N}_2$, and $\mathfrak{N}_3$ into one low-latitude supernormal point and to combine the material for the normal points $\mathfrak{N}_5$, $\mathfrak{N}_6$, $\mathfrak{N}_7$, $\mathfrak{N}_8$, and $\mathfrak{N}_9$ into a single high-latitude supernormal point. The combining of the material in this way has been done so as to carry out the averaging with respect to the relative values of $(\overline{NN}_\phi - F_\phi)$ and not with respect to their absolute values. To accomplish this for the low-latitude material, the values of $(\overline{NN}_\phi - F_\phi)$ for a particular one of the three normal points $\mathfrak{N}_1$, $\mathfrak{N}_2$, and $\mathfrak{N}_3$ have been multiplied by a factor such that the value of $(\overline{N^2} - F_0)$ for that normal point is reduced to the mean value of $(\overline{N^2} - F_0)$ for the three normal points taken together. This has been done for each of the three normal points, and these three sets of reduced values for $(\overline{NN}_\phi - F_\phi)$ have then been combined according to the weights given in Table 1 to provide the values of $(\overline{NN}_\phi - F_\phi)$ for the low-latitude supernormal point. The corresponding procedure has been applied to obtain the appropriate mean values of $(\overline{NN}_\phi - F_\phi)$ for the high-latitude supernormal point, and these values of $(\overline{NN}_\phi - F_\phi)$ for the low- and the high-latitude supernormal points, which will be referred to as the "zero approximations," are given in Table 10.

The reduction in this way to supernormal points has been found to remove the greater part of the irregularities in $(\overline{NN}_\phi - F_\phi)$; however, when the functions $\overline{NN}_\phi$ are determined from equation (31), smaller but still marked irregularities become apparent (cf. Table 10′). The procedure which has been adopted for obtaining first approximations

TABLE 10

ZERO, FIRST, AND FINAL APPROXIMATIONS TO $(\overline{NN}_\phi - F_\phi)$

| | Zero Approximation | First Approximation | Final Approximation |
|---|---|---|---|
| | Lower Latitudes | | |
| $(\overline{N^2} - F_0)$ | 870.54 | 870.50 | 870.40 |
| $(\overline{NN}_1 - F_1)$ | 847.41 | 846.00 | 846.20 |
| $(\overline{NN}_2 - F_2)$ | 816.38 | 816.60 | 816.50 |
| $(\overline{NN}_3 - F_3)$ | 797.36 | 798.20 | 799.20 |
| $(\overline{NN}_4 - F_4)$ | 792.86 | 790.10 | 791.40 |
| $(\overline{NN}_5 - F_5)$ | 785.01 | 786.20 | 787.60 |
| $\overline{N}^2$ | 778.45 | 778.45 | 778.45 |
| | Higher Latitudes | | |
| $(\overline{N^2} - F_0)$ | 4976.1 | 4976.1 | 4974.0 |
| $(\overline{NN}_1 - F_1)$ | 4820.0 | 4830.0 | 4830.0 |
| $(\overline{NN}_2 - F_2)$ | 4683.8 | 4683.8 | 4675.0 |
| $(\overline{NN}_3 - F_3)$ | 4615.2 | 4607.0 | 4602.0 |
| $(\overline{NN}_4 - F_4)$ | 4565.7 | 4563.0 | 4574.0 |
| $(\overline{NN}_5 - F_5)$ | 4538.2 | 4543.0 | 4562.0 |
| $\overline{N}^2$ | 4538.2 | 4538.2 | 4538.2 |

TABLE 10′

ZERO, FIRST, AND FINAL APPROXIMATIONS TO $\overline{NN}_\phi$

| | Zero Approximation | First Approximation | Final Approximation |
|---|---|---|---|
| | Lower Latitudes | | |
| $\overline{N^2}$ | 933.63 | 944.44 | 937.57 |
| $\overline{NN}_1$ | 855.4 | 850.5 | 854.2 |
| $\overline{NN}_2$ | 819.3 | 817.8 | 815.5 |
| $\overline{NN}_3$ | 789.1 | 796.2 | 798.2 |
| $\overline{NN}_4$ | 798.9 | 789.0 | 790.1 |
| $\overline{NN}_5$ | 782.8 | 785.5 | 786.9 |
| $\overline{N}^2$ | 778.45 | 778.45 | 778.45 |
| | Higher Latitudes | | |
| $\overline{N^2}$ | 5578.3 | 5481.2 | 5420.0 |
| $\overline{NN}_1$ | 4771.3 | 4819.8 | 4851.0 |
| $\overline{NN}_2$ | 4684.0 | 4679.9 | 4662.0 |
| $\overline{NN}_3$ | 4626.5 | 4611.6 | 4596.0 |
| $\overline{NN}_4$ | 4554.4 | 4551.4 | 4570.0 |
| $\overline{NN}_5$ | 4533.5 | 4539.9 | 4560.0 |
| $\overline{N}^2$ | 4538.2 | 4538.2 | 4538.2 |

to the corrected observational values for $(\overline{NN}_\phi - F_\phi)$ is the following. From the values of $\overline{NN}_\phi$ in Table 10′ for the zero approximations, the corresponding correlation functions $(\overline{N^2} - \overline{NN}_\phi)/(\overline{N^2} - \overline{N}^2)$ have been determined. The obvious irregularities in these functions were then removed by making small changes in the values of the zero approximations to $(\overline{NN}_\phi - F_\phi)$, and the resulting values represent the "first approximations." These values for the first approximations to $(\overline{NN}_\phi - F_\phi)$ are included in Table 10, and the corresponding values of $\overline{NN}_\phi$ are given in Table 10′. The correlation functions corresponding to these are plotted in Figure 1.

### III. THE EFFECTS OF ABSORPTION WITHIN OUR OWN GALAXY

*The determination of the optical half-thickness of the Galaxy from the Lick counts.*—If we tentatively assume that the fluctuations in the galactic absorption are negligible in their effects upon the observed counts of the nebulae, then we can determine the optical half-

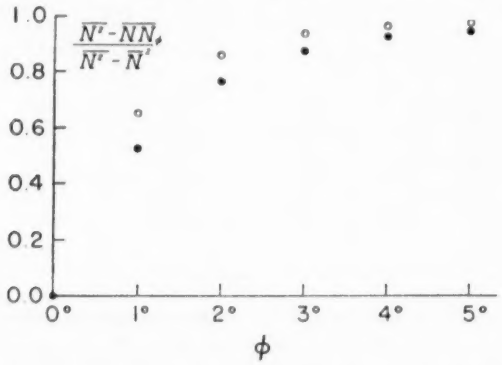


FIG. 1.—Correlation functions corresponding to the first approximations to $(\overline{NN}_\phi - F_\phi)$. The open and the filled circles refer to the observational material for the high and the low latitudes, respectively.

thickness of the Galaxy, $\bar{\tau}_{1/2}$, from the observational material in a quite straightforward manner. In this case, regardless of whether or not there is a dispersion in the absolute magnitudes of the nebulae, we have, upon assuming a cosecant law for the galactic absorption (cf. eq. [61] of Paper I),

$$\frac{1}{1.5\ \log_{10} e} \log_{10}\left[\frac{\overline{N(b_i)}}{\overline{N(b_j)}}\right] = \bar{\tau}(b_j) - \bar{\tau}(b_i) = \bar{\tau}_{1/2}\,[\operatorname{cosec} b_j - \operatorname{cosec} b_i]\,, \qquad (32)$$

where $N(b_i)$ is the number of nebulae per square degree at a galactic latitude $b_i$ and $\tau(b_i)$ is the optical thickness of the Galaxy at this latitude. The values of $\log_{10} \overline{N}$ corresponding to the observed values of $\overline{N}$ have been plotted versus the cosecant of the galactic latitude, and the straight line which best represents the data has been determined (cf. Fig. 2). From the slope of this straight line it is found that

$$\bar{\tau}_{1/2} = 0.76\,. \qquad (33)^4$$

If it had been assumed, on the other hand, that the fluctuations in the number of nebulae per square degree were due entirely to fluctuations in the galactic absorption,

[4] It will be recalled that, in order to convert an optical thickness $\tau$ into a difference in magnitudes $\Delta m$, we have: $\Delta m = 1.08\tau$.

then the corresponding determination of $\bar{\tau}_{1/2}$ would have followed from the analysis of a plot of $\overline{\log_{10} N}$ versus cosecant $b$, and $\tau_{1/2}$ would have been determined from the straight line which best fitted the data when plotted in this way. The actual situation undoubtedly lies somewhere between these two extreme situations. However, the satisfactory way in which a straight line can be fitted to the observational data when plotted as in Figure 2 and the results of the discussion of the next section indicate that the above determination of $\bar{\tau}_{1/2}$—based upon the assumption that the effects of fluctuations in the galactic absorption are negligible—is a satisfactory first approximation.

In the foregoing it has been tacitly assumed that the observed galactic-latitude effect in the Lick counts of the nebulae is due solely to galactic absorption. However, before too great significance is attached to the value in equation (33) for $\bar{\tau}_{1/2}$—which is rather larger than the values obtained in previous investigations—a careful study will be required in order to determine whether there are systematic variations in the plate limit of the

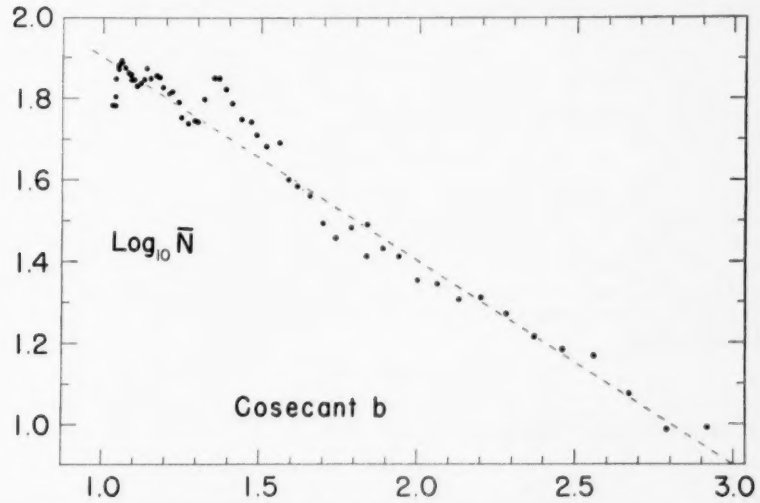


FIG. 2.—Plot of $\log_{10} \bar{N}$ versus cosecant $b$ for the determination of the optical half-thickness of the Galaxy. The dashed line corresponds to an optical half-thickness of 0.76.

counts for stellar objects, as well as possible systematic effects in the relative visibilities of galaxies and stars of the same integrated magnitudes due to the effects of the galactic obscuration and the diffuse galactic light.

In any case, in comparing the observed galactic-latitude effect with the corresponding theoretical expectations, we may use the observed value of 0.76 for $\bar{\tau}_{1/2}$, since any systematic effect in the effective plate limit for the nebulae can be treated formally as an absorption effect.

*The effects of fluctuations in the galactic absorption upon the observed counts of the extragalactic nebulae.*—In order to determine the effects of fluctuations in the galactic absorption upon the observed counts of the nebulae, we shall make use of the developments of Paper I. In that paper the statistical treatment developed by Chandrasekhar and Münch[5] was applied to the description of the distribution of the absorbing matter

[5] *Ap. J.*, **115**, 103, 1952.

within our own Galaxy. Since the parameters characterizing the distribution of the absorbing material on this picture have been determined entirely from observations relating to the regions in and near the galactic plane[6] and since the "effective" optical half-thickness determined from this work was of the order of 0.20, as contrasted with the value of 0.76 for $\bar{\tau}_{1/2}$ which was determined in the present discussion, it seems best to proceed in the following way.

Let us first determine the value for the absorption parameter $a^2$, which is required in order to explain, on the basis of fluctuations in the galactic absorption alone, the observed value for $(\overline{N^2} - \overline{N}^2)/\overline{N}^2$ obtained from the counts of the nebulae. For this case we have (cf. eqs. [21] and [26] of Paper I)

$$\frac{\overline{N^2} - \overline{N}^2}{\overline{N}^2} = \frac{1}{1 + \frac{2}{4} T_0} \frac{2}{4} T_0 , \tag{34}$$

while from the counts of the nebulae for the higher galactic latitudes we have

$$\frac{\overline{N^2} - \overline{N}^2}{\overline{N}^2} \cong 0.194 . \tag{35}$$

From equations (34) and (35) we then obtain

$$T_0 \cong 1.07 \times 10^{-1} . \tag{36}$$

Since the $e^{-t/\tau_0}$ form for the correlation coefficient describing the fluctuations in brightness of the Milky Way was found to fit the data for the Milky Way quite satisfactorily, we shall use equation (44) of Paper I in order to obtain the theoretical value for $T_0/a^2$. Taking $\tau_0 = 0.01$ (the value determined from the study of the fluctuations in brightness of the Milky Way) and $\bar{\tau}$ corresponding to the galactic latitude of the observational data from which the value given in equation (35) was derived (assuming $\bar{\tau}_{1/2}$ to be equal to 0.76), we obtain

$$\frac{T_0}{a^2} = 1.80 \times 10^{-2} \tag{37}$$

so that, from equations (36) and (37), we find that

$$a^2 \cong 6 . \tag{38}$$

It will be observed that this value is from two to three times smaller than the values determined from the investigations of the fluctuations in brightness of the Milky Way.

It will, however, be recalled that the writer's analysis[7] indicated an "effective" optical half-thickness of only 0.20 for the absorbing matter relevant to the observations for the low latitudes. This value refers to the absorbing matter within the confines of the Galaxy as defined by the regions of appreciable star density, so that the absorption parameters determined from such studies characterize only this absorbing matter. If we should assume that it is only in this portion of the total optical half-thickness that there are appreciable fluctuations, we then obtain

$$\frac{T_0}{a^2} = 4.60 \times 10^{-3} \tag{39}$$

for a galactic latitude of 56° and for $\tau_0 = 0.01$. Hence in this case the value of $a^2$ determined from the observed value of $(\overline{N^2} - \overline{N}^2)/\overline{N}^2$ is

$$a^2 \cong 23 , \tag{40}$$

[6] Cf. *ibid.*, and Limber, *Ap. J.*, **117**, 145, 1953.

[7] *Ap. J.*, **117**, 145, 1953.

which is not too much larger than the values obtained from the studies of the fluctuations in brightness of the Milky Way.

If the material for the lower latitudes be analyzed in the same way, it is found that the resulting values for $a^2$ are reduced to about 3.8 and 14 for the cases $(\bar{\tau}_{1/2})_{eff} = 0.76$ and 0.20, respectively. Thus we see that for the case of $(\bar{\tau}_{1/2})_{eff} = 0.76$ the disagreement which was found for the higher latitudes is even more marked for the lower latitudes; on the other hand, the value of $a^2$ for the case of $(\bar{\tau}_{1/2})_{eff} = 0.20$ is now quite consistent with the predictions from the absorption theory.

Next, calculations have been carried out to determine the theoretical correlation functions which would correspond to the effects introduced upon a uniform distribution of nebulae by fluctuations in the galactic absorption alone. As before, it has been assumed that $\tau_0 = 0.01$ and that the correlation coefficient has the form $e^{-t/\tau_0}$. These functions have been calculated for values of the optical thickness ranging from 0.44 to 1.68

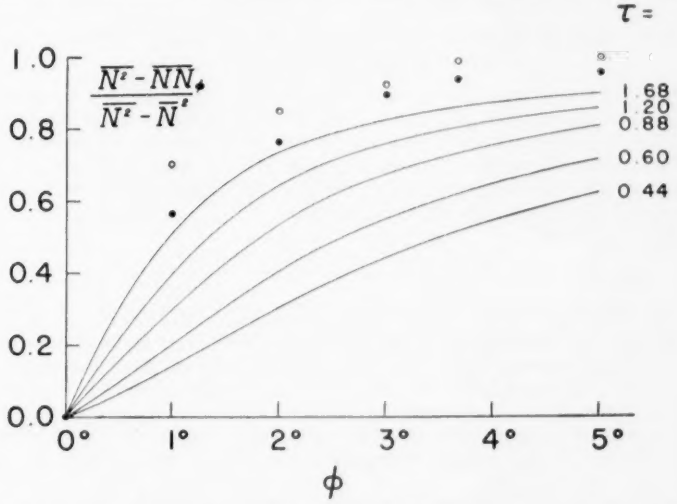


FIG. 3.—Theoretical correlation functions for the case in which the observed fluctuations in the number of nebulae are due entirely to fluctuations in the galactic absorption. The open and the filled circles are the points which correspond to the observational material for the high and the low latitudes, respectively, for the first approximations to $(\overline{NN}_\phi - F_\phi)$.

and are plotted in Figure 3. The observational curves from Figure 1 have been plotted in this same figure for purposes of comparison. It is seen that if one assumes that the fluctuations extend throughout a layer with an effective optical half-thickness of 0.76, then the theoretical curve which should fit the observational curve for the higher latitudes falls much too far below it for the differences to be explained in terms of observational errors. Further, it is difficult to believe that the theoretical model employed in representing the distribution of the absorbing matter could be so greatly in error as to give rise to the observed difference. The agreement between the observational curve for the lower latitudes and that for the theoretical correlation function which should correspond to it is much better; nevertheless, when these results are considered together with those for the $a^2$ discussion for this case, it would appear that any attempt at explaining the observed data in terms of fluctuations in the galactic absorption for such a model can be ruled out.

If it be alternatively assumed that the relevant absorbing layer is much thinner, then, although we have seen that the results of the calculations for $a^2$ can be made consistent with the observations when interpreted as due solely to fluctuations in the absorption, the corresponding theoretical correlation functions are seen to fall so far below the observational curves as to be ruled out completely. It is further obvious that if the observed correlation functions for the nebulae were due chiefly to absorption fluctuations, then the correlation functions for the higher latitudes should fall off somewhat more slowly than those for the lower latitudes, which is certainly contrary to the observed trend.

From the results of these considerations it appears that we can rather conclusively rule out the possibility that fluctuations in the galactic absorption play a prominent role in the observed fluctuations in the counts of the extragalactic nebulae. As a result, we shall neglect the effects of fluctuations in the galactic absorption in the further work and shall therefore consider only cases I and III of Paper I.

## IV. THE DETERMINATION OF THE PARAMETERS CHARACTERIZING THE SPACE DISTRIBUTION OF THE NEBULAE

*General.*—In the general case the seven parameters $\sigma$, $\bar{\rho}$, $r_0$, $\beta^2$, $m_0'$, $M_0$, and $\bar{\tau}(b)$ will enter into the analysis. Here $\sigma$ is—as in Paper I—the dispersion in the absolute magnitudes of the extragalactic nebulae; the other symbols also have their meanings of Paper I and will be further discussed as they are encountered in the subsequent work. For reasons both of mathematical simplicity and of physical significance, it will be convenient to introduce still another parameter, $\Theta$, such that

$$\Theta \equiv \frac{1}{r_0}\, 10^{\left[m_0' - M_0 + 5 - 2.5\bar{\tau}(b)\log_{10} e\right]/5}. \tag{41}$$

Thus $\Theta$ is the distance in units of the microscale $r_0$ of an extragalactic nebula of absolute magnitude $M_0$ (the mean absolute magnitude of the nebulae) and apparent magnitude $m_0'$ (the limiting apparent magnitude of the counts), as seen through a galactic optical thickness $\bar{\tau}(b)$. The parameters $m_0'$, $M_0$, $\bar{\tau}(b)$, and $r_0$ then enter the calculations only through $\Theta$. Once $\Theta$ has been determined from a comparison of the theory with the observations, the effects of any future corrections to the currently accepted values for $m_0'$, $M_0$, and $\bar{\tau}(b)$ can then be readily incorporated to give the corresponding revised values for $r_0$ and $\bar{\rho}$.

From the expressions of Paper I for cases I and III, the theoretical values for $\overline{N^2}$ and $\overline{NN_\phi}$ ($\phi = 0^\circ$, $1^\circ$, $2^\circ$, $3^\circ$, $4^\circ$, and $5^\circ$) have been evaluated for the case in which the correlation coefficient is of the gaussian form for several sets of the parameters $\sigma$ and $\Theta$. In order to indicate the effects of the particular form chosen for the correlation coefficient, calculations have also been carried out for two sets of parameters for the case when the correlation coefficient has the form: $e^{-r/r_0}$. The results of all these calculations are given in Table 11.

*The determination of $\Theta$ from the observations.*—The theoretical correlation functions $(\overline{N^2} - \overline{NN_\phi})/(\overline{N^2} - \bar{N}^2)$ have been calculated from the data of Table 11 and are plotted in Figures 4, 5, 6, and 7. The correlation functions for the first approximations to $(\overline{NN_\phi} - F_\phi)$ have been plotted in these same figures for comparison; and, although the $\Theta$ parameters describing the theoretical curves for $\sigma = 1^m$ have not been well selected for a comparison with the observational curves, there can be no question that the best fit to the observational curves is to be obtained for $\sigma = 2^m$. Thus, for example, in the case of $\sigma = 0^m$ and $\log_{10}\Theta = 1.685$ we see that the value of the theoretical correlation function at $\phi = 1^\circ$ is less than half that for the observational curve corresponding to the higher latitudes; and yet for $\phi = 3^\circ$ the values for the two curves are very nearly equal.

For $\sigma = 2^m$ the agreement throughout the whole range of values for $\phi$ from $1^\circ$ to $5^\circ$ is well within the uncertainties of these first approximations to the true observational curves. For $\sigma = 1^m$ we can safely conclude both from an extrapolation to larger values of $\Theta$ from the two theoretical curves which have been evaluated and also from an interpolation between the theoretical curves for the cases $\sigma = 0^m$ and $\sigma = 2^m$ that, to obtain agreement between theory and observation at $\phi = 3^\circ$, say, the theoretical curves for $\sigma = 1^m$ will fall markedly below the observational curves at $\phi = 1^\circ$. Upon using the

TABLE 11

THEORETICAL VALUES FOR $\overline{NN}\phi/\bar{\rho}^2 r_0^6$ AND $\overline{N^2}/\bar{\rho}^2 r_0^6$

(i) $\Gamma(r) = e^{-r^2/r_0^2}$

| $\log_{10}\Theta$ | 1.685 | 1.651 | 1.601 | 1.384 | 1.350 | 1.300 |
|---|---|---|---|---|---|---|
| | $\sigma = 0^m$ | | | | | |
| $\overline{N^2}/\bar{\rho}^2 r_0^6$ | 133+ | 83.2+ | 42.2+ | 2.08+ | 1.30+ | 0.660+ |
| $\overline{NN}_1/\bar{\rho}^2 r_0^6$ | 8.51 $\beta^2$ | 5.74 $\beta^2$ | 3.25 $\beta^2$ | 0.258 $\beta^2$ | 0.174 $\beta^2$ | .0980 $\beta^2$ |
| $\overline{NN}_2/\bar{\rho}^2 r_0^6$ | 5.10 $\beta^2$ | 3.69 $\beta^2$ | 2.30 $\beta^2$ | 0.222 $\beta^2$ | 0.152 $\beta^2$ | .0868 $\beta^2$ |
| $\overline{NN}_3/\bar{\rho}^2 r_0^6$ | 1.35 $\beta^2$ | 1.17 $\beta^2$ | 0.878 $\beta^2$ | 0.154 $\beta^2$ | 0.111 $\beta^2$ | .0683 $\beta^2$ |
| $\overline{NN}_4/\bar{\rho}^2 r_0^6$ | 0.259 $\beta^2$ | 0.251 $\beta^2$ | 0.233 $\beta^2$ | 0.0860 $\beta^2$ | 0.0671 $\beta^2$ | .0463 $\beta^2$ |
| $\overline{NN}_5/\bar{\rho}^2 r_0^6$ | 0.0620 $\beta^2$ | 0.0620 $\beta^2$ | 0.0615 $\beta^2$ | 0.0406 $\beta^2$ | 0.0347 $\beta^2$ | .0263 $\beta^2$ |
| $\overline{N^2}/\bar{\rho}^2 r_0^6$ | 0.0200 $\beta^2$ | 0.0200 $\beta^2$ | 0.0200 $\beta^2$ | 0.0178 $\beta^2$ | 0.0163 $\beta^2$ | .0138 $\beta^2$ |
| | 133 | 83.2 | 42.2 | 2.08 | 1.30 | 0.660 |

| $\log_{10}\Theta$ | 1.350 | 1.204 | 1.048 | 0.748 | 0.601 |
|---|---|---|---|---|---|
| | $\sigma = 1^m$ | | $\sigma = 2^m$ | | |
| $\overline{N^2}/\bar{\rho}^2 r_0^6$ | 9.04+ | 1.16+ | 40.9+ | 0.638+ | 0.0846+ |
| $\overline{NN}_1/\bar{\rho}^2 r_0^6$ | 0.270 $\beta^2$ | 0.0502 $\beta^2$ | 0.262 $\beta^2$ | .00820 $\beta^2$ | .00150 $\beta^2$ |
| $\overline{NN}_2/\bar{\rho}^2 r_0^6$ | 0.183 $\beta^2$ | 0.0392 $\beta^2$ | 0.0785 $\beta^2$ | .00464 $\beta^2$ | .00114 $\beta^2$ |
| $\overline{NN}_3/\bar{\rho}^2 r_0^6$ | 0.0881 $\beta^2$ | 0.0260 $\beta^2$ | 0.0256 $\beta^2$ | .00246 $\beta^2$ | .000654 $\beta^2$ |
| $\overline{NN}_4/\bar{\rho}^2 r_0^6$ | 0.0429 $\beta^2$ | 0.0148 $\beta^2$ | 0.0102 $\beta^2$ | .00134 $\beta^2$ | .000415 $\beta^2$ |
| $\overline{NN}_5/\bar{\rho}^2 r_0^6$ | 0.0194 $\beta^2$ | 0.00880 $\beta^2$ | 0.00471 $\beta^2$ | .000818 $\beta^2$ | .000268 $\beta^2$ |
| $\overline{N^2}/\bar{\rho}^2 r_0^6$ | 0.00901 $\beta^2$ | 0.00494 $\beta^2$ | 0.00240 $\beta^2$ | .000580 $\beta^2$ | .000179 $\beta^2$ |
| | 9.04 | 1.16 | 40.9 | 0.638 | 0.0846 |

(ii) $\Gamma(r) = e^{-r/r_0}$

| $\log_{10}\Theta$ | $\sigma = 0^m$ | | $\log_{10}\Theta$ | $\sigma = 0^m$ | |
|---|---|---|---|---|---|
| | 1.601 | 1.384 | | 1.601 | 1.384 |
| $\overline{N^2}/\bar{\rho}^2 r_0^6$ | 42.2+ | 2.08+ | $\overline{NN}_4/\bar{\rho}^2 r_0^6$ | 42.2+ | 2.08+ |
| $\overline{NN}_1/\bar{\rho}^2 r_0^6$ | 3.57 $\beta^2$ | 0.278 $\beta^2$ | $\overline{NN}_5/\bar{\rho}^2 r_0^6$ | 0.758 $\beta^2$ | 0.116 $\beta^2$ |
| $\overline{NN}_2/\bar{\rho}^2 r_0^6$ | 2.66 $\beta^2$ | 0.233 $\beta^2$ | $\overline{N^2}/\bar{\rho}^2 r_0^6$ | 0.478 $\beta^2$ | 0.0891 $\beta^2$ |
| $\overline{NN}_3/\bar{\rho}^2 r_0^6$ | 1.82 $\beta^2$ | 0.190 $\beta^2$ | | 42.2 | 2.08 |
| | 1.19 $\beta^2$ | 0.150 $\beta^2$ | | | |

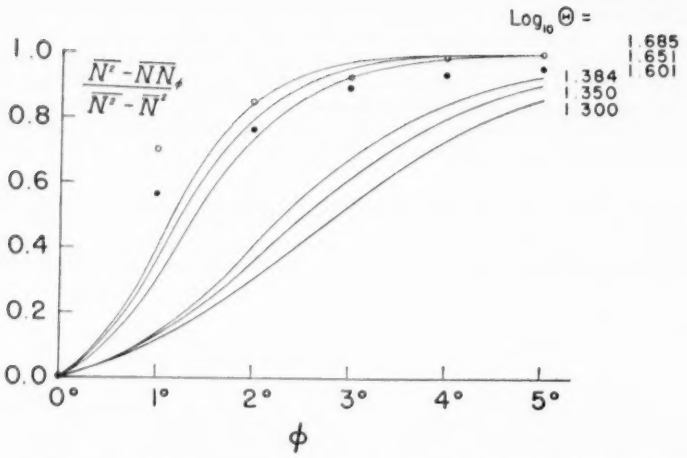


FIG. 4.—Theoretical correlation functions for $\sigma = 0^m$. The open and the filled circles are the points which correspond to the observational material for the high and the low latitudes, respectively, for the first approximations to $(\overline{NN}_\phi - F_\phi)$.

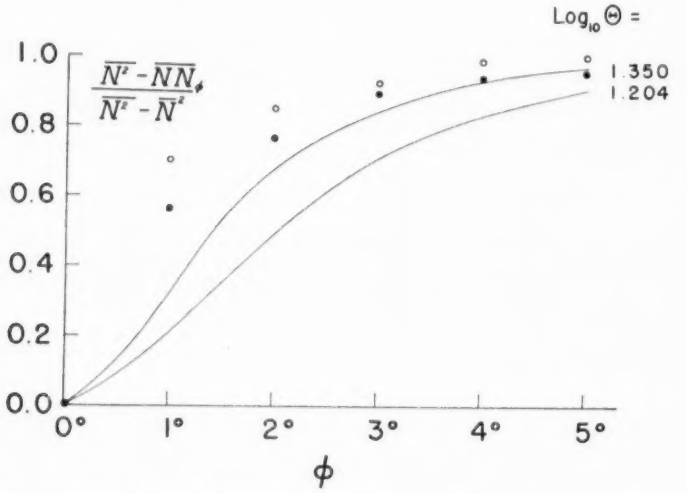


FIG. 5.—Theoretical correlation functions for $\sigma = 1^m$. The open and the filled circles are the points which correspond to the observational material for the high and the low latitudes, respectively, for the first approximations to $(\overline{NN}_\phi - F_\phi)$.

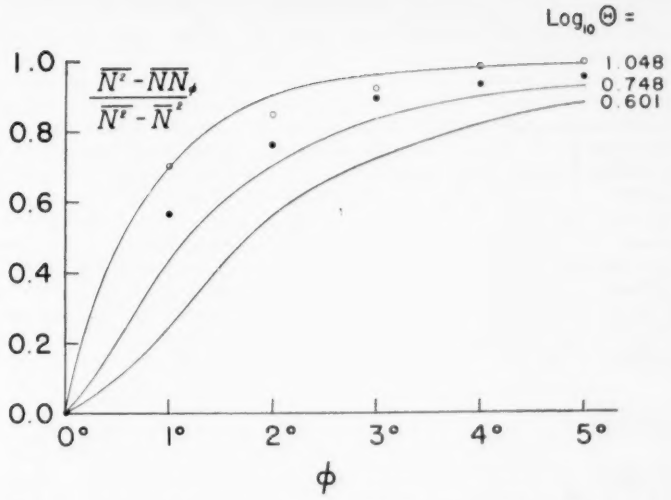


FIG. 6.—Theoretical correlation functions for $\sigma = 2^m$. The open and the filled circles are the points which correspond to the observational material for the high and the low latitudes, respectively, for the first approximations to $(\overline{NN_\phi} - F_\phi)$.

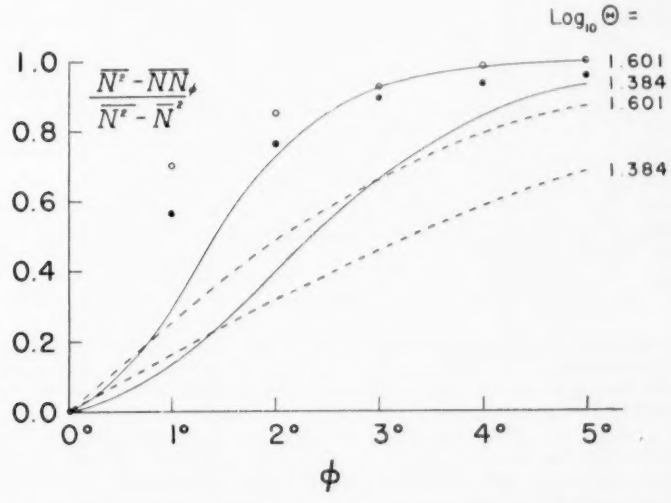


FIG. 7.—Theoretical correlations for $\sigma = 6^m$. The solid curves correspond to the $e^{-r^2/r_0^2}$ form for the correlation coefficient, while the dashed curves correspond to the $e^{-r/r_0}$ form. The open and the filled circles are the points which correspond to the observational material for the high and the low latitudes, respectively, for the first approximations to $(\overline{NN_\phi} - F_\phi)$.

broader base line which is available between $\phi = 1^\circ$ and $\phi = 4^\circ$ or $5^\circ$, the foregoing conclusions are even more strongly borne out, although the differences between the several theoretical curves are then smaller and approach more nearly the uncertainties in the observational curves. On the basis of these considerations, a dispersion of 2 mag. in the absolute magnitudes of the nebulae has been taken as the value which is determined from the analysis of the observations according to the theoretical model adopted.

Second and final approximations to $(\overline{NN}_\phi - F_\phi)$ have been made in such a way that, in doing as little violence as possible to the actual observational data, the observational correlation functions have been made to take on exactly the theoretical forms for $\sigma = 2^m$. The results for these final approximations to $(\overline{NN}_\phi - F_\phi)$ are given with those for the zero and first approximations in Table 10, and the values of $\overline{NN}_\phi$ for these final approximations are given with those for the zero and first approximations in Table 10′. In Figure 8 the observational correlation functions for these final approximations are plotted, together with the three theoretical curves for $\sigma = 2^m$. In Figure 9 the final approximations to $(\overline{NN}_\phi - F_\phi)$ are plotted, together with the zero approximations.

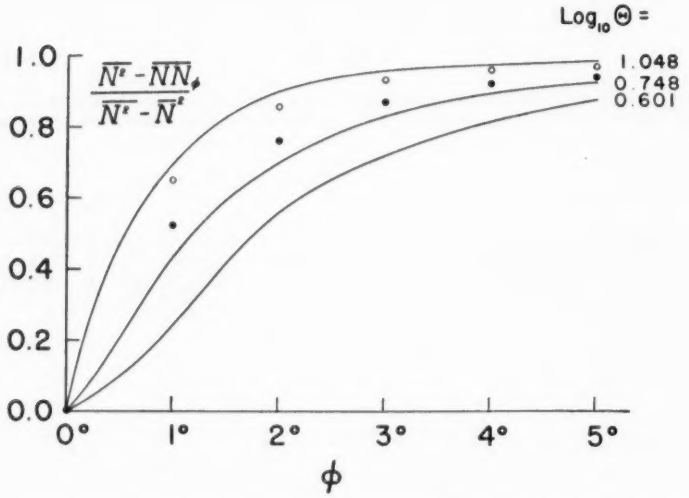


FIG. 8.—Final comparison of the theoretical and observational correlation functions. The curves are the theoretical correlation functions for $\sigma = 2^m$. The open and the filled circles are the points which correspond to the observational material for the high and the low latitudes, respectively, for the final approximations to $(\overline{NN}_\phi - F_\phi)$.

The comparison presented in Figure 9 is extremely important, in that it shows quite clearly just how much violence has had to be done to the observational values for $(\overline{NN}_\phi - F_\phi)$ in order to achieve a perfect fit for the case $\sigma = 2^m$. The value of this comparison over that of Figure 6, for example, lies in the fact that the values of $(\overline{NN}_\phi - F_\phi)$ for the zero approximations are essentially observed quantities—corrected though they are by a rather lengthy process. If these observed values for $(\overline{NN}_\phi - F_\phi)$ are transformed by equation (31) into values for $\overline{NN}_\phi$, then the uncertainties and irregularities in $(\overline{NN}_\phi - F_\phi)$ give rise to uncertainties in $\overline{NN}_\phi$ which are not simply and directly related to those in the observed quantities, and hence a satisfactory direct comparison of theory

and observation is not possible. On the other hand, in the comparisons presented by Figure 9 we are able to compare theoretical values directly with quantities which are essentially observed quantities, and thus the role of the observational uncertainties, as they affect the comparison, can be readily visualized. From Figure 9 or Table 10 it is seen that, for both the high- and the low-latitude supernormal points, the zero and the final approximations differ by less than two units in the third place except for $\phi = 5°$, where the differences are only slightly greater than this. These differences are almost certainly within the probable errors for both the observational curves.

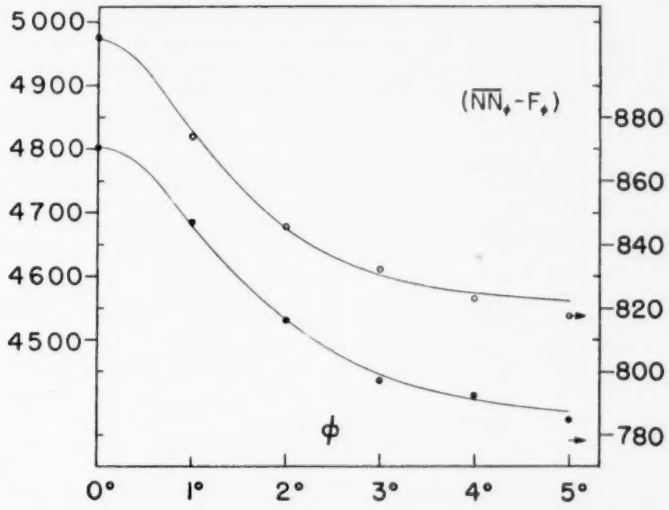


FIG. 9.—Zero and final approximations to $(\overline{NN}_\phi - F_\phi)$. The open circles and the upper curve represent the zero and the final approximations, respectively, to $(\overline{NN}_\phi - F_\phi)$ for the higher-latitude material. The scale for $(\overline{NN}_\phi - F_\phi)$, which is at the left-hand side of the figure, is the one which is appropriate to these data. The filled circles and the lower curve represent the zero and the final approximations, respectively, for the lower-latitude material; and the scale on the right-hand side of the figure is the one appropriate to these data. The small arrows indicate the positions of $\overline{N}^2$ for the two cases.

It should perhaps be noted that the value of 2 mag. which has been determined here for the dispersion in the absolute magnitudes of the nebulae is quite consistent with Holmberg's recent result.[8] His analysis of thirty-nine near-by systems led him to conclude that the dispersion was "not less than $1^m85$," the implication being that, for the known types of the extragalactic nebulae, the luminosity function is characterized by a dispersion of $1^m85 \pm 0^m2$.

It will also be noted that the theoretical correlation functions for the $e^{-r/r_0}$ form for the correlation coefficient give less satisfactory agreement with the observations than do the corresponding functions for the gaussian form. This would seem to apply as well for the cases $\sigma = 1^m$ and $\sigma = 2^m$. In any case it is safe to conclude that any theoretical curves which fit the observational curves even approximately and have the $e^{-r/r_0}$ form for their correlation coefficient will correspond to a value of $\sigma$ which is decidedly greater than 2 mag.

[8] *Lund Medd.*, Ser. II, No. 128, 1950.

In order to determine the effect of differences in the mean galactic absorption upon the theoretical curves, we can consider the differences in $\Theta$ for a given value of $\sigma$ to be due entirely to differences in $\bar{\tau}(b)$. The theoretical curves for a given value of $\sigma$ then provide theoretical curves for given values of $m_0'$, $M_0$, and $r_0$ for various values of $\bar{\tau}(b)$. When the differences in $\Theta$ for a given value of $\sigma$ are interpreted in this way, the corresponding values of $\Delta\bar{\tau}$ for the different pairs of curves can be obtained. These values for $\Delta\bar{\tau}$ are given in Table 12. For the case of $\sigma = 2^m$, interpolations have been carried out in this table to obtain $\Delta\bar{\tau}$ for those two theoretical curves which best fit the observational curves for the final approximations. This gives the value 0.65. We next insert the values of $N$ from the material for the low and for the high latitudes into equation (32) and determine the effective value of $\Delta\bar{\tau}$ for these two groups of data. If it is assumed that $\bar{\tau}_{1/2} = 0.76$, we obtain in this way $\Delta\bar{\tau} = 0.59$. A comparison of this value with that determined above from the correlation-curves indicates an even better agreement than was to be expected from two such limited statistical samples.

TABLE 12

VALUES OF $\Delta\tau$ FOR THE THEORETICAL CURVES

| $\log_{10}\Theta$ | $\Delta\tau$ | $\log_{10}\Theta$ | $\Delta\tau$ |
|---|---|---|---|
| | $\sigma = 0^m$ | | $\sigma = 1^m$ |
| 1.685 | | 1.350 | |
| | 0.24 | | 0.67 |
| 1.651 | | 1.204 | |
| | 0.16 | | |
| 1.601 | | | $\sigma = 2^m$ |
| | 1.00 | | |
| 1.384 | | 1.048 | |
| | 0.24 | | 1.39 |
| 1.350 | | 0.748 | |
| | 0.16 | | 0.67 |
| 1.300 | | 0.601 | |

TABLE 13

FINAL VALUES FOR $\sigma$, $\beta^2$, AND $\Theta$

$\sigma = 2^m$
$\beta^2 = 25$
$\log_{10}\Theta = 0.98$ } From the higher-latitude material
$\Theta = 9.55$

Interpolations have also been carried out for the case of $\sigma = 2^m$, to determine that value for $\Theta$ which best fits the observational correlation-curve characterizing the observations for the higher latitudes. In this way the value given in Table 13 has been obtained, and it is this value which will be taken as the final value for $\Theta$ as determined from the observations. The observations for the higher latitudes have been used rather than those for the lower latitudes, since the former are both better determined statistically and less affected by galactic absorption.

*The determination of $\beta^2$ from the observations.*—We shall next consider the expression $(\overline{N^2} - \bar{N}^2)/\bar{N}^2$. Equating the theoretical values for this expression, which are derived from the material in Table 11 for the case of $\sigma = 2^m$, to the observational value appropriate to the higher galactic latitudes (cf. eq. [35]), we obtain the values of $\beta^2$ which correspond to the three theoretical curves. If we then interpolate to the value of $\Theta$ given in Table 13, we obtain the final value for $\beta^2$; this value is included with the final values for $\sigma$ and $\Theta$ in Table 13.

From equations (2) and (3) of Paper I, we see that $\beta$ can be interpreted physically as the root-mean-square deviation from the mean space density of the nebulae in units of the mean density itself:

$$\beta = \frac{\sqrt{[\overline{\rho^2} - \bar{\rho}^2]}}{\bar{\rho}}, \tag{42}$$

and hence the result given in Table 13 for $\beta^2$ indicates that the deviations from the mean density are quite appreciable.

*The determination of $r_0$ and $\bar{\rho}$.*—As has been noted, the numerical values for both $r_0$ and $\bar{\rho}$ in parsecs and number of nebulae per cubic parsec, respectively, depend in a quite sensitive way upon the values of $m_0'$, $M_0$, and $\bar{\tau}$ which are used in their determination. Since there is some uncertainty at present in the values which should be used for these quantities, the method for the determination of the quantities $r_0$ and $\bar{\rho}$ will be described in some detail for the case of general $m_0'$, $M_0$, and $\bar{\tau}$, so that revisions to the presently accepted values for $m_0'$, $M_0$, and $\tau$ can be readily applied to provide revised values for $r_0$ and $\bar{\rho}$. We proceed by first taking from Table 13 the value of $\Theta$ determined for the higher latitudes. Then for a particular value of the quantity $m_0' - M_0 + 2.5\bar{\tau}'\log_{10}e$ appropriate to these same higher latitudes, we obtain $r_0$ directly from equation (41). Having determined $r_0$ in this way, we then determine from Table 11 the value of $\overline{N}^2/\bar{\rho}^2 r_0^6$ for $\sigma = 2^m$ and for the value of $\Theta$ given in Table 13. It should be noted that the values of $\overline{N}^2/\bar{\rho}^2 r_0^6$ for a given value of $\sigma$ are simply proportional to the sixth power of $\Theta$, so that, knowing for one value of $\Theta$ and $\sigma$ the value of $\overline{N}^2/\bar{\rho}^2 r_0^6$, we need not resort to interpolation but can actually calculate the values of this quantity for any other values of $\Theta$ for this same $\sigma$. When $\overline{N}^2/\bar{\rho}^2 r_0^6$ and $r_0$ have been determined, the value for $\bar{\rho}$ can be deduced from the expression

$$\bar{\rho} = \frac{\overline{N}_{\text{obs}}}{r_0^3 \sqrt{[\overline{N}^2/\bar{\rho}^2 r_0^6]}}, \tag{43}$$

where $N_{\text{obs}}$ is the appropriate observational value for $\overline{N}$. For the higher galactic latitudes,

$$\overline{N}_{\text{obs}} \cong 67.4. \tag{44}$$

Let us now apply this technique to two particular sets of values for $m_0'$, $M_0$, and $\bar{\tau}'$. The value for $M_0$, which was obtained from Holmberg's study,[9] is $-13.5$ mag.; and when this is corrected for the change in the distance scale, we obtain $-14.9$ mag. We shall use this value for $M$ and Shane's tentative value of 18.4 mag. for $m_0'$, and we shall consider two values for $\bar{\tau}_{1/2}$:

$$\text{(i)}\quad \bar{\tau}_{1/2} = 0.76, \qquad \bar{\tau}' = 0.915;$$

$$\text{(ii)}\quad \bar{\tau}_{1/2} = 0.23, \qquad \bar{\tau}' = 0.279.$$

Case i is the situation which is consistent with the present observations, while case ii is included simply to show the sensitivity of the results to changes in $\bar{\tau}_{1/2}$ and in $m_0'$ and $M_0$. The value actually taken for case ii is the Hubble value for the optical half-thickness of the Galaxy, which, in magnitudes, is 0.25.

Using the value for $\Theta$ from Table 13, together with the above values for $m_0'$, $M_0$, and $\tau'$, we obtain

$$\text{(i)}\quad r_0 = 3.0 \times 10^6 \text{ parsecs} \tag{45}$$

and

$$\text{(ii)}\quad r_0 = 4.2 \times 10^6 \text{ parsecs}. \tag{46}$$

[9] *Ibid.*

The corresponding values for $\tilde{\rho}$ are

$$\text{(i)} \quad \tilde{\rho} = 6.0 \times 10^{-19} \text{ nebulae per cubic parsec} \tag{47}$$

and

$$\text{(ii)} \quad \tilde{\rho} = 2.3 \times 10^{-19} \text{ nebulae per cubic parsec} . \tag{48}$$

Finally, it will be of interest to use the material for the lower latitudes in obtaining $\beta^2$, $r_0$, and $\tilde{\rho}$. Since the spatial-distribution properties of the extragalactic nebulae should be statistically isotropic, we should, for perfect observations and for perfect theoretical analysis, obtain exactly the same values for these quantities whether the analysis is carried out for one galactic latitude or another. The differences between the high- and low-latitude values for $\beta^2$, $r_0$, and $\tilde{\rho}$ will therefore provide an excellent measure of the observational uncertainties as they affect these quantities; and included in these differences will also be any internal inconsistencies due to the inadequacy of the proposed theoretical model.

In this connection it should be remembered that observations for a given galactic latitude provide essentially four independent observational parameters for the present treatment: $\overline{N}^2$, $\overline{N^2}$, and at least two parameters characterizing the correlation function. The theoretical model which has been used has just four adjustable parameters: $r_0$, $\tilde{\rho}$, $\beta^2$, and $\sigma$; and hence there is no formal difficulty in fitting theory and observation. However, where observations exist for two different galactic latitudes, an additional four or more observationally independent parameters are introduced, whereas the only additional adjustable parameter which enters into the theoretical description is the value of $\Delta\tau$ corresponding to the two sets of observations. Thus, when the data for two different latitudes are used, the solution for $r_0$, $\tilde{\rho}$, $\beta^2$, and $\sigma$ is overdetermined, and the theoretical model is put to a significant test of its ability truly to characterize the actual distribution of the nebulae.

The calculations for $\beta^2$, $r_0$, and $\tilde{\rho}$ from the material for the lower latitudes have been carried out, and the results are

$$\beta^2 = 21 \tag{49}$$

and, for case (i),

$$r_0 = 3.2 \times 10^6 \text{ parsecs} \tag{50}$$

and

$$\tilde{\rho} = 7.0 \times 10^{-19} \text{ nebulae per cubic parsec} . \tag{51}$$

The comparison of these results with the earlier ones shows that the differences in the values of these quantities when determined from the material for the high and for the low galactic latitudes are not large, and it does not seem at all impossible to explain these differences in terms of observational uncertainties alone, which have arisen because of the limited sizes of the statistical samples used.

## V. CONCLUDING REMARKS

The proposed theoretical model has been found to be consistent with the counts of the nebulae which have been obtained by Shane and Wirtanen. More specifically, the agreement of the observations with the theoretical predictions for the case of $\sigma = 2^m$ is in every respect as satisfactory as one could expect when one considers the various possible sources of error in the observational data as well as in the various possible deviations from the general assumptions which have been made regarding the theoretical model.

It should perhaps be emphasized that—other than $\tilde{\rho}$—only the three parameters, $r_0$, $\beta^2$, and $\sigma$ (or $\Theta$, $\beta^2$, and $\sigma$), have been used to characterize the spatial distribution of the nebulae on this model. As a result, we are unable to distinguish between a variety of possible distributions which have $r_0$, $\beta^2$, and $\sigma$ in common. However, from the uncertainties in the observational data and from the nature of the integral equations which

are, in fact, being solved, it would seem that any attempt at a determination of a greater number of parameters in a statistical treatment relying solely upon such data as are provided in the Lick counts will require the greatest caution and discretion.

In concluding, I very gratefully acknowledge my indebtedness to Professor C. D. Shane, who generously made available to me the results of the counts of the nebulae which have been carried out by himself and Mr. C. A. Wirtanen. I should also like to acknowledge my debt to Professor J. Neyman and to Dr. Elizabeth L. Scott for making available to me a wealth of material from their statistical discussion of this same problem, even though their material has not actually been used in the work of the present paper; and I should like to thank them as well for the encouragement and interest which they have expressed in the present investigation. My thanks go also to Professor John W. Tukey for critically reading a preliminary draft of this paper and for suggesting a number of improvements which have been incorporated in the present paper. Finally, it is to Professor Chandrasekhar that I acknowledge an even greater debt both for his initial suggestion that such a treatment might prove useful and for his continued interest, encouragement, and help throughout the period during which this work was in progress.

# A STOCHASTIC MODEL OF A FLUCTUATING DENSITY FIELD. II

ALLADI RAMAKRISHNAN
Department of Physics, University of Madras
*Received November 4, 1953; revised January 22, 1954*

ABSTRACT

The problem of the fluctuations in brightness of the Milky Way is discussed in the light of the new picture of continuous distribution of matter. The results of the previous paper are extended to the case of finite $t$, where $t$ is the extent of the astrophysical system.

In the previous paper,[1] a stochastic model of a fluctuating density field was proposed and applied to the astrophysical problem of the fluctuations in brightness of the Milky Way on the basis of the new picture of continuous distribution of matter suggested by Chandrasekhar and Münch. The higher moments of the probability distribution of the brightness $I(t)$ as measured by the observer when the system extends from 0 to $t$ were obtained as $t$ tends toward infinity. Since writing that paper, the author has succeeded in obtaining the moments even in the case of finite $t$. Incidentally, it was also noted, with some surprise, that the moments even in the case of discrete clouds could be obtained by an interesting use of Theorem I of Paper I.

We continue to use the same notation as in Paper I. We obtained

$$\epsilon\{ I^n(t) \} = n! \int_0^t \int_{t_1}^t \int_{t_2}^t \cdots \int_{t_{n-1}}^t e^{-[nt_1 + (n-1)(t_2 - t_1) + \ldots + (t_n - t_{n-1})]} \tag{1}$$

$$[1 + \{ n^2 t_1 + (n-1)^2 (t_2 - t_1) + \ldots + (t_n - t_{n-1}) \} a^2 \tau_0] \, dt_1 dt_2 \ldots dt_n .$$

In Paper I this integral was evaluated when $t$ tends to infinity. We shall now show that it can be obtained explicitly even for finite $t$. We first note that the term

$$1 + \{ n^2 t_1 + (n-1)^2 (t_2 - t_1) + \ldots + (t_n - t_{n-1}) \} a^2 \tau_0 ,$$

occurring in equation (1), can be replaced by

$$e^{[n^2 t_1 + (n-1)^2 (t_2 - t_1) + \ldots + (t_n - t_{n-1})] a^2 \tau_0}$$

if we assume, as we did in Paper I, that terms $O(\tau_0^2)$ can be neglected. Equation (1) can then be written in an elegant iterative form as follows:

$$\epsilon\{ I^n(t) \} = n \int_0^t e^{-a_n \tau} \epsilon\{ I^{n-1}(t - \tau) \} \, d\tau , \tag{2}$$

where

$$a_n = n(1 - na^2 \tau_0) \tag{3}$$

$$\epsilon\{ I^n(t) \} = 1 \qquad \text{for all } t \qquad \text{if} \qquad n = 0 . \tag{4}$$

An identical equation was solved recently by the author,[2] and there is no need to repro-

[1] *Ap. J.*, **119**, 443, 1954. This paper is referred to as "Paper I."

[2] *Proc. Cambridge Phil. Soc.*, **49**, 473, 1953.

duce the method, which can be adapted to this case by suitable changes in notation. We find

$$\epsilon\{ I^n(t) \} = n! \sum_{k=0}^{n} \frac{e^{-a_k t}}{\prod_{j=0,\ j\neq k}^{n} (a_j - a_k)} . \tag{5}$$

Using equation (3) and neglecting terms of $O(\tau_0^2)$, we obtain

$$\epsilon\{ I^n(t) \} = n! \sum_{k=0}^{n} \frac{(-1)^n e^{-kt}}{(n-k)!\,k!} [1 + \{ (n-1)\,k + \tfrac{1}{2} n(n+1) + lk^2 \} a^2 \tau_0]$$

$$= \left\{ 1 + \frac{n(n+1)}{2} a^2 \tau_0 \right\} \{ (1 - e^{-t})^n - n(n-1+t)\, e^{-t} (1 - e^{-t})^{n-1} a^2 \tau_0 \tag{6}[3]$$

$$+ n(n-1)\, e^{-2t} (1 - e^{-t})^{n-2} l a^2 \tau_0 .$$

When $t$ tends to infinity, only the first term in the summation corresponding to $k = 0$ survives, and we obtain the result of Paper I.

## COMPARISON WITH THE DISCRETE CASE

Now consider the case of discrete clouds. If a single cloud has a transparency factor $q$, i.e., it cuts down radiation of intensity $I$ to $Iq$, and if $\lambda$ is the frequency of clouds per unit distance, Chandrasekhar and Münch[4] obtained the result

$$\epsilon\{ I^n(t) \} = n! \sum_{k=0}^{n} \frac{e^{-\lambda(1-q^k)t}}{\lambda^n \prod_{j=0,\ j\neq k}^{n} (q^k - q^j)} . \tag{7}$$

Note that this expression is the same as equation (5) with $\lambda(1 - q^k)$ in the place of $a_k$. Adopting the limiting procedure of the previous paper, we write $q = e^{-\tau_*}$ and let $\tau_*$ tend to zero, $\lambda$ to infinity in such a manner that $\lambda\tau_*$ tends to unity. In such a case

$$\lambda(1 - q^k) \to k \left( 1 - \frac{k\tau_*}{2} \right) + O(\tau_*^2) . \tag{8}$$

Comparing this quantity with $a_k = k(1 - ka^2\tau_0)$, we find that $\frac{1}{2}\tau_*$ corresponds to $a^2\tau_0$ as observed by Chandrasekhar and Münch. Identical expressions are thus obtained for $\epsilon\{I^n(t)\}$ in the "continuous" and "discrete" cases.

We shall now derive equation (7) by an application of Theorem I of Paper I.

Between $\tau$ and $\tau + d\tau$, radiation of intensity magnitude $\beta d\tau = d\tau$ ($\beta = 1$) is produced; but in its passage through a distance $\tau$ before reaching the observer, because of the interception of discrete clouds it is cut in intensity to $Q(\tau)d\tau$, where $Q(\tau)$ is the *cumulative transparency factor* of the clouds occurring between 0 and $\tau$ [$1 \geq Q(\tau) \geq 0$]. Hence $Q(\tau)$ is a stochastic variable with a probability frequency-distribution function $P(Q; \tau)$ satisfying the stochastic differential equation,

$$\frac{\partial P(Q;\tau)}{\partial \tau} = -P(Q;\tau)\,\lambda + \int_Q^1 P\left( \frac{Q}{q'}; \tau \right) \frac{\lambda \psi(q')}{q'}\, dq' , \tag{9}$$

$$P(Q; 0) = \delta(Q - 1) , \tag{10}$$

[3] The referee has pointed out that eq. (6) can be compared with the corresponding equation in a paper by D. N. Limber (*Ap. J.*, **117**, 134, 1953, eq. [23]). If the appropriate approximations are made in the latter's equation, agreement is found.

[4] *Ap. J.*, **112**, 380, 393, 1950.

where $\delta$ is the Dirac delta function and $\psi(q')$ the probability frequency function of $q'$, the transparency factor of a single cloud. If the transparency factor of a single cloud is exactly $q$, as we shall assume later, we write $\psi(q') = \delta(q' - q)$. From equations (9) and (10) we obtain

$$\epsilon\{Q^n(\tau)\} = \int_0^1 Q^n P(Q;\tau)\, dQ = e^{-\lambda(1-q_n)\tau}, \tag{11}$$

where

$$q_n = \int_0^1 q^n \psi(q)\, dq. \tag{12}$$

Our object is to calculate $\epsilon\{I^n(t)\}$, and we immediately recognize that

$$I(t) = \int_0^t Q(\tau)\, d\tau. \tag{13}$$

Thus, using the nomenclature of Paper I, we are now dealing with a stochastic field of $Q$, and hence Theorem I can be directly applied to obtain the moments of $I(t)$. First we have to evaluate

$$\epsilon\{Q(t_1)\,Q(t_2)\ldots Q(t_n)\}, \tag{14}$$

which, by definition, is equal to

$$\int_0^1\int_0^1\ldots\int_0^1 Q_1Q_2\ldots Q_n \Pi(Q_1, Q_2, \ldots, Q_n; t_1, t_2, \ldots, t_n)\, dQ_1dQ_2\ldots dQ_n, \tag{15}$$

where

$$\Pi(Q_1, Q_2, \ldots, Q_n; t_1, t_2, \ldots, t_n)\, dQ_1dQ_2\ldots dQ_n$$

represents the joint probability that $Q(t_1)$ lies between $Q_1$ and $Q_1 + dQ_1$; $Q(t_2)$ lies between $Q_2$ and $Q_2 + dQ_2$; ... ; and $Q(t_n)$ lies between $Q_n$ and $Q_n + dQ_n$. Using simple probability arguments, we notice that, if $t_1 < t_2 < t_3 < \ldots < t_n$,

$$\begin{aligned}\Pi(Q_1, Q_2, \ldots, Q_n; t_1, t_2, \ldots, t_n)\, dQ_1dQ_2\ldots dQ_n \\ = P(Q_1; t_1)\, P\left(\frac{Q_2}{Q_1}; t_2 - t_1\right)\ldots P\left(\frac{Q_n}{Q_{n-1}}; t_n - t_{n-1}\right)\frac{dQ_1dQ_2\ldots dQ_n}{Q_1Q_2\ldots Q_{n-1}}.\end{aligned} \tag{16}$$

Applying the transformation,

$$Q_1 = g_1, \qquad \frac{Q_2}{Q_1} = g_2, \qquad \frac{Q_3}{Q_2} = g_3, \ldots, \qquad \frac{Q_n}{Q_{n-1}} = g_n, \tag{17}$$

we find, using equations (13) and (10), that

$$\begin{aligned}\epsilon\{Q(t_1)\,Q(t_2)\ldots Q(t_n)\} = \int_0^1\int_0^1\ldots\int_0^1 g_1^n g_2^{n-1}\ldots g_n P(g_1; t_1)P(g_2; t_2 - t_1)\ldots \\ \times P(g_n; t_n - t_{n-1})\, dg_1 dg_2\ldots dg_n, \qquad (t_1 < t_2 < \ldots < t_n)\end{aligned} \tag{18}$$

$$= \epsilon\{Q^n(t_1)\}\,\epsilon\{Q^{n-1}(t_2 - t_1)\}\ldots\epsilon\{Q(t_n - t_{n-1})\}. \tag{19}$$

Using equation (11), the above expression reduces to

$$e^{-\lambda[(1-q_n)t_1 + (1-q_{n-1})(t_2-t_1) + \ldots + (1-q_1)(t_n - t_{n-1})]}, \qquad (t_1 < t_2 < \ldots < t_n). \tag{20}$$

Now we apply Theorem I and obtain

$$\epsilon\{ I^n(t) \} = n! \int_0^t \int_{t_1}^t \cdots \int_{t_{n-1}}^t e^{-\lambda[(1-q_n)t_1 + (1-q_{n-1})(t_2-t_1) + \cdots + (1-q_1)(t_n - t_{n-1})]} \times dt_1 dt_2 \cdots dt_n . \tag{21}$$

This equation can be written in iterative form as

$$\epsilon\{ I^n(t) \} = n \int_0^t e^{-\lambda(1-q_n)\tau} \epsilon\{ I^{n-1}(t-\tau) \} d\tau . \tag{22}$$

Comparing the above equation with equation (5), we obtain its solution as

$$\epsilon\{ I^n(t) \} = n! \sum_{k=0}^{n} \frac{e^{-\lambda(1-q_k)t}}{\prod_{j=0,\ j\neq k}^{n} (q_k - q_j)} . \tag{23}$$

If the transparency factor of a single cloud is exactly $q$, i.e., if $\psi(q') = \delta(q' - q)$, we have merely to replace $q_n$ by $q^n$. The solution then is identical with equation (7).

# NOTES

## THE COMPOSITE SPECTRUM OF HD 50820*

J. S. Plaskett[1] found several peculiarities in the spectrum of HD 50820,[2] most of which could be explained if it were a spectroscopic binary. Thus the hydrogen and helium lines suggested a B3 star, while the numerous metallic lines between $H\beta$ and $H\delta$ suggested a spectral type of F. The metallic lines faded below about λ 4150, as would be expected from the superposition of the continuum of the hotter star. However, Plaskett's measures of velocities from the two sets of lines were equal and constant throughout his series of plates (within the errors of measurement); and this fact led him to reject the binary hypothesis, presumably because he felt that the probability of observing a binary system at right angles to the plane of its orbit was small. Since he occasionally observed an emission line at $H\beta$, he tried to explain the spectrum in terms of a "shell" like that of $\upsilon$ Sgr, but found that this explanation was not satisfactory.

Four plates of this star were taken at the McDonald Observatory with the Cassegrain quartz spectrograph on January 10, 12, and 13, 1952. They show the spectrum to be clearly composite: one star is a beautiful example of a "pole-on" Be3 V star, with strong, narrow, single emission components centrally placed on the broad absorption lines of hydrogen. The helium lines are narrow, as in typical "pole-on" Be stars. The emission lines can be clearly seen as far as *H*22, while the absorption lines can be resolved only as far as *H*16 or *H*17. Thus the star resembles 11 Cam, 12 Aur, HD 37998, and HD 58050, in that the Balmer emission lines toward the series limit are comparatively strong.[3] This may be an effect of self-absorption in the lower members of the series. The hydrogen emission lines are clearly much stronger than they were when this star was observed by Plaskett. Merrill[4] has remarked that they are variable.

The metallic-line spectrum has a rather "washed-out" appearance, owing to superposition of the continuum of the hotter star. The appearance of the G band, *Ca* I 4226, and the *Fe* I lines place it as an F star; but it is difficult to find the subdivision because of the interference from the hotter spectrum.

Two further plates were obtained at the Yerkes Observatory with the small spectrograph and 12-inch camera. One was in the photographic and one was in the visual region. The former (taken on January 12, 1953) shows that the strength of the hydrogen emission lines was approximately the same as it had been a year previously. The latter (taken on February 18, 1953) shows that the late-type component completely dominates the spectrum in the visual region. The only feature due to the hotter star is a strong emission line of *Ha*; other lines are all absorption lines of *Fe* I, *Ca* I, *Na* I, *Ti* I, *Mg* I, *Cr* I, etc.

Measures of the four McDonald plates yielded velocities for the B and the F stars which were not significantly different from each other, in view of the scatter between individual lines, and which were in reasonable agreement with the measures of J. S. Plaskett. It follows, therefore, that the line of sight must be nearly at right angles to the

* *Contributions from the McDonald Observatory, University of Texas*, No. 236.

[1] *Pub. Dom. Ap. Obs. Victoria*, **4**, 1, 1931.

[2] MWC 827; $\alpha_{1900} = 6^h49^m.7$; $\delta_{1900} = -1°38'$; $m_v = 6.25$.

[3] G. R. Burbidge and E. M. Burbidge, *Ap. J.*, **118**, 252, 1953.

[4] *Ap. J.*, **110**, 387, 1949.

plane of the orbit of the binary system. Since we assume that the axes of rotation of the components of a binary system are parallel to the axis of orbital motion, the line of sight must make only a small angle with the axis of the Be star. This is a fine illustration of the theory that the Be stars which have been classified as "pole-on" are those in which the line of sight makes a small angle with the axis of rotation of the star.[5]

Plaskett judged that if the star were a binary, the two components would have approximately equal intensities at λ 4800. The late-type component would thus have a slightly brighter visual magnitude than the B star. The absolute visual magnitude of a B3 V star is −2.0; thus the F star must be of luminosity class II.[6] The spectrum is not inconsistent with this; but the best check would be to compare the visual spectrum, where interference from the B component disappears, with stars of standard spectral types and luminosity classes.

E. Margaret Burbidge
G. R. Burbidge

8a Botolph Lane
Cambridge, England
November 15, 1953

[5] O. Struve, *Ap. J.*, **73**, 94, 1931, and subsequent papers; A. Slettebak, *Ap. J.*, **110**, 498, 1949; G. R. Burbidge and E. M. Burbidge, *Ap. J.*, **117**, 407, 1953.

[6] P. C. Keenan and W. W. Morgan, *Astrophysics*, ed. J. A. Hynek (New York: McGraw-Hill Book Co., 1951), p. 23.

## THE POLARITY OF THE SUN'S MAGNETIC FIELD AND THE RICHARDSON-SCHWARZSCHILD OSCILLATION

In a recent paper, Richardson and Schwarzschild[1] have analyzed the motion in heliographic latitude of 1800 sunspot groups and 400 individual spots. They found an apparently significant oscillation with a 22-year period, in the sense that in "even" sunspot cycles (such as that started in 1914) the apparent motions were directed toward the equator, while in "odd" cycles the motions were poleward. This oscillation has a semi-amplitude in latitude displacement of 5°.5. The authors further concluded that, in accord with the equatorial acceleration in angular velocity, a given element of photospheric matter that oscillates in latitude must also oscillate in longitude. They deduced a semi-amplitude of displacement in longitude of 170° and concluded that such displacements in longitude should distort a permanent dipole-like field, producing toroidal magnetic fields opposite in sign in the northern and southern hemispheres and changing sign every 11 years. They pointed out that such oscillating toroidal fields would have just the right characteristics to be thought of as the large-scale fields from which the magnetic fields of sunspots could arise by local perturbations, provided that the general field of the sun has the proper polarity.

Since two conflicting definitions of the magnetic polarity of the sun's main field have appeared in the literature, this note is written to point out that the observed magnetic polarities of sunspots as predicted by the Richardson-Schwarzschild oscillation are in accord with the positive magnetic polarity as reported for the sun from observations with the solar magnetograph during the last 18 months.[2]

The definition of magnetic polarity as currently employed for the sun and stars is that

[1] "On the Possibility of a 22-Year Oscillation of the Sun," in *Convegno* [Volta] *di scienze fisiche, matematiche e naturali* (Rome: Accademia nazionale dei Lincei, 1953), p. 228.

[2] H. W. Babcock and H. D. Babcock, *Pub. A.S.P.*, **64**, 282, 1952; H. W. Babcock, *Ap. J.*, **118**, 387, 1953.

a magnetic vector pointing toward the observer is positive in sign.[3] This is the direction in which a "free" positive (north-seeking) magnetic pole would move. Hence the north geographic pole (as seen by an external observer) would be said to have negative magnetic polarity and the sun's north heliographic pole is of positive magnetic polarity. This agrees with the alternative definition that, as seen from the north pole of rotation, a spin in the positive direction of a sphere having a positive electric charge will induce a field of positive magnetic polarity.

HORACE W. BABCOCK

MOUNT WILSON AND PALOMAR OBSERVATORIES
CARNEGIE INSTITUTION OF WASHINGTON
CALIFORNIA INSTITUTE OF TECHNOLOGY
December 16, 1953

[3] H. W. Babcock and T. G. Cowling, *M.N.*, **113**, 357, 1953.

# REVIEWS

*General Catalogue of Stellar Radial Velocities*. By RALPH ELMER WILSON. ("Carnegie Institution of Washington Publications," No. 601; "Papers of the Mount Wilson Observatory," Vol. **8**.) 1953. Pp. 344+x. $2.50, paper-bound; $2.85, cloth-bound.

Since the publication of J. H. Moore's catalogue of radial velocities (*Pub. Lick Obs.*, Vol. **18**), now more than twenty years ago, the number of stars for which radial velocities were published has been more than doubled. The compilation of all these data, scattered in the astronomical literature, and their reduction to a homogeneous system, has been an enormous task, and Dr. Wilson has put all workers in statistical astronomy (and many outside this field) under his obligation by the publication of the new catalogue. There is no doubt that it will play a role in the study of stellar motions in the next decades at least as important as Moore's catalogue did in the last twenty years.

The arrangement of the pertinent data for each star, with the most reliable velocity and an indication of its quality in the *General Catalogue* and with the more detailed information with regard to the values published by different observatories in the Notes to this catalogue, is well chosen. The inclusion of about 1000 hitherto unpublished velocities is another welcome feature of the catalogue. It contains 15,106 stars, gaseous nebulae, and globular clusters. No data on extragalactic objects are presented. Interstellar line velocities are included.

It is stated in the Introduction to the catalogue that "the present seems to be a logical time for publication, for it marks not only the completion of approximately half a century of effective radial velocity work, but also the beginning of a new era in astrophysics, in which the emphasis has changed from studies of stellar motions and the dynamics of the stellar system to the application of new techniques to the study of stellar atmospheres and of extragalactic systems." It seems to the reviewer that a more optimistic view with regard to the study of stellar motions and to the use of the new catalogue is justified. It rather looks as if the study of stellar motions will reveal essential information for the study of stellar evolution and of the evolution of the galaxy. The publication of the new catalogue, therefore, may well be a milestone marking a new era of increased interest in the study of radial velocities.

A. BLAAUW

*Yerkes Observatory*

ABSTRACTS OF ASTROPHYSICAL JOURNAL
SUPPLEMENT SERIES

Supplement No. 4, Volume I, pages 91–119, May, 1954

# PHOTOMETRIC INVESTIGATION OF THE ECLIPSING BINARY UX URSAE MAJORIS

H. L. Johnson,* Barbara Perkins, and W. A. Hiltner
Yerkes and McDonald Observatories

The eclipsing binary UX Ursae Majoris, with the shortest known period ($4^h43^m$), has been observed in detail photoelectrically at three effective wave lengths—ultraviolet, blue, and yellow—on eleven nights during the years 1951–1953.

A "typical" light-curve appears to be one with a bright shoulder before principal minimum, a principal minimum with a depth of about 1.1 mag., a standstill on the ascending branch of the primary minimum, a slow decrease in brightness to phase 0.7, and a light-increase to the bright shoulder before primary minimum. No secondary minimum was observed.

The light-curve does not repeat. Differences as great as 0.5 mag. in the ultraviolet are observed. Fluctuations on a smaller scale, of the order of 0.2 mag. in the ultraviolet and approximately half as great in the blue and yellow, are often present. Frequently these fluctuations display a period near 20 minutes. Shorter-period fluctuations are probably present but not resolved.

The anomalies of the light-curves can best be interpreted in terms of absorption of radiation from the primary star rather than from the existence of bright areas on the surface of that star.

* Now at the Lowell Observatory, Flagstaff, Arizona.

# THE OBSERVATORY

FOUNDED 1877

* * *

A Magazine presenting current developments in Astronomy by means of Articles, Correspondence, Notes on discoveries and Reviews of important astronomical books. The papers read at the Meetings (Astronomical & Geophysical) of the Royal Astronomical Society and the discussions which follow are also fully reported.

* * *

*Annual subscription for 6 issues, post free, £1 (U.S.A. and Canada, $3.00) should be sent to*

*The Editors,* ROYAL GREENWICH OBSERVATORY

Herstmonceux Castle, Hailsham, Sussex, England

*Announcing*

## MEASUREMENTS OF DOUBLE STARS, III

By GEORGE VAN BIESBROECK

PUBLICATIONS OF THE YERKES OBSERVATORY, VOLUME VII, PART VI

"This work lists measurements of the position angles and separations of about 2,500 close double stars, mostly in the years 1935 to 1951, with the 40-inch Yerkes refractor and the 82-inch McDonald reflector. New orbits are given for 19 binary systems, and new dynamical parallaxes are published for many slow-moving pairs."—*Sky and Telescope*

*244 pages, paper, $10.00*

THE UNIVERSITY OF CHICAGO PRESS

5750 ELLIS AVENUE CHICAGO 37, ILLINOIS

# THE SUN

## *The Solar System*

### VOLUME I

***Edited by* GERARD P. KUIPER**

***The Sun***, the first of four volumes intended to collect and systematize all significant information on the sun, the planets, the satellites, the comets, and the smaller bodies of the solar system, is written by twenty-three solar physicists from six different countries. It is designed with a dual purpose. On the one hand, it is an invaluable reference handbook for the specialist. On the other hand, it is intelligible to anyone versed in the physical sciences.

*The Sun* covers the divisions of solar physics comprehensively: the solar interior and energy production, the photosphere and the Fraunhofer spectrum; the chromosphere and the solar electrodynamics; and the many modern techniques of solar observation. All are discussed in detail. The book contains, in addition, many new illustrations and over one thousand references to the literature.

New models are given for the solar interior, based on integrations using the latest information on nuclear cross-sections. The photosphere models are critically reviewed, and a new compromise solution is proposed. Similarly, a very recent model for sunspots is reviewed. For both the chromosphere and the corona the temperature and density data are critically examined. An extensive treatment of solar radio astronomy adds significantly to the optical studies of solar phenomena treated in other chapters.

A special feature of *The Sun* is its two tables of solar observatories and their equipment, accessories, and programs. Other features include the latest results on the magnetic field and the solar component of cosmic rays, recent additions to instrumental techniques, and a record, as complete as possible, of the far-ultraviolet solar spectrum photographed on rocket flights.

*Many illustrations, 784 pages, $12.50*

---

**THE UNIVERSITY OF CHICAGO PRESS**